[redacted]

[redacted]

NASA-CR-120839

Gulf-GA-A11049

[redacted]

[redacted] (Title Unclassified)

STUDIES OF THERMIONIC MATERIALS FOR SPACE POWER APPLICATIONS

SUMMARY REPORT

JUNE 1, 1968 THROUGH JANUARY 31, 1971

Prepared for
National Aeronautics and Space Administration
Lewis Research Center
under Contract NAS 3-11822

[redacted]

[redacted] RESTRICTED DATA ATOMIC ENERGY ACT 1954

Issued: January 25, 1972

GULF GENERAL ATOMIC COMPANY, P.O. BOX 608, SAN DIEGO, CALIFORNIA 92112

[redacted]

229

[redacted]

GULF GENERAL ATOMIC
P.O. BOX 608, SAN DIEGO, CALIFORNIA 92112

Copy No. 18

NASA-CR-120839

Gulf-GA-A11049

[redacted]

STUDIES OF THERMIONIC MATERIALS FOR SPACE POWER APPLICATIONS

SUMMARY REPORT

JUNE 1, 1968 THROUGH JANUARY 31, 1971

Sponsored by
National Aeronautics and Space Administration
Lewis Research Center

Technical Management
NASA-Lewis Research Center
Nuclear Systems Division
J. W. R. Creagh

[redacted]
Excluded from automatic downgrading
[redacted]

[redacted]
RESTRICTED DATA
ATOMIC ENERGY ACT 1954

Project: 6082
Contract: NAS 3-11822

Issued: January 25, 1972

[redacted]
CONFIDENTIAL

PREVIOUS SUMMARY REPORTS

Contract NAS 5-1253	GA-3523, Final Report for the Period Ending August 31, 1962. (U)
Contract NAS 3-2301	GA-3642, Final Report for the Period Ending August 31, 1962. (U)
Contract NAS 3-2532	GA-4769, Final Report for the Period Ending August 31, 1963. Part I (U), Part II (C/RD)
Contract NAS 3-4165	NASA CR-54322, GA-5665, Summary Report for the Period September 1, 1963 through August 31, 1964. (C/RD)
Contract NAS 3-6471	NASA CR-54980, GA-6860, Summary Report for the Period September 1, 1964 through November 23, 1965. (C/RD)
Contract NAS 3-8504	NASA CR-72315, GA-7682, Summary Report for the Period November 23, 1965 through January 31, 1967. (C/RD)
Contract NAS 3-8504	NASA CR-72327, GA-7745, Semi-Annual Report for the Period February 1, 1967 through July 31, 1967. (C/RD)
Contract NAS 3-6471	NASA CR-72517, GA-8974, Summary Report for the Period November 23, 1965 through September 30, 1968. (C/RD)
Contract NAS 3-8504	NASA CR-72627, GA-8956, Summary Report for the Period February 1, 1967 through July 31, 1969. (C/RD)
Contract NAS 3-8504	NASA CR-72947, Gulf-GA-11035, Summary Report for the Period August 1, 1969 through December 7, 1970. (C/RD)

(This page is Unclassified)

CONTENTS

CONTENTS (Continued)

[redacted]

FIGURES

[redacted]

[redacted]

FIGURES (Continued)

(This page is Unclassified)

FIGURES (Continued)

FIGURES (Continued)

FIGURES (Continued)

FIGURES (Continued)

FIGURES (Continued)

FIGURES (Continued)

FIGURES (Continued)

TABLES

TABLES (Continued)

(This page intentionally left blank)

INTRODUCTION

(U) This report describes the work carried out under Contract NAS 3-11822 from June 1, 1968 through January 31, 1971 for the development of materials for nuclear thermionic application. Two tasks were involved during this reporting period. These are:

1. Study of effect of tungsten cladding structures on carbide fuel component transport rates.

2. Preparation and evaluation of (110) preferentially oriented cylindrical vapor-deposited tungsten emitters.

Other tasks on thermionic material research and development were carried out concurrently under Contracts NAS 3-6471, NAS 3-8504, NAS 3-12980, and NAS 3-13463. A list of previously published reports on thermionic material work sponsored by NASA at Gulf General Atomic is shown on the page next to the title page.

SUMMARY

(C-RD)(Gp-1) The effect of microstructures of tungsten cladding on the transport rates of carbide fuel components was studied at temperatures of thermionic interest. Hyperstoichiometric 90UC-10ZrC (C/U = 1.04) containing 4 wt% tungsten was clad with various types of tungsten material of 40 mil thickness. These include (1) chloride tungsten prepared by hydrogen reduction of tungsten chlorides, (2) columnar-grained fluoride tungsten prepared by hydrogen reduction of WF_6, (3) modified fluoride tungsten prepared at San Fernando Laboratory, (4) powder metallurgy tungsten, (5) arc-cast tungsten, and (6) duplex tungsten consisting of 10 mils of chloride tungsten deposited on 30 mils of columnar-grained fluoride tungsten, powder metallurgy tungsten, or arc-cast tungsten substrates. Screening tests of 1000 hour duration were first carried out at 2073°K. Selected samples were then subjected to long-term tests up to 10,000 hours at temperatures of thermionic interest. Vacuum work functions of the test samples were followed as a function of time in vacuum emission cells for planar emitters. The fuel components transported through the cladding were collected on a water-cooled collector and analyzed for uranium, zirconium and carbon contents. For some test samples, C^{14} was incorporated into the carbide fuel material in order to improve the sensitivity of carbon analysis. In the presence of carbide fuel,

the (110) oriented chloride tungsten maintained the same high vacuum work function (~4.95 eV) as that of an unfueled emitter at all the temperatures tested. The fluoride tungsten, however, exhibited a vacuum work function higher than that of an unfueled emitter (4.75 versus 4.5 eV) at these test temperatures, although the value decreased slightly with the lowering of the temperature. Claddings of equiaxial grain structures showed much lower fuel transport rates than claddings of columnar grain structures. Of all the claddings studied at 2073°K, chloride tungsten had the lowest uranium transport rate while columnar fluoride tungsten had the highest, the difference being about two orders of magnitude (2.9×10^{-11} gm/cm^2 hr versus 3.4×10^{-9} gm/cm^2 hr). For the 10,000 hour long term test at 1923°K, the chloride-arc-cast duplex tungsten cladding had lower fuel transport rates than the other types of duplex tungsten cladding studied, the uranium and the carbon transport rates being 1×10^{-11} and 2×10^{-11} gm/cm^{2}hr respectively. A reaction layer of UWC_2 phase of less than 1 mil thickness was observed at the fuel-cladding interface in all the cases studied. The vacuum work function of the cladding, however, did not seem to be affected by the formation of such an interaction layer. The results indicate that the microstructures of the tungsten cladding strongly affect the transport rates of carbide fuel components and therefore should have significant influence on the electrode work functions and the thermionic performance stability of carbide fueled converters.

(U) The conditions for preparing (110) oriented cylindrical chloride tungsten emitters of high vacuum work functions were investigated. A

deposition apparatus for cylindrical emitters was fabricated. Specimen sets were deposited on fluoride tungsten substrates for the evaluation of the effect of various deposition parameters on the degree and uniformity of the (110) preferred orientation and the vacuum work function, using X-ray examination techniques and a vacuum emission cell specially designed and built for such purposes. The deposition parameters studied are: (1) gas pressure in deposition chamber, (2) H_2/W ratio in gaseous reactant, (3) mandrel temperature, (4) oxygen and nitrogen impurities in gaseous reactants, (5) change of W/Cl ratio in gaseous reactants, (6) WF_6 addition, and (7) helium diluent in gaseous reactants. The evaluation results established the following reference conditions for the deposition of emitters: chlorine flow rate, 360 c.c./min.; hydrogen flow rate 350 c.c./min.; chamber gas pressure, 6 torr; mandrel temperature 1323°K; temperature of tungsten chip column providing the tungsten chlorides by chlorination, 4 inches at 873°K and 4 inches at 1273°K. Specimens prepared under the reference conditions yielded vacuum work functions of 4.9-5.0 eV. Strong deviations from the reference conditions, such as the use of H_2/W much higher or lower than the stoichiometric value 3.0, and the presence of oxygen and nitrogen impurities, WF_6, or large amount of helium diluent, led to lower vacuum work functions. In the range of 4.8 to 5.0 eV, an approximately linear relationship exists between the vacuum work function ϕ and the tilt angle θ within which 90% of the <110> axes scanned by the X-rays are located. The relationship allows the prediction of ϕ to within ±0.05 eV from θ determined by X-rays. Long-term tests showed that the

high vacuum work function (4.9-5.0 eV) of a cylindrical emitter was stable and the chloride tungsten to fluoride tungsten bond remained in excellent shape after 4850 hours at 2073°K.

(This page intentionally left blank)

PRECEDING PAGE BLANK NOT FILMED

PART I. STUDY OF EFFECT OF TUNGSTEN CLADDING STRUCTURES ON CARBIDE FUEL COMPONENT TRANSPORT RATES

1.1. OBJECTIVES

(C-RD)(Gp-1) It is generally recognized that excessive transport of carbide fuel components through tungsten emitter cladding in a cesiated converter affect electrode work functions and lower converter electrical output and efficiency.[1],[2] Means for minimizing such material transports is thus essential to the improvement of the performance and efficiency of a thermionic fuel element.

(C-RD)(Gp-1) During 1964-1967, the uranium transport rates from carbide fuel materials through CVD (chemical-vapor-deposited) fluoride tungsten cladding prepared by the hydrogen reduction of WF_6 were measured in the temperature range 2023-2223°K. This work was carried out in conjunction with long-term diffusion emission studies[3][4] and life testing of out-of-pile fueled converters.[5] For 90UC-10ZrC containing 2 mol% of excess carbon,[4] the uranium and carbon transports rates were of the order of 10^{-8} and 10^{-9} gm/cm^2 hr respectively at 2073°K for a cladding thickness of

of 40 mils, which correspond to the formation of several hundred monolayers of deposit on the collector surface. The fuel material dissolved tungsten during the test and the excess carbon concentration decreased to less than 1 mol% at the end of the test.

(C-RD)(Gp-1) Significant progress was made during 1966-1967 in improving both the tungsten cladding and the carbide fuel materials. For the carbide fuel materials, techniques[6] were developed to insure hyperstoichiometry (C/U = 1.03 - 1.05) and to incorporate 4 wt% of tungsten (together with its carbon share in the ratio of one carbon atom to two tungsten atoms) into UC-ZrC. The addition of tungsten together with its carbon share prevents the dissolution of the tungsten cladding by the fuel and the increase of uranium activity of the fuel due to tungsten dissolution. Both the addition of tungsten and the insured hyperstoichiometry of the fuel material should help to lower the uranium activity and therefore the uranium transport rate through the cladding. For the claddings, conditions for the deposition of tungsten of (110) preferred crystal orientation by the hydrogen reduction of tungsten chlorides were established.[7] Deposits of vacuum work functions as high as 5 eV were prepared. Such chloride tungsten deposits can be deposited on CVD fluoride tungsten substrates to form a stable duplex structure which combines the advantage of an emitting surface of high vacuum work function and a substrate of proven mechanical stability. Upon thermal treatment at high temperatures, chloride tungsten develops equiaxial grain structures which are similar to that obtained in

arc-cast or powder metallurgy tungsten. Since the uranium transport rate from UO_2 through equiaxial grained arc-cast and powder metallurgy tungsten cladding has been shown to be orders of magnitude lower than that through columnar grained fluoride tungsten,[8] it was believed that this might also be true for the transport of carbide fuel components through claddings consisting of chloride tungsten either as a single layer or as a deposit on other types of tungsten, such as fluoride tungsten, power metallurgy tungsten and arc-cast tungsten.

(C-RD)(Gp-1) In view of the above described improvements in carbide fuel and tungsten cladding, experiments were planned under this contract for the study of the fuel component transport behaviors of such fuel-cladding systems. Specifically, information was sought for answering the following questions.

1. How are the rates of transport of fuel components from hyper-stoichiometric (C/U = 1.03 - 1.05) tungsten-containing (4 wt% W) 90UC-10ZrC through tungsten claddings affected by the grain structure of the claddings in the temperature range of thermionic interest and upon thermal cycling?

2. How are the vacuum work functions of tungsten claddings of various types of grain structures affected by such fuel component transports? Can chloride tungsten maintain its high vacuum work function in the presence of such fuel component transports?

(C-RD)(Gp-1) Short-term screening tests were carried out on various types of tungsten claddings to gain preliminary information on their fuel component transport behaviors and vacuum emission properties. Selected cases were then subjected to long-term life tests. Experimental techniques and test results are described below in this order.

1.2. SCREENING TESTS

1.2.1. Experimental Equipment and Procedures

1.2.1.1. Fuel and Cladding Materials. (C-RD)(Gp-1) The 90UC-10ZrC fuel material was prepared by the isostatic cold pressing and sintering techniques developed under Contract NAS 3-8504.[9] Figure 1 shows the microstructures of the fuel material after outgassing for 50 hours at 2073°K. Chemical analysis yielded a composition of $U_{0.426}Zr_{0.047}W_{0.025}C_{.502}$ which corresponded to a C/U ratio of 1.04, allowing one C to each Zr and one C to every two W.

(C-RD)(Gp-1) Six types of tungsten claddings were selected for the screening tests. Cast tungsten and powder metallurgy tungsten were obtained from Dr. A. I. Kaznoff of General Electric, Vallecitos Nuclear Center through the NASA Project Manager. Columnar fluoride tungsten and modified fluoride tungsten were procured from San Fernando Laboratory (SFL)

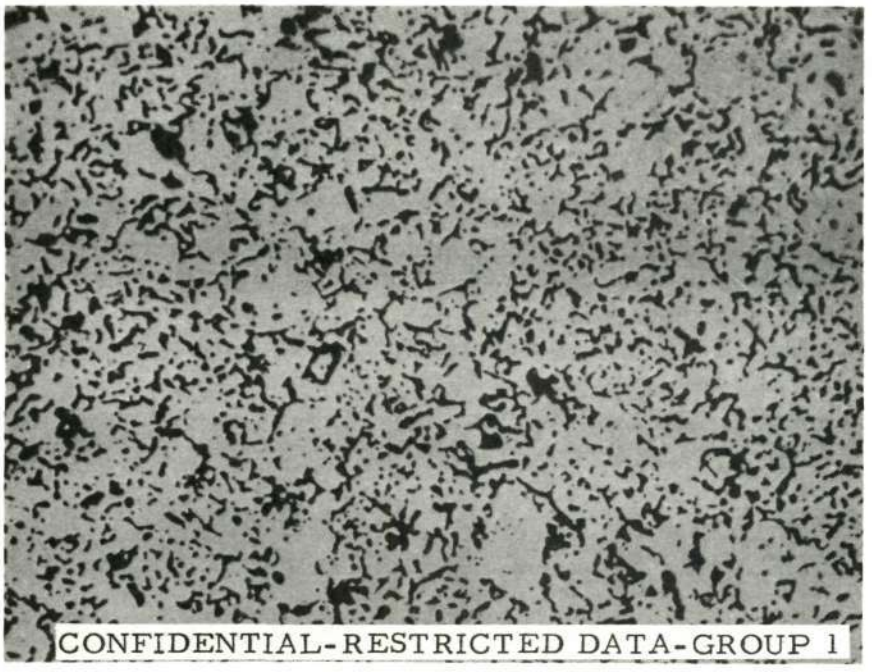

M 31488-1 250X

(a) Unetched

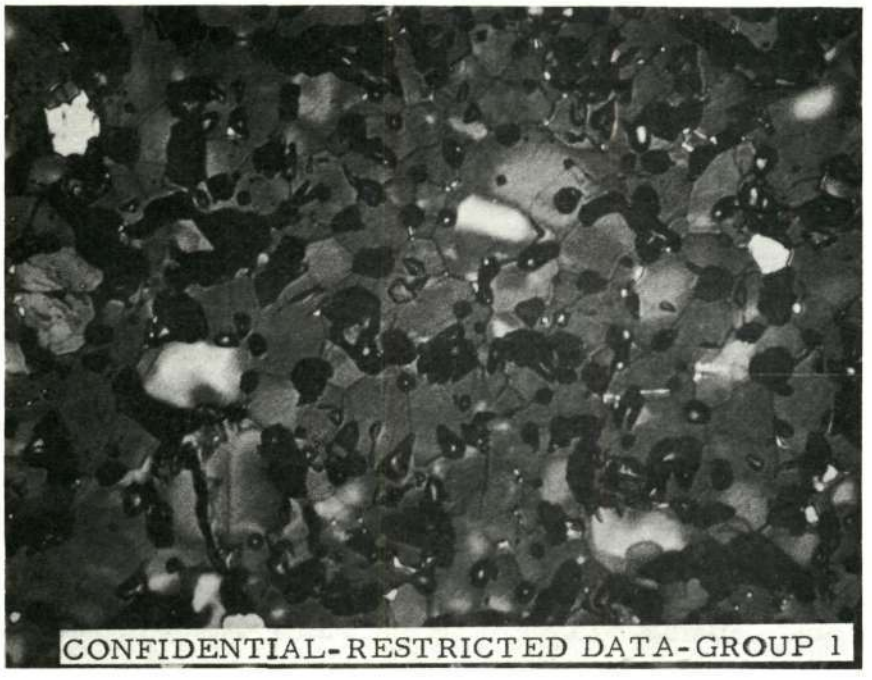

M 21488-2 1000X

(b) Etched

Fig. 1. (U) Microstructures of carbide fuel material used in screening test samples

of Fansteel Metallurgical Corporation. Chloride tungsten and duplex tungsten were prepared at Gulf General Atomic according to the procedures developed under Contract NAS 3-8504 during 1967 - 1968.[7] These tungsten materials were outgassed at 2123°K for 200 hours and then characterized with regard to their microstructures, degree of preferred orientation, and impurity contents. Figure 2 shows the microstructures of these tungsten materials. The chloride tungsten had the largest grain size, while the SFL modified fluoride tungsten was less columnar in grain structure than the conventional fluoride tungsten. Table 1 contains the chemical analysis results. Among the six types of tungsten materials studied, the cast tungsten had the highest oxygen and nitrogen concentrations; the powder metallurgy tungsten had the highest iron impurity concentration; while the chloride tungsten appeared to be the purest.

1.2.1.2. Sample Configuration. (C-RD)(Gp-1) Samples of planar configuration were used. Figure 3 illustrates schematically the arrangement of the fuel wafer in the test sample, and shows the dimensions of the various parts. The fuel wafer, supported by a cast tungsten spacer, was encapsulated inside the fuel cavity with chloride tungsten. The encapsulated sample was machined to the required dimensions. The emitting surface of each sample was prepared by surface grinding, followed by polishing with 1-micron diamond paste, and electropolishing in NaOH to remove disturbed metal. The six samples prepared were designated as F_1 (columnar fluoride tungsten), E_1 (SFL modified fluoride tungsten), C_1 (arc-cast tungsten), P_1 (powder metallurgy tungsten),

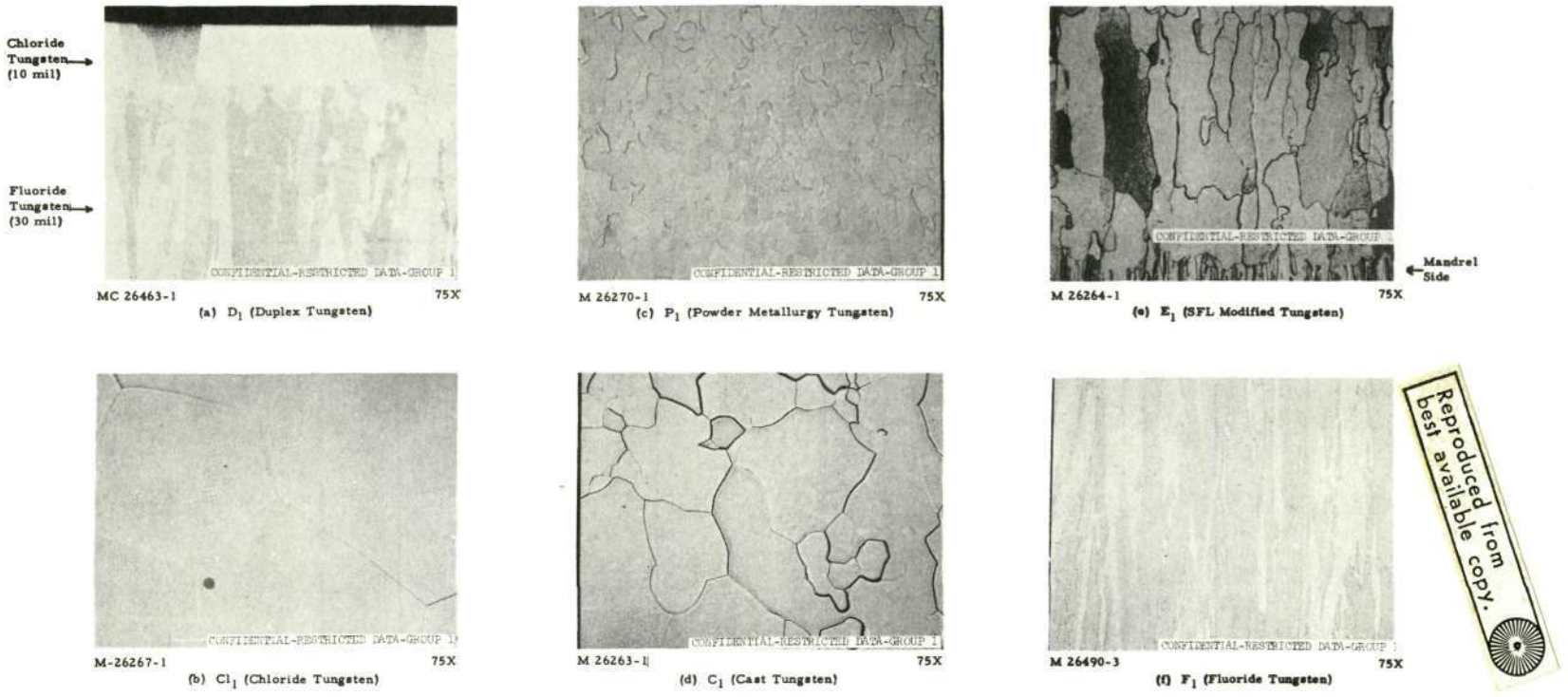

Fig. 2. (C-RD)(Gp-1) Typical grain structures of the cross sections of the six types of tungsten claddings used in fuel transport rate study after 200 hours at 2123°K

TABLE 1

(U) IMPURITY CONTENTS IN VARIOUS TYPES OF TUNGSTEN CLADDING MATERIALS AFTER 200 HOURS AT 2123°K IN VACUUM

(All concentrations are in PPM)

(This table is Unclassified)

Type of Tungsten	C	F	Cl	O	N	Al	Bi	Fe	Mg	Mn	Ni	Pb	Si
Columnar Fluoride F_1	5	15	9	6	<1	ND	4.0	6.2	0.1	0.2	ND	ND	ND
Arc Cast C_1	2	<3	0*	29	5	0.8	ND	5.0	0.1	ND	ND	3.4	1.2
Powder Metallurgy P_1	4	<3	0*	3	<1	1.1	ND	50.5	0.1	ND	2.1	ND	ND
SFL Modified Fluoride E_1	12	6	12	15	2	ND	ND	ND	ND	0.6	ND	3.5	ND
Chloride Cl_1	2	<3	5	2	1	0.8	ND	ND	ND	0.2	ND	ND	ND
Duplex D_1	3	<3	15	3	<1	0.4	ND	ND	ND	ND	1.3	ND	ND

*Less than 5 ppm

ND - Means not detected at the limit of sensitivity.

(This page is Unclassified)

TABLE 1 (Continued)

The Elements searched for and their limits of sensitivity are as follows:

Element	Concentration (PPM)	Element	Concentration (PPM)	Element	Concentration (PPM)
Ag	0.02	Ga	2.0	Rh	10.0
Al	0.3	Hf	100.0	Ru	40.0
As	10.0	Hg	5.0	Sb	1.0
Au	1.0	In	10.0	Si	1.0
B	1.0	Ir	400.0	Sn	0.9
Be	0.1	Mg	0.05	Sr	10.0
Bi	0.05	Mn	0.1	Te	25.0
Cd	3.5	Mo	15.0	Th	80.0
Ce	20.0	Na	200.0	Ti	5.0
Cr	8.0	Nb	1.0	Tl	4.0
Co	5.0	Ni	0.3	V	2.0
Cu	0.3	P	0.8	Zn	10.0
Fe	4.0	Pb	3.0	Zr	20.0

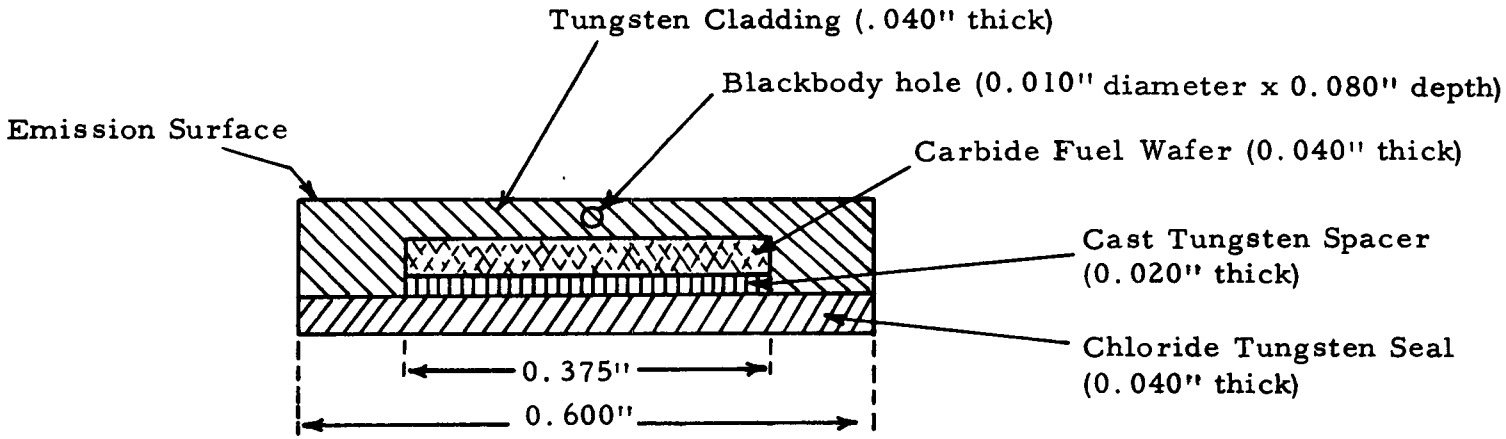

Fig. 3. (U) Configuration and dimension of test sample

D_1 (duplex fluoride-chloride tungsten) and Cl_1 (chloride tungsten). Figures 4 through 7 show the degree of preferred crystal orientations of the emitting surfaces of Cl_1, D_1, E_1, and F_1. Cl_1 and D_1 possessed (110) preferred crystal orientation, while E_1 and F_1 possessed (100) preferred crystal orientation. C_1 had a very weak (110) preferred orientation; no X-ray pole figure plot could be made because of the very high background created by the randomly oriented grains which predominated the structure. The grain orientations of P_1 were essentially random. For the duplex structure, the thickness of the chloride tungsten layer was 10 mils and the thickness of the fluoride tungsten substrate was 30 mils.

1.2.1.3. Vacuum Emission Studies. (C-RD)(Gp-1) The vacuum emission characteristics of the test samples were studied in a vacuum emission cell which was described previously in the Ref. 3 report. The sample was held in a tungsten holder and heated by electron bombardment of the chloride tungsten seal side. The temperature of the emitting surface was measured with a calibrated micro-optical pyrometer sighting into a blackbody hole located about 10 mils under the emitting surface. The current-voltage relationship between the emitting surface and a water-cooled copper-plated stainless steel collector-guard ring assembly was determined at an emitter temperature of 2073°K, from which the effective work function of the emitting surface was calculated.

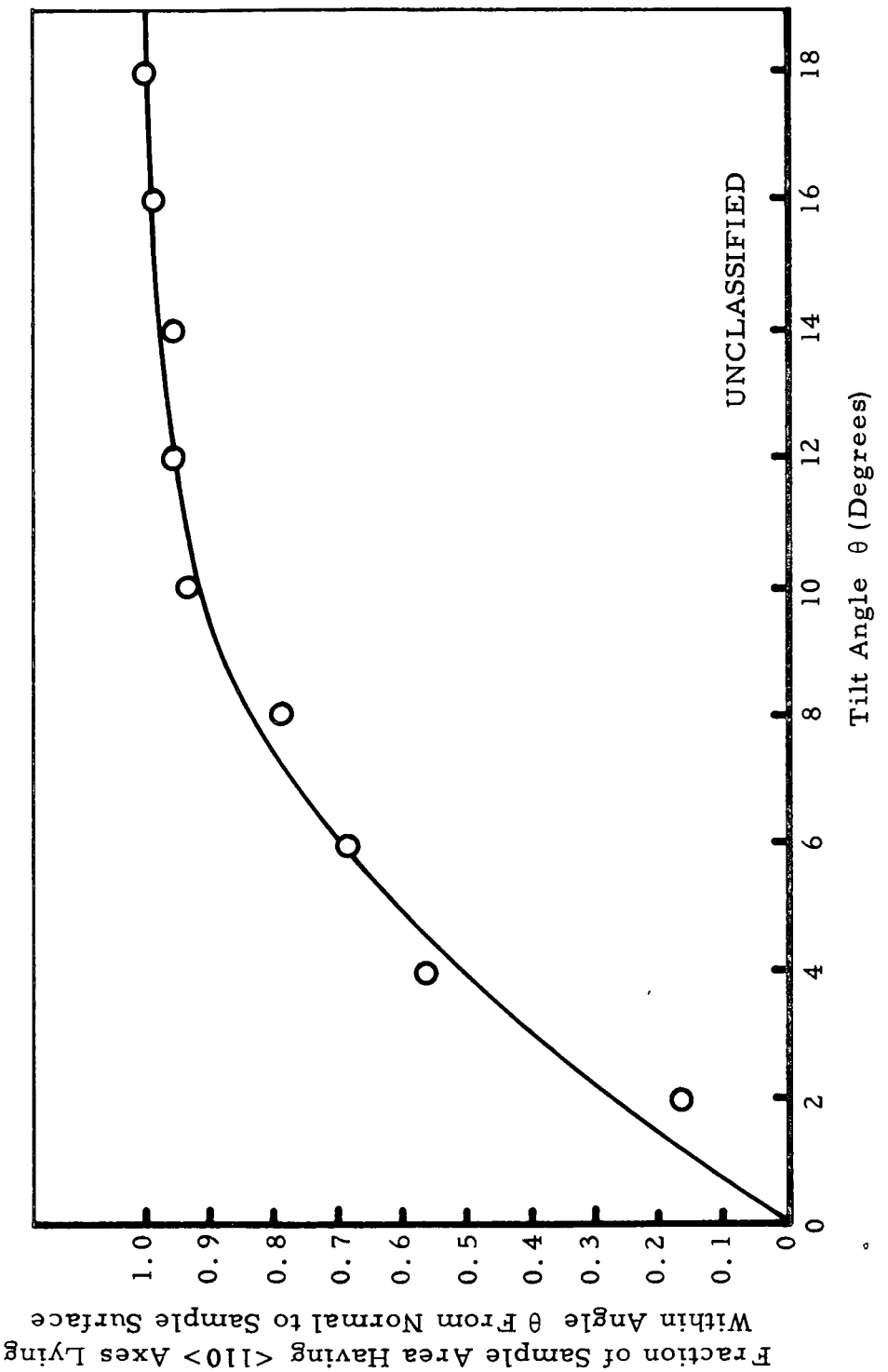

Fig. 4. (U) Spatial distribution of the <110> axes in vapor deposited chloride tungsten sample Cl_1

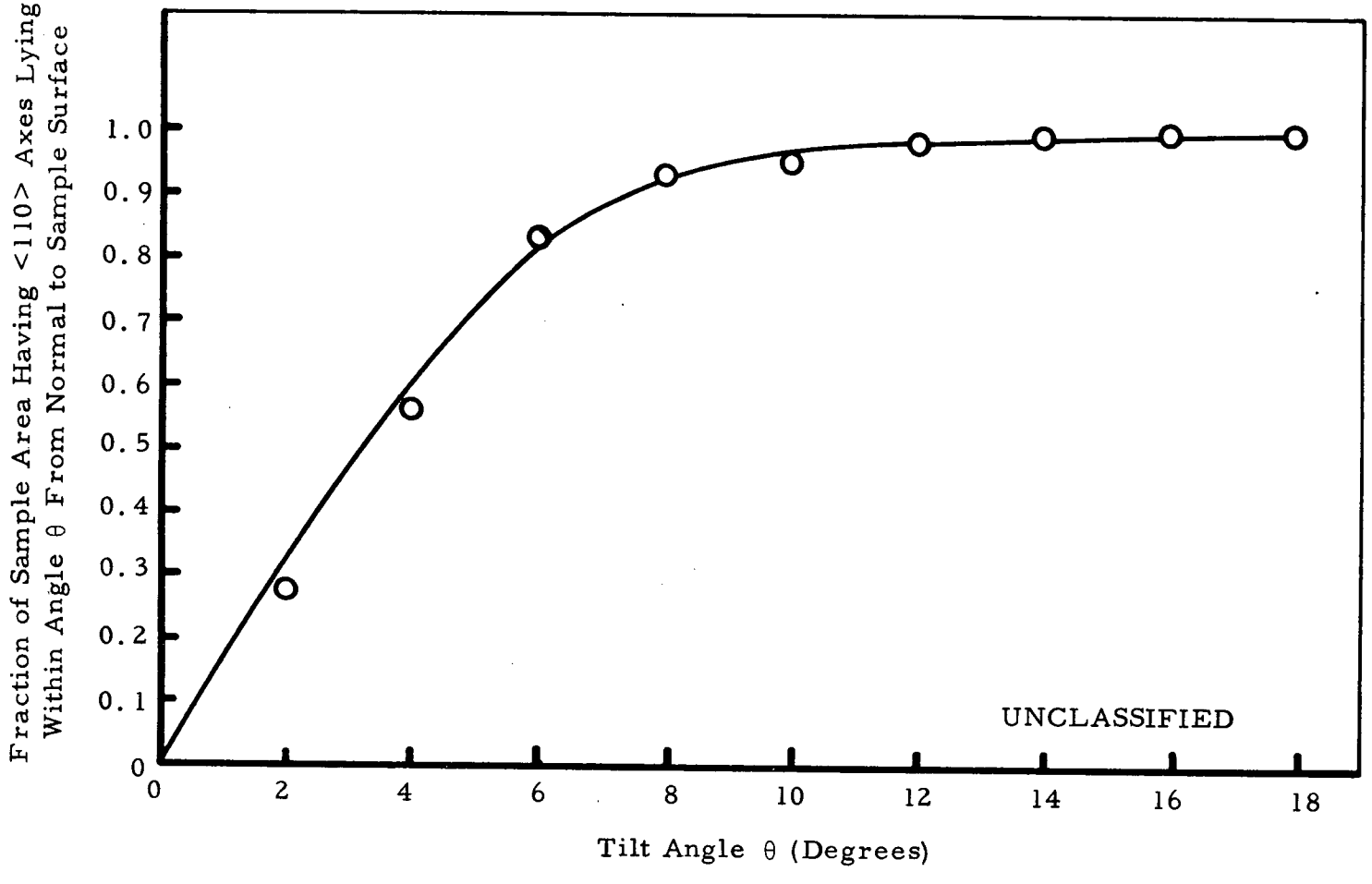

Fig. 5. (U) Spatial distribution of the <110> axes in duplex tungsten sample D_1 (vapor deposited chloride tungsten on vapor deposited fluoride tungsten)

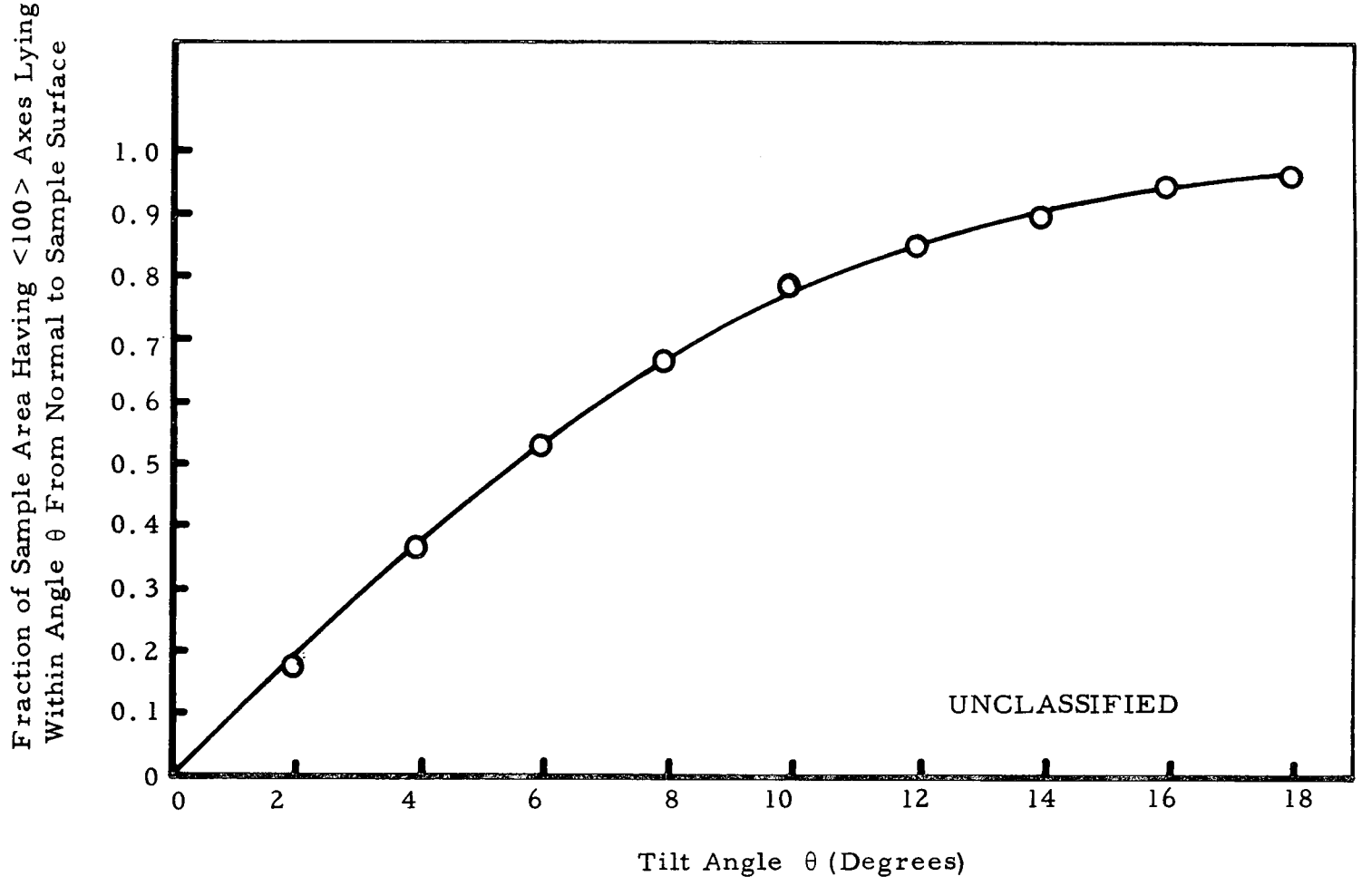

Fig. 6. (U) Spatial distribution of the <100> axes in vapor deposited SFL modified fluoride tungsten sample E_1

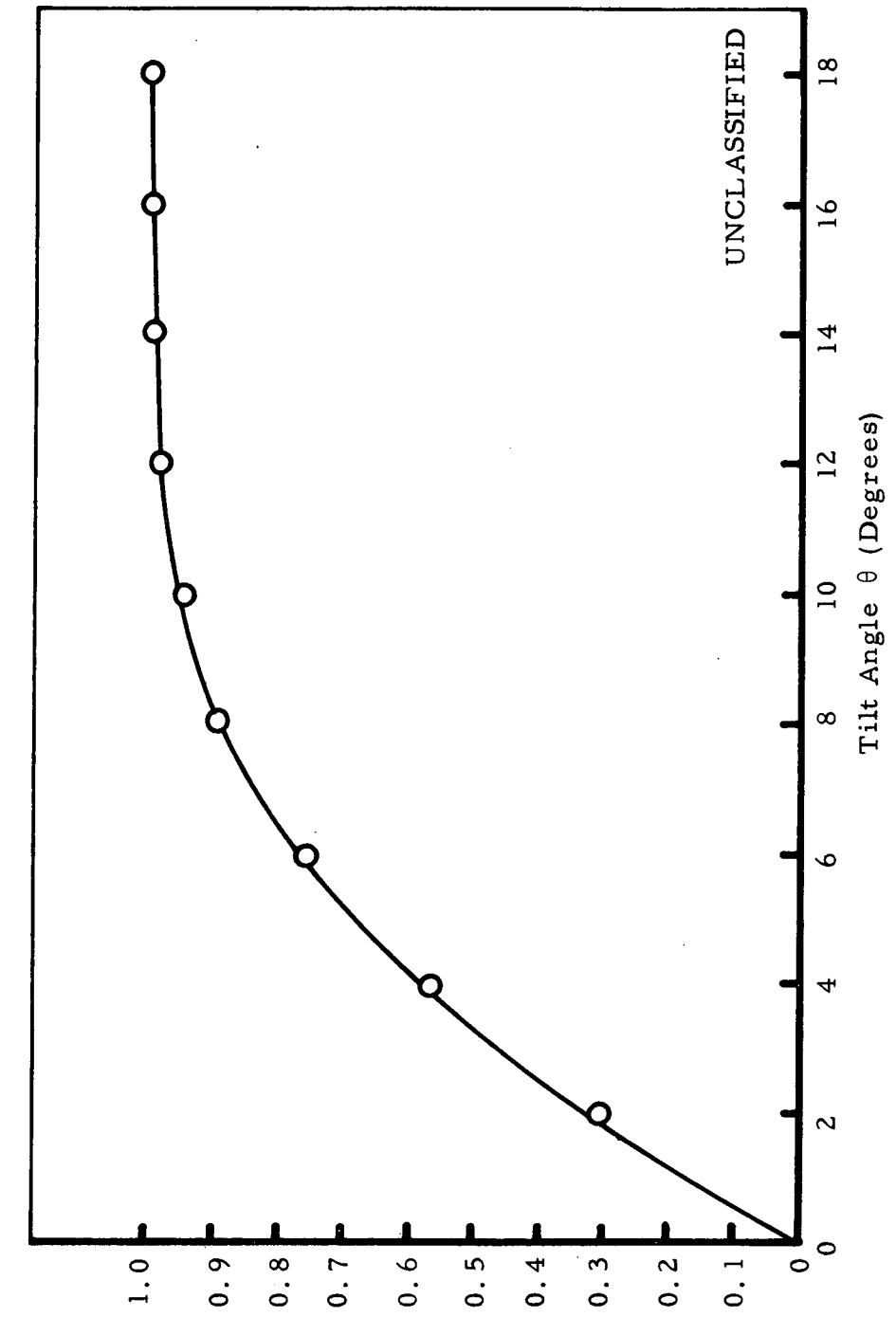

Fig. 7. (U) Spatial distribution of the <100> axes in vapor deposited fluoride tungsten sample F_1

Measurement was made once every 100 hours for a total period of 1000 hours. The temperature of the sample was then lowered to 1673°K and the vacuum work function of the emitting surface was determined once every 24 hours for a total period of 100 hours in order to detect whether significant accumulation of fuel components on the emitter surface could occur at this lower temperature. Subsequently each test sample was installed in a thermionic emission microscope and the degree of its electron emission uniformity was observed for 24 hours at 2073°K.

1.2.1.4. Determination of Transport Rates of Fuel Components Through Cladding, and Post-Test Microstructures and Preferred Crystal Orientation of the Cladding. (C-RD)(Gp-1) After the completion of each test, the collector-guard ring assembly was transferred under argon atmosphere into a stainless steel container in which the deposit collected on the surface of the assembly was converted to CO_2 at 623°K by reacting with oxygen. The gaseous product, after passing through a Cu_2O column to insure the completion of the conversion, was then analyzed for its CO_2 content by gas chromatography. The residue on the surface of the collector-guard ring assembly was then dissolved in a mixture of HF and HNO_3 and the uranium and zirconium contents of the solution obtained were determined by a colorimetric method, using Arsenazo-III as the color developing agent. The sensitivity of the carbon determination was about 1.5 micrograms and that for the uranium and zirconium determinations was about 0.01 microgram. From the analytical results, the average transport rates for C, U and Zr were calculated from the area of the fuel-cladding

interface facing the collector-guard ring assembly and the testing time at 2073°K. The 100 hour period at 1673°K was neglected in the calculation since its contribution to the fuel component transports should be much less than that for the 1000 hour period at 2073°K.

(C-RD)(Gp-1) Each test sample was examined with X-ray to determine the degree of preferred crystal orientation in the cladding. It was then sectioned across the fuel-cladding interface and the microstructures and the phases present near the fuel-cladding interface were determined by metallographic and electron microprobe techniques.

1.2.2. Test Results

1.2.2.1. Vacuum Emission Studies. (C-RD)(Gp-1) Figure 8 shows the effective vacuum work functions of the six test samples studied as a function of testing time. Several conclusions can be drawn from these results.

1. The data obtained on Sample $C1_1$ and D_1 indicate that (110) oriented chloride tungsten can maintain its high vacuum work function (~4.95 eV) when in contact with the carbon rich carbide fuel material used in this experiment. These values are similar to that for unfueled chloride tungsten emitters.

2. The vacuum work functions of Sample E_1 and Sample F_1 are higher than that of unfueled fluoride tungsten emitters (4.75 and 4.76 eV versus 4.5 eV). This has also been observed

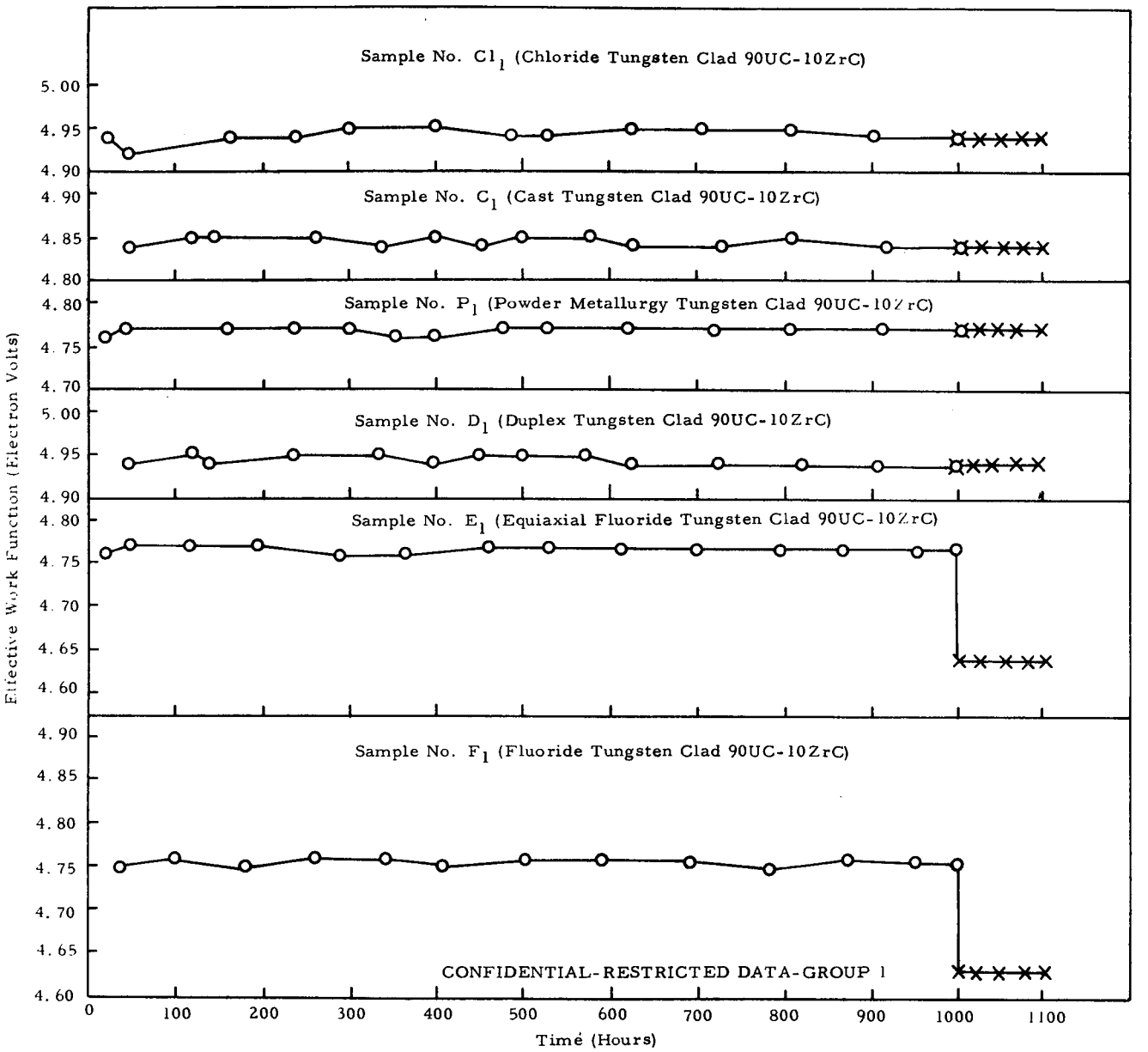

Fig. 8. (U) Effective work functions as a function of time at 2073°K and 1673°K of various tungsten clad 90UC-10ZrC samples

Note: O denotes 2073°K points
X denotes 1673°K points

previously[4] for fluoride tungsten emitters fueled with carbon-rich carbide fuels. It is believed that this is due to the adsorption of carbon on the emitting surface. The same may also be true for Sample P_1 (4.77 eV).

3. The higher vacuum work function of Sample C_1 (4.85 eV) than that of Samples F_1, E_1, and P_1 is probably due to the presence of a weak (110) preferred orientation on its emitting surface.

4. All six test samples maintained stable vacuum work functions at 2073°K, indicating no significant change in their emitting surfaces during the 1000 hour test period.

5. Samples $C1_1$, C_1, P_1, and D_1 showed no change in their vacuum work functions when their temperatures were lowered down from 2073°K to 1673°K, implying no changes in their surface conditions upon cooling. Samples E_1 and F_1 however, showed a slight decrease in their vacuum work functions from 4.76 eV to 4.63 eV. Such a work function change is believed to be due to a change in the concentrations of adsorbed fuel components on their emitting surfaces when their temperatures were lowered. It is interesting to note that Samples E_1 and F_1 exhibited higher uranium and zirconium transport rates through the cladding than the other four samples studied (see below).

(C-RD)(Gp-1) Figure 9 contains the post-operational thermionic emission patterns of the test samples at 2073°K. The fluoride tungsten Samples F_1 and E_1 gave more uniform emission patterns. No enhanced emission patch due to uranium adsorption was observed in all the cases studied.

1.2.2.2. Fuel Component Transport Rates. (C-RD)(Gp-1) Table 2 summarizes the analytical results on U, Zr and C transport rates through the claddings of the six test samples. These results indicate the following:

1. The uranium transport rate of the columnar fluoride tungsten Sample F_1 is about a factor of three lower than that obtained previously[4] in 10,000 hour tests from samples of columnar fluoride tungsten clad hyperstoichiometric 90UC-10ZrC (C/U = 1.02) containing no tungsten additions at 2073°K. Thus the addition of tungsten (with its carbon share) to the carbide fuel material did lead to a reduction of uranium activity and uranium transport rate through the cladding.

2. Of the six samples studied, the uranium transport rates decrease in the order of: $F_1 > E_1 > P_1 \approx D_1 > C_1 > Cl_1$, the relative magnitude being 117, 55, 3, 3, 1.5, and 1 respectively. Claddings of more columnar grain structures showed higher uranium transport rates,

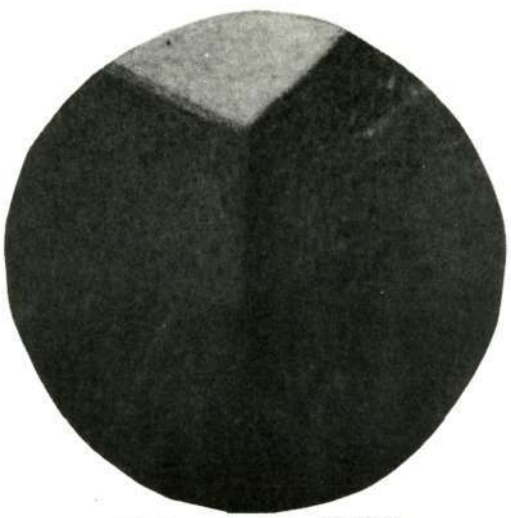

(a) Sample $C1_1$ (100X)

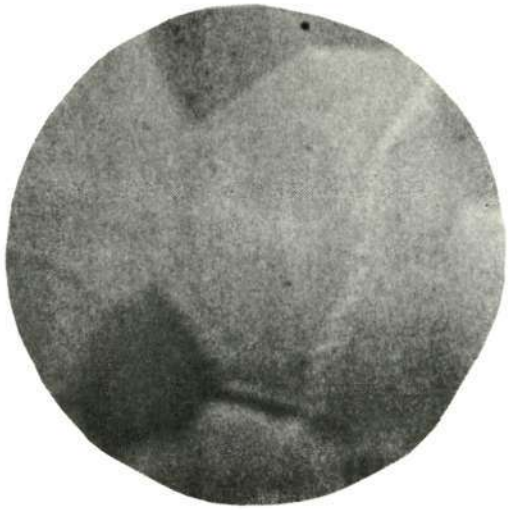

(b) Sample D_1 (100X)

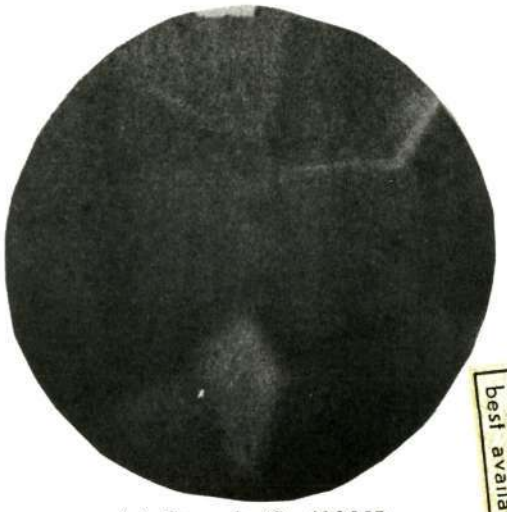

(c) Sample C_1 (100X)

(d) Sample P_1 (300X)

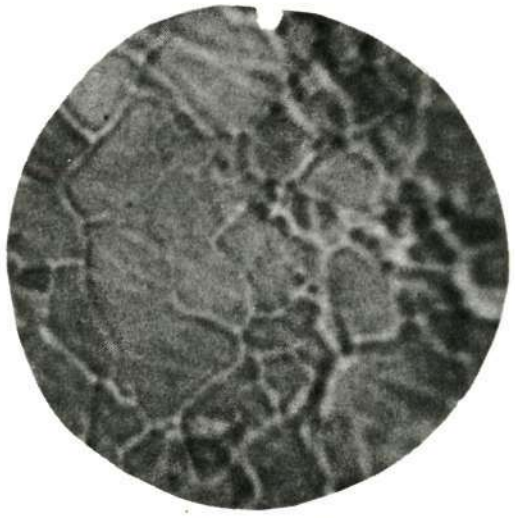

(e) Sample E_1 (300X)

(f) Sample F_1 (300X)

UNCLASSIFIED

Fig. 9. (U) Thermionic emission patterns of the six screening test samples at 2073°K

TABLE 2

(U) FUEL COMPONENT TRANSPORT RATES OBTAINED IN SCREENING TESTS

(This table is classified Confidential-Restricted Data-Group 1)

Sample	U		Zr		C	
	Total Amount (Microgram)	Average Flux gm/cm^2hr	Total Amount (Microgram)	Average Flux gm/cm^2hr	Total Amount (Microgram)	Average Flux gm/cm^2hr
Columnar fluoride tungsten F_1	2.4	3.4×10^{-9}	0.2	2.9×10^{-10}	<1.5	$<2.1 \times 10^{-9}$
SFL Modified fluoride tungsten E_1	1.1	1.6×10^{-9}	0.1	1.5×10^{-10}	<1.5	$<2.1 \times 10^{-9}$
Chloride tungsten Cl_1	0.02	2.9×10^{-11}	<0.01	$<1.5 \times 10^{-11}$	<1.5	$<2.1 \times 10^{-9}$
Duplex tungsten D_1	0.06	8.6×10^{-11}	<0.01	$<1.5 \times 10^{-11}$	<1.5	$<2.1 \times 10^{-9}$
Powder metallurgy tungsten P1	0.06	8.6×10^{-11}	<0.01	$<1.5 \times 10^{-11}$	<1.5	$<2.1 \times 10^{-9}$
Cast tungsten C_1	0.03	4.3×10^{-11}	<0.01	$<1.5 \times 10^{-11}$	<1.5	$<2.1 \times 10^{-9}$

in agreement with the results obtained previously on uranium transport from UO_2 through tungsten claddings.[8]

3. The zirconium transport rate of F_1 is the highest. No substantial reduction was achieved by using the SFL modified fluoride tungsten E_1 as the cladding. The zirconium transport rates for the other four types of claddings studied are lower than that for E_1. No quantitative data can be given, however, since in each case the amount of zirconium collected on the collector-guard ring assembly was below the detection limit of the analytical method. Here again, the reduction of fuel component transport through claddings of equiaxial grain structures is demonstrated.

4. The amount of carbon collected on the collector-guard ring assembly was below the detection limit of the analytical method for all the six samples studied. Either tests of longer duration or more sensitive analytical methods (e.g. the use of C^{14} as a tracer) are needed for quantitative determinations of the carbon transport rates.

1.2.2.3. Post-Test Microstructures and Degree of Preferred Crystal Orientation. (C-RD)(Gp-1) Figure 10 shows the post-test appearances of the surfaces of the six samples studied. It is interesting to note that although Sample P_1 has the smallest grain size and therefore more grain boundary per

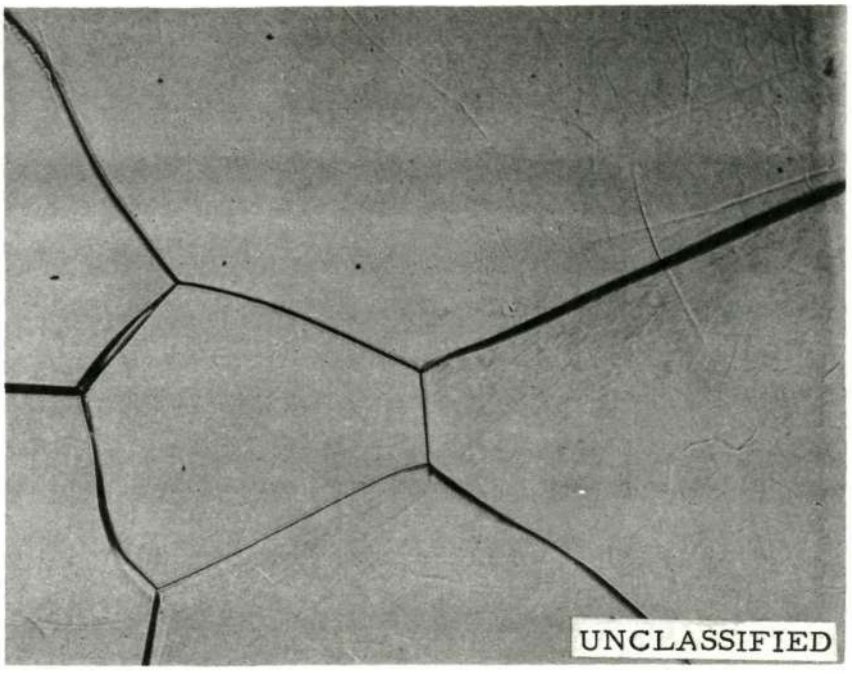

M 28079-1 75X

Fig. 10(a). (U) Post-test surface grain structures of chloride tungsten cladding of Sample Cl_1

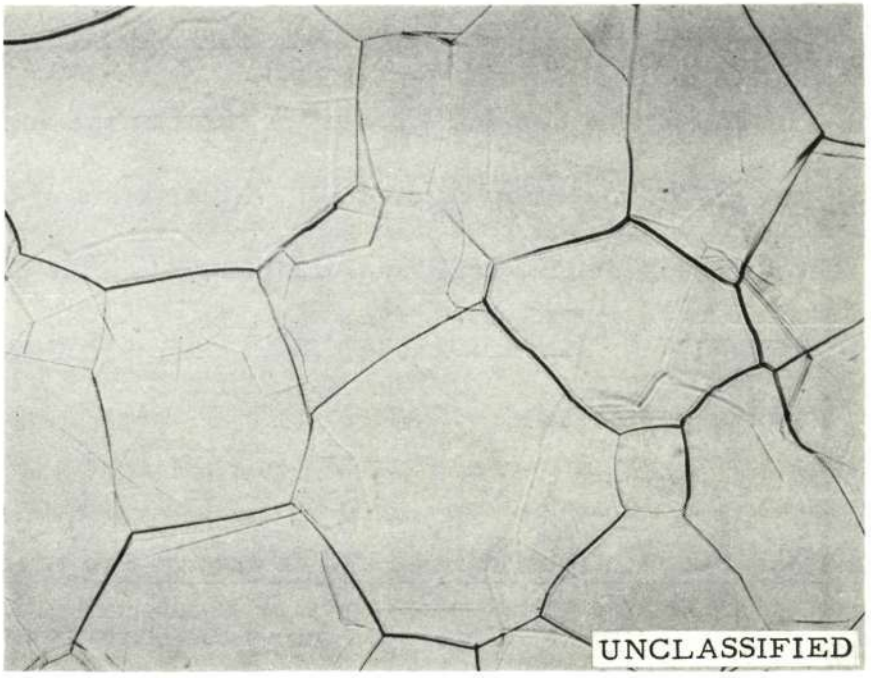

M 28074-1 75X

Fig. 10(b). (U) Post-test surface grain structures of duplex tungsten cladding of Sample D_1

(This page is Unclassified)

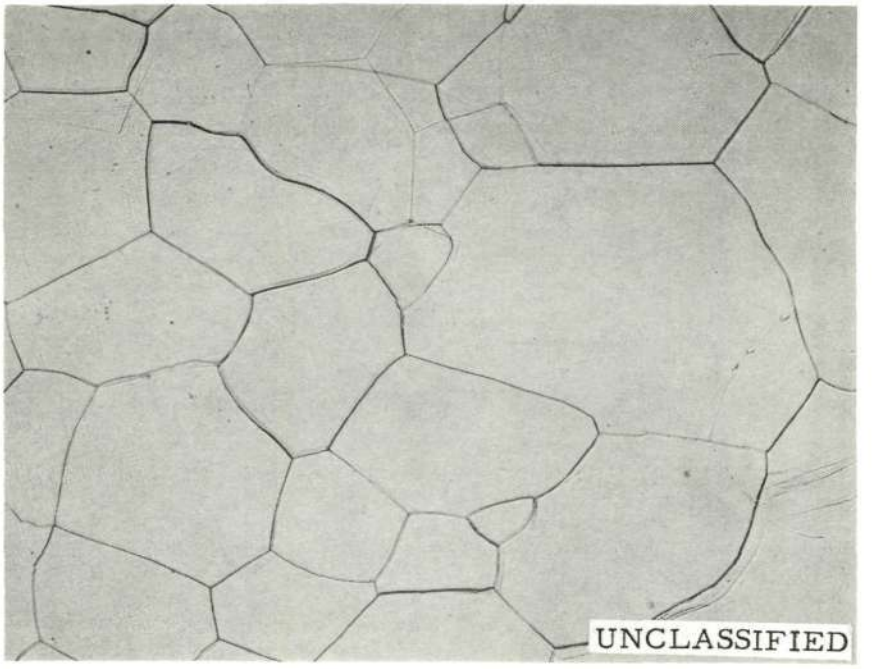

M 38076-1 75X

Fig. 10(c). (U) Post-test surface grain structures of cast tungsten cladding of Sample C_1

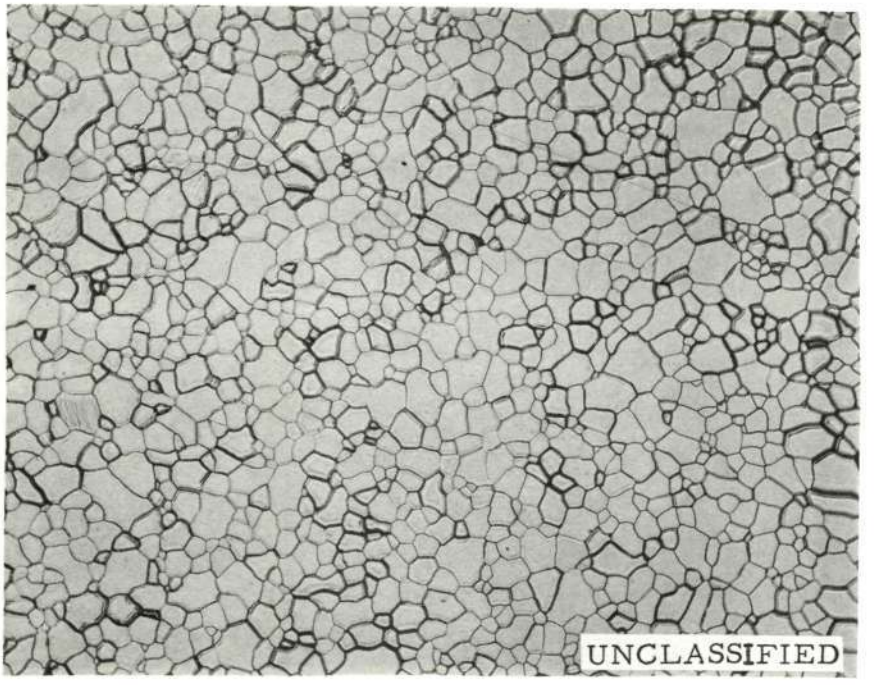

M 28077-1 75X

Fig. 10(d). (U) Post-test surface grain structures of powder metallurgy tungsten cladding of Sample P_1

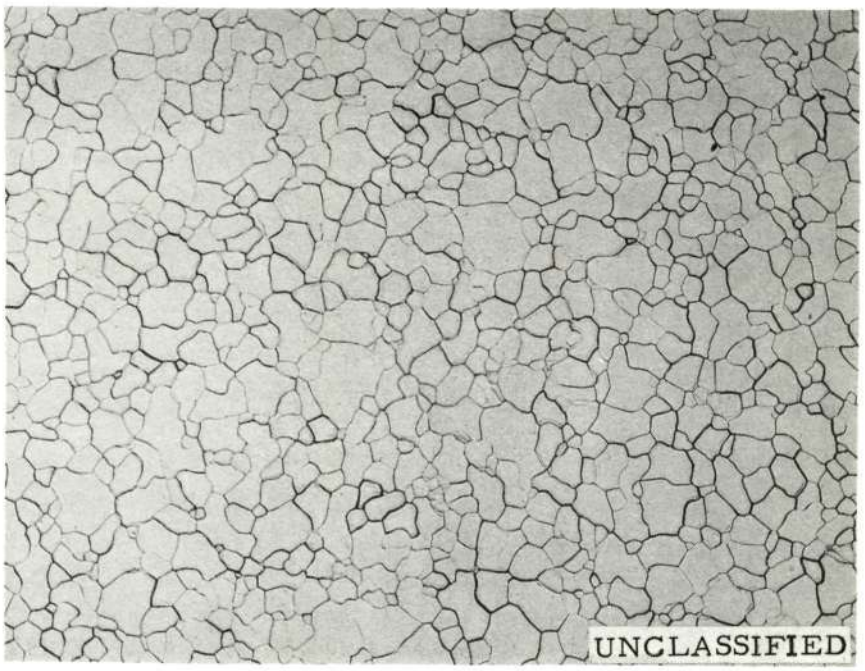

M 28075-1 75X

Fig. 10(e). (U) Post-test surface grain structures of SFL modified fluoride tungsten cladding of Sample E_1

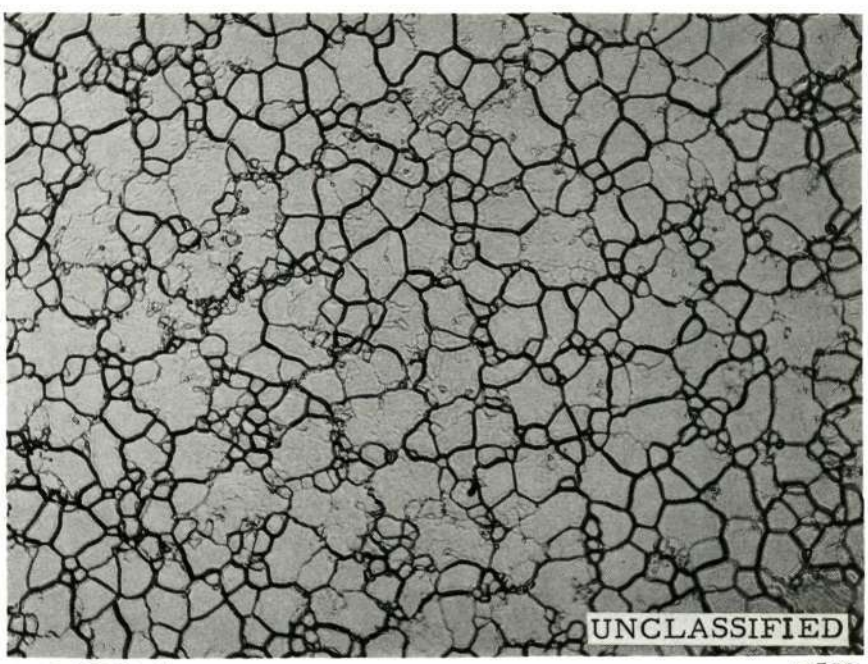

M 28078-1 75X

Fig. 10(f). (U) Post-test surface grain structures of columnar fluoride tungsten cladding of Sample F_1

unit area across the diffusion path, its uranium and zirconium transport rates are lower than that for Samples F_1 and E_1. This is probably because the grains in P_1 are more equiaxial and therefore the diffusion path is much longer. Sample $C1_1$ has the largest grain size and an equiaxial grain structure; accordingly it has the lowest uranium and zirconium transport rates.

(C-RD)(Gp-1) Figures 11 through 14 compares the post-test degree of preferred crystal orientation with the pre-test data for Samples $C1_1$, D_1, E_1 and F_1. The change, if any, is insignificant. Sample C_1 retained the same weak (110) orientation as that in the pre-test state. The grain structure of Sample P_1 remained random.

(C-RD)(Gp-1) Figure 15 shows the unetched fuel-clad interfaces at 1000X magnification. An interaction layer of several microns in thickness was observed in each case. Electron microprobe examination identified the layer as the UWC_2 phase. Previous studies[10] of the compatibility between tungsten and hyperstoichiometric carbide at 2073°K for 100-150 hours failed to find such an interaction layer. This is probably because the testing time was too short and the test was carried out under isothermal conditions. The presence of a thermal gradient in the fuel material, such as that present in the test sample heated by electron bombardment from one side, may drive carbon to the fuel-cladding interface at the other side of the sample and enhances the interaction there. Figure 16 illustrates the microstructures of the claddings of the six test samples in the etched conditions. The

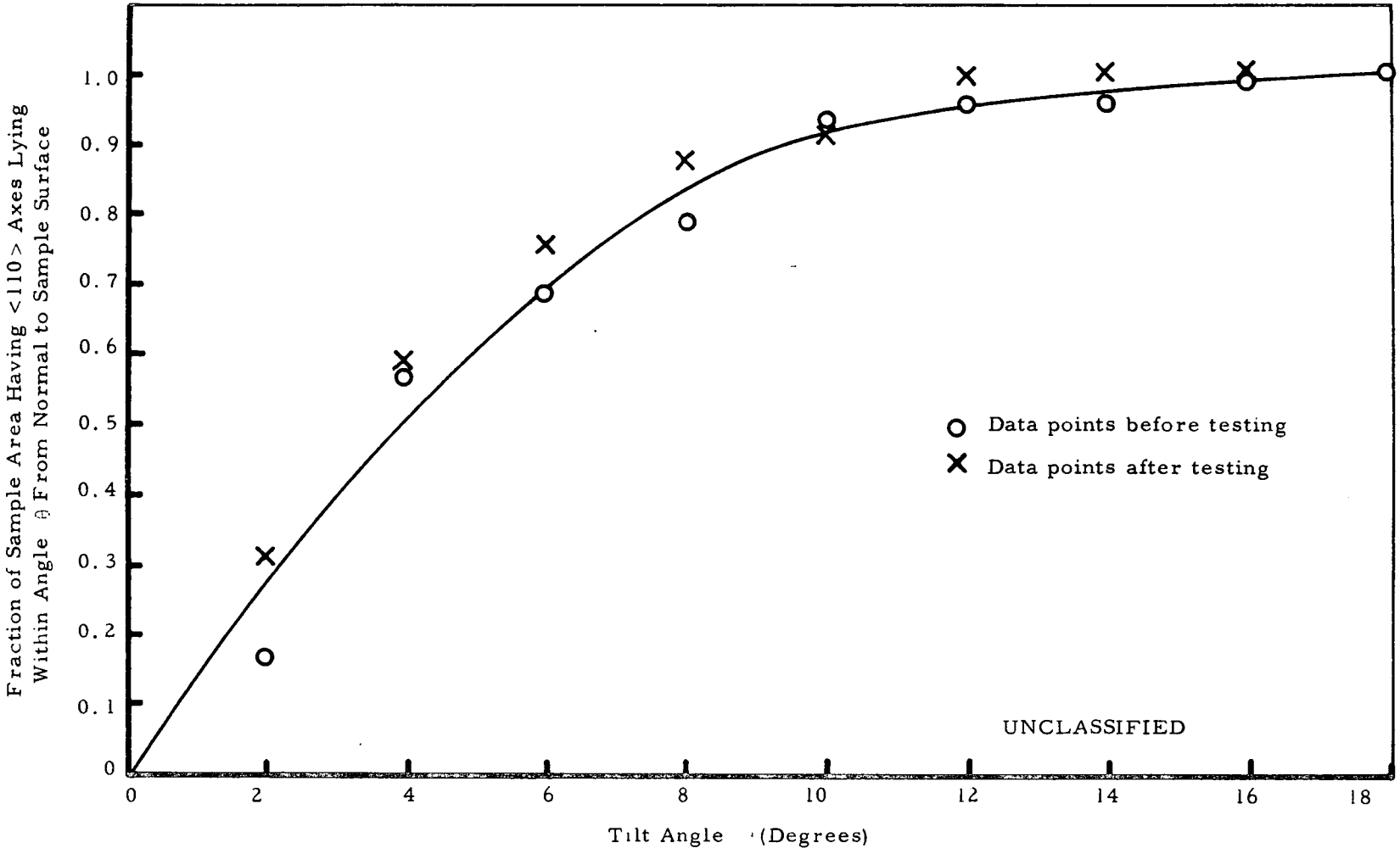

Fig. 11. (U) Comparison of the post-test and the pre-test spatial distributions of the <110> axes in chloride tungsten sample Cl_1

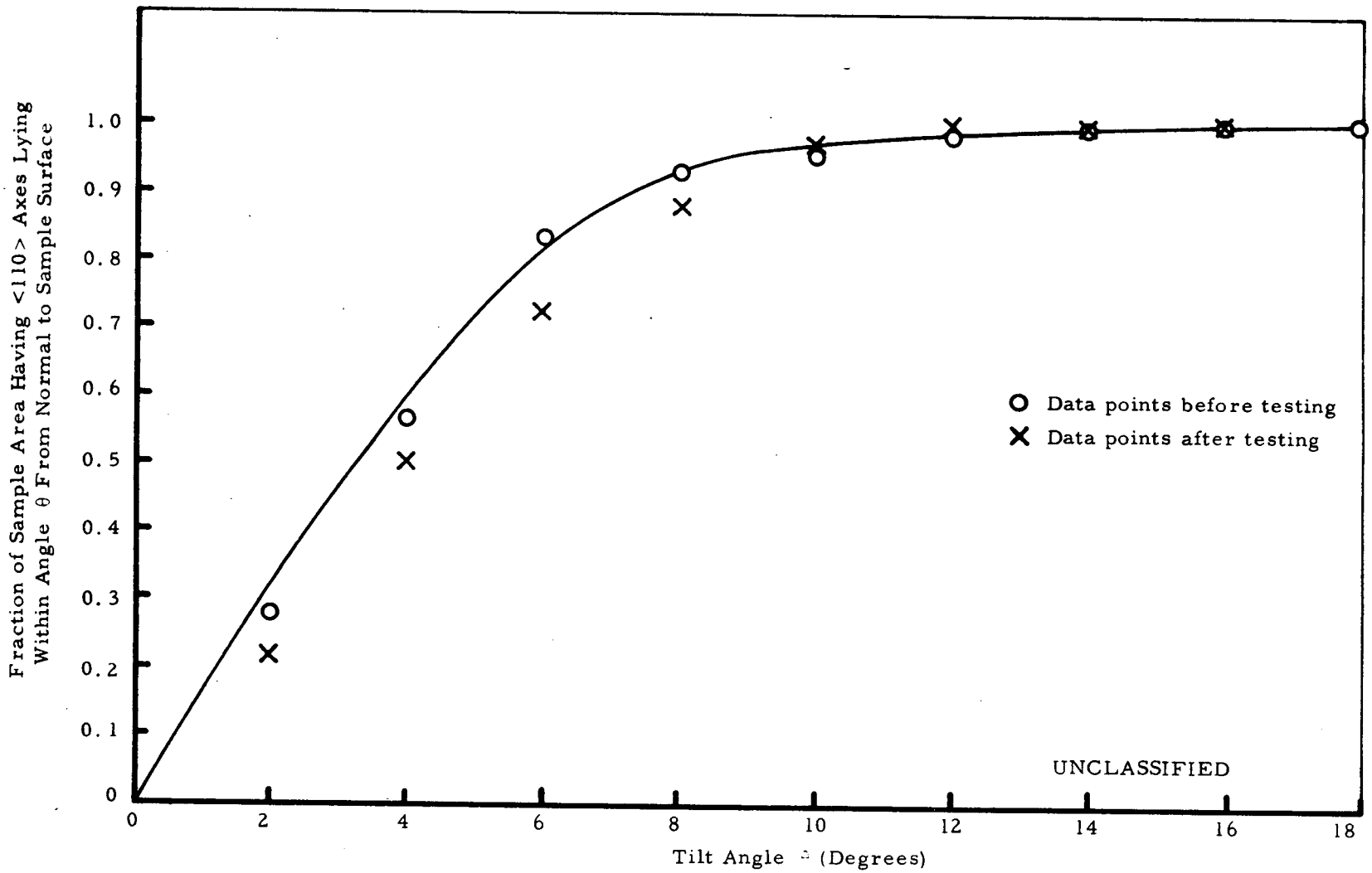

Fig. 12. (U) Comparison of the post-test and the pre-test spatial distributions of the <110> axes in chloride-fluoride duplex tungsten sample D_1

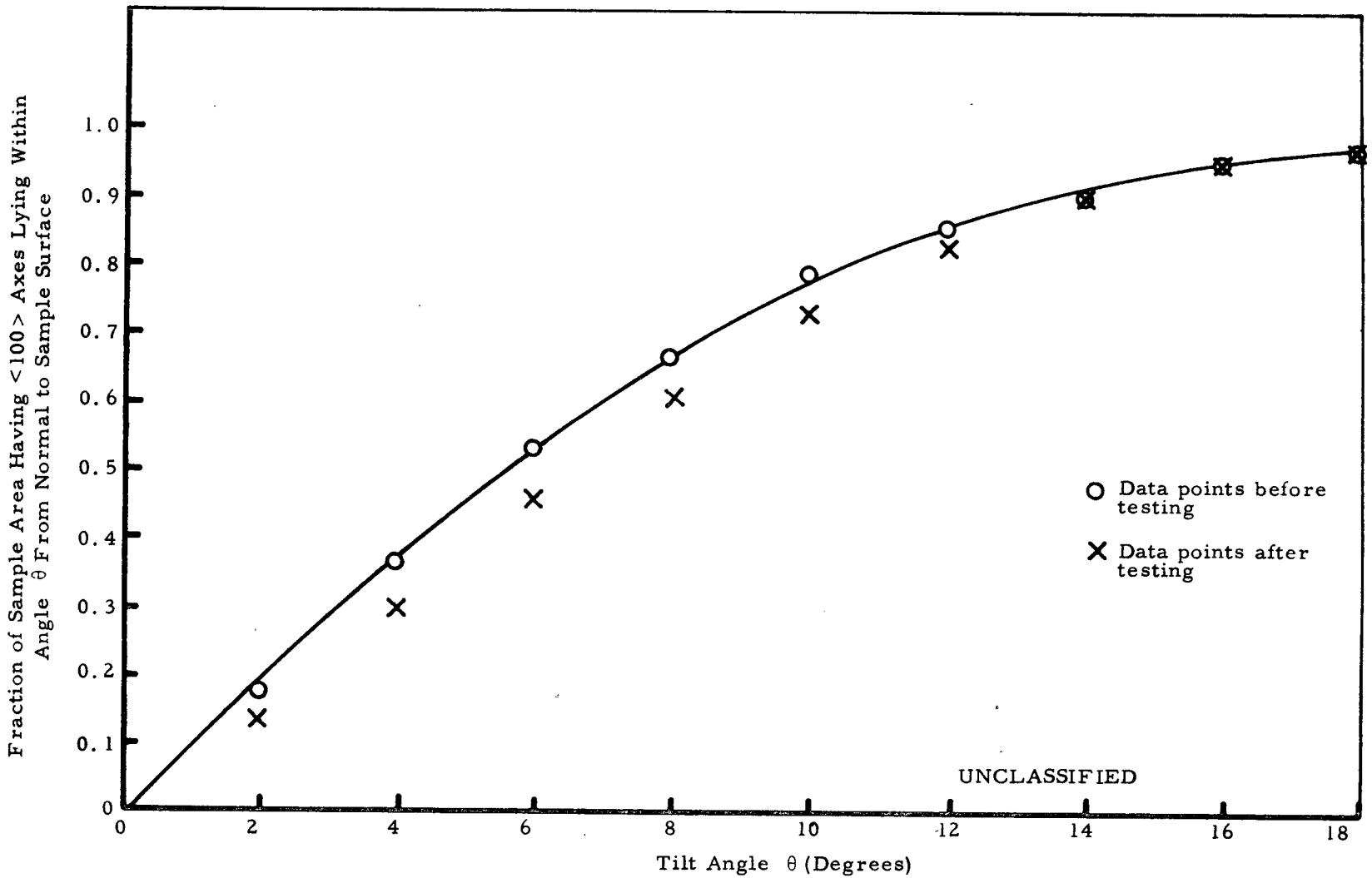

Fig. 13. (U) Comparison of the post-test and the pre-test spatial distributions of the <100> axes in SFL modified fluoride tungsten sample E_1

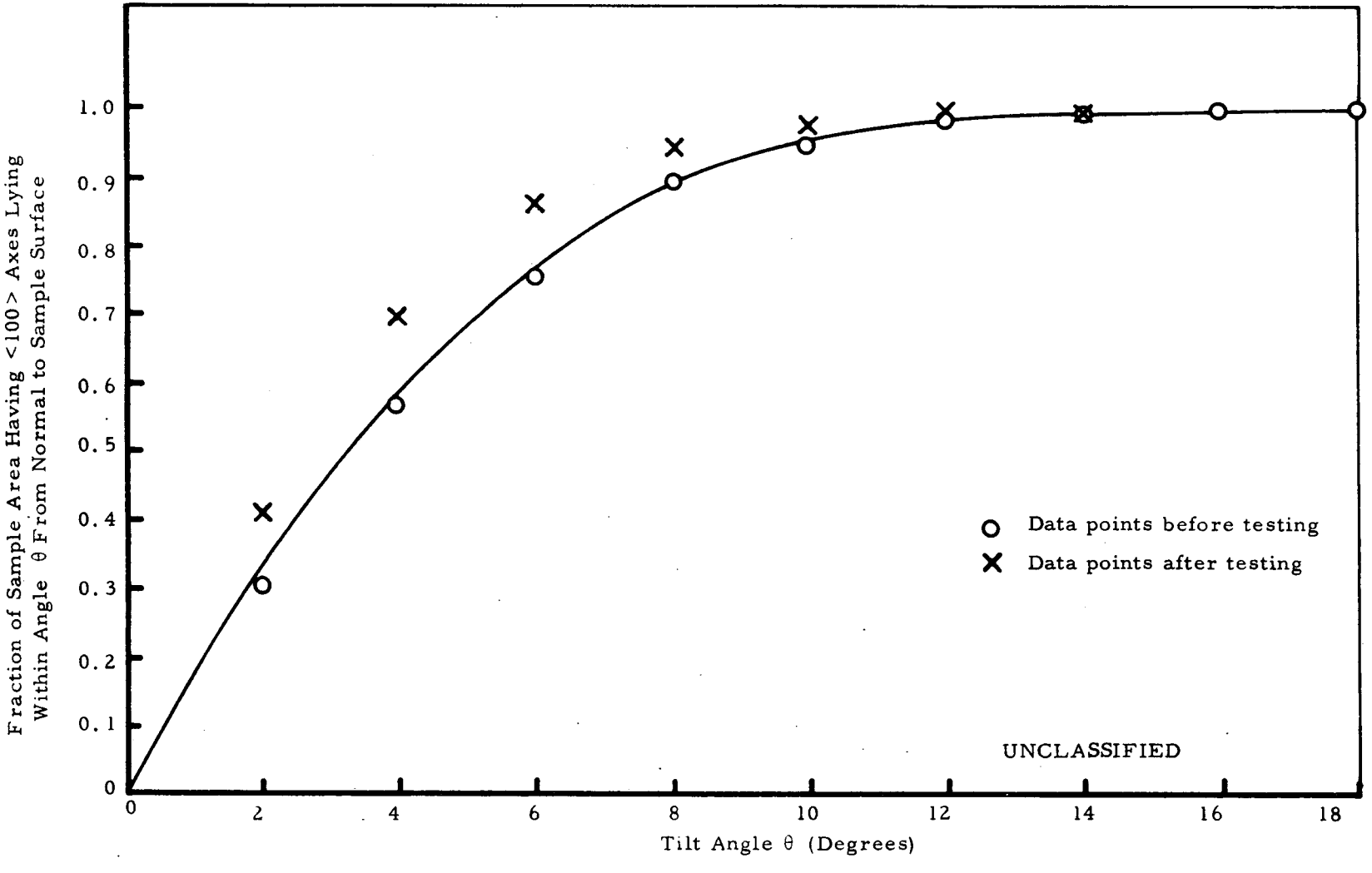

Fig. 14. (U) Comparison of the post-test and the pre-test spatial distributions of the <100> axes in fluoride tungsten sample F_1

(This page is Unclassified)

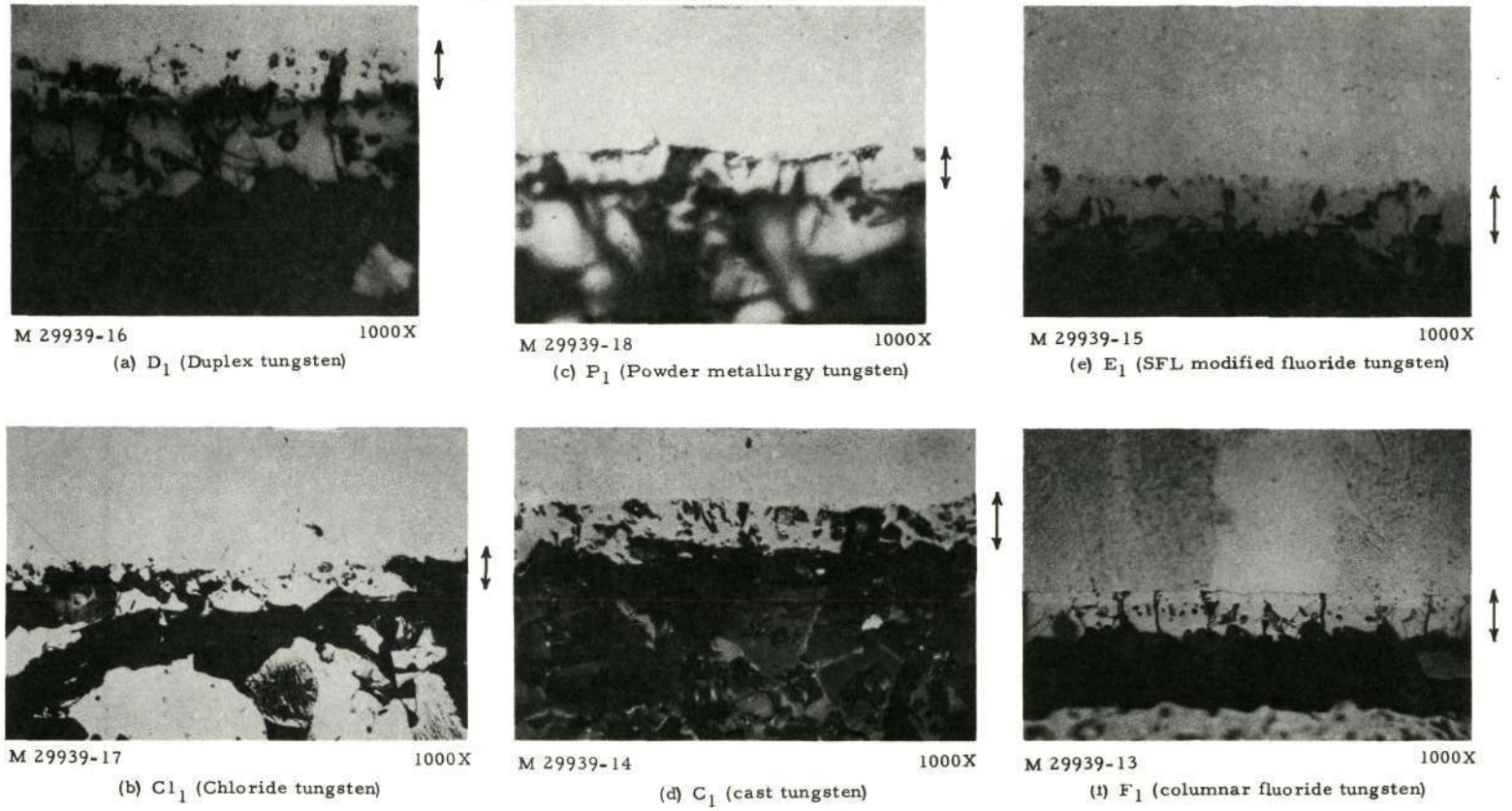

M 29939-16 1000X
(a) D_1 (Duplex tungsten)

M 29939-18 1000X
(c) P_1 (Powder metallurgy tungsten)

M 29939-15 1000X
(e) E_1 (SFL modified fluoride tungsten)

M 29939-17 1000X
(b) Cl_1 (Chloride tungsten)

M 29939-14 1000X
(d) C_1 (cast tungsten)

M 29939-13 1000X
(f) F_1 (columnar fluoride tungsten)

Fig. 15. (U) Reaction layers (indicated by ↕) at the fuel-cladding interfaces of six screening test samples after 1000 hours at 2073°K and 100 hours at 1673°K

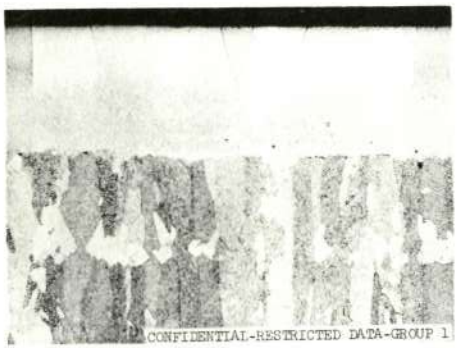

M 29939-20 100X

(a) D_1 (Duplex tungsten)

M 29939-35 100X

(c) P_1 (Powder metallurgy tungsten)

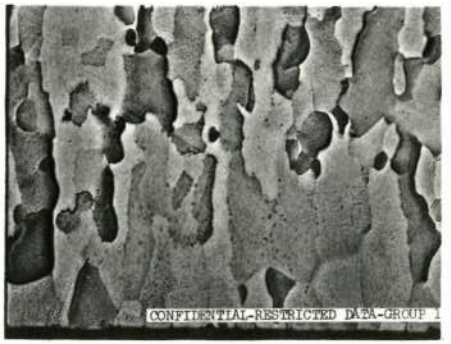

M 29939-34 100X

(e) E_1 SFL modified fluoride tungsten)

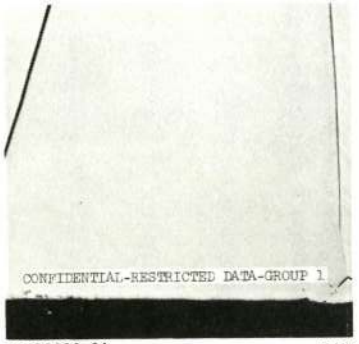

M 29939-36 100X

(b) Cl_1 (Chloride tungsten)

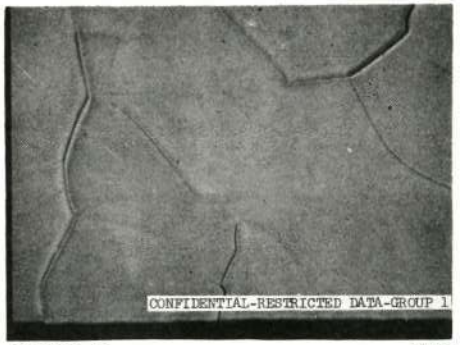

M 29939-33 100X

(d) C_1 (Cast tungsten)

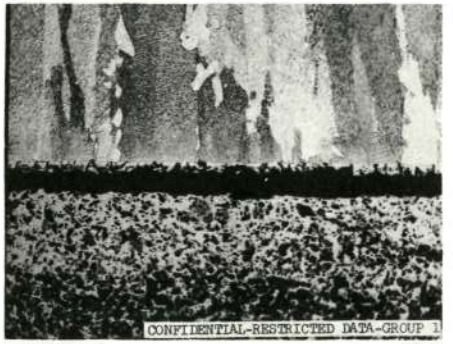

M 29939-19 100X

(f) F_1 (Columnar fluoride tungsten)

Fig. 16. (U) Post-test microstructures of the cross sections of the claddings of Samples D_1, Cl_1, P_1, C_1, E_1, and F_1

interaction layers of these samples were lost in the etching operation (except Sample F_1). The microstructures of the claddings showed no significant changes from the pre-test conditions, and the bond between the fluoride tungsten substrate and the chloride tungsten layer of Sample D_1 remained in excellent shape.

1.3. LONG-TERM LIFE TESTS

(C-RD)(Gp-1) On the basis of the screening test results, five types of tungsten claddings were selected for long-term life tests of their fuel transport and vacuum emission properties. These are: columnar fluoride tungsten, chloride tungsten, chloride-fluoride duplex tungsten, chloride-cast duplex tungsten, and chloride-powder metallurgy duplex tungsten. The columnar fluoride tungsten was selected to determine its performance over a range of temperatures. The chloride tungsten was selected because it has the lowest fuel component transport rates and a high vacuum work function. The chloride-fluoride duplex tungsten was selected because it combines the advantages of a high work function emitting surface and a substrate of proven grain structural stability. The chloride-cast duplex tungsten and the chloride-powder metallurgy duplex tungsten were selected because each contains a high work function emitting surface and a substrates of lower fuel component transport lrates than that of the fluoride tungsten substrate. Such duplex tungsten structures therefore may have lower fuel component transport rates than that of the chloride-fluoride duplex tungsten cladding.

1.3.1. Experimental Equipment and Procedures

(C-RD)(Gp-1) The sample configuration was the same as that shown in Fig. 3. The test samples were designated as F_2 (columnar fluoride tungsten), Cl_2 (chloride tungsten), D_2 (chloride-fluoride duplex tungsten), DAC (chloride-arc-cast duplex tungsten), and DPM (chloride-powder metallurgy duplex tungsten). The fluoride tungsten cladding of F_2 and the fluoride tungsten substrate of D_2 were obtained from the same fluoride tungsten disc as that used for the preparation of the screening test samples F_1 and D_1. The arc-cast and powder metallurgy tungsten substrate materials for DAC and DPM were each cut from the respective pieces used for the preparation of the screening test samples C_1 and P_1. Techniques and conditions for depositing the chloride tungsten of Cl_2, D_2, DAC, DPM were similar to that used for the preparation of the screening test samples Cl_1 and D_1. Figures 17 through 21 show the spatial distributions of the crystal axes of preferred orientation ((100) for F_2, (110) for the others) in the long-term life test samples. Table 3 lists the impurity contents of these tungsten materials after outgassing at 2123°K in vacuum for 200 hours. The carbide fuel wafers for F_2, Cl_2 and D_2 were taken from the same carbide cylinder as that for the six screening test samples, which had a C/U ratio of 1.04.

(C-RD)(Gp-1) To improve the sensitivity for the determination of carbon transport rates, C^{14} was incorporated into the carbide fuel materials of DAC and DPM. The C^{14}-containing carbon powder was purchased from

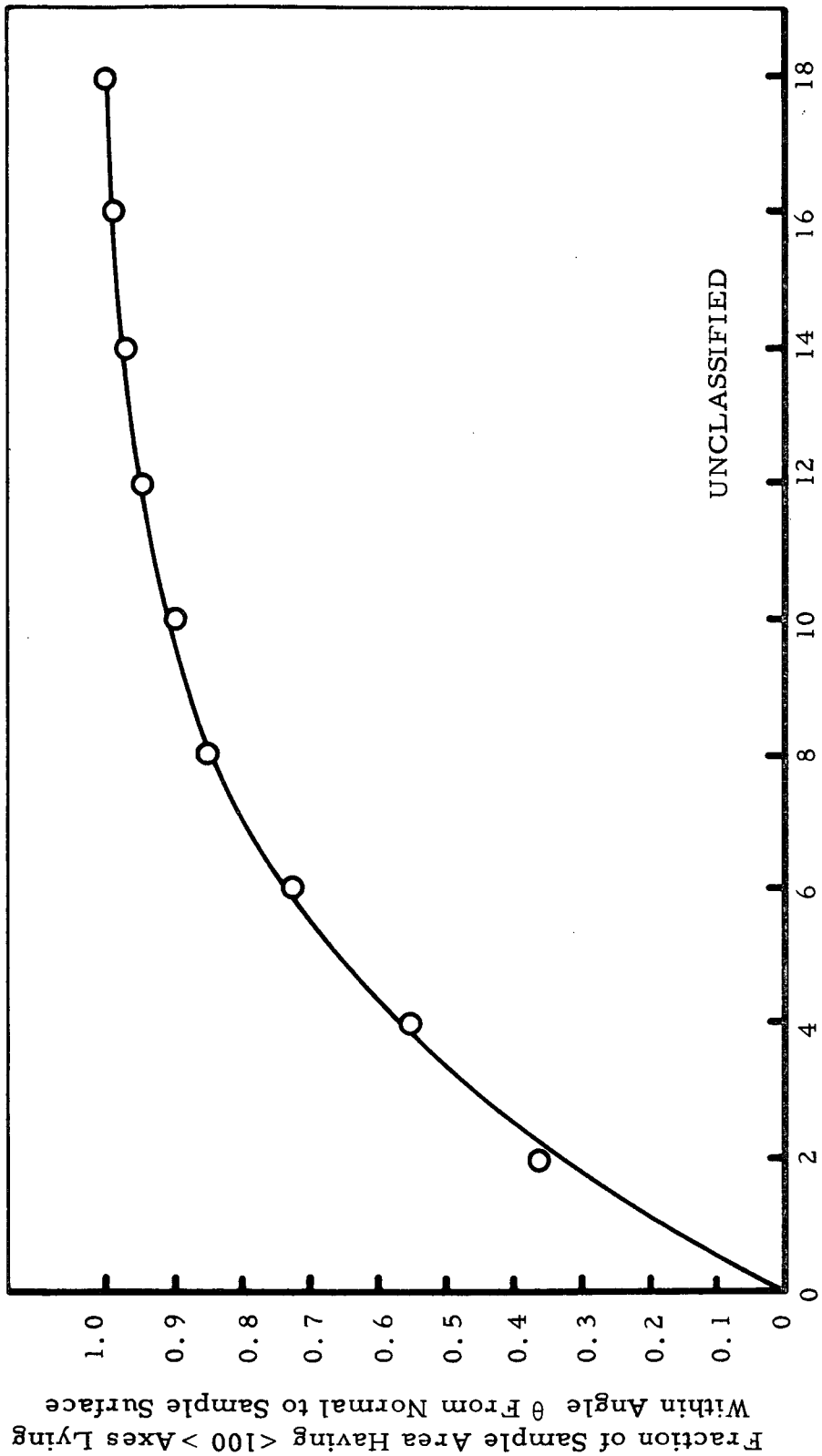

Fig. 17. (U) Spatial distribution of the <100> axes in columnar fluoride tungsten sample F_2

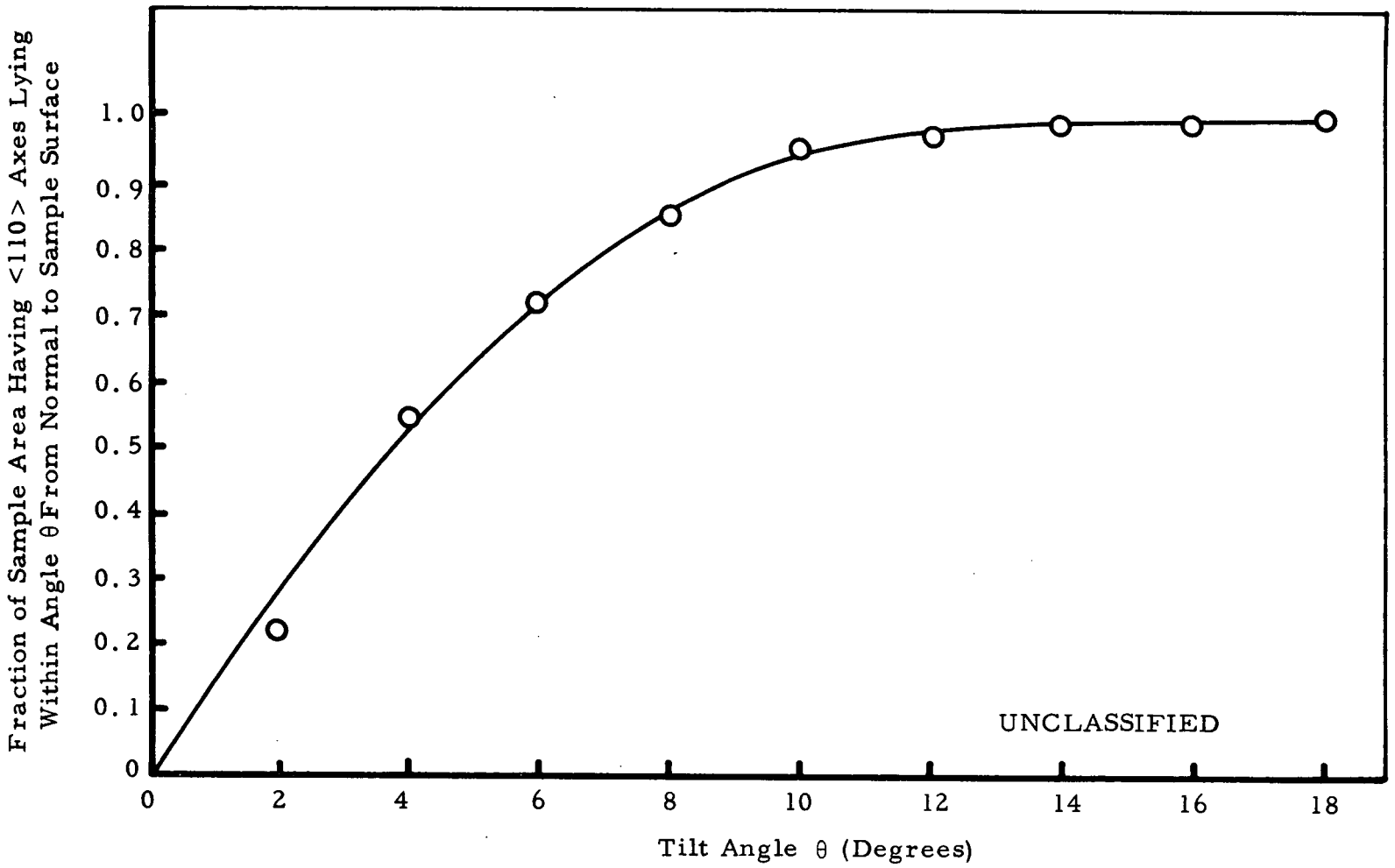

Fig. 18. (U) Spatial distribution of the <110> axes in chloride tungsten sample Cl_2

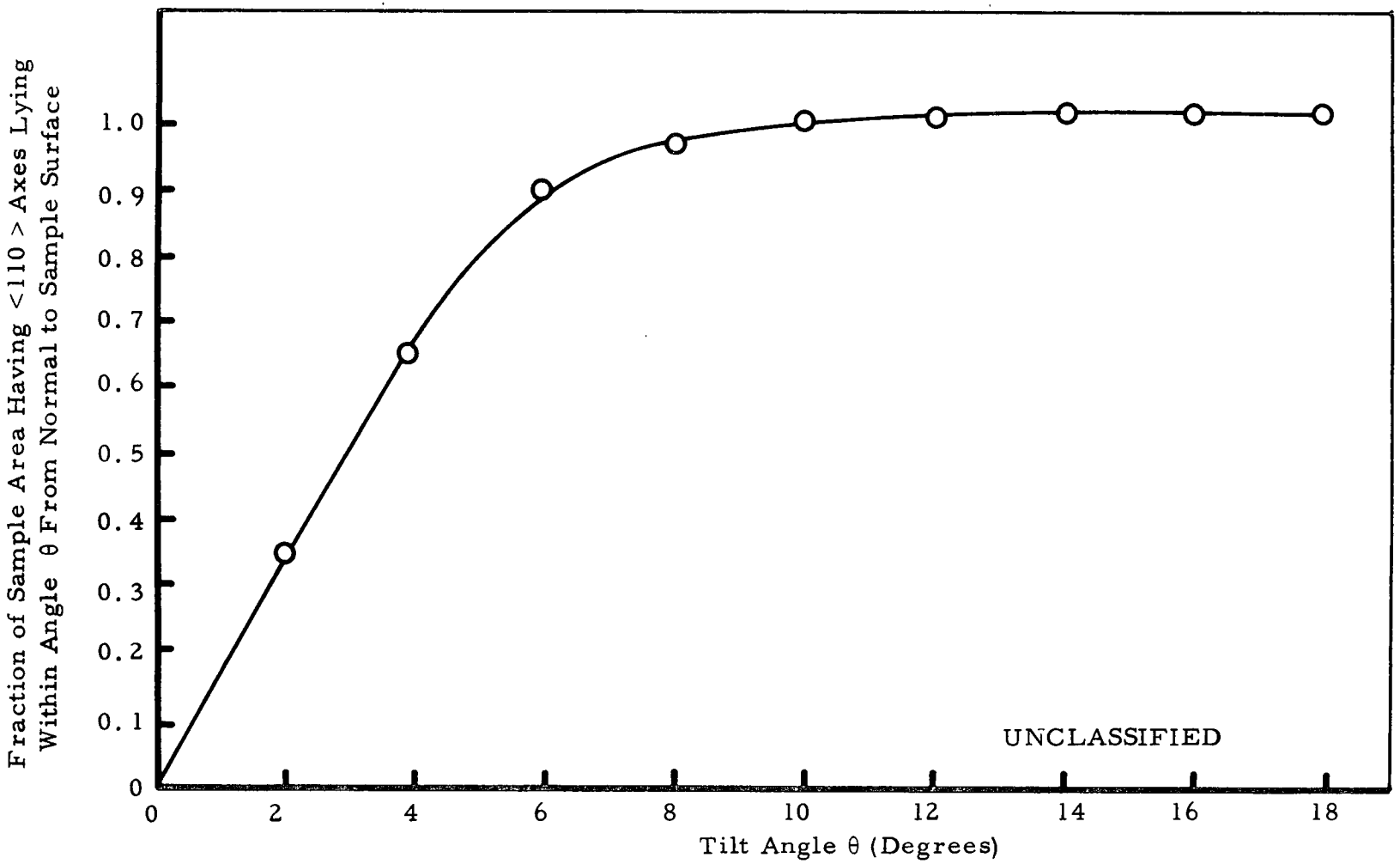

Fig. 19. (U) Spatial distribution of the <110> axes in chloride-fluoride duplex tungsten sample D_2

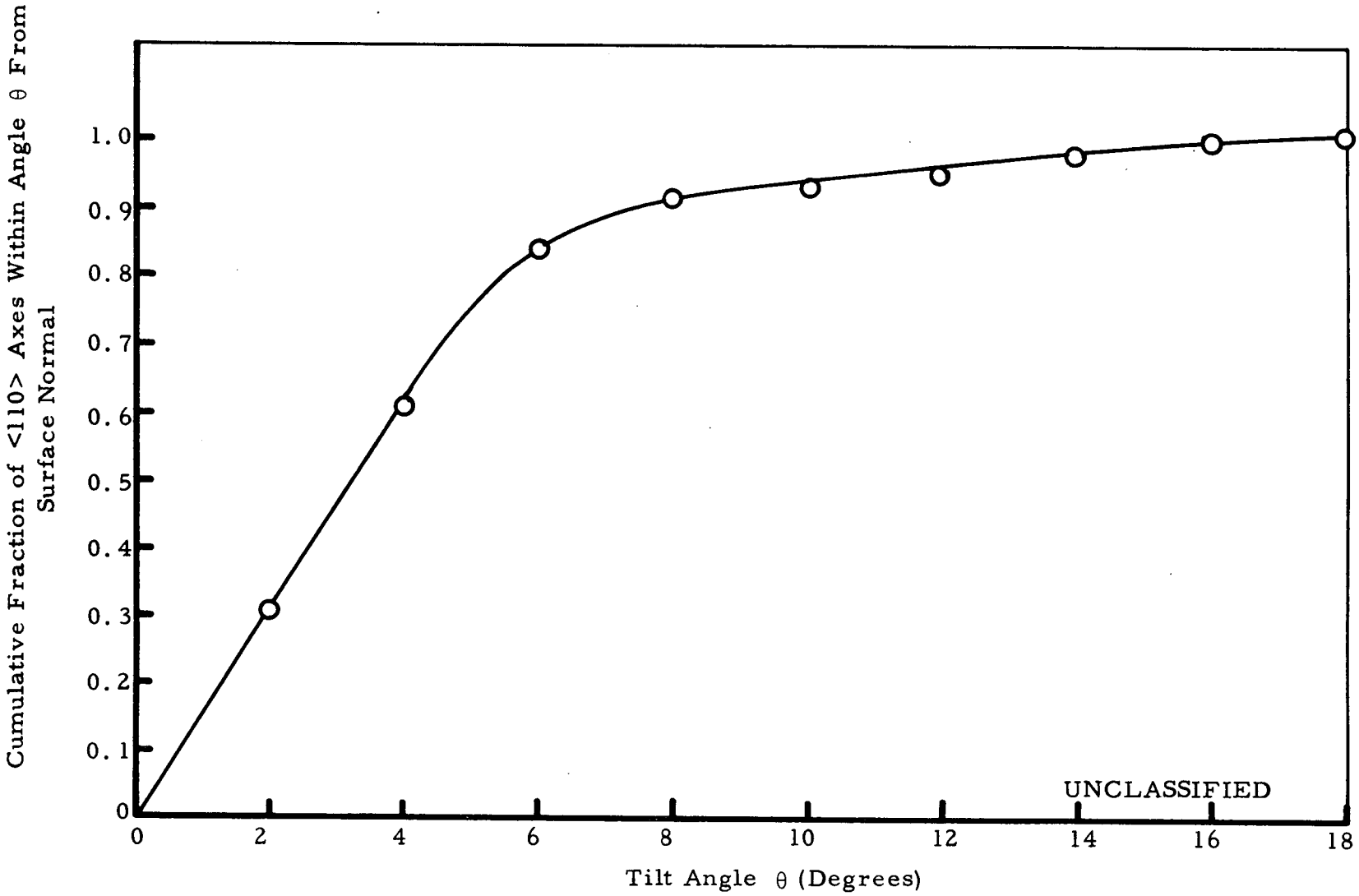

Fig. 20. (U) Spatial distribution of the <110> axes in chloride-arc cast duplex tungsten sample DAC

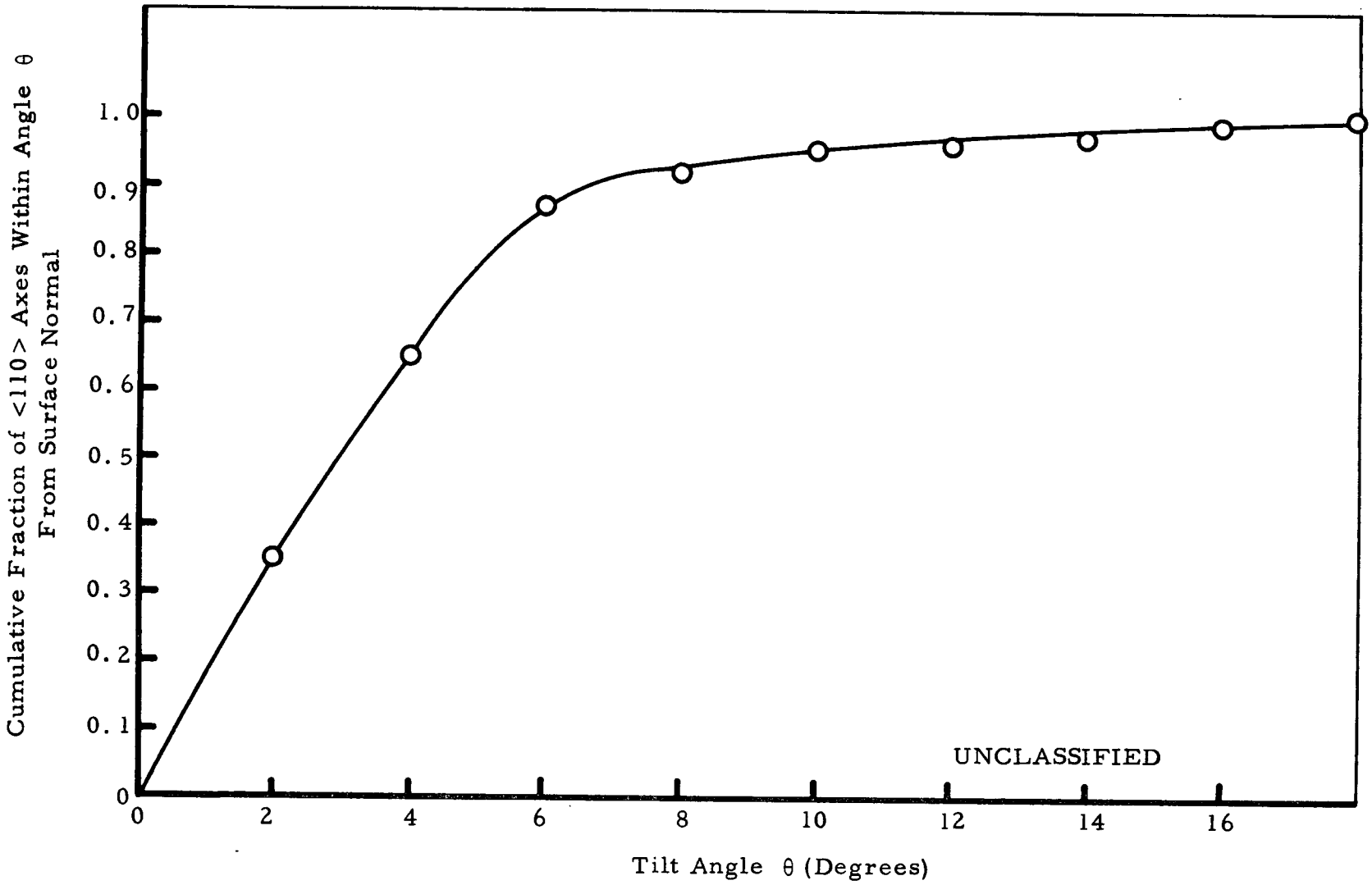

Fig. 21. (U) Spatial distribution of the <110> axes in chloride-powder metallurgy duplex tungsten sample DPM

TABLE 3

(U) IMPURITY CONTENTS IN LONG-TERM LIFE TEST TUNGSTEN CLADDING MATERIAL AFTER 200 HOURS AT 2123°K IN VACUUM
(ALL CONCENTRATIONS ARE IN PPM)

(This table is Unclassified)

Type of Tungsten	Impurity Contents												
	C	F	Cl	O	N	Al	Bi	Fe	Mg	Mn	Ni	Pb	Si
Columnar fluoride F_2	5	15	9	6	<1	ND	4.0	6.2	0.1	0.2	ND	ND	ND
Chloride Cl_2	3	<3	8	2	<1	1.2	ND	ND	ND	ND	ND	ND	1.5
Chloride-fluoride duplex D_2	3	<3	12	5	<1	0.5	ND	ND	ND	ND	ND	ND	1.1
Chloride-cast duplex DAC	2	<3	8	15	3	0.8	ND	4.5	0.1	ND	ND	3.0	1.1
Chloride-powder metallurgy DPM	4	<3	6	3	<1	1.0	ND	40.0	0.1	ND	1.5	ND	ND

ND = not detected at the limit of sensitivity

(This page is Unclassified)

the International Chemical and Nuclear Corporation and had a specific activity of about 1 millicurie per milligram. Sufficient amount of this carbon powder was blended into the 90UC-10ZrC powder to yield a specific activity of about 1 millicurie per 1 gram of carbon in the fuel material, or about 200 disintegration per minute per 0.1 microgram of carbon in the fuel material. For a counting efficiency of 25%, 0.01 microgram of carbon could be detected without difficulty. The composition of the carbide fuel material thus prepared was $U_{0.424}Zr_{0.046}W_{0.030}C_{.500}$ which corresponded to a C/U ratio of 1.039, allowing one C for each Zr and one C for every two W.

(C-RD)(Gp-1) The procedure used to determine the carbon content in the C^{14}-containing deposit on the surface of the collector-guard ring assembly was different from that used previously. The deposit was reacted with oxygen according to the method described in Section 1.2.1.4. The CO_2 formed was absorbed in 50 c.c. of 1 N NaOH. 10 milligrams of Na_2CO_3 was added as a carrier. The carbonate ions were then precipitated as $CaCO_3$ by the addition of 10 c.c. of 1% $CaCl_2$ solution. The $CaCO_3$ precipitate, collected on a sintered glass filter, was counted for its β activity. The counting results were then converted into weight of carbon on the collector-guard ring assembly surface by using a calibration curve. The latter was constructed from the counting results for the $CaCO_3$ precipitated from aliquots taken of 100 c.c. of 1 N NaOH solution in which the CO_2 formed by the oxidation of 10 milligrams of the C^{14}-containing fuel material was collected.

(C-RD)(Gp-1) Other experimental techniques, such as that used for the study of the vacuum emission characteristics, the determination of the uranium and zirconium contents of the deposit on the surface of the collector-guard ring assembly, the metallographic examinations of the microstructures and the X-ray determination of the preferred crystal orientation, were the same as that used in the screening tests.

1.3.2. Test Results

1.3.2.1. Vacuum Emission Studies. (C-RD)(Gp-1) Figure 22 shows the thermal history and the vacuum work function of F_2 as a function of testing time. The vacuum work function was stable at all three testing temperatures ($1673^{\circ}K$, $1873^{\circ}K$, and $2073^{\circ}K$). There was a slight decrease in vacuum work function when the testing temperature was lowered, presumably due to the change in adsorbed fuel component concentrations on the emitting surface. However, the change was reversible and the vacuum work function was higher than that of unfueled fluoride tungsten even at $1673^{\circ}K$ (4.65 eV versus 4.5 eV), probably due to the adsorption of carbon on the emitting surface. Figure 23 illustrates the thermionic emission pattern of F_2 at $2073^{\circ}K$. No emission enhancement due to uranium adsorption could be noticed. Thus the results for F_2 were in good agreement with that obtained on the screening test sample F_1.

(C-RD)(Gp-1) Figure 24 shows the thermal histories and the vacuum work functions for the chloride tungsten sample Cl_2 and the three duplex tungsten

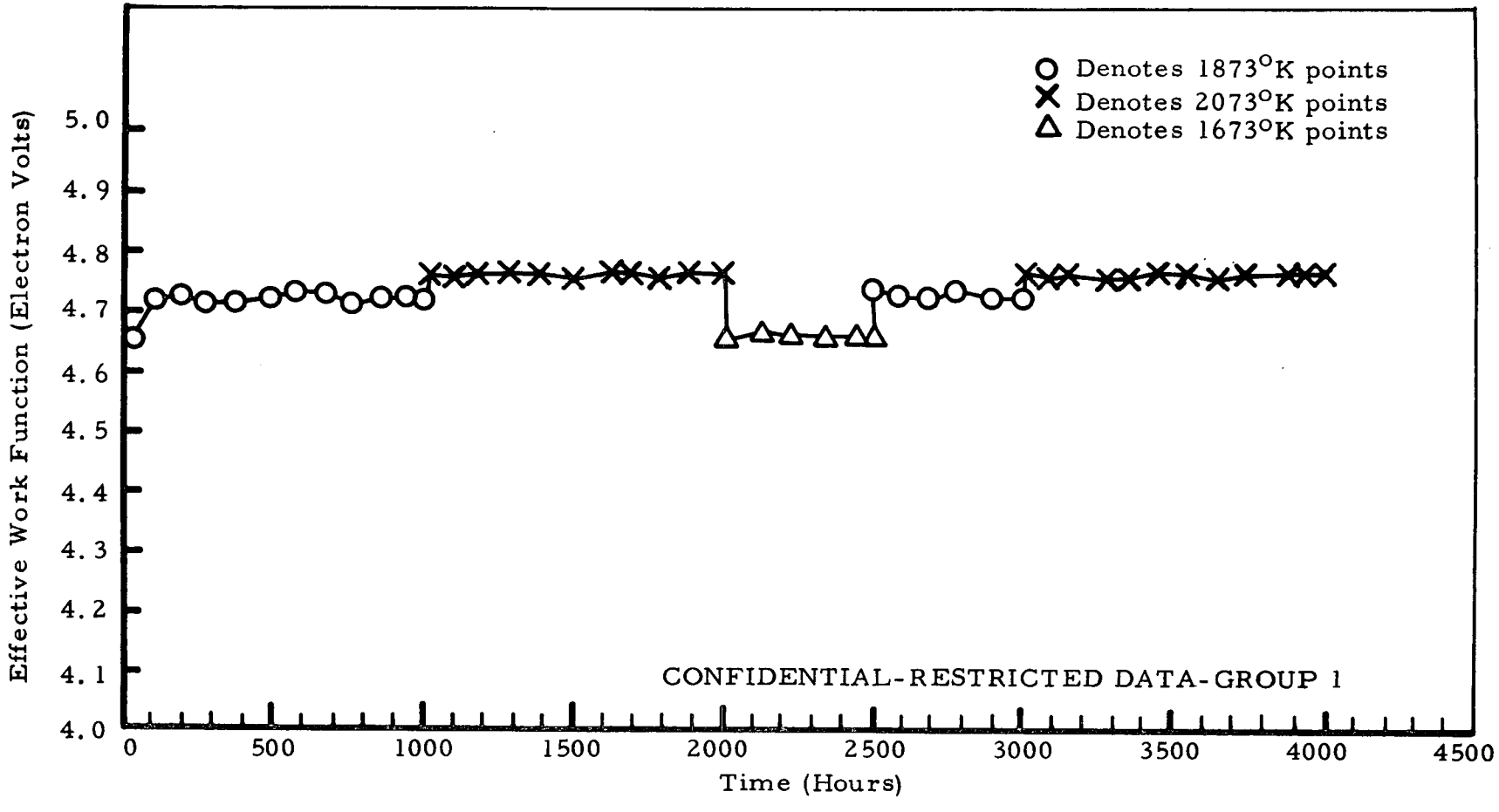

Fig. 22. (U) Effective work function of Sample F_2 (fluoride tungsten clad 90UC-10ZrC) as a function of time at 1873°K, 2073°K, and 1673°K

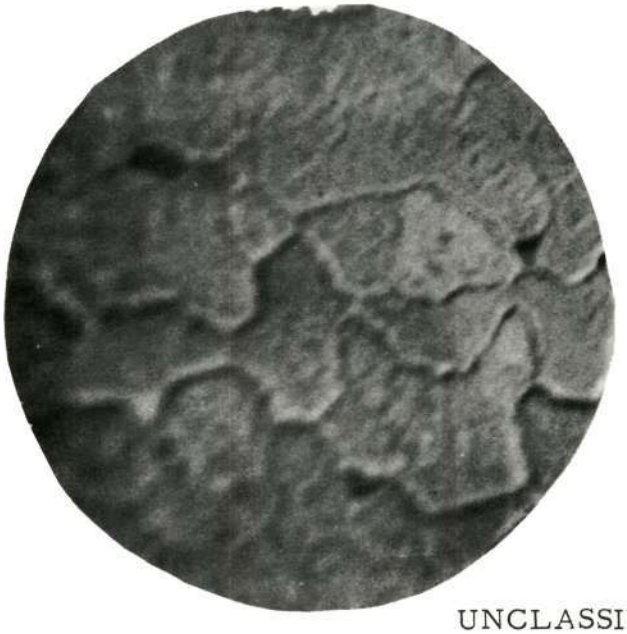

UNCLASSIFIED

Fig. 23. (U) Thermionic emission pattern of F_2 at 2073°K (300X)

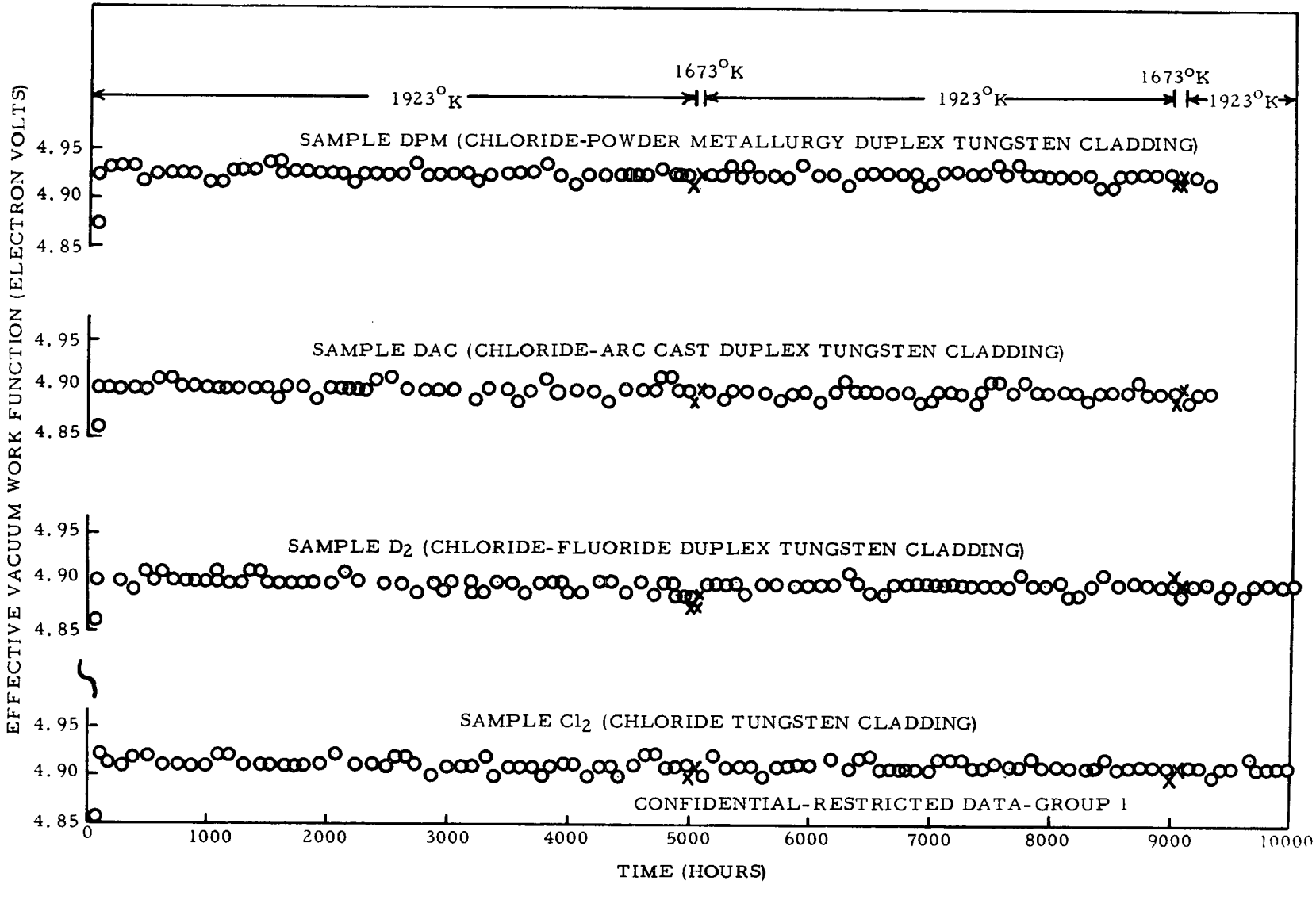

Fig. 24. (U) Effective vacuum work functions of various tungsten clad 90UC-10ZrC samples as a function of time at 1923°K and 1673°K

samples D_2, DAC and DPM. All four test samples maintained their high vacuum work functions, both at 1923°K and after cooling to 1673°K at testing times of 5000 and 9000 hours. The thermionic emission patterns of these duplex tungsten samples at 1923°K are shown in Fig. 25. The patterns were similar to that obtained from chloride tungsten emitting surfaces. No evidence of surface contamination by uranium could be detected.

1.3.2.2. Fuel Component Transport Rates. (C-RD)(Gp-1) Table 4 summarizes the average fuel component transport rates for the five types of tungsten claddings over the entire testing periods (4000 hours for Sample F_2, 10,000 hours for the other samples). It can be seen that the results for the columnar fluoride tungsten cladding were in general agreement with that obtained during the screening test (see Table 2). Lowering the temperature from 2073°K to 1923°K, the uranium transport rates for the chloride tungsten cladding and the chloride-fluoride duplex tungsten cladding decreased by about a factor of two. The chloride tungsten cladding and the chloride-arc cast duplex tungsten cladding showed comparable fuel component transport rates. Tungsten cladding of such grain structures exhibited very low fuel component transport rates ($\sim 10^{-11}$ gm/cm^2 hr). The chloride-arc cast duplex tungsten seems to be a better cladding material than the chloride-fluoride duplex tungsten from the point of view of minimizing fuel component transport rates through the cladding.

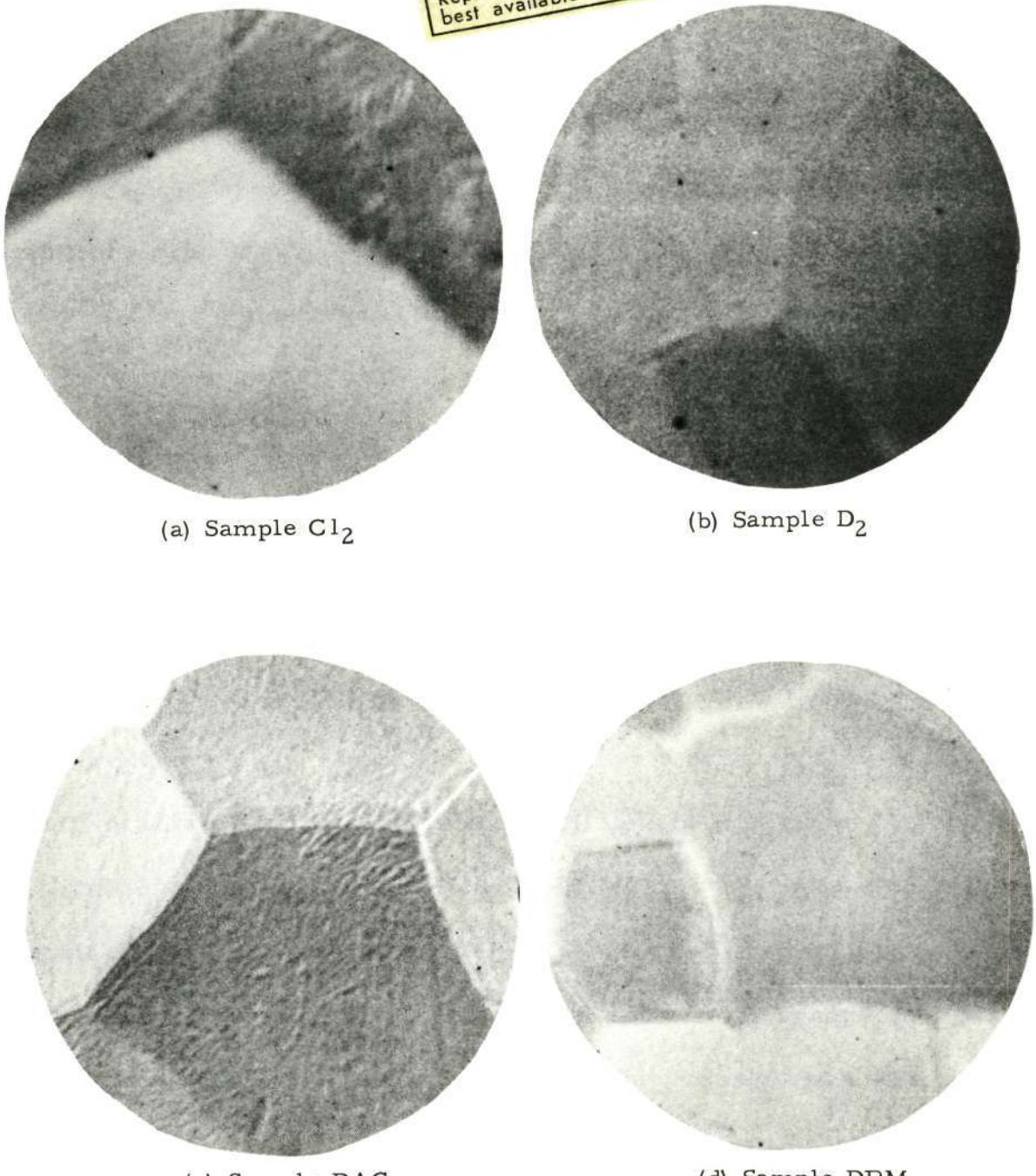

(a) Sample Cl_2

(b) Sample D_2

(c) Sample DAC

(d) Sample DPM

UNCLASSIFIED

Fig. 25. (U) Thermionic emission patterns at 1923°K for four duplex tungsten samples after 10,000 hours at 1923°K (75X)

(This page is Unclassified)

TABLE 4

(U) FUEL COMPONENT TRANSPORT RATES
OBTAINED IN LONG-TERM TESTS

(This table is classified Confidential-Restricted Data-Group 1)

Sample	U		Zr		C	
	Total Amount (Microgram)	Average Flux gm/cm^2 hr.	Total Amount (Microgram)	Average Flux gm/cm^2 hr.	Total Amount (Microgram)	Average Flux gm/cm^2 hr.
Columnar fluoride tungsten F_2	7.5	2.6×10^{-9}	0.70	2.5×10^{-10}	4.3	1.52×10^{-9}
Chloride tungsten Cl_2	0.11	1.5×10^{-11}	<.01	$<10^{-12}$	<1.5	$<2.1 \times 10^{-10}$
Chloride-fluoride duplex tungsten D_2	0.36	5×10^{-11}	0.02	3×10^{-12}	<1.5	$<2.1 \times 10^{-10}$
Chloride-arc cast duplex tungsten DAC	0.07	1×10^{-11}	<.01	$<10^{-12}$	0.14	2×10^{-11}
Chloride-powder metallurgy duplex tungsten DPM	0.25	3.5×10^{-11}	<.01	$<10^{-12}$	0.49	7×10^{-11}

Note: Sample F_2 was heated at 2073°K for 2000 hours, 1873°K for 1500 hours and 1673°K for 500 hours. Fluxes were based on the 4000 hour test time. Samples Cl_2, D_2, DAC and DPM were heated at 1923°K for 9800 hours and at 1673°K for 200 hours. Fluxes were based on the 10,000 hour test time.

1.3.2.3. Post-Test Microstructures and Degree of Preferred Crystal Orientation. (C-RD)(Gp-1) Figure 26 contains the grain structures of the emitting surface of the five long-term test samples. Figures 27 through 31 compare their post-test X-ray pole figure data with the pre-test results. The scatter of the post-test data points for Samples Cl_2, D_2, DAC and DPM is due to their large grain sizes, since the angular distribution of the axes of preferred crystal orientation is no longer continuous when the grain size is too large. However, the points are still centering around the pre-test curves, and the grain growth does not seem to affect the vacuum work functions of these samples. Figure 32 illustrates the post-test appearances of the interfaces between the chloride tungsten layers and the fluoride, arc-cast, and powder metallurgy tungsten substrates of Samples D_2, DAC and DPM. It can be seen that in each case the bond is in excellent condition. Figure 33 shows the appearances of the fuel-cladding interfaces of these test samples. A reaction layer, identified by electron microprobe analysis to be the UWC_2 phase, was found between the carbide fuel and the tungsten cladding in each case. The average thickness of this layer was about 15 microns for Sample F_2 and about 10 microns for the other samples. For cladding of bigger grain sizes, such as the chloride tungsten and the arc-cast tungsten, selective penetration of the reaction layer into the cladding was more pronounced. In the case of the chloride tungsten Sample Cl_2, spikes of about 25 micron length were observed. These spikes were shown to be the UWC_2 phase containing less than 1% zirconium. The presence of a tungsten-rich phase, probably

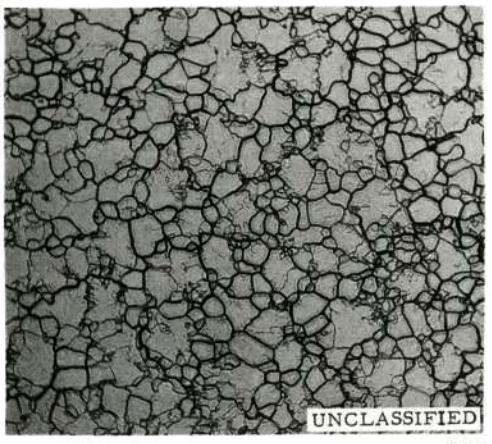

M 28078-2 50X
(a) Columnar fluoride tungsten F_2

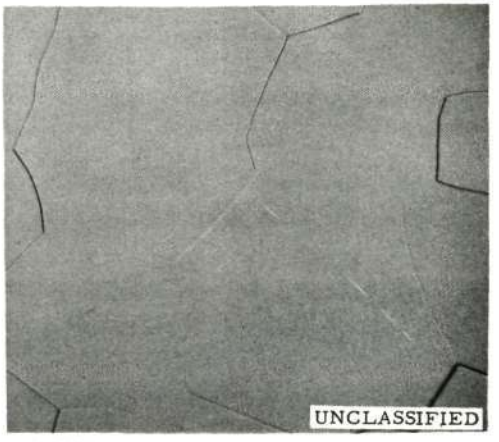

M 29939-8 50X
(b) Chloride tungsten Cl_2

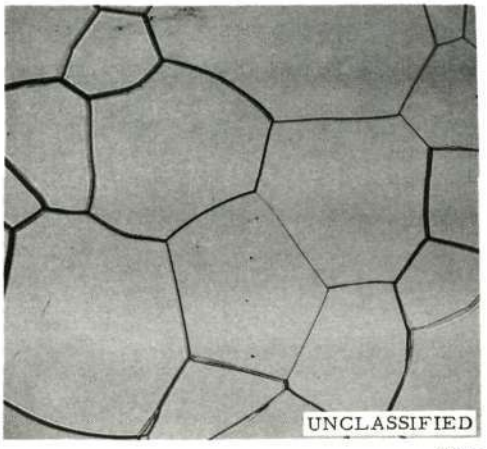

M 33291-2 50X
(c) Chloride-fluoride duplex tungsten D_2

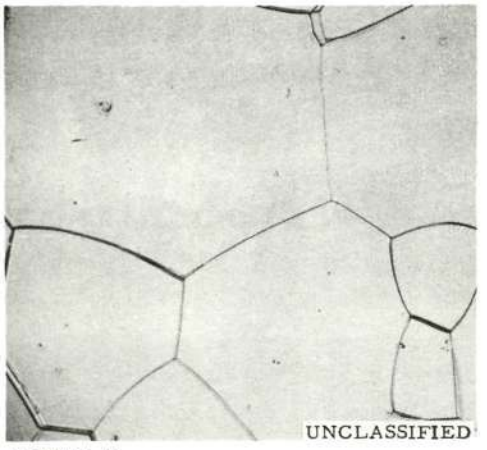

M 33291-3 50X
(d) Chloride-arc cast duplex tungsten DAC

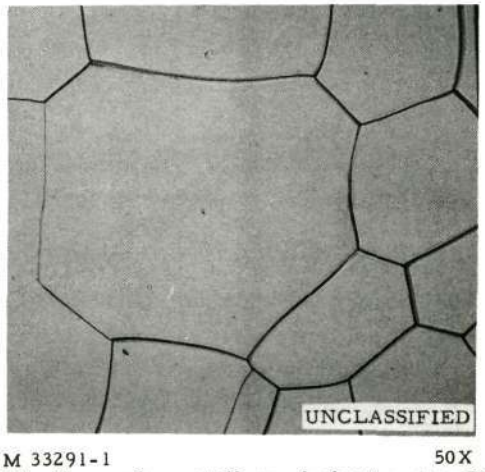

M 33291-1 50X
(e) Chloride-powder metallurgy duplex tungsten DPM

Fig. 26. (U) Post-test surface grain structures of the five long-term test samples

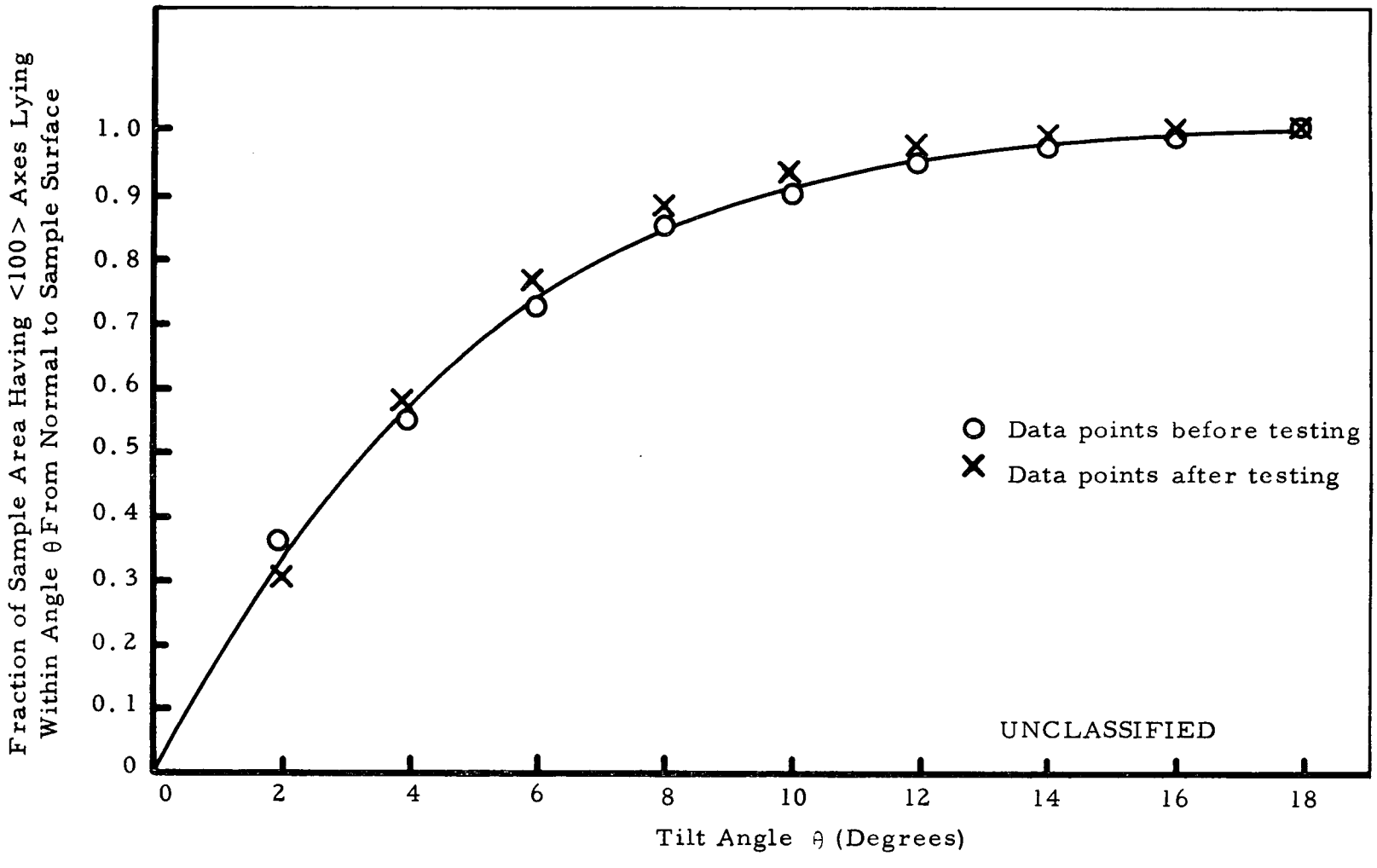

Fig. 27. (U) Comparison of the post-test and the pre-test spatial distributions of the <100> axes in columnar fluoride tungsten sample F_2

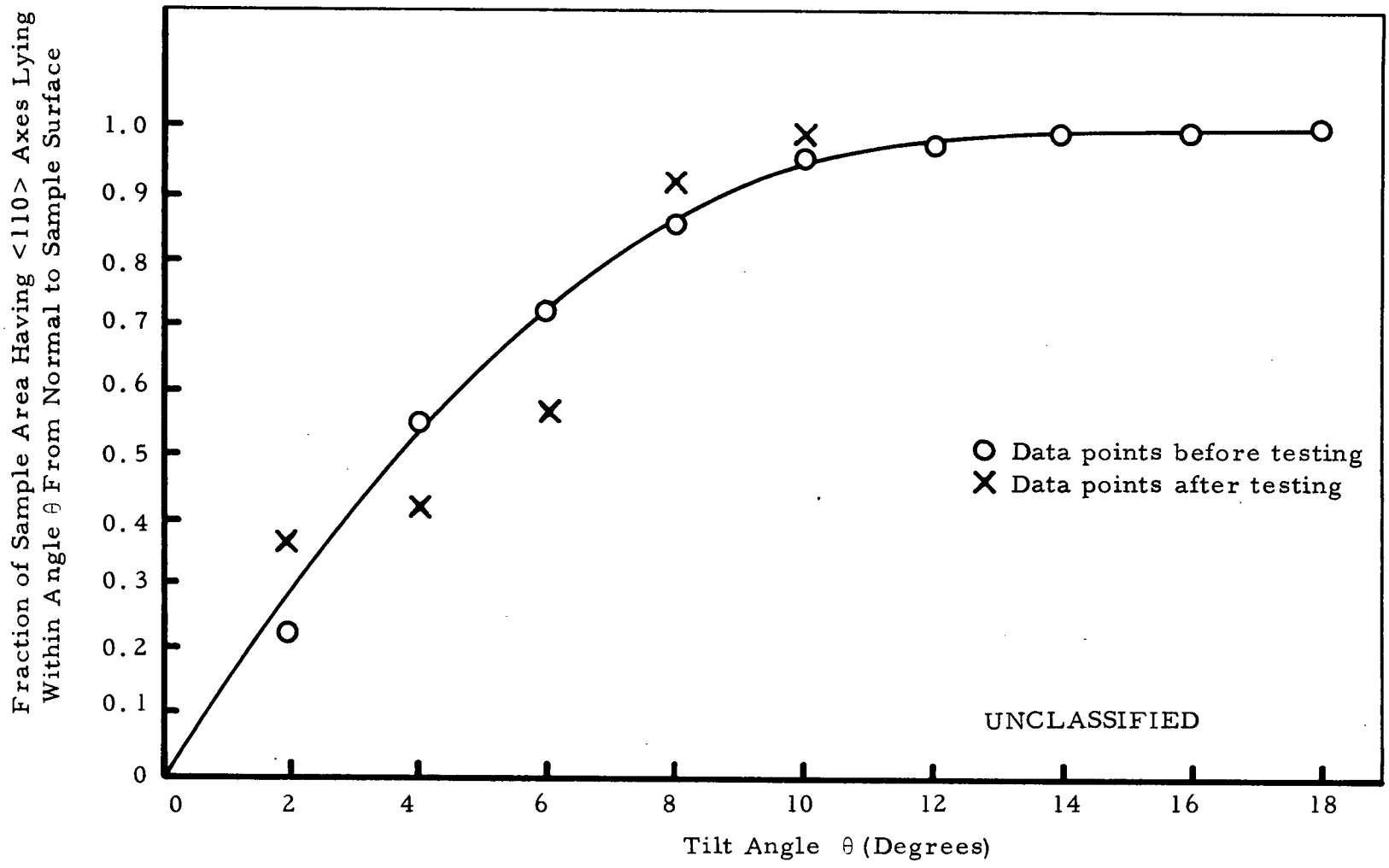

Fig. 28. (U) Comparison of the post-test and the pre-test spatial distributions of the <110> axes in chloride tungsten sample Cl_2

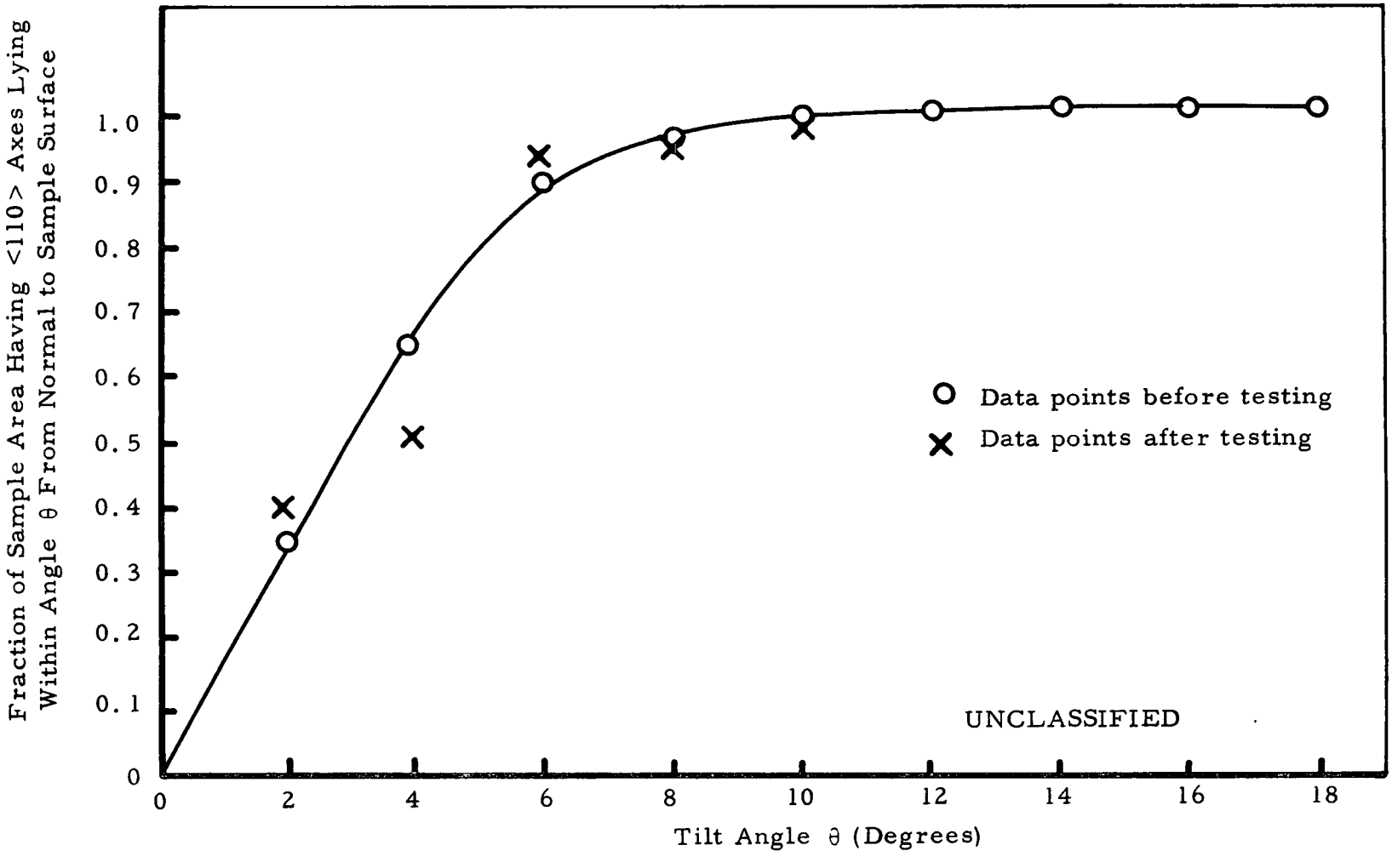

Fig. 29. (U) Comparison of the post-test and the pre-test spatial distributions of the <110> axes in chloride-fluoride duplex tungsten sample D_2

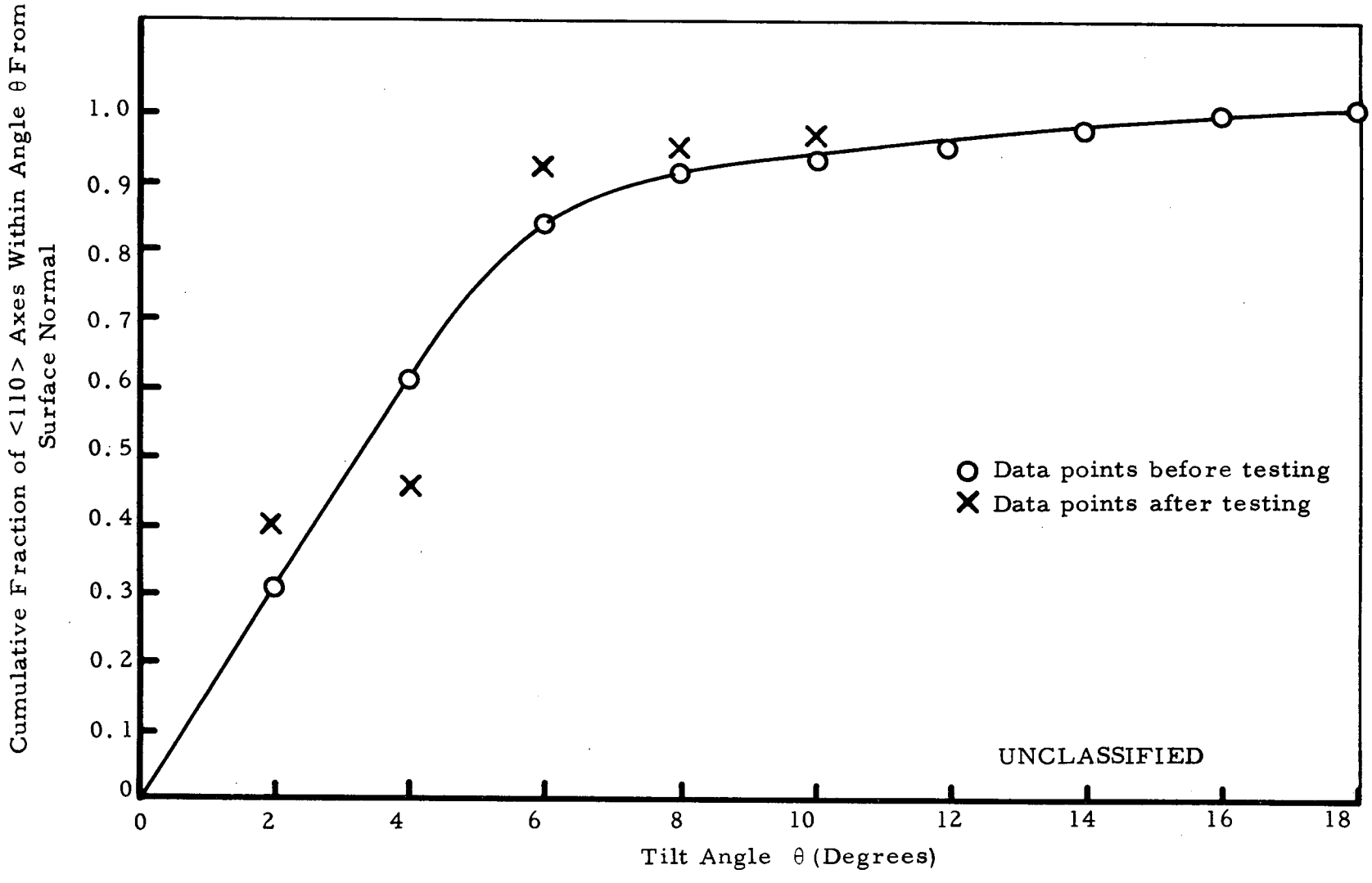

Fig. 30. (U) Comparison of the post-test and the pre-test spatial distributions of the <110> axes in chloride-arc cast duplex tungsten sample DAC

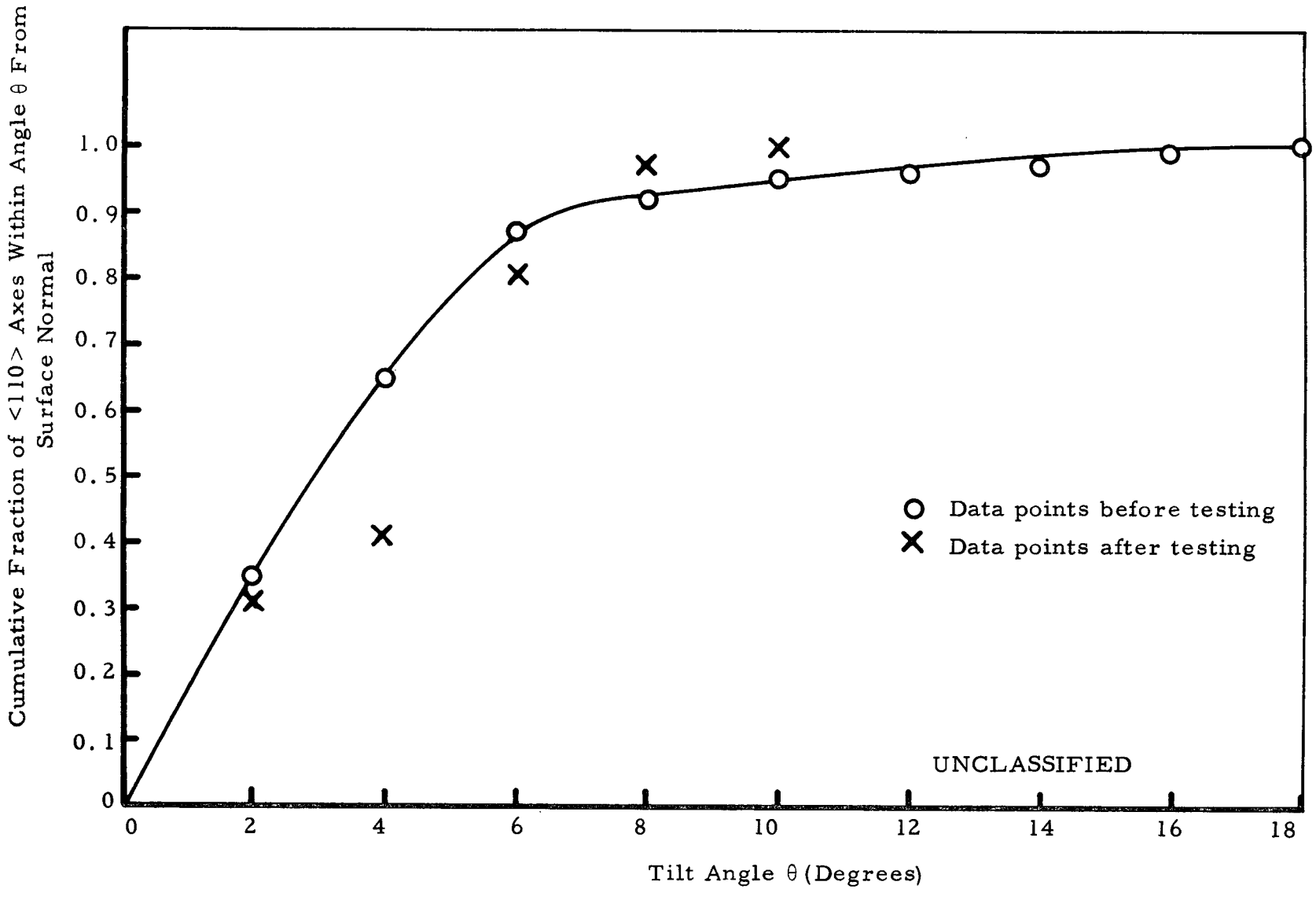

Fig. 31. (U) Comparison of the post-test and the pre-test spatial distributions of the <110> axes in chloride-powder metallurgy duplex tungsten sample DPM

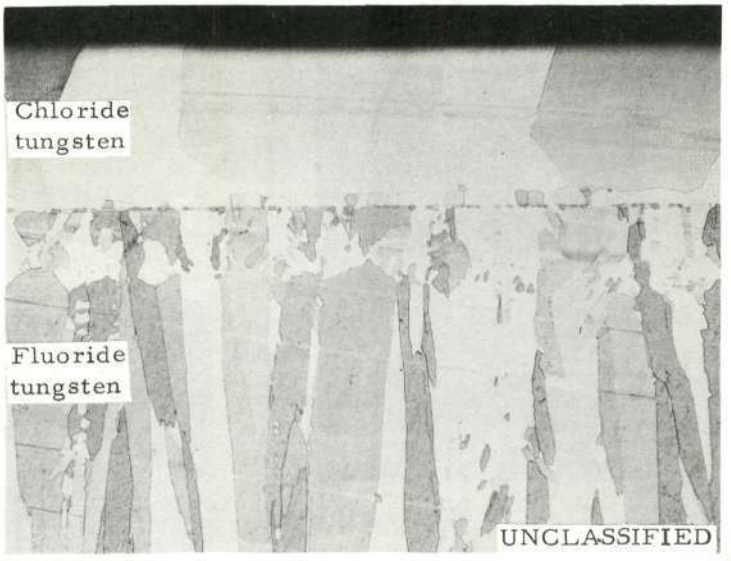

M 26465-1 75X

(a) Chloride-fluoride duplex tungsten Sample D_2

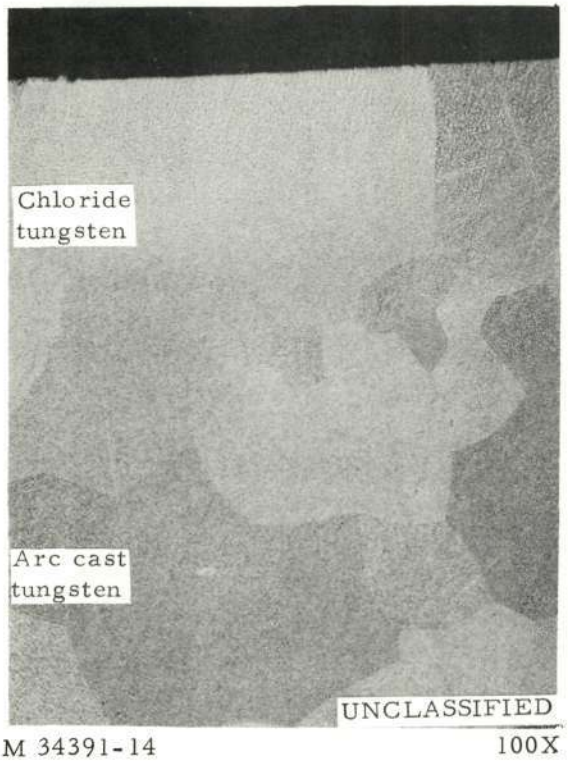

M 34391-14 100X

(b) Chloride-arc cast duplex tungsten Sample DAC

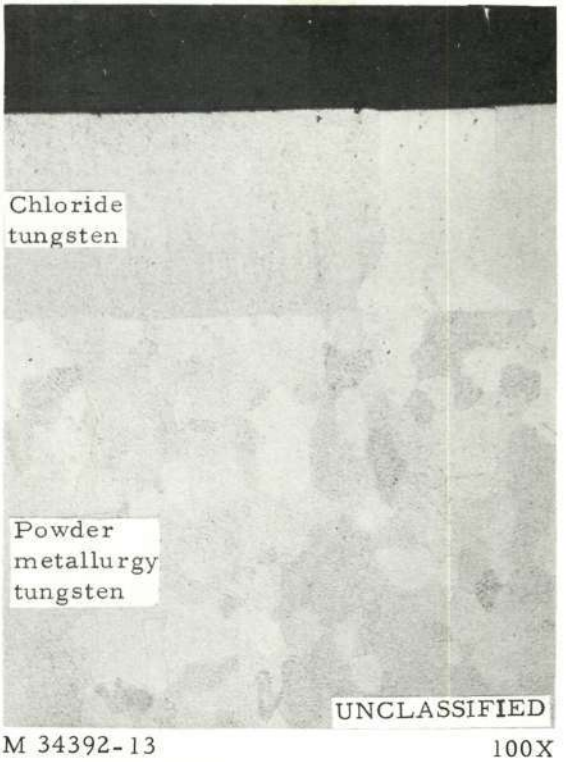

M 34392-13 100X

(c) Chloride-powder metallurgy tungsten Sample DPM

Fig. 32. (U) Post-test appearance of the interfaces between the chloride tungsten layers and the fluoride, arc-cast and powder metallurgy tungsten substrates of Samples D_2, DAC, and DPM

(This page is Unclassified)

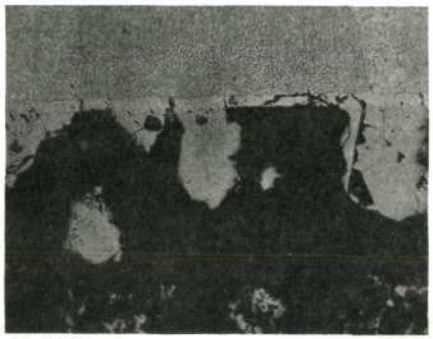

M 33291-4 150X

(a) Columnar fluoride tungsten Sample F_2

Reaction layer

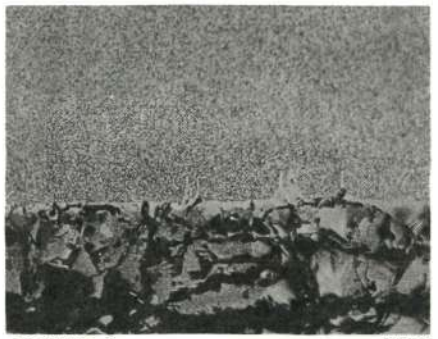

M 33292-3 250X

(b) Chloride tungsten Sample Cl_2

Reaction layer

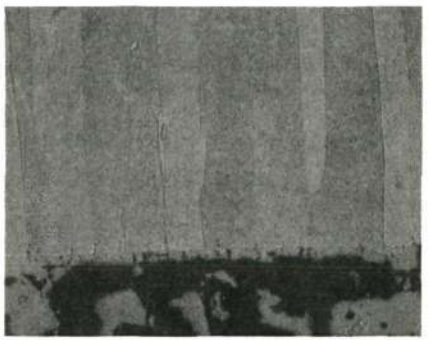

M 33293-6 250X

(c) Chloride-fluoride duplex tungsten Sample D_2

Reaction layer

M 34391-9 250X

(d) Chloride-arc cast tungsten Sample DAC

Reaction layer

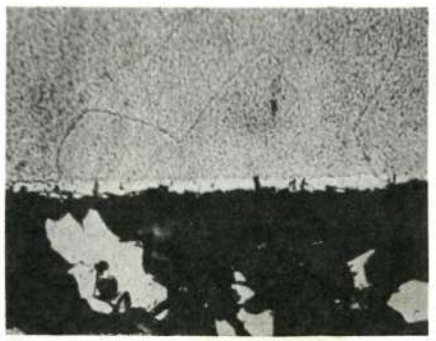

M 34392-9 250X

(e) Chloride-powder metallurgy tungsten Sample DPM

Reaction layer

Fig. 33. (U) Post-test appearances of fuel-cladding interfaces of the five test samples

W_2C, was detected between the reaction layer and the tungsten cladding in some locations. A zirconium-rich fuel region was found between the reaction layer and the fuel proper. It seems that the 90UC-10ZrC, after becoming alloyed with the tungsten carbide to form the UWC_2 phase, left a zirconium-rich region behind. All the fuel materials examined contained a few wt% of dissolved tungsten and UWC_2 dispersions, as in the pre-test state.

1.4. CONCLUSIONS AND DISCUSSIONS

(C-RD)(Gp-1) The test results indicate that hyperstoichiometric (C/U = 1.04) 90UC-10ZrC containing 4 wt% tungsten additive has no serious effect on the vacuum work function of columnar fluoride tungsten in the temperature range 2073°K to 1673°K. The previously observed[1] "uranium effect" which caused the vacuum work function of columnar fluoride tungsten cladding to fall below 4.5 eV at temperatures below 2073°K has been eliminated by the use of such improved carbide fuel material. Of particular importance is that chloride tungsten, either in the form of a single layer or as an emitting layer over other types of tungsten substrates, can maintain its high vacuum work function (~4.9 eV) in the temperature range 2073°K to 1673°K in the presence of such carbide fuel material. This implies that carbide fueled chloride tungsten and duplex tungsten should show promise as high performance thermionic emitters in cesiated converters.

(C-RD)(Gp-1) While the fuel component transport does not seem to affect the vacuum work functions of the various types of tungsten claddings studied, the deposition of the fuel components transported through the cladding on the collector surface of a cesiated converter may affect the collector work function and the electrode emittance. Converters containing carbide fueled columnar fluoride tungsten emitters are expected to show degradation of thermionic performance and efficiency, since columnar fluoride tungsten cladding has the highest fuel component transport rates among the various types of tungsten claddings studied. On the other hand, converters containing carbide fueled chloride tungsten and chloride-arc cast duplex tungsten claddings which have much lower fuel component transport rates may yield stable and high thermionic performance. These predictions have been bourne out by the test results of two out-of-pile cesiated converters. Converter LC-8[2] contains a carbide fueled columnar fluoride tungsten emitter and has exhibited thermionic performance and efficiency degradation in the temperature range 1873°K to 2073°K, which was shown to be caused mainly by the deposition of fuel components on the collector surface. Another converter contains a carbide fueled chloride-arc cast duplex tungsten emitter and has yielded stable and high thermionic performance for 10,000 hours at an average emitter temperature of 1873°K, with the test continuing.

(C-RD)(Gp-1) An interaction layer of UWC_2 phase was observed at the fuel-cladding interfaces in all the cases studied. The reaction rate, however, was very slow (< 20 microns in 10,000 hours at 1923°K). Neither

the structural integrity nor the vacuum work functions of the tungsten claddings studied were impaired by the formation of such an interaction layer. Thus, the formation of such an interaction layer does not seem to pose a serious problem to the life and performance of out-of-pile cesiated converters containing carbide fueled high performance emitters.

(C-RD)(Gp-1) Both the vacuum work function measurements and the out-of-pile converter test results point out that by proper selections of composition and stoichiometry of carbide fuel material and microstructures of tungsten cladding, it should be possible to achieve carbide fueled thermionic fuel elements of stable and high thermionic performance. In-pile tests of such fuel-cladding systems, however, are needed to confirm that the fuel component transport rates are not enhanced by irradiation effects. For instance, the rate of interaction between carbide fuel and tungsten cladding has been found to be much higher in-pile than out-of-pile.[11] Mechanism for such acceleration of reaction rate and methods for minimizing such fuel-cladding interaction are currently being investigated. The approaches under consideration are the lowering of the C/U ratio of the carbide fuel material, the increase of the tungsten concentration in the carbide fuel material and the use of carbide diffusion barriers. It is believed that these approaches will further reduce fuel component transport rates through the tungsten cladding and add more safety margin for the in-pile operation of carbide fueled high performance thermionic converters.

PART II. PREPARATION AND EVALUATION OF (110) ORIENTED CYLINDRICAL TUNGSTEN EMITTER

2.1. OBJECTIVES

(U) In 1966 under a NASA sponsored program at GGA,[12] it was shown that (110) oriented tungsten deposits of 5 eV vacuum work function could be obtained by the hydrogen reduction of tungsten chlorides. Long-term (1000 hours) tests, using thermally stabilized planar samples, demonstrated the stability of such high work function at 2073°K.

(U) Since converters containing (110) oriented chloride tungsten emitters of high vacuum work functions yielded better thermionic performance than converters containing (100) oriented fluoride tungsten emitters,[13],[14],[15] there was strong incentive for understanding how the degree of (110) preferred orientation and the vacuum work function of the deposit would be affected by varying the deposition parameters. In 1967, under another NASA sponsored program at GGA,[7] the conditions (e.g. mandrel temperature, chlorine and hydrogen flow rates) under which (110) oriented planar chloride tungsten samples of 4.9-5.0 eV vacuum work functions could be reproducibly prepared were established. The stability of such high vacuum work functions at 2073°K was again demonstrated in 1000 hour tests made on five samples deposited on

molybdenum mandrels* and another five samples deposited on fluoride tungsten mandrels.

(U) Since the thermionic fuel element contains emitters of cylindrical configuration, the objective of this work was to determine the effects of varying deposition parameters on the production of cylindrical emitters having a high degree of (110) orientation and high vacuum work functions. A deposition apparatus for cylindrical samples was assembled. X-ray pole figure machine and vacuum emission cells were developed for the study of the distributions of the <110> crystal axes and the vacuum work function along the axial direction of a cylindrical emitter. Samples were deposited on fluoride tungsten mandrels under various deposition conditions and evaluated for their microstructures, impurity contents, degrees of (110) preferred orientation and vacuum work functions. Selected samples were studied for the stability of their vacuum work functions at 2073°K. Deposition techniques, evaluation methods and evaluation results are described below.

2.2. PREPARATION OF CYLINDRICAL CHLORIDE TUNGSTEN SAMPLES

2.2.1. Deposition Apparatus

(U) The preparation of the samples was carried out at San Fernando Laboratories of Fansteel Corporation. The basic design of the deposition

* The molybdenum mandrel was removed by dissolving in HNO_3 + HCl before the measurement of vacuum work function was made.

apparatus is shown in Fig. 34. The fluoride tungsten mandrel was supported on a boron nitride insulating collar and covered on the top end with a molybdenum plug containing a blackbody hole for temperature monitoring by optical pyrometry. High frequency induction was used to heat the mandrel. The deposition chamber was made of Vycor with provision for rotating the mandrel through a Teflon seal during the deposition. The tungsten chlorides were generated in a Vycor chlorinator by reacting fluoride tungsten chips with chlorine gas. The temperature of the chlorinator was maintained with a Nichrome resistance furnace and measured with a Chromel-Alumel thermocouple located in a Vycor thermocouple well. The exhaust gas from the deposition chamber was evacuated continuously through a trapping system during the deposition. Pressure in the deposition chamber could be adjusted by bleeding inert gas into the exhausting system at a controlled rate. Several modifications to this basic design were made during trial runs. These will be described in the sections concerning these trial runs.

2.2.2. Studies of the Chlorination of Fluoride Tungsten Chips

(U) A series of tungsten chlorination runs was conducted to define the conditions required to produce WCl_6 from the chlorinator. These runs are summarized in Table 5. In each case a charge of fluoride tungsten chips was loaded into the Vycor chlorinator (30 mm diameter, 200 mm long). The chips were thoroughly cleaned in HF + HNO_3, rinsed in $NaHCO_3$ and then distilled water prior to the loading operation. They were further cleaned

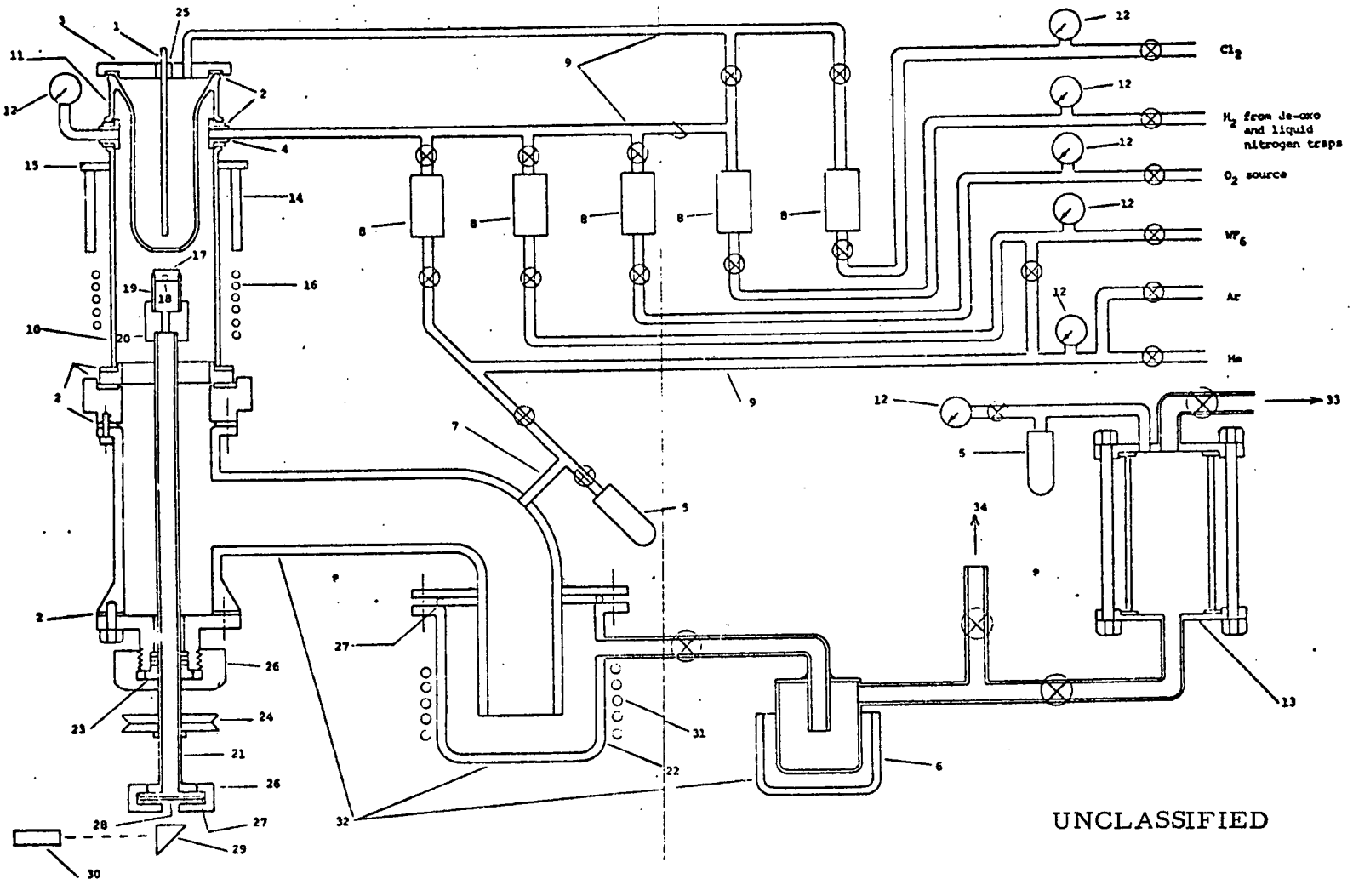

Fig. 34. (U) Chloride tungsten deposition system

KEY TO FIGURE 34

1. Thermocouple Well - Vycor Glass
2. Viton Seal
3. Brass Seal Plate
4. Brass Seal Plate/Manifold Combination Ring
5. TC Gauge Plus Mercury Manometer in 1-10 mm Range
6. Liquid Nitrogen Trap
7. Inert Gas Source for Trapping System Protective Blanket Between Runs and to Trim System Pressure During Depositions
8. Flowmeter
9. Copper Lines
10. Vycor Glass Chamber, 38 mm Diameter
11. Vycor Glass Chlorinator, 30 mm Diameter
12. Pressure Gauge
13. KOH Trap for HCl
14. Nichrome Resistance Heater
15. Heat Shield - Steel
16. Induction Heater Coil
17. Molybdenum End Plug
18. Black Body Hohlraum
19. Tungsten Tubing Substrate made by WF_6/H_2 Reduced CVD
20. Boron Nitride Insulating Collar
21. Stainless Steel Support Tube

KEY TO FIGURE 34 (Continued)

22. Steel Primary Condensate Collection Chamber

23. Rotating Seal - Teflon

24. Gear System

25. Teflon Seal

26. Brass Coupling

27. O-Rings

28. Quartz Window

29. Stationary Prism

30. Pyrometer

31. Water Cooling Coil

32. All Steel Trapping System

33. Mechanical Pump(s)

34. Water Aspirator System for Elimination of Post Deposition Condensate Wastes

TABLE 5

(U) CHLORINATION STUDY RUNS FOR WCl_6 FORMATION

(This table is Unclassified)

Run No.	Run Time	Heated W Bed Length	Maximum Temp. of W Bed (°K)	Cl_2* Flow	W Used	Cl/W Ratio
1.	60 min.	4"	1123	360 cc/min.	3.43 gm.	--
2.	30 min.	4"	1123	360 cc/min.	8.54 gm.	--
3.	60 min.	8"	1123	360 cc/min.	14.02 gm.	--
4.	30 min.	4"	1148	360 cc/min.	25.03 gm.	--
5.	30 min.	4"	1173	360 cc/min.	15.75 gm.	--
6.	30 min.	8"	1173	360 cc/min.	26.17 gm.	--
7.	60 min.	8"	1123	360 cc/min.	58.57 gm.	5.42
8.	60 min.	8"	1148	360 cc/min.	59.49 gm.	5.54
9.	60 min.	8"	1273	360 cc/min.	60.65 gm.	5.36
10.	60 min.	4"	1273	360 cc/min.	55.40 gm.	5.84
11.	60 min.	2 @ 4" = 8"	873°K/1273°K Top Bottom	360 cc/min.	54.62 gm.	5.95
12.	60 min.	2 @ 4" = 8"	873°K/1273°K Top Bottom	600 cc/min.	90.75 gm.	5.97
13.	60 min.	2 @ 4" = 8"	873°K/1273°K Top Bottom	150 cc/min.	23.46 gm.	4.39

Note: The W/Cl ratios for Run No. 1 through 6 were all below 5.00
Oxygen and nitrogen contents of chlorine were less than 50 ppm each.

*
Standard temperature and pressure.

in situ in hydrogen at 1223-1273°K for 1 hour before the chlorination run. All runs were conducted at a 5 torr residual chamber pressure, and unreacted chlorine was measured with a flowmeter located at the exhaust of the Kinney KC-15 evacuation pump. Calculation of the Cl/W ratio of the chlorination product was carried out by the equation:

$$Cl/W = \frac{2\,(B-C)}{A}$$

where

$$A = \frac{\text{Reacted weight of tungsten}}{\text{Atomic weight of tungsten}} = \text{Reacted gram mole of tungsten}$$

$$B = \frac{(\text{metered flow of chlorine feed in standard c. c. /min})(\text{run time in minutes})}{22,400 \text{ standard c. c. /gram-mole}}$$

$$C = \frac{\text{Total amount of unreacted chlorine in standard c. c.}}{22,400 \text{ standard c. c. /gram-mole}}$$

The quantity A was determined by weighing the tungsten chips before and after a run. B was held at a predetermined value and monitored by a flowmeter during the run. C was determined by the graphical integration of residual chlorine flow in the exhaust gas as a function of time. A typical plot of such residual chlorine flow is shown in Fig. 35.

(U) The results in Table 5 indicate that the Cl/W ratio in the chlorination product increased with the temperature of the chlorinator. However, too long a heating zone tended to lower the Cl/W ratio because of the WCl_6 formed in the upper part of the chlorinator could react with the tungsten

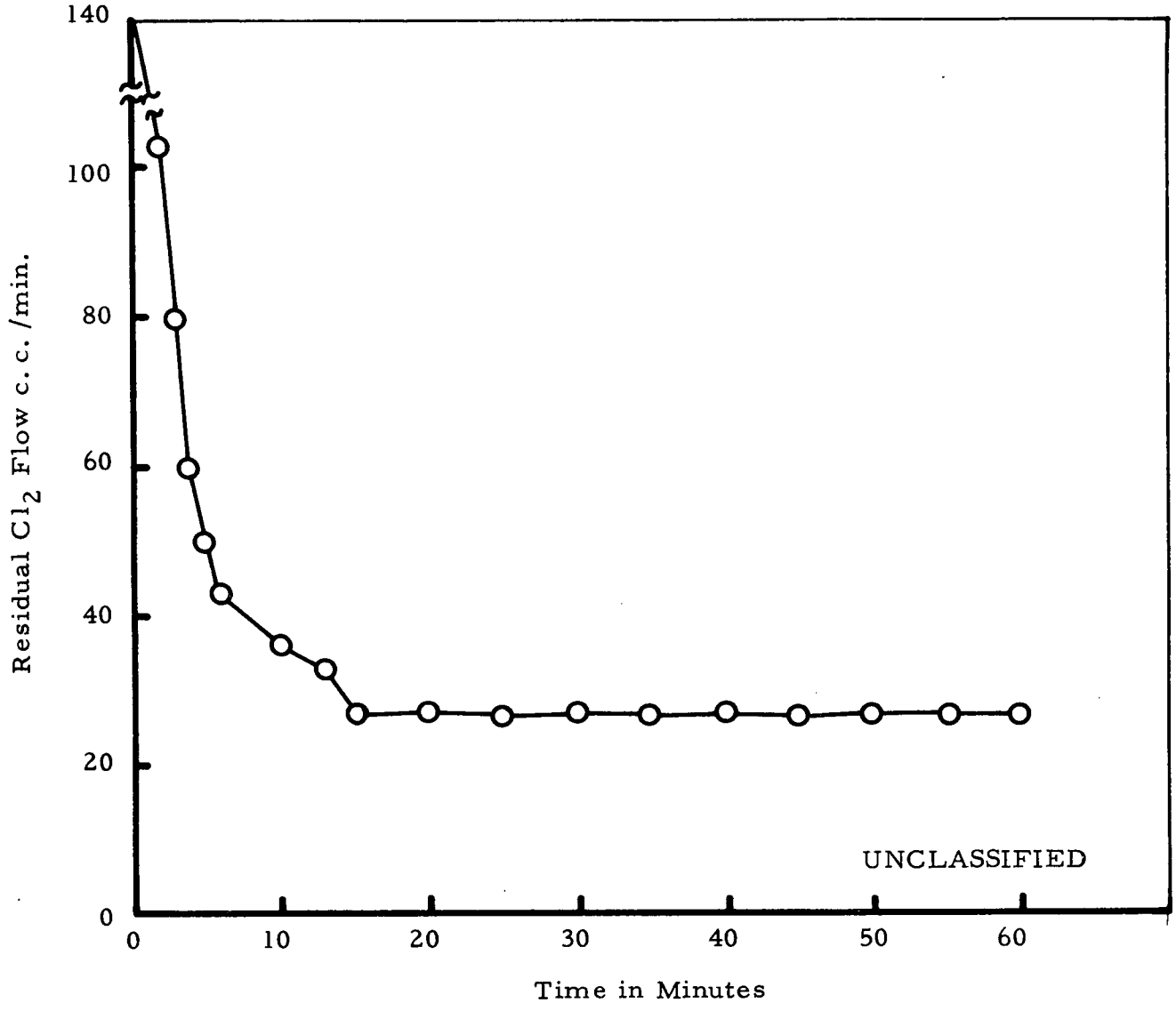

Fig. 35. (U) Residual Cl_2 flow (standard temperature and pressure) chart for chlorination study run No. 11

chips in the lower part of the chlorinator to form subhalides (e.g. compare Run No. 9 with Run No. 10). The best results were obtained by using two 4 inch long heaters for the chlorinator, one as a preheater at 873°K and the other held at 1273°K for the chlorination reaction. Cl/W ratios of 5.95 - 5.97 were obtained at chlorine flow rate of 360 c.c./min. to 600 c.c./min. Lower chlorine flow rate (e.g. 150 c.c./min.) yielded a low Cl/W ratio (see Run No. 13), probably due to the longer residence time for the WCl_6 formed in the chlorinator and thus more opportunity to react with the tungsten chips to form subhalides.

(U) Since the work plan included the use of WCl_5 in addition to WCl_6 as the starting material in order to find out how the valence state of the tungsten chloride would affect the composition and the structure of the deposit, another series of tungsten chlorination runs was carried out to define the conditions for producing WCl_5. The results of these runs are shown in Table 6. It can be seen that a Cl/W ratio close to five can be obtained when the top four inches of the furnace is maintained at 1173°K instead of 873°K.

2.2.3. Analysis of Impurity Contents of Fluoride Tungsten Substrates

(U) Samples taken from the mandrels used for this work were found to contain impurities in the following ranges (in ppm): C, 3-14; F, <3-8; Cl, <3; H, 0.3-3.6; O, 2.6-13; N, 0.5-1; Si, <1-4.6. The length of the mandrel was in the range of 5 to 6 inches.

TABLE 6

(U) CHLORINATION STUDY RUNS FOR WCl_5 FORMATION

(This table is Unclassified)

Run No.	Run Time	Heated W Bed Length	Maximum Temp. of W Bed	Cl_2 Flow	W Used	Cl/W Ratio
1	60 min.	2 @ 4" = 8"	1123°K Top/ 1273°K Bottom	360 cc/min.	63.88 gm.	5.12
2	60 min.	2 @ 4" = 8"	1123°K Top/ 1223°K Bottom	360 cc/min.	60.57 gm.	5.42
3	60 min.	2 @ 4" = 8"	1173°K Top/ 1273°K Bottom	360 cc/min.	63.36 gm.	5.08
4*	60 min.	2 @ 4" = 8"	1173°K Top/ 1273°K Bottom	360 cc/min.	63.5 gm.	5.11

*
Duplicate run to establish reproducibility

2.2.4. Practice and Trial Runs

(U) All fluoride tungsten mandrels used in the work described in Part II of this report had an outside diameter of 0.605 inch and an inside diameter of 0.545 inch. Deposition of the chloride tungsten layer was carried out after the fluoride tungsten mandrel was ground to a surface finish of 4 microinch and cleaned in hydrogen at 1323°K for one hour.

(U) Three practice runs, designated as PR-1, PR-2, and PR-3, were made to check out the design of the deposition apparatus. The deposition conditions are shown in Table 7. The first run, PR-1, was terminated prematurely when the chamber became plated and began suscepting to the induction heating. Runs PR-2 and PR-3 were also troubled by the plating of the glass; however, they were taken to the 60 minute completion mark. This trouble was attributed to the high pressure (15 torr) in the deposition system. It was therefore decided to lower the chamber pressure to 10 torr maximum for all further depositions to discourage the plating of the wall of the deposition chamber.

(U) Eleven trial runs, designated as R-1 through R-11, were carried out for preliminary testing and evaluation of the ranges of interest for each of the influential deposition parameters. R-1 was terminated after only 15 minutes when arcing between the mandrel and the deposit on the chamber punctured a hole through the chamber wall. The chamber diameter was therefore enlarged from 38 mm to 45 mm to reduce the plating on the chamber wall and R-2 was carried out. The run was terminated after 30 minutes when

TABLE 7

(U) PRACTICE DEPOSITION RUNS

(This table is Unclassified)

Run No.	Run Time	Cl_2 Flow	H_2 Flow	Chamber He Flow*	Bleed He Flow**	Pressure	Mandrel Temp.	H_2/W Ratio
PR-1	30 min.	360 cc/min.	445 cc/min.	325 cc/min.	Yes	15 mm	1323°K	3.7:1.0
PR-2	60 min.	360 cc/min.	445 cc/min.	650 cc/min.	Yes	15 mm	1323°K	3.7:1.0
PR-3	60 min.	360 cc/min.	445 cc/min.	650 cc/min.	Yes	15 mm	1323°K	3.7:1.0

*The presence of helium gas in the chamber during deposition was intended to improve the uniformity of the axial distribution of the deposit thickness.

**Helium was added downstream from the deposition chamber to adjust the gas pressure in the chamber during deposition.

UNCLASSIFIED

the entrance to the KOH trap was blocked by unreacted WCl_6 powder and the chamber pressure began to rise. The unreacted WCl_6 was carried to the trap in the form of a "sandstorm" by the helium bleed gas added immediately downstream of the deposition chamber. This run, while better than others, still produced some chamber plating. To alleviate the "sandstorm" problem, the position of the helium bleed was changed to a point downstream of the KOH trap. To further reduce the tendency toward chamber plating, the chamber diameter was again increased from 45 mm to 51 mm. R-3 and R-4 were carried out under these conditions. The accumulation of WCl_6 in the KOH trap was still observed during these runs. Since no chemical reaction with the KOH had been detected in previous runs, the presence of the KOH trap had become apparently superfluous. The KOH was therefore substituted by glass wool packing. The glass wool worked very well to trap the unreacted WCl_6 powder without plugging the system. R-5 through R-11 proceeded smoothly without incident. The deposition parameters for R-1 through R-11 are described in Table 8. Seven of these samples (R-3, R-4, R-5, R-8, R-9, R-10 and R-11) were evaluated with respect to their dimensions, microstructures, impurity contents and degrees of (110) preferred orientation. The evaluation results will be given in a subsequent section of this report.

2.2.5. Preparation of Specimen Sets for the Evaluation of Deposition Parameters

(U) On the basis of the evaluation results for the trial run samples R-3, R-4, R-5, R-8, R-9, R-10, and R-11, a set of reference deposition conditions

TABLE 8

(U) TRIAL DEPOSITION RUNS
(This table is Unclassified)

Run No.	Run Time	Cl_2 Flow	H_2 Flow	Chamber He Flow	Bleed He Flow	Pressure	Mandrel Temp	H_2/W Ratio
R-1	15 min.	360 cc/min.	445 cc/min.	650 cc/min.	Yes	10 mm	1323°K	3.7:1.0
R-2	30 min.	360 cc/min.	445 cc/min.	162 cc/min.	Yes	10 mm	1323°K	3.7:1.0
R-3	120 min.	360 cc/min.	350 cc/min.	325 cc/min.	Yes	10 mm	1323°K	3.0:1.0
R-4	120 min.	360 cc/min.	445 cc/min.	650 cc/min.	Yes	10 mm	1323°K	3.7:1.0
R-5	120 min.	360 cc/min.	445 cc/min.	325 cc/min.	Yes	10 mm	1373°K	3.7:1.0
R-6	30 min.	360 cc/min.	350 cc/min.	325 cc/min.	Yes	10 mm	1373°K	3.0:1.0
R-7	30 min.	360 cc/min.	350 cc/min.	650 cc/min.	Yes	10 mm	1373°K	3.0:1.0
R-8	120 min.	360 cc/min.	445 cc/min.	975 cc/min.	No	6 mm	1323°K	3.7:1.0
R-9	120 min.	360 cc/min.	350 cc/min.	650 cc/min.	No	6 mm	1323°K	3.0:1.0
R-10	120 min.	360 cc/min.	445 cc/min.	650 cc/min.	No	6 mm	1373°K	3.7:1.0
R-11	120 min.	360 cc/min.	350 cc/min.	650 cc/min.	No	6 mm	1373°K	3.0:1.0

was selected. The parameters for the reference deposition conditions were: chlorine flow rate, 360 c. c. /min.; hydrogen flow rate, 350 c. c. /min.; chamber helium flow rate, 650 c. c. /min.; bleed helium flow rate, 0 c. c. /min.; chamber pressure, 6 torr; mandrel temperature, 1323°K; tungsten chip furnace temperature, 4 inch length at 873°K plus remaining 4 inch at 1273°K. The H_2/W ratio was 3 and the Cl/W ratio was 6 in the gas reactants under these conditions. The parameters of these reference deposition conditions were changed, one at a time, and specimen sets of chloride tungsten over fluoride tungsten substrates were prepared under each of these modified deposition conditions. A total of 15 sets of specimens was deposited and each set consisted of three specimens prepared under identical conditions. The designations of the sets and the specimens, and the deposition conditions are given below. After machining and electropolishing to the required dimensions, these specimens were evaluated for their microstructures, impurity contents, degree of preferred crystal orientation, and vacuum work functions. Details of the evaluation techniques and results are given in the following section.

2.3. EVALUATION TECHNIQUES AND RESULTS

2.3.1. Evaluation Techniques

2.3.1.1. Microstructures. (U) Microstructures of the cross sections of the specimens prepared were examined by standard metallographic techniques

for grain size and morphology, and the bond between the chloride tungsten deposit and the fluoride tungsten substrate.

2.3.1.2. Impurity Contents

Carbon. (U) The carbon content was determined by burning a sample taken from the specimen in oxygen, using a Leco No. 521 furnace, and collecting the CO_2 formed on a molecular sieve for conductometric analysis, with helium as a reference.

Oxygen and Nitrogen. (U) The oxygen and nitrogen contents were determined by the standard vacuum fusion method.

Chlorine and Fluorine. (U) The chlorine and fluorine contents were determined by burning a sample taken from the specimen in wet oxygen and collecting the HCl and HF formed in water. The chlorine content of the solution was determined by neutron activation analysis. The fluorine content of the solution was determined by reacting the solution with AMADC-F (Lanthalum-Alizarian fluorine blue), followed by chlorimetric analysis with a Beckmann spectrophotometer.

Metallic Impurities. (U) The metallic impurity contents were determined by the standard spectrochemical analysis method.

2.3.1.3. Preferred Crystal Orientation. (U) The presence of preferred crystal orientation in the chloride tungsten deposit was determined by the X-ray diffraction method. The specimen was positioned so that the tangential plane to the cylindrical surface at the point of contact with the X-ray formed the required Bragg angle θ_B with the incident X-ray beam (Fig. 36(a)). During the exposure to the X-ray beam, the specimen was rotated about its cylindrical axis so that enough crystal grains were examined to make the results meaningful. If the (h, k, l) lattice plane was oriented preferentially along the radial direction of the sample, then the (h, k, l) diffraction ring should exhibit a much higher intensity at its central portion in the form of a short arc, the length of which could be used as a qualitative indication of the degree of the preferred orientation in the deposit. A typical example is shown in Fig. 36(b).

(U) The experimental arrangement for the determination of the distribution of the crystallographic axis of preferred orientation in the specimen is shown schematically in Fig. 37(a). The two-dimensional-distribution of the crystallographic axis of preferred orientation within the plane CABD was obtained by following the intensity of the diffracted X-ray beam as the specimen was tilted slowly through an angle θ about the line FG. The specimen was rotated about its own axis during the exposure to X-ray to insure that the number of crystal grains examined was large enough to make the results meaningful. Means were also provided to move the sample axially so that the above described distribution of the crystallographic axis of preferred

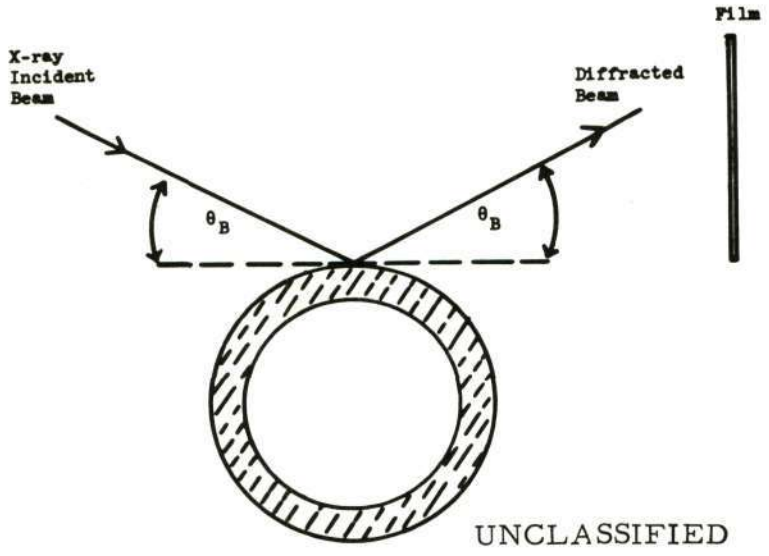

Fig. 36(a). (U) Schematic arrangement for determining the presence of preferred crystal orientation in cylindrical samples

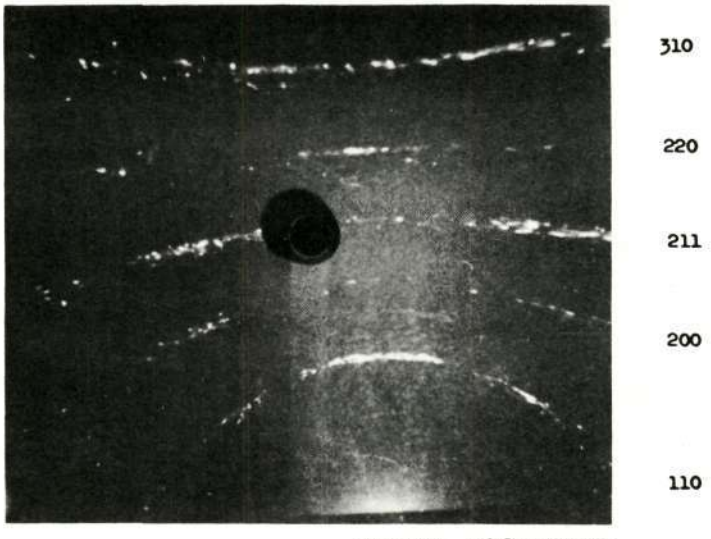

Fig. 36(b). (U) Example illustrating intensity distribution in X-ray diffraction patterns obtained from (110) oriented cylindrical chloride tungsten emitter

orientation could be determined as a function of axial position as a check of the structural homogeneity of the whole emitter surface. The device built for this purpose is shown in Fig. 37(b). The X-ray results were expressed in the form of a plot showing the cumulative fraction of the orientation axes scanned by the X-ray beam as a function of the angle of deviation θ from the normal to the surface of the specimen. A specimen having a high degree of preferred orientation should yield a plot in which a large portion of the axes of preferred orientation is located within a small value of θ.

2.3.1.4. Vacuum Work Function. (U) Figure 38(a) is a schematic of the emission cell for determining the vacuum work function. The special feature of this cell is that the specimen could be moved axially in a high vacuum by means of a screw-drive, linear-ball-bushing, bellows mechanism. In doing so, the emitter work function could be measured at various axial positions for the evaluation of the uniformity of the emission characteristics over the entire specimen surface. The specimen was about three inches long, with the measurement made over an effective emitting length of 2 inches. The collector and the guard rings were made of copper, and separated by Al_2O_3 ring spacers. The gap between the collector and the guard ring was 15 mils. The length of the collector was 5/16 inch, and the spacing between the specimen surface and the collector-guard ring assembly was 20 mils at a specimen temperature of 2073°K. The specimen was heated by electron bombardment and the temperature of the emitting surface was measured by sighting a micro-optical pyrometer through slots cut into the Al_2O_3 spacers. Emittance

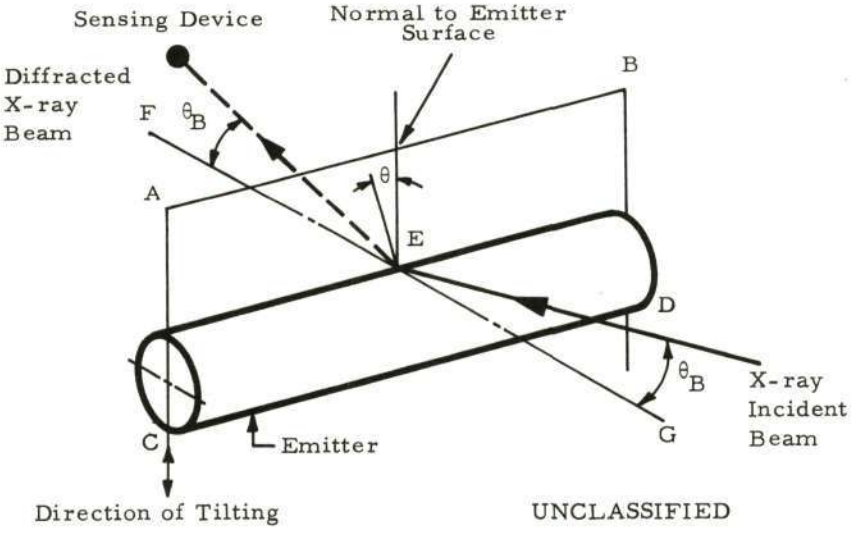

Fig. 37(a). (U) Schematic illustration of arrangement for obtaining distribution of lattice direction of preferred orientation in the plane CABD which is perpendicular to the plane defined by the incident X-ray beam and the sensing device. During X-ray exposure, the emitter is rotated about its axis and tilted about the line FG which is tangential to the cylindrical surface at the point E and perpendicular to the direction of the cylindrical axis of the emitter

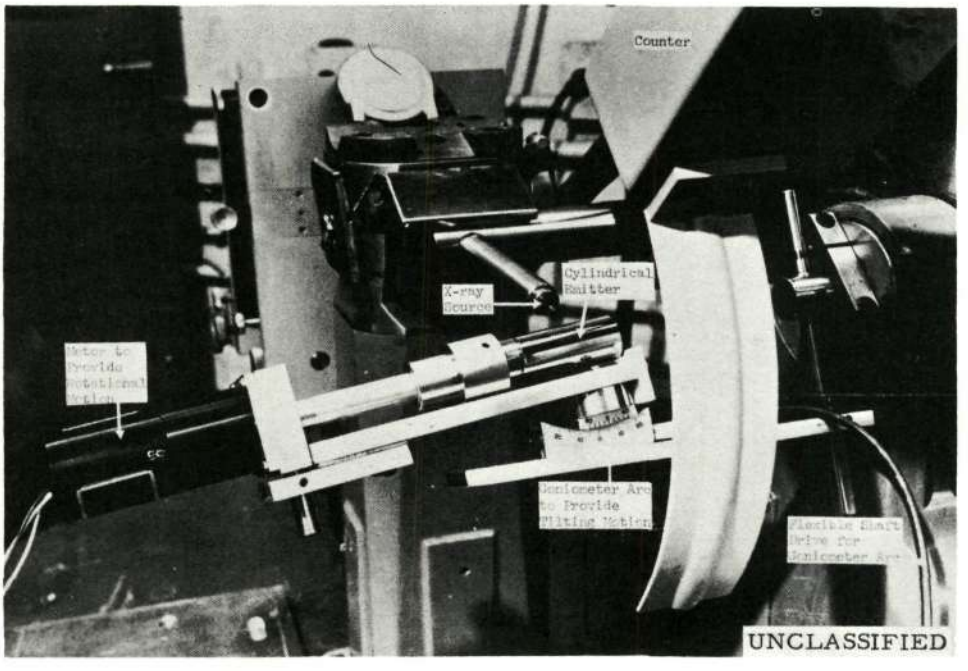

Fig. 37(b). (U) Experimental arrangement for determining the angular distribution of the axis of preferred crystal orientation in plane CABD of Fig. 37(a)

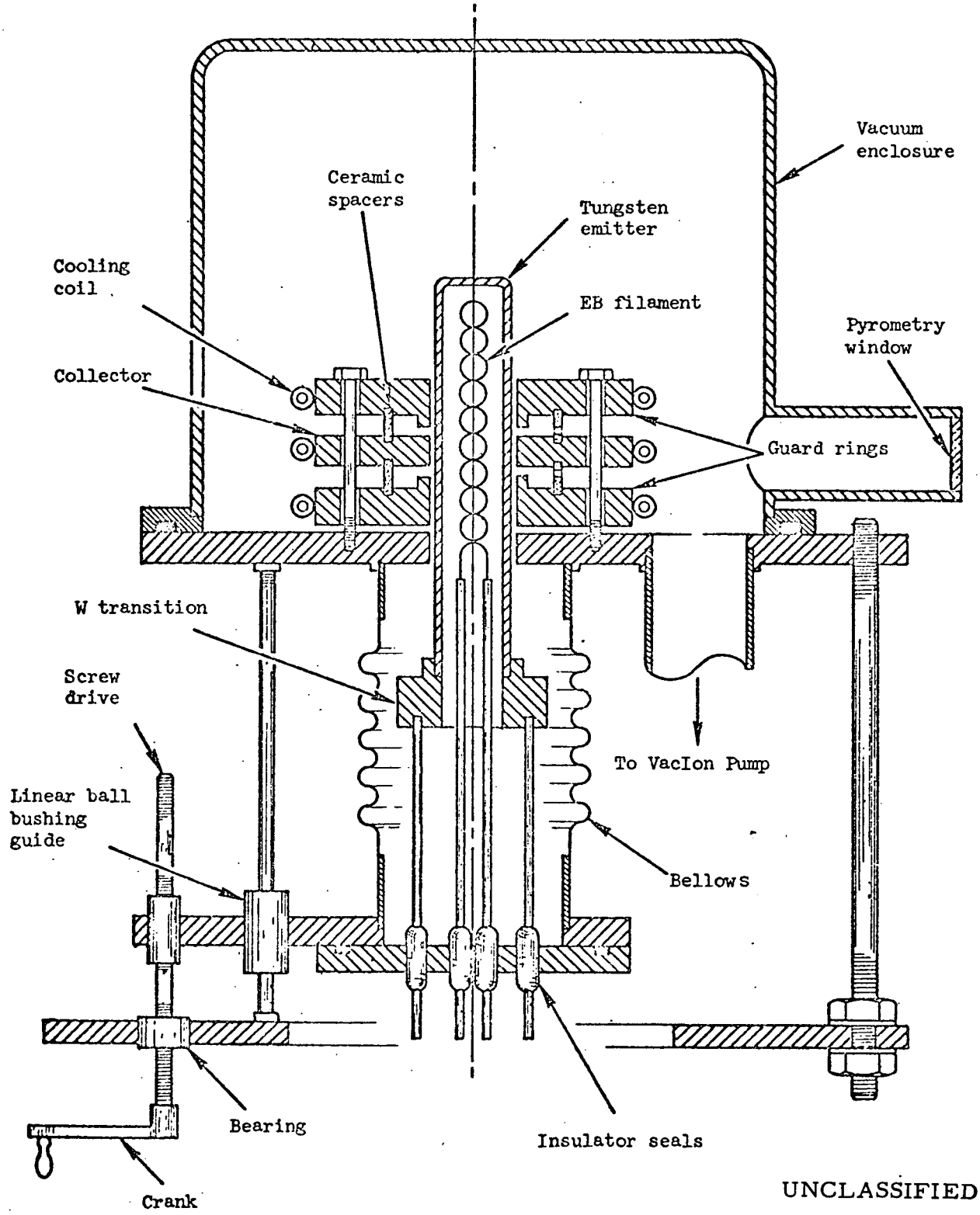

Fig. 38(a). (U) Schematic arrangements of vacuum emitter cell for measuring the axial distribution of vacuum work function of cylindrical emitter

corrections were made by using data obtained on the relationship between surface temperature and blackbody hohlraum temperature with a calibration sample over the temperature range of interest. The system was enclosed in a stainless steel container and the vacuum was maintained with an ion pump in the 10^{-8} torr range during measurements. Figure 38(b) shows the assembled vacuum emission cell. From the current-voltage relationship obtained when a d. c. potential was applied between the sample and the collector-guard ring assembly, the emission current density was plotted versus the square root of the field. The emission current density at zero field, J_o (amp/cm^2), was used for the calculation of the effective vacuum work function ϕ by using the Richardson-Dushman equation

$$J_o = A T^2 \exp\left(\frac{-\phi}{kT}\right)$$

where A = 120 amp/cm^2 $^oK^2$, T = temperature of the emitting surface in ^oK, and k = Boltzmann constant. To insure that a steady value of ϕ was obtained, the measurement was usually continued for a period of at least 250 hours.

2.3.2. Evaluation Results

2.3.2.1. Trial Runs. (U) A total of eleven specimens was prepared under the conditions shown in Table 8. Seven of these specimens contained more than 10 mils of chloride tungsten layer and were subject to chemical, metallographic and X-ray evaluations.

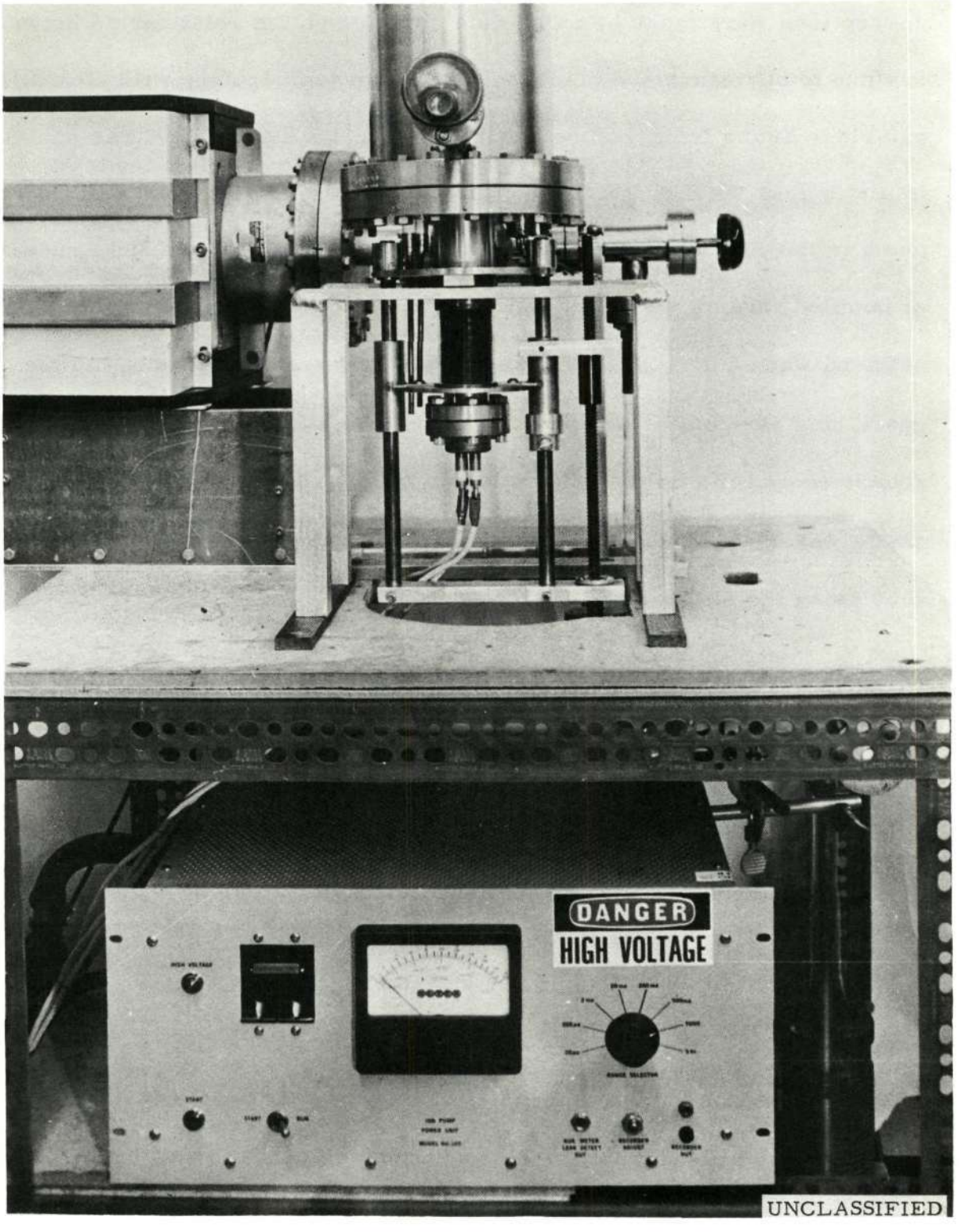

Fig. 38(b). (U) Photograph of the vacuum emission cell test stand

(U) Table 9 lists the dimensions of these specimens in the as-deposited conditions. Table 10 and Figs. 39 through 52 show the evaluation results. The impurity contents and the microstructures of these specimens were determined in the as-deposited conditions. The distributions of the (110) axes were measured after the specimens were ground to 0.625 inch O. D. (4 microinch surface finish) and electropolished.

(U) The results can be summarized as follows

1. All samples prepared by using a H_2/W ratio of 3.7:1.0, except R-5, exhibited $\{110\}$ orientation only for part of the 2 inch length (measured from the end* of each specimen). All specimens prepared by using a H_2/W ratio of 3.0:1.0 exhibited $\{110\}$ orientation for the whole 2 inch length. (Compare Figs. 39 through 45.)

2. For specimens prepared by using a H_2/W ratio of 3.0:1.0 and showing $\{110\}$ orientation for the whole 2 inch length, the variation of $\{110\}$ axes distribution with axial position was much less in R-9 and R-11 prepared at a chamber pressure of 6 torr. than that in R-3 prepared at a chamber pressure of 10 torr. (Compare Figs. 43 and 45 with Fig. 39.)

*The end of the specimen referred to in this report is the top closed end of the specimen, which faces the tungsten chip reservoir.

TABLE 9

(U) DIMENSION MEASUREMENTS OF AS-DEPOSITED TRIAL RUN SPECIMENS

(This table is Unclassified)

Run No.	Length (inch)	1/8 Inch From End	1/2 Inch From End	1 Inch From End	1-1/2 Inch From End	2 Inch From End
R-3	4 1/8	.729	.695	.685	.670	.662
R-4	3 3/4	.763	.690	.680	.663	.662
R-5	4 1/16	.707	.675	.668	.660	.656
R-8	4 1/16	.703	.693	.682	.666	.658
R-9	4 1/16	.666	.668	.663	.657	.652
R-10	5 9/16	.715	.684	.675	.668	.659
R-11	5 9/16	.693	.690	.680	.667	.656

TABLE 10

(U) DEPOSITION CONDITIONS AND EVALUATION RESULTS FOR SEVEN TRIAL RUN SPECIMENS
(This table is Unclassified)

Run No.	R-3	R-4	R-5	R-8	R-9	R-10	R-11
Run time (min.)	120	120	120	120	120	120	120
Cl_2 flow rate (c. c. /min.)	360	360	360	360	360	360	360
H_2 flow rate (c. c. /min.)	350	445	445	445	350	445	350
Chamber He flow rate (c. c. /min.)	325	650	325	975	650	650	650
Bleed He flow	Yes	Yes	Yes	No	No	No	No
Chamber pressure (mm)	10	10	10	6	6	6	6
Mandrel temperature (^{o}K)	1323	1323	1373	1323	1323	1373	1373
H_2/W mole ratio	3.0:1.0	3.7:1.0	3.7:1.0	3.7:1.0	3.0:1	3.7:1	3.0:1
Impurity contents (ppm)							
N	<1	<1	<1	<1	<1	<1	<1
O	0.2	36	16	5.8	2.1	4.5	1.6
C	10	8	7	8	7	8	8
F	<1	<1	1	<1	<1	<1	<1
Cl	42 ± 24	30 ± 14	14 ± 2	8 ± 1.5	16 ± 2	32 ± 7.5	15 ± 2
Metallic	Si <1.0; Fe <4.0; Mg <.02; Ni <0.3 Mn <0.1; Cu <0.3	Same as R-3	Same as R-3	Same as R-3 plus Al <0.3	Same as R-8	Same as R-8	Same as R-3
{110} Orientation							
1/8 inch from end	Yes	Yes	Yes	Yes	Yes	Yes	Yes
1 inch from end	Yes — Fig. 39	No — Fig. 40	Yes — Fig. 41	No — Fig. 42	Yes — Fig. 43	No — Fig. 44	Yes — Fig. 45
2 inches from end	Yes	No	Yes	No	Yes	No	Yes
Microstructures	Fig. 46	Fig. 47	Fig. 48	Fig. 49	Fig. 50	Fig. 51	Fig. 52

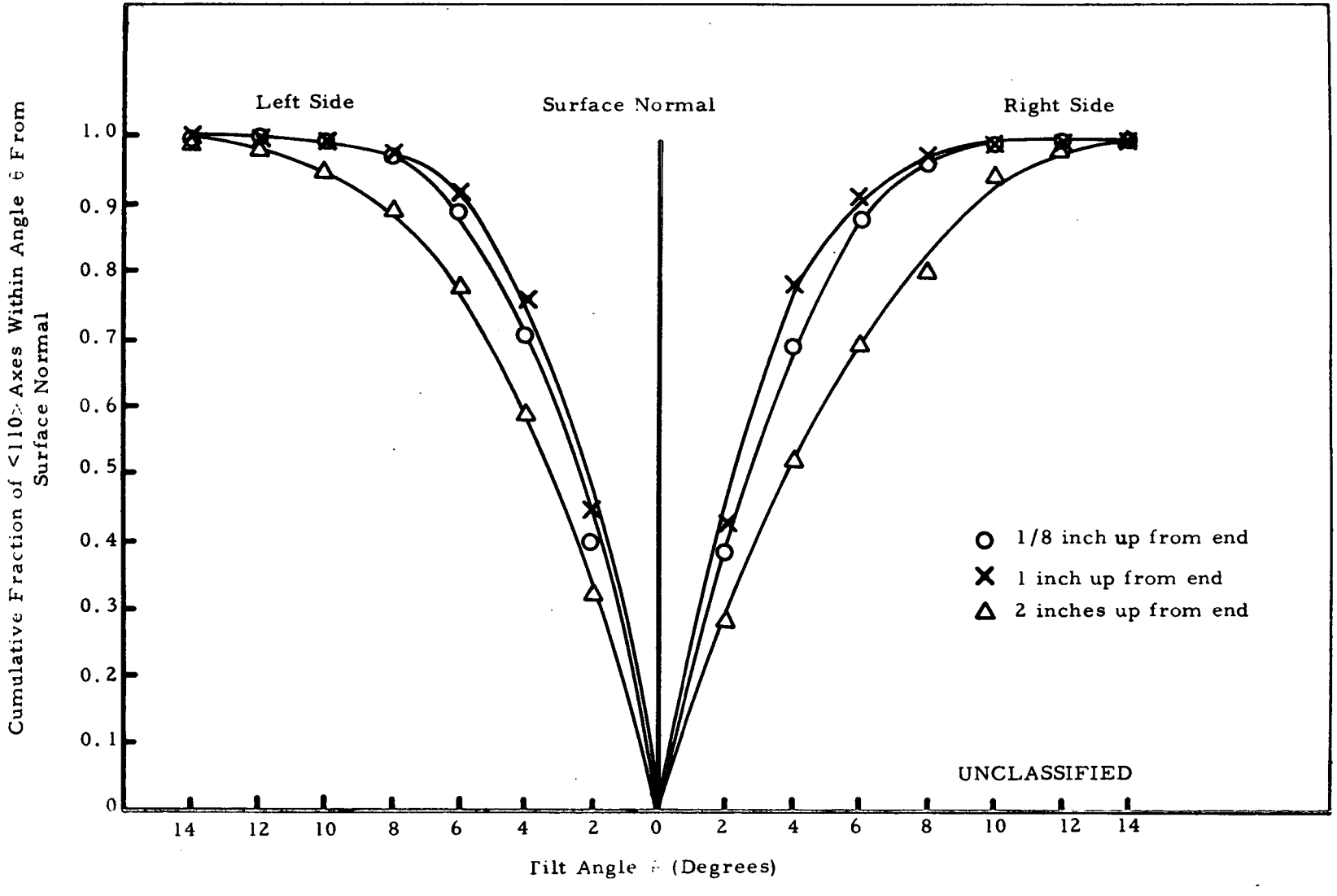

Fig. 39. (U) Distribution of <110> axes in trial run specimen R-3

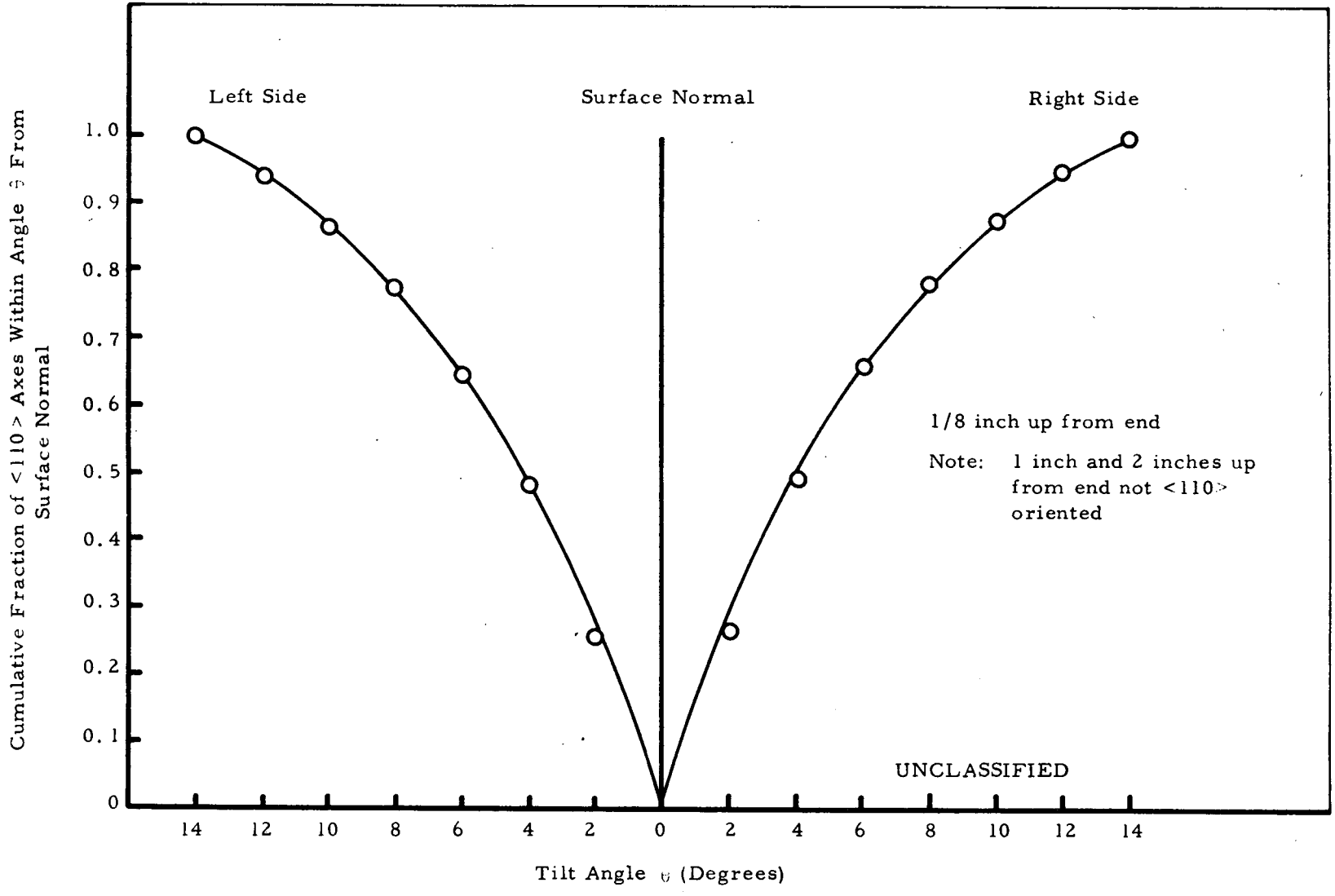

Fig. 40. (U) Distribution of <110> axes in trial run specimen R-4

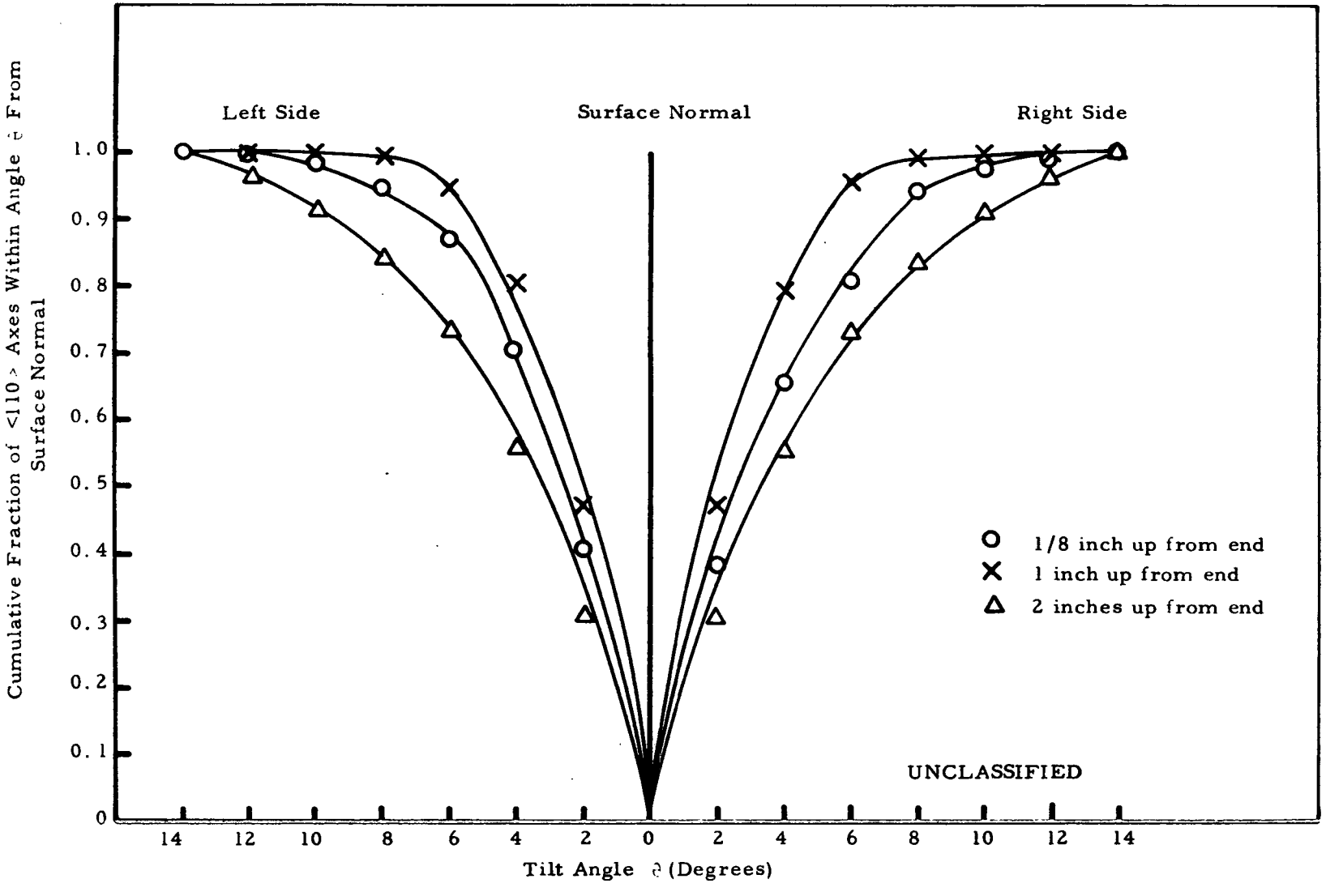

Fig. 41. (U) Distribution of <110> axes in trial run specimen R-5

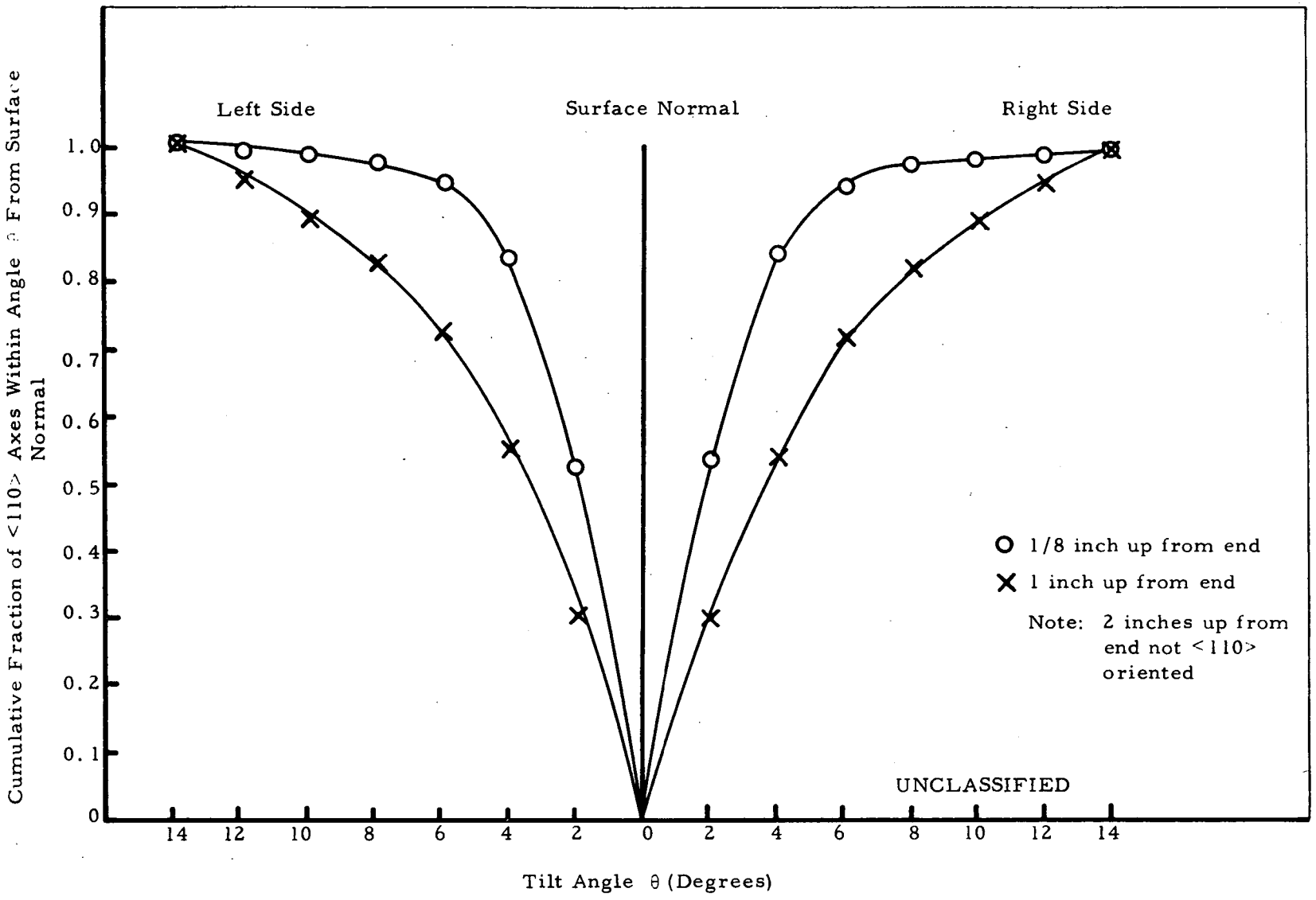

Fig. 42. (U) Distribution of <110> axes in trial run specimen R-8

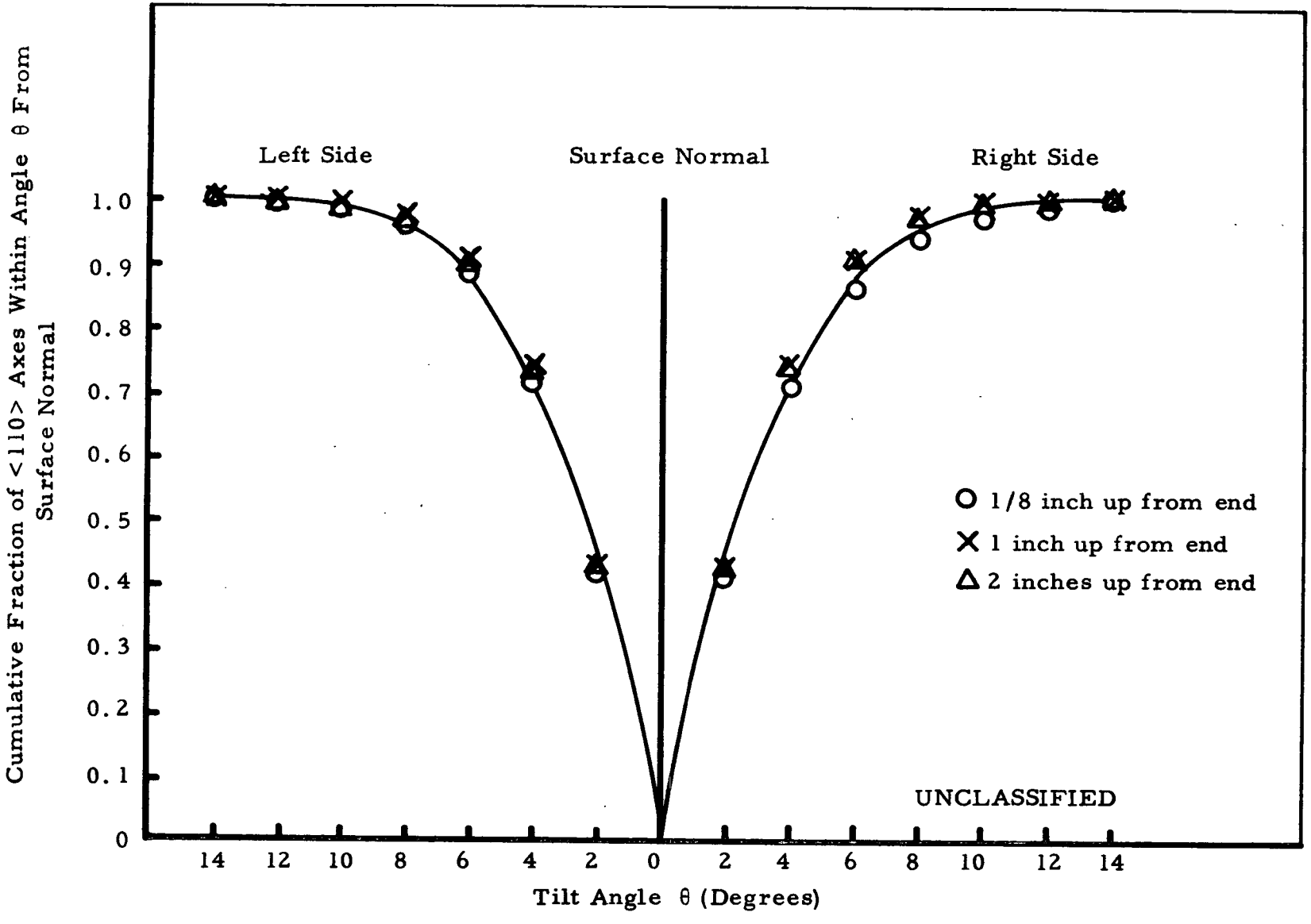

Fig. 43. (U) Distribution of <110> axes in trial run specimen R-9

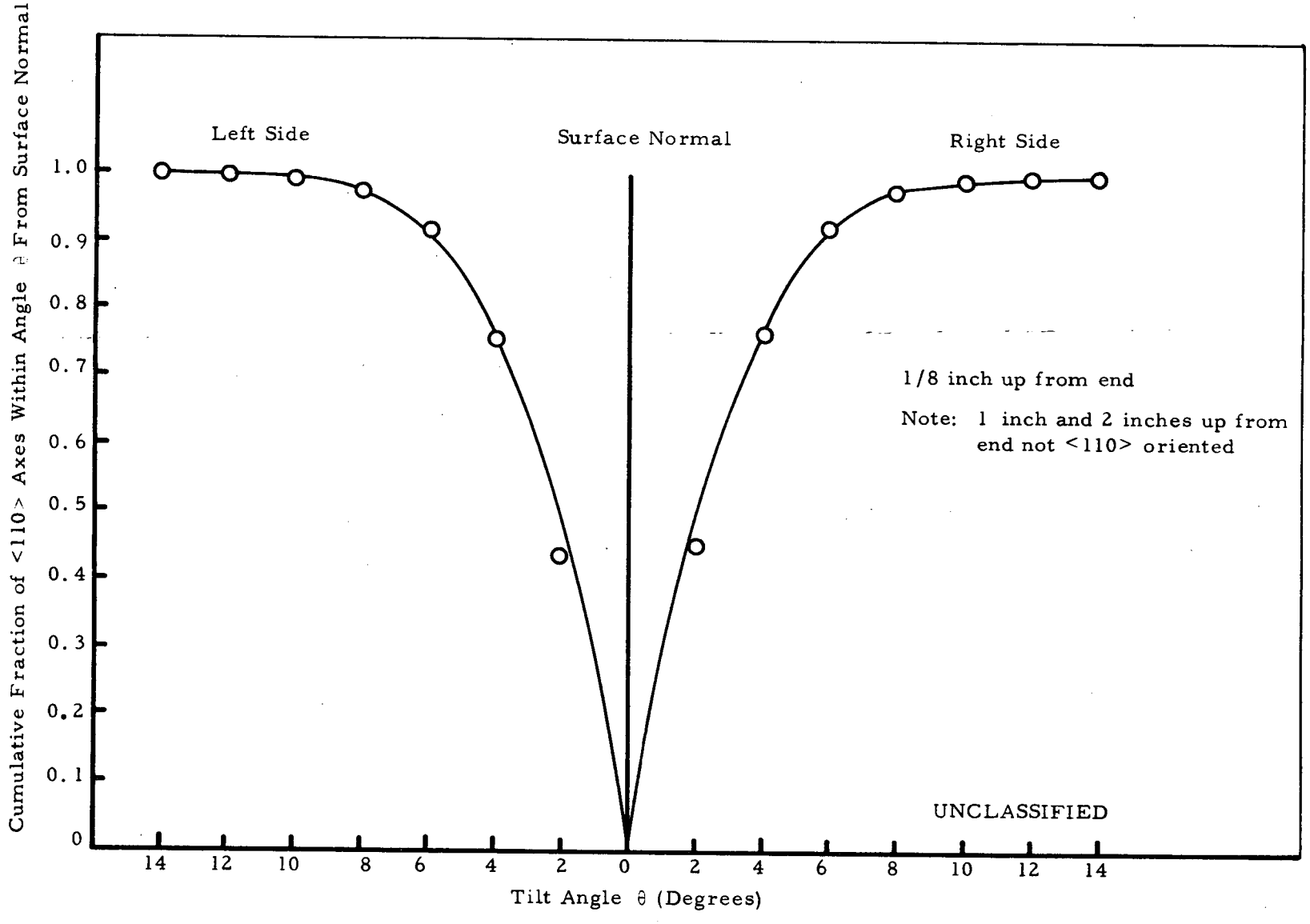

Fig. 44. (U) Distribution of <110> axes in trial run specimen R-10

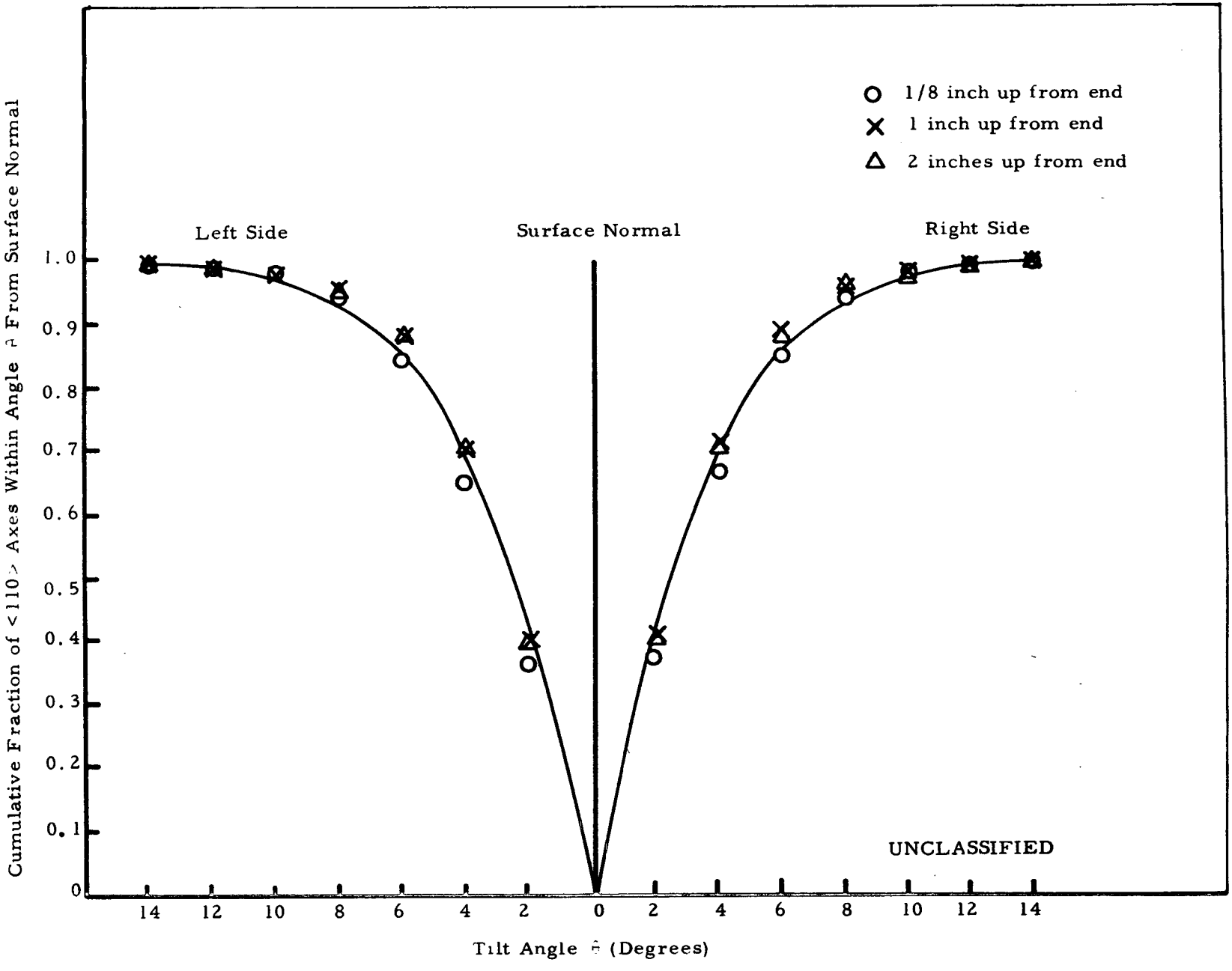

Fig. 45. (U) Distribution of <110> axes in trial run specimen R-11

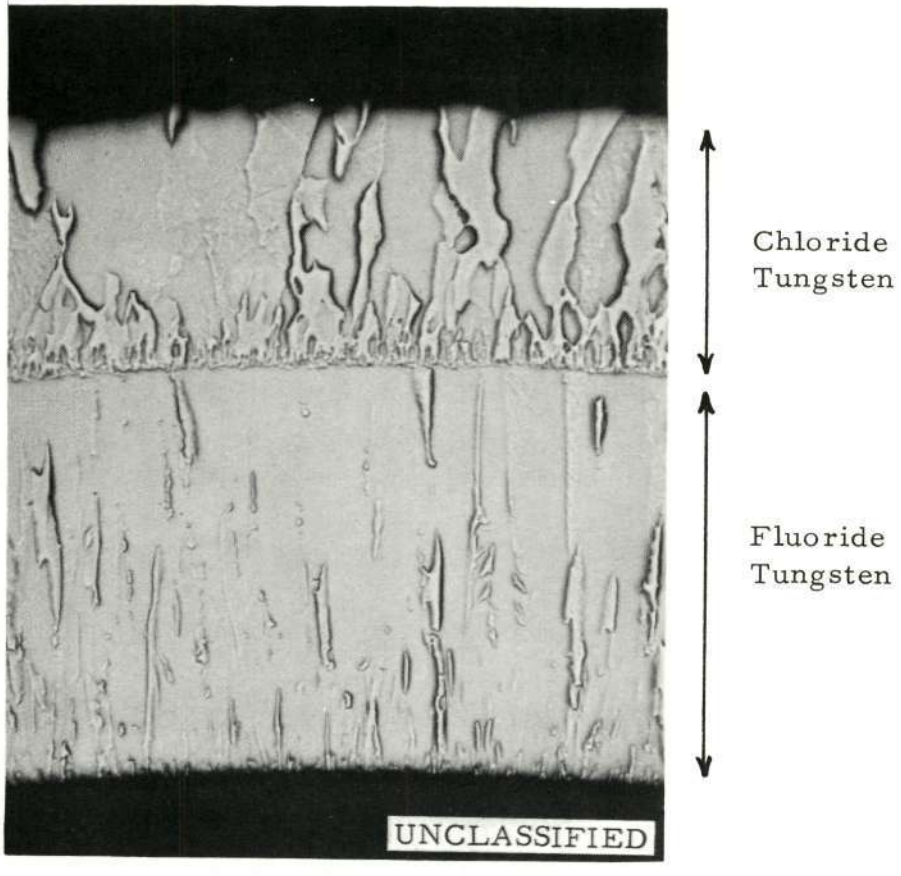

Fig. 46. (U) Cross section view of as-deposited trial run specimen R-3

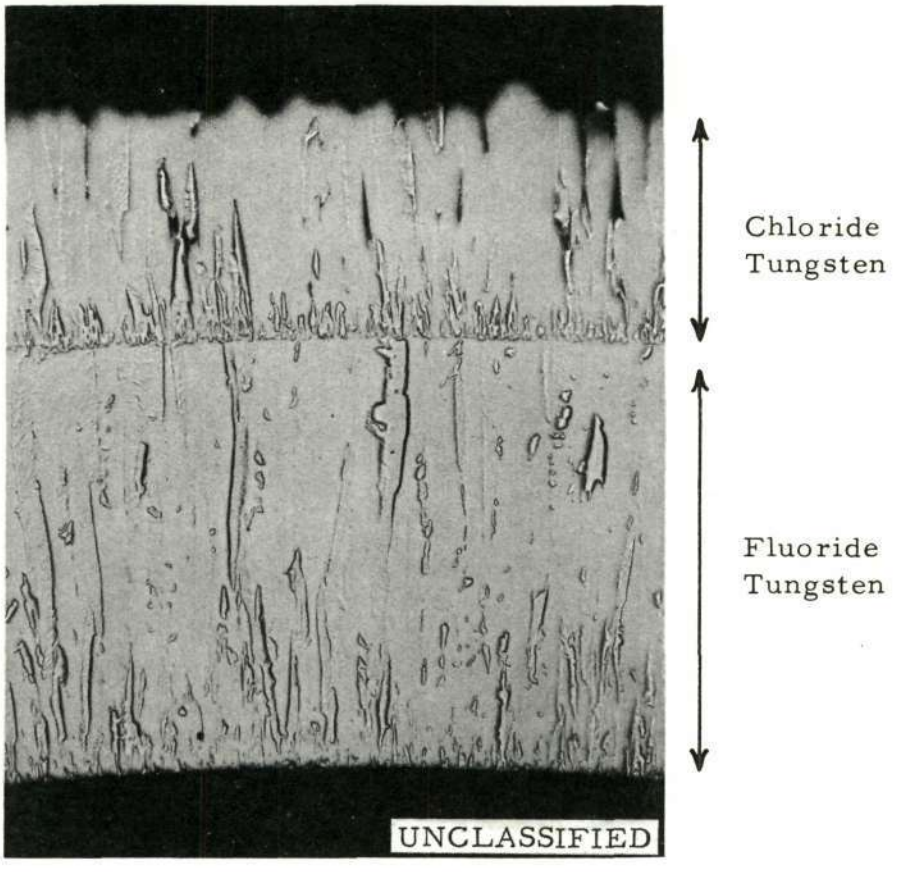

M 27635-1 75X

Fig. 47. (U) Cross section view of as-deposited trial run specimen R-4

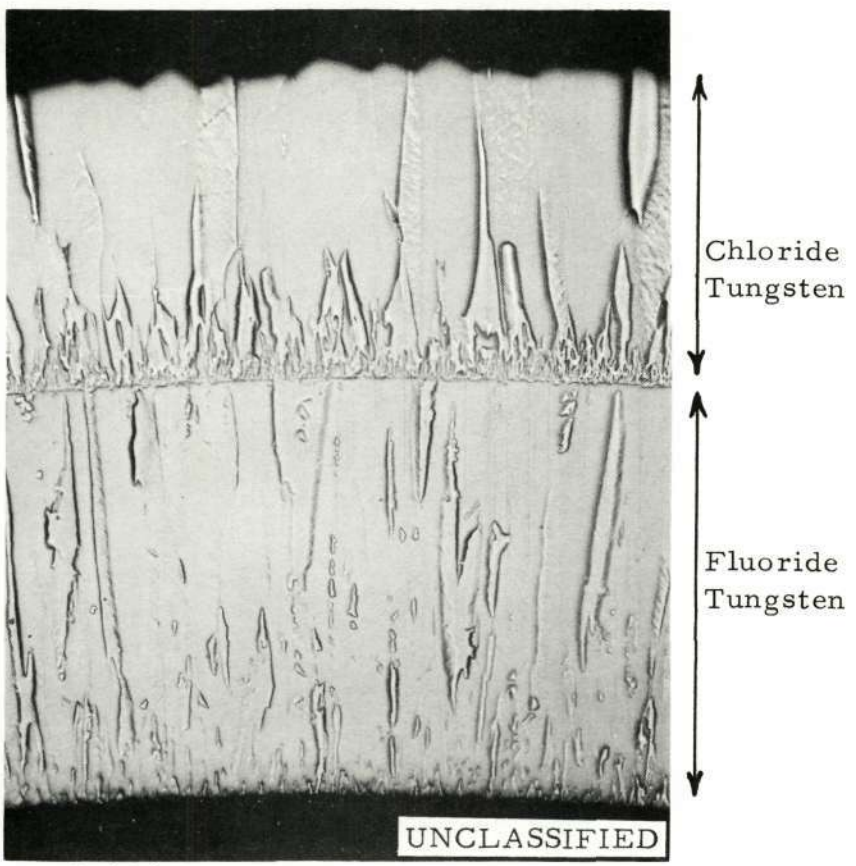

Fig. 48. (U) Cross section view of as-deposited trial run specimen R-5

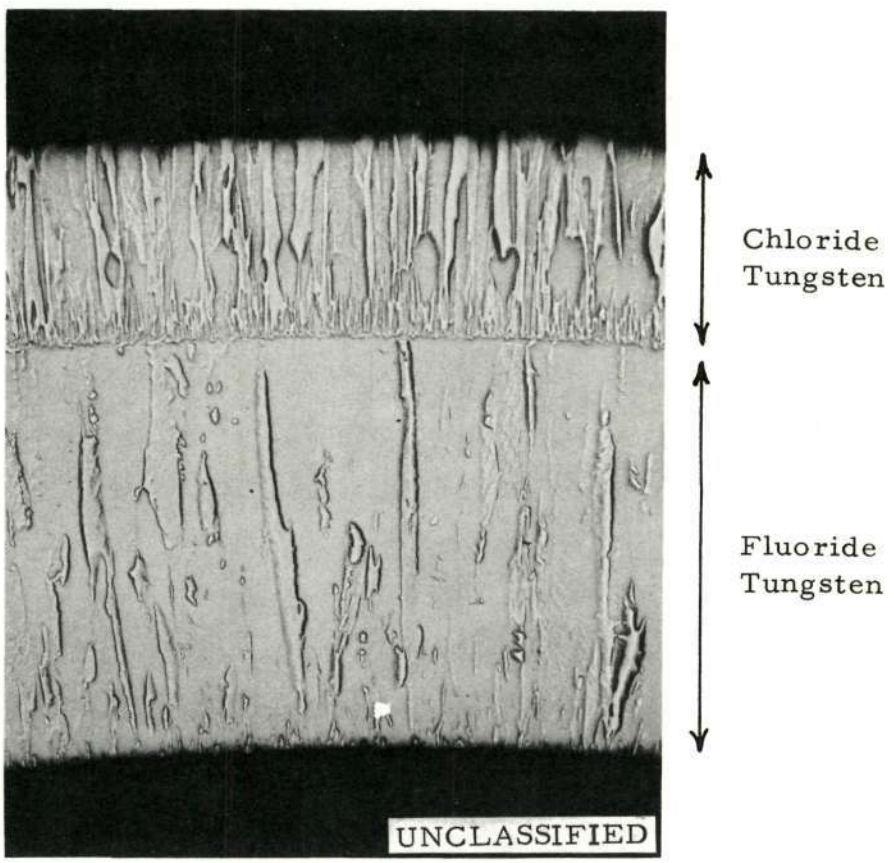

M 27637-1 75X

Fig. 49. (U) Cross section view of as-deposited trial run specimen R-8

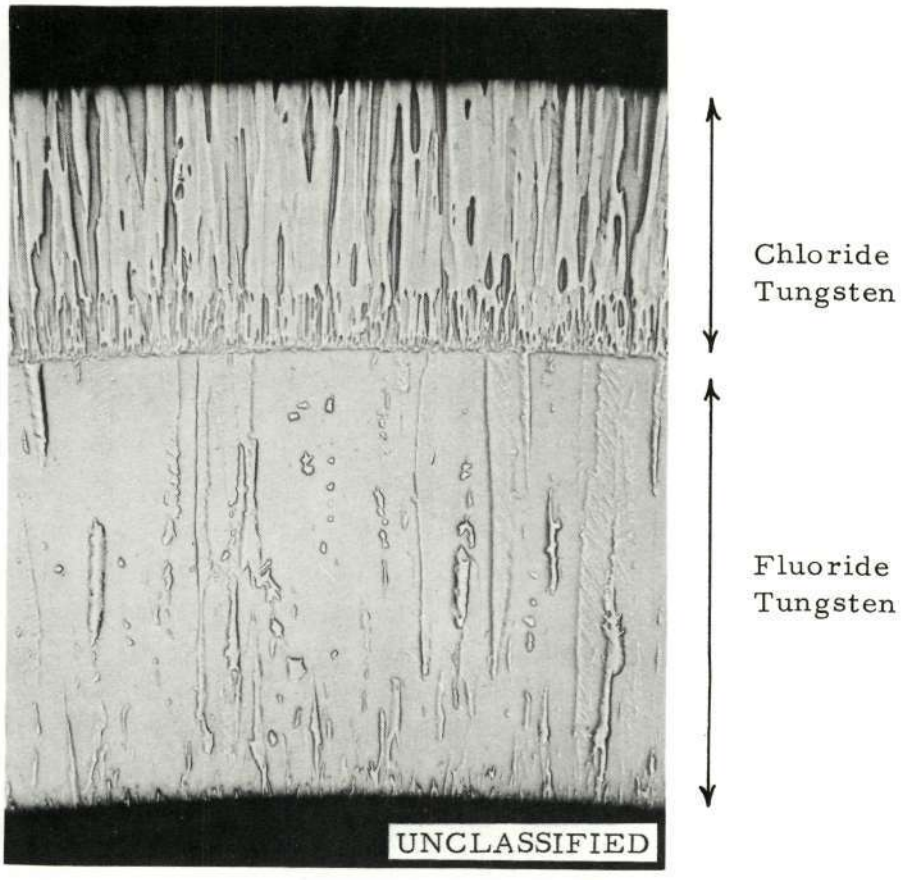

Fig. 50. (U) Cross section view of as-deposited trial run specimen R-9

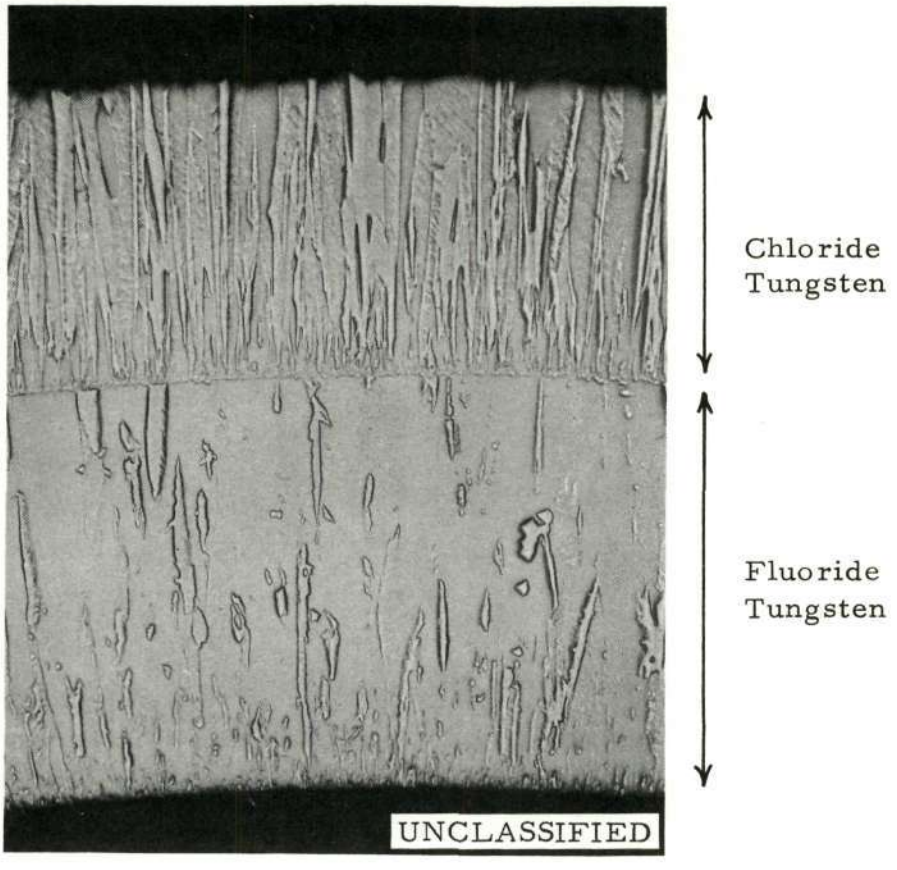

Fig. 51. (U) Cross section view of as-deposited trial run specimen R-10

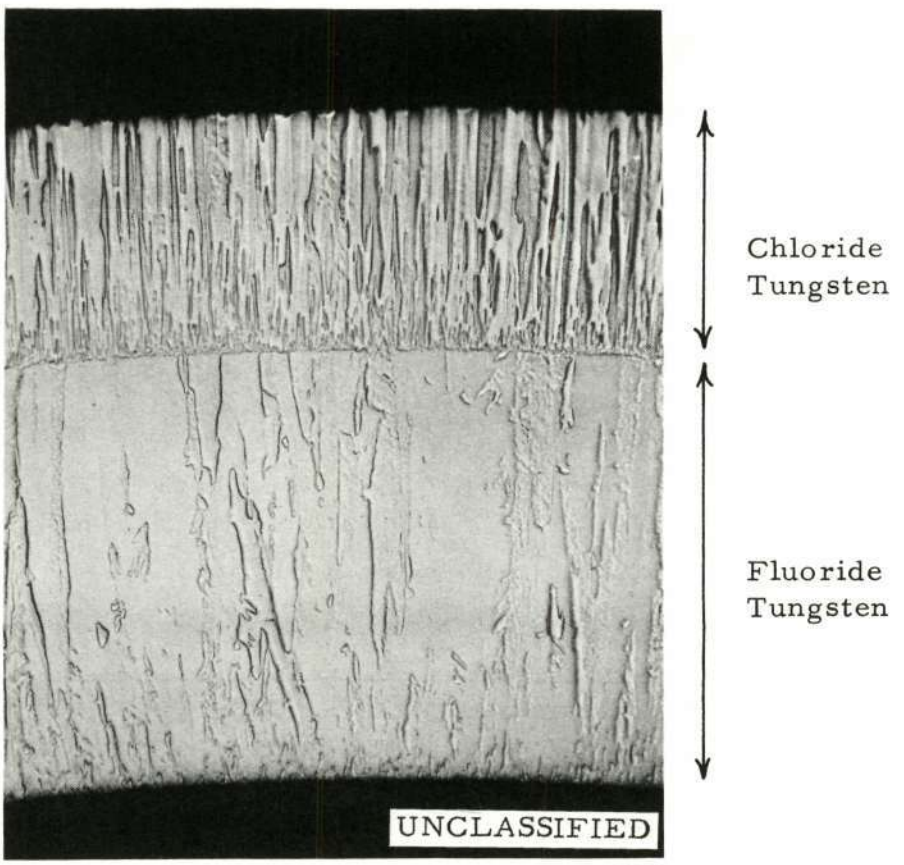

Fig. 52. (U) Cross section view of as-deposited trial run specimen R-11

3. R-9 which was prepared at a mandrel temperature of 1323°K was slightly better oriented than R-11 which was prepared at a mandrel temperature of 1373°K.

4. No correlation existed between the observed impurity contents and the degree of {110} orientation and its axial uniformity.

5. Chloride tungsten deposits prepared at a chamber pressure of 10 torr had larger grain sizes than those prepared at a chamber pressure of 6 torr. (Compare Figs. 46, 47, and 48 with Figs. 49, 50, 51, and 52.)

(U) Since R-9 appears to be the best oriented one among the seven trial run specimens evaluated, its deposition conditions were selected as the reference deposition conditions for more detail evaluations of deposition parameters.

2.3.2.2. Evaluation of Deposition Parameters

Effect of Gas Pressure in Deposition Chamber. (U) The trial run results indicate a lower chamber pressure (6 torr versus 10 torr) yielded a better oriented deposit. Speciman Set A_1 (R-12, R-13, R-14) and Specimen Set A_2 (R-15, R-16, R-17) were prepared in order to find out whether the degree of (110) orientation in the chloride tungsten deposit could be further improved by lowering the chamber pressure to 3 torr. The specimens in Set A_1 were deposited under the reference conditions, while the specimens

in Set A_2 were deposited under the same conditions as that for Set A_1 except that the chamber pressure was kept at 3 torr during the deposition.

(U) Table 11 lists the as-deposited dimensions of Set A_1 and Set A_2 specimens. R-12 and R-15 were used for the comparison of the impurity contents. R-13 and R-16 were used for the comparison of the degree of (110) orientation after grinding to 0.625 inch O.D. and electropolishing. R-14 and R-17 were used for the comparison of the microstructures. All specimens were studied by X-rays for their preferred crystal orientation. The evaluation results are shown in Table 12 and Figs. 53 through 56. The results can be summarized as follows.

1. The rate of deposition was slower at lower chamber pressure, presumably because the residence time of the gaseous reactant was less since a high pumping rate was used to maintain the low chamber pressure. The deposits were smoother and the deposition chamber was cleaner when the chamber pressure was at a lower value.

2. There was no significant difference in non-metallic impurity contents, although the metallic impurity contents were slightly higher in the specimen (R-15) prepared at lower chamber pressure.

3. There was no significant difference in the as-deposited microstructures (Fig. 55 versus Fig. 56).

TABLE 11

(U) DIMENSION MEASUREMENTS OF AS-DEPOSITED SET A_1 AND SET A_2 SPECIMENS

(This table is Unclassified)

Set	Run No.	Length (Inch)	Diameter (Inch)				
			1/8 Inch From End	1/2 Inch From End	1 Inch From End	1-1/2 Inch From End	2 Inches From End
A_1	R-12	5-9/16	.663	.667	.665	.657	.651
	R-13	5-5/8	.655	.662	.656	.652	.650
	R-14	5-5/8	.653	.655	.654	.648	.647
A_2	R-15	5-9/16	.640	.643	.643	.639	.639
	R-16	5-9/16	.624	.633	.638	.637	.635
	R-17	5-9/16	.650	.660	.662	.662	.657

TABLE 12

DEPOSITION CONDITIONS AND EVALUATION RESULTS FOR SET A_1 AND SET A_2 SPECIMENS (U)

(This table is Unclassified)

Set No.	A_1			A_2		
Run No.	R-12	R-13	R-14	R-15	R-16	R-17
Deposition Time (Min.)	120	120	120	120	120	120
Deposition Conditions	Reference Conditions			Reference Conditions Except Chamber Pressure = 3 Torr Instead of 6 Torr		
Unique Parameter Evaluated	Impurity Contents	Distribution of Preferred Orientation Fig. 53	Micro-structures Fig. 55	Impurity Contents	Distribution of Preferred Orientation Fig. 54	Micro-structures Fig. 56
Impurity Contents (ppm)						
N	<1			<1		
O	3.6			6.9		
C	10			9		
F	<1			<1		
Cl	10.5 ± 1.5			8.2 ± 1		
Metallic	Si <1.0; Fe<4.0 Mg<0.02 Mn<0.1 Ni<0.3 Cu<0.3 Al<0.3			Si 2.0 Fe 7.8 Mg 1.0 Mn<0.1 Mn 9.0 Cu 4.0 Al<0.3		
(110) Orientation						
1/8 inch from end	Yes	Yes	Yes	Yes	Yes	Yes
1 inch form end	Yes	Yes	Yes	Yes	Yes	Yes
2 inch from end	Yes	Yes	Yes	Yes	Yes	Yes

UNCLASSIFIED

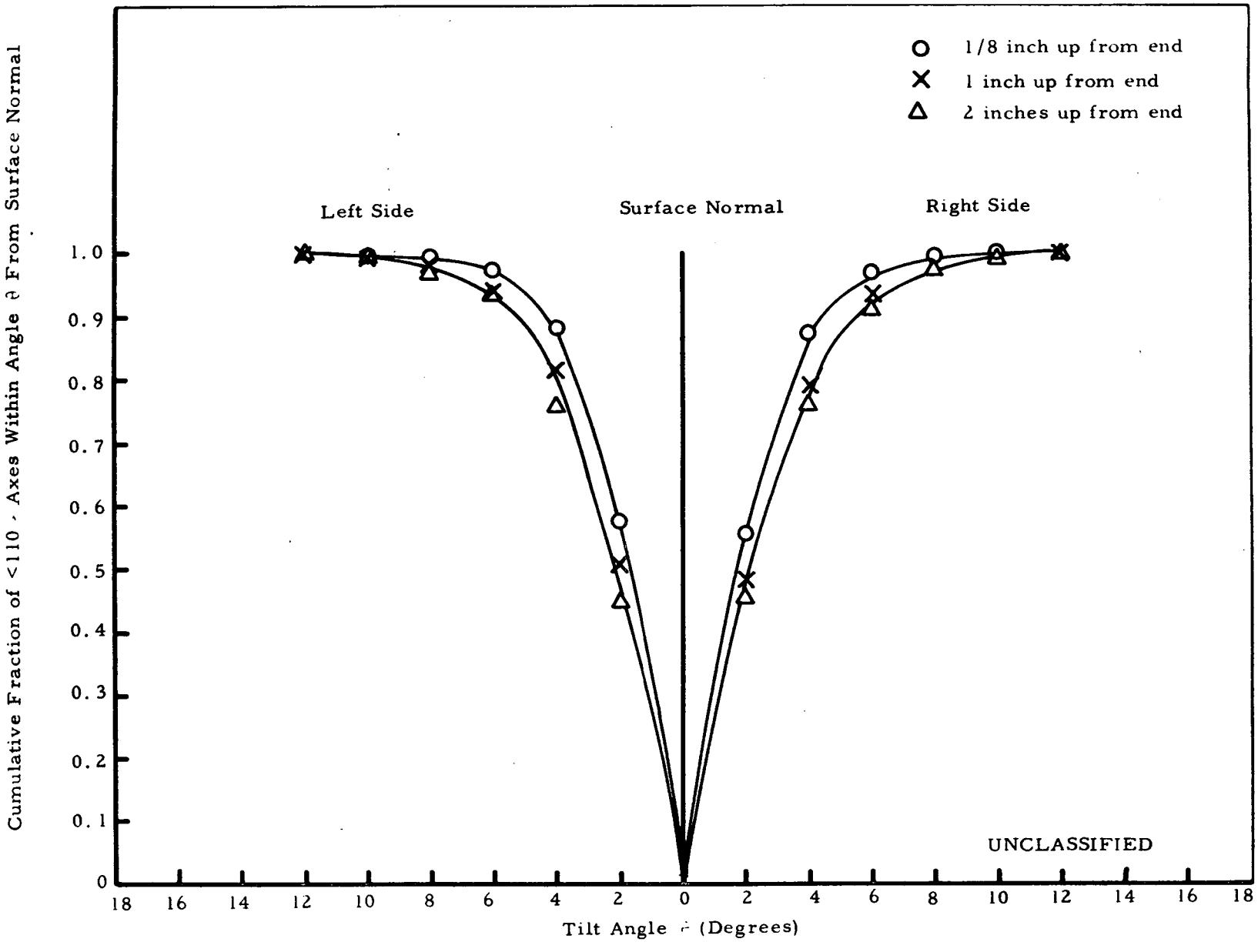

Fig. 53. (U) Distribution of <110> axes in R-13 of specimen set A_1

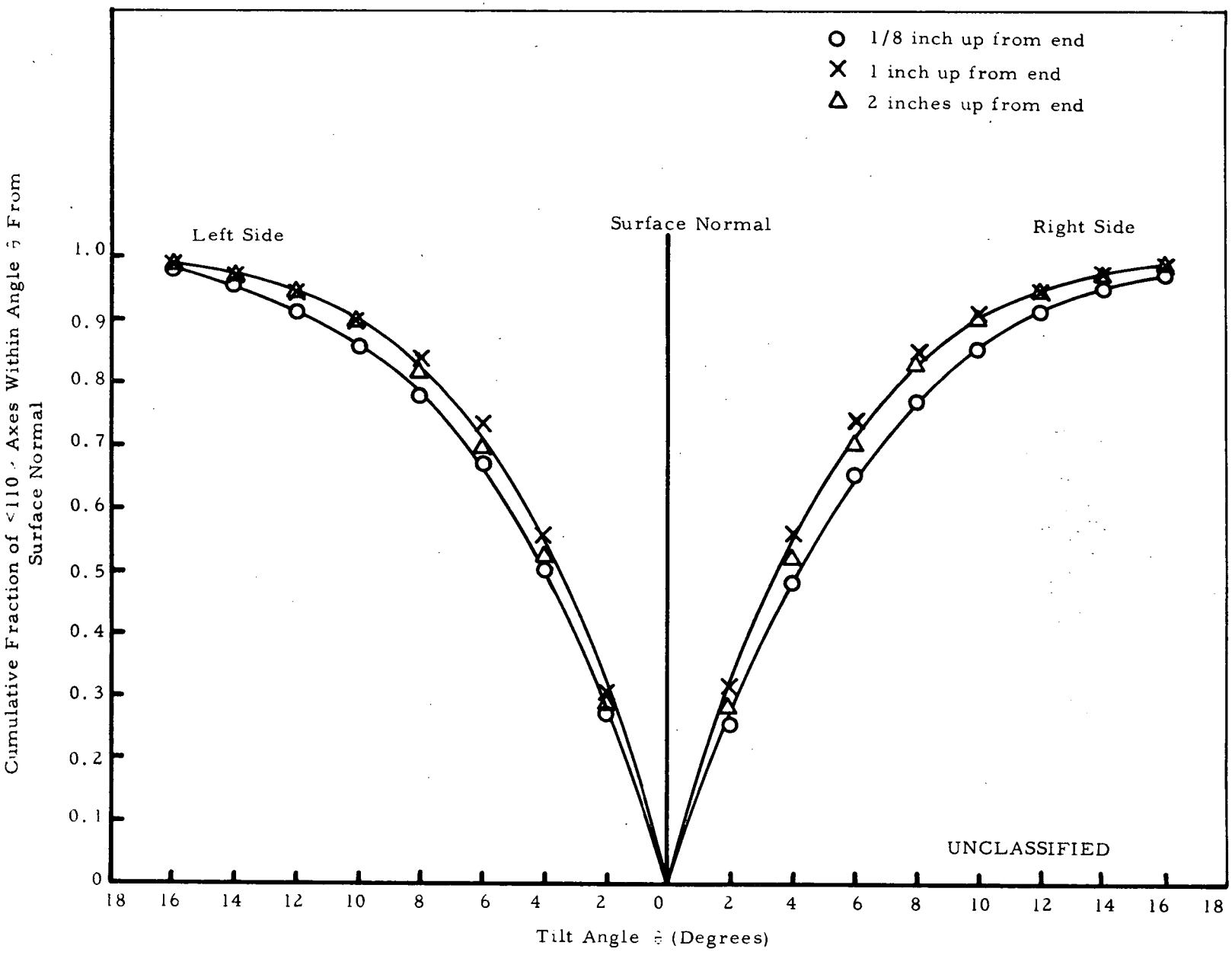

Fig. 54. (U) Distribution of <110> axes in R-16 of specimen set A_2

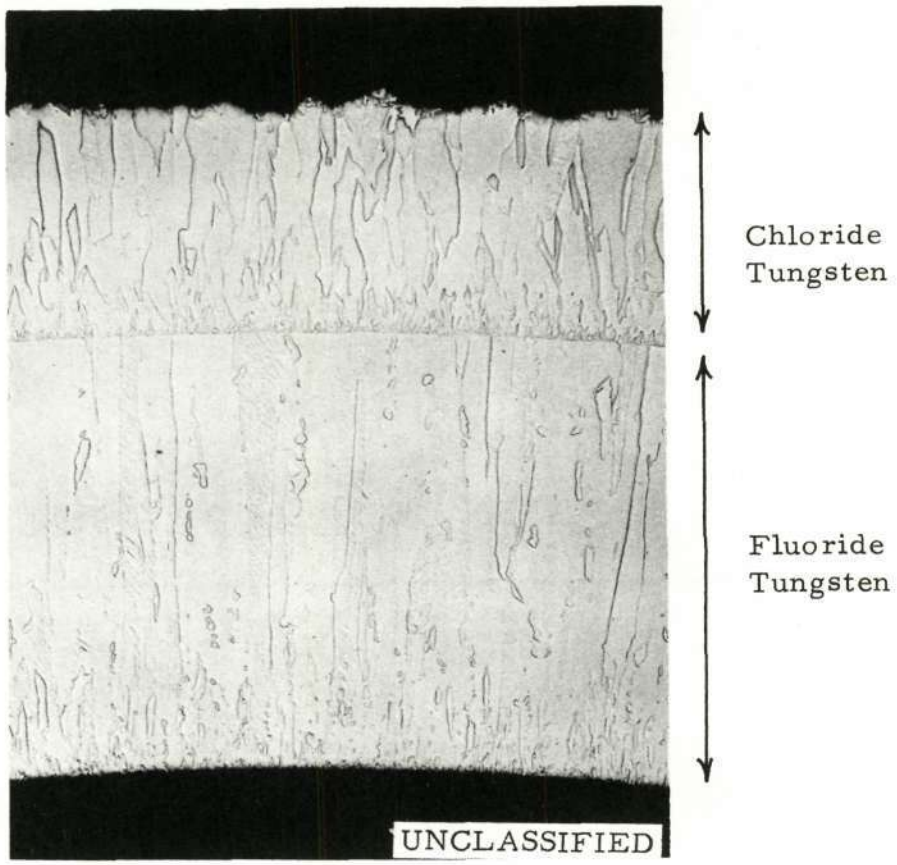

M 28353-1 75X

Fig. 55. (U) Cross section view of as-deposited specimen R-15 of Set A_1

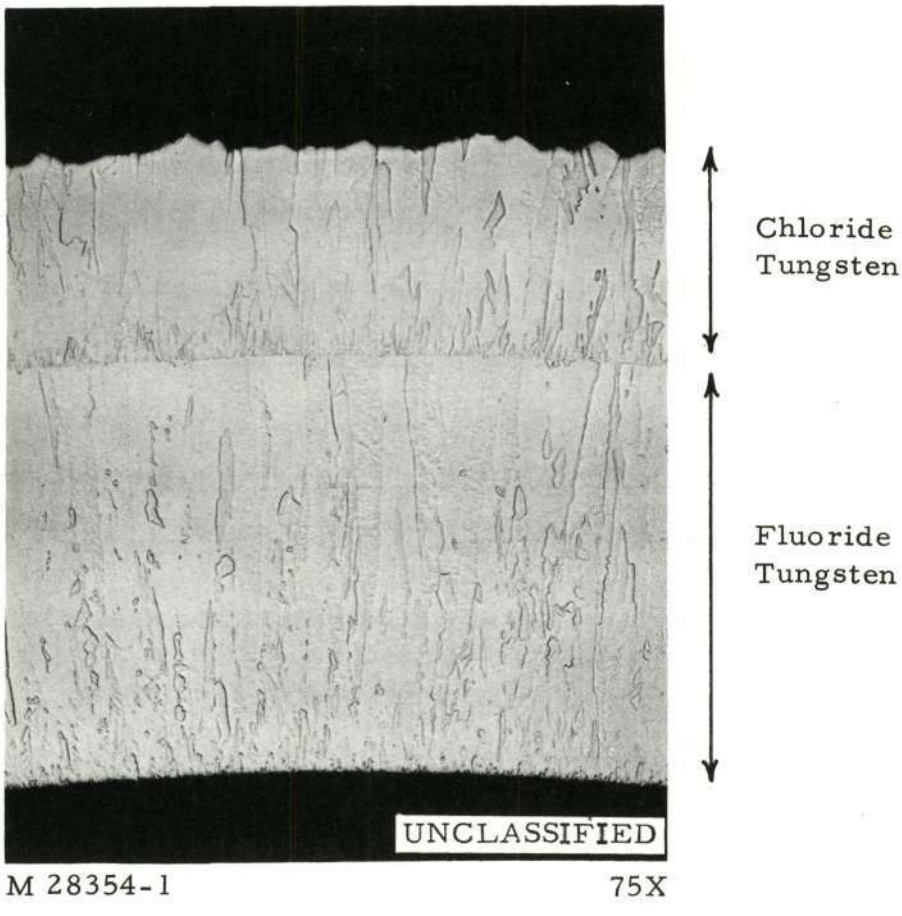

Fig. 56. (U) Cross section view of as-deposited specimen R-17 of Set A_2

4. The deposit prepared at 6 torr chamber pressure was better oriented than the deposit prepared at 3 torr chamber pressure (Fig. 53 versus Fig. 54).

(U) On the basis of these observations, it is concluded that a chamber pressure of 6 torr is preferred over a chamber pressure of 3 torr. The trial run results showed that a chamber pressure of 6 torr also yielded a better oriented deposit than a chamber pressure of 10 torr. It seems that a chamber pressure in the vicinity of 6 torr represents the optimum choice.

Effect of H_2/W Ratio in the Gaseous Reactant. (U) The trial run results indicated that a H_2/W ratio of 3.0 yielded a better oriented deposit than a H_2/W ratio of 3.7. The study was extended to a wider range of H_2/W ratios in this part of the work. Three sets of specimens, B_1 (R-18, R-19, R-20), B_2 (R-21, R-22, R-23) and B_3 (R-24, R-25, R-26) were prepared, with H_2/W ratios of 2.3, 3.3, and 6.4 respectively.

(U) Table 13 lists the as-deposited dimensions of the specimens of these three sets. R-18, R-21, and R-24 were used for the comparison of the impurity contents. R-19, R-22 and R-25 were used for the comparison of the microstructures. R-20, R-23, and R-26 were used for the comparison of the degree of (110) orientation after grinding to 0.625 inch O.D. and electropolishing. All specimens were studied by X-rays for their preferred crystal orientation. The evaluation results are shown in Table 14 and Figs. 57 through 62. The results can be summarized as follows.

TABLE 13

(U) DIMENSION MEASUREMENTS OF AS-DEPOSITED SET B_1, SET B_2, AND SET B_3 SPECIMENS

(This table is Unclassified)

Set	Run No.	Length (Inch)	Diameter (Inch)				
			1/8 Inch From End	1/2 Inch From End	1 Inch From End	1-1/2 Inch From End	2 Inches From End
B_1	R-18	5-1/2	.612	.616	.621	.622	.622
	R-19	5-1/2	.615	.619	.622	.623	.622
	R-20	5-1/2	.627	.629	.631	.629	.628
B_2	R-21	5-1/2	.660	.661	.659	.654	.649
	R-22	5-1/2	.654	.656	.654	.649	.645
	R-23	5-1/2	.658	.660	.657	.651	.645
B_3	R-24	5-1/2	.693	.680	.670	.662	.657
	R-25	5-1/2	.683	.670	.657	.650	.644
	R-26	5-1/2	.657	.665	.652	.645	.642

TABLE 14

(U) DEPOSITION CONDITIONS AND EVALUATION RESULTS FOR SETS B_1, B_2, AND B_3 SPECIMENS

(This table is Unclassified)

Set No.	B_1			B_2			B_3		
Run No.	R-18	R-19	R-20	R-21	R-22	R-23	R-24	R-25	R-26
Deposition Time (Min.)	120	120	120	120	120	120	120	120	120
Deposition Conditions	Reference Conditions Except H_2 Flow Rate = 270 c.c./min. H_2/W = 2.3			Reference Conditions Except H_2 Flow Rate = 380 c.c./min. H_2/W = 3.3			Reference Conditions Except H_2 Flow Rate = 750 c.c./min. H_2/W = 6.4		
Unique Parameter Evaluated	Impurity Contents	Microstructures Fig. 57	Distribution of Preferred Orientation Fig. 60	Impurity Contents	Microstructures Fig. 58	Distribution of Preferred Orientation Fig. 61	Impurity Contents	Microstructures Fig. 59	Distribution of Preferred Orientation Fig. 62
Impurity Contents (ppm)									
N	1			<1			<1		
O	2.1			0.5			4.9		
C	15			15			14		
F	4			6			7		
Cl	8.0 ± 1			11.3 ± 1.5			14 ± 2.1		
Metallic	Si <1.0 Fe 10.4 Mg 0.1 Ni 0.7 Cu <0.3 Ag 0.3			Si 4.0 Fe 3.8 Mg 0.1 Ni 0.7 Cu <0.3 Ag 0.4 Mn <0.2			Si 3.9 Fe 14.2 Mg 0.2 Ni 1.4 Cu <0.3 Ag 0.4 Al <0.5		
(110) Orientation									
1/8 inch from end	Yes	Yes	Yes	Yes	Yes	Yes	Yes	Yes	Yes
1 inch from end	Yes	Yes	Yes	Yes	Yes	Yes	Yes	Yes	Yes
2 inches from end	Yes	Yes	Yes	Yes	Yes	Yes	Yes	Yes	Yes

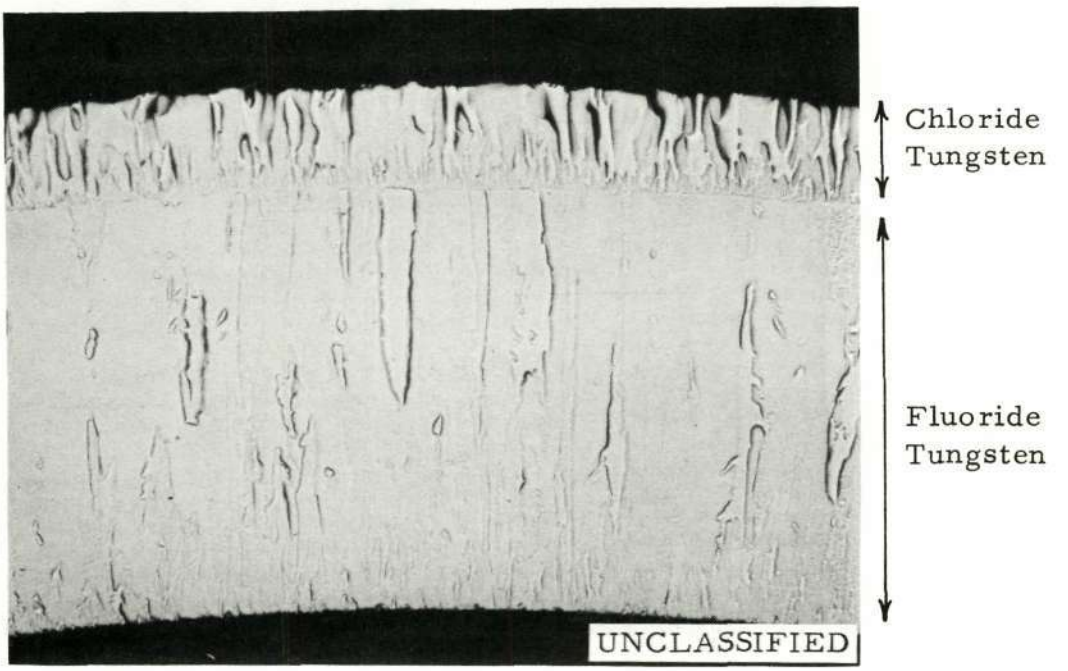

M 28642-1 75X

Fig. 57. (U) Cross section view of as-deposited specimen R-19 of Set B_1

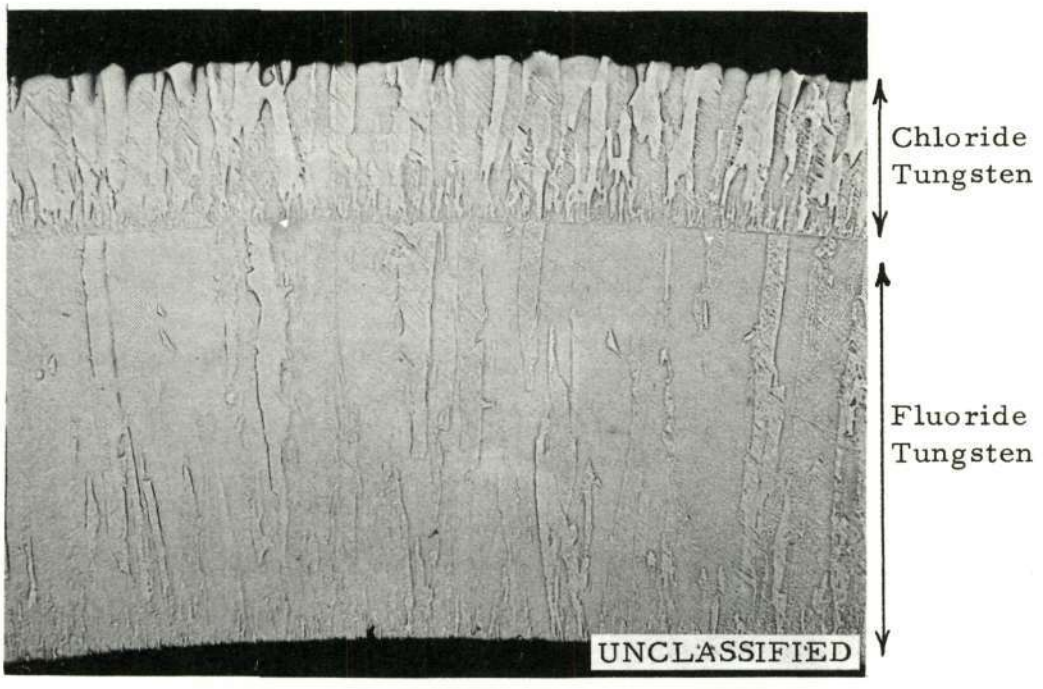

M 28643-1 75X

Fig. 58. (U) Cross section view of as-deposited specimen R-22 of Set B_2

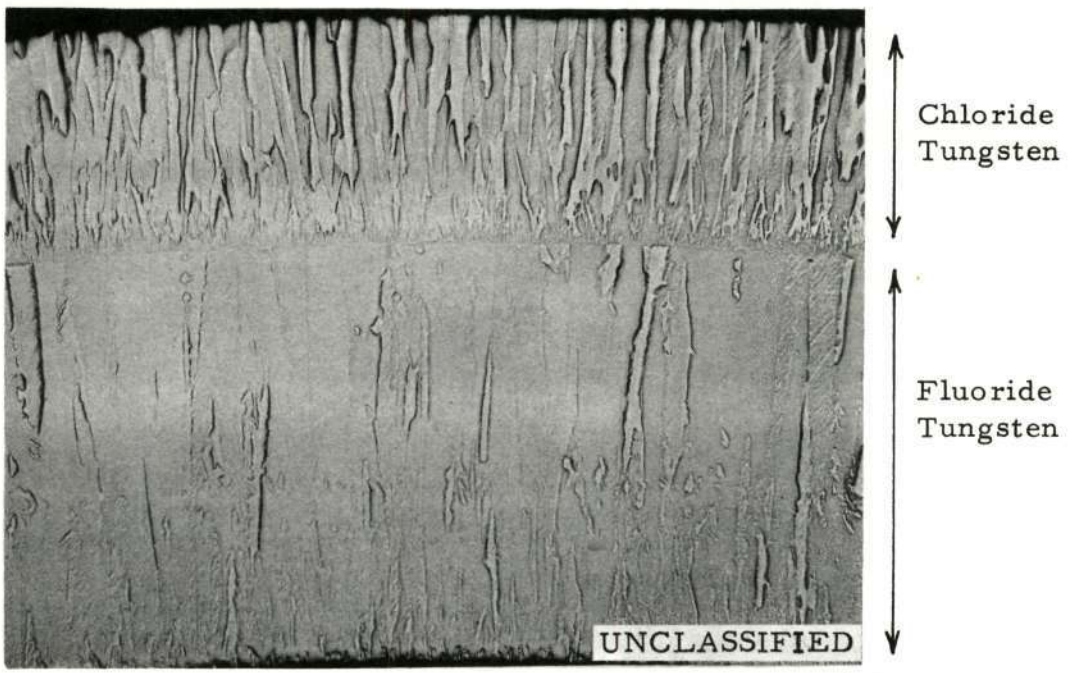

M 28644-1 75X

Fig. 59. (U) Cross section view of as-deposited specimen R-25 of Set B_3

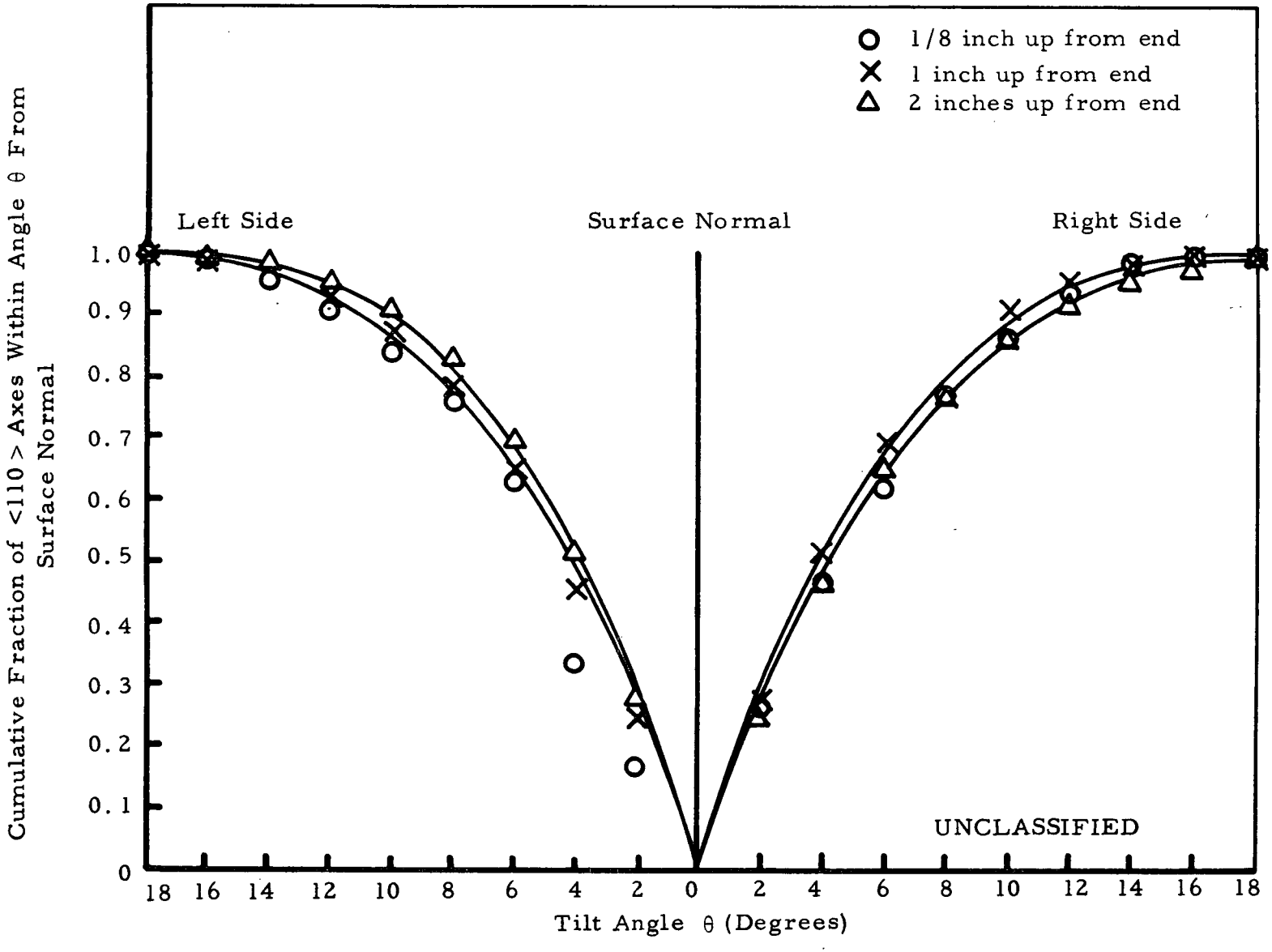

Fig. 60. (U) Distribution of <110> axes in R-20 of specimen set B_1

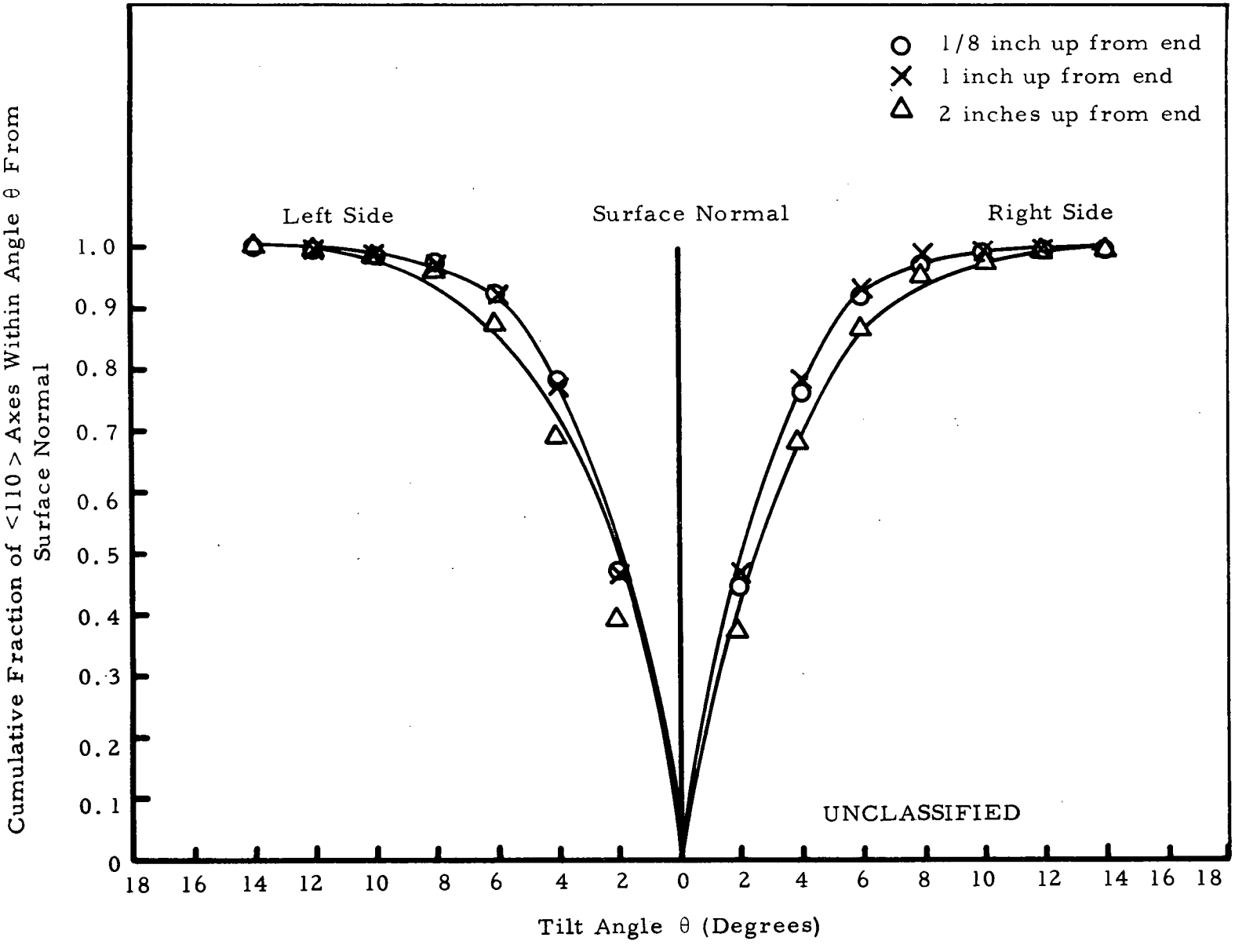

Fig. 61. (U) Distribution of <110> axes in R-23 of specimen set B_2

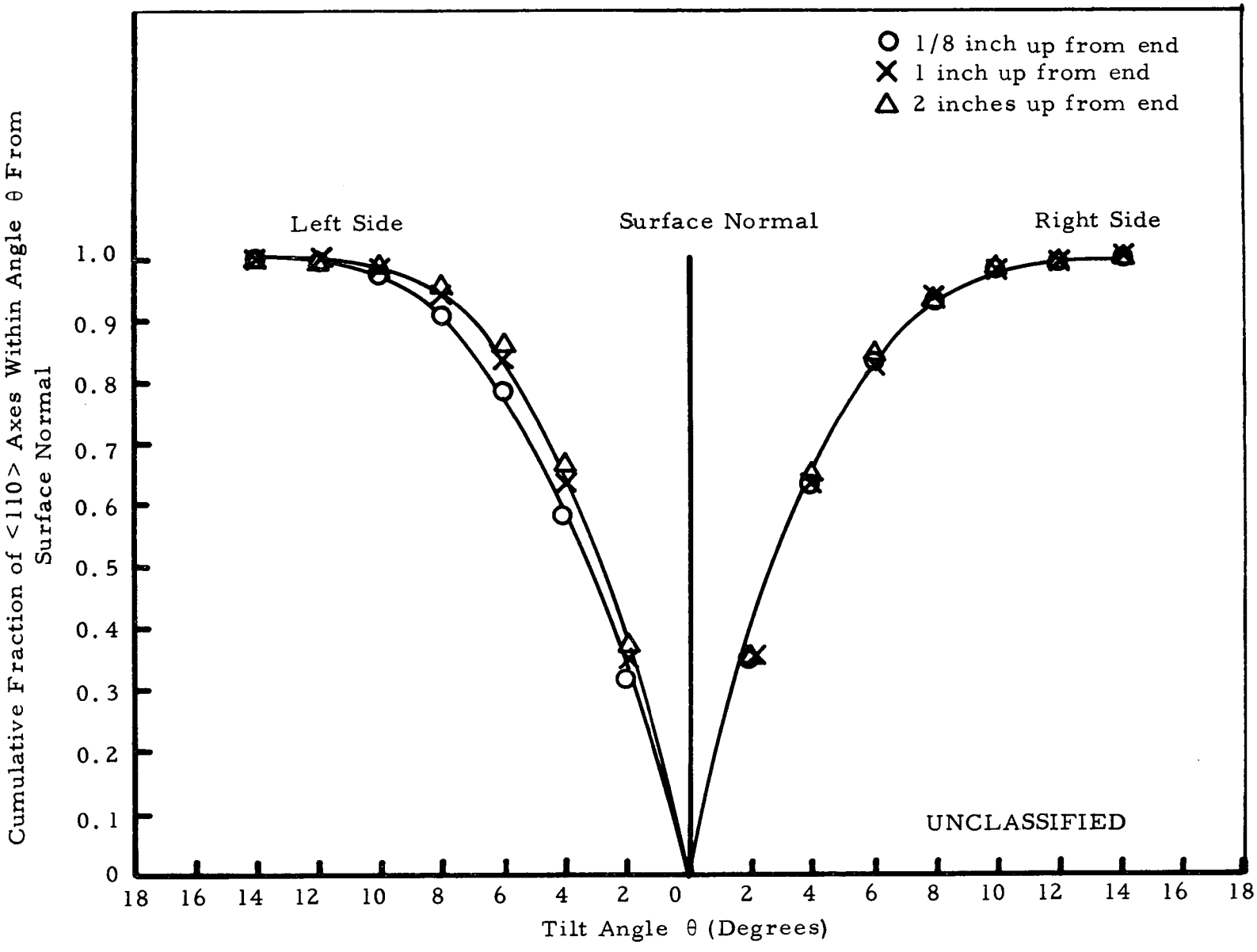

Fig. 62. (U) Distribution of <110> axes in R-26 of specimen set B_3

1. The deposition rate increased with the H_2/W ratio in the gaseous reactants (see Table 13).

2. There were no significant differences in the as-deposited impurity contents and microstructures of these samples.

3. The deposit prepared at a H_2/W ratio of 3.3 was better oriented than that prepared at a H_2/W ratio of 2.3 or a H_2/W ratio of 6.4 (compare Figs. 60, 61, and 62). It was as well oriented as the deposit (R-9) prepared at the stoichiometric H_2/W ratio 3.0. H_2/W ratio higher than 3.0 did not seem to impair the degree of (110) orientation as much as H_2/W ratio lower than 3.0. (Compare Figs. 60 and 62.)

(U) On the basis of these observations, it is concluded that a better (110) oriented chloride tungsten deposit can be obtained if the H_2/W ratio in the gaseous reactants is maintained at close to the stoichiometric value (i.e. $H_2/W = 3.0$).

Effect of Mandrel Temperature. (U) Specimen Sets C_1 and C_2 were prepared for the evaluation of the effect of mandrel temperature. Set C_1 (R-27, R-28, R-29) was prepared at a mandrel temperature of 1348°K and Set C_2 (R-30, R-31, R-32) was prepared at a mandrel temperature of 1298°K, other conditions being the same as the reference deposition conditions. Table 15 lists the as-deposited dimensions of the specimens of these sets. R-27 and R-30 were used for the comparison of the degree of (110) orientation after

TABLE 15

(U) DIMENSION MEASUREMENTS OF AS-DEPOSITED SETS C_1 AND C_2 SPECIMENS

(This table is Unclassified)

Set	Run No.	Length (Inch)	Diameter (Inch)				
			1/8 Inch From End	1/2 Inch From End	1 Inch From End	1-1/2 Inch From End	2 Inches From End
C_1	R-27	5-1/2	.656	.654	.647	.643	.639
	R-28	5-1/2	.661	.666	.659	.651	.646
	R-29	5-1/2	.669	.669	.664	.654	.648
C_2	R-30	5-1/2	.642	.653	.647	.645	.641
	R-31	5-1/2	.650	.652	.657	.653	.646
	R-32	5-1/2	.662	.665	.665	.651	.649

grinding to 0.625 inch O. D. and electropolishing. R-28 and R-31 were used for the comparison of the impurity contents. R-29 and R-32 were used for the comparison of the microstructures. All specimens were studied by X-rays for their preferred crystal orientation. The evaluation results are shown in Table 16 and Figs. 63 through 66. The results are summarized as follows.

1. The deposition rate on the top 1/2 inch of the mandrel was slightly higher (see Table 15) and the chloride tungsten grains were coarser (compare Fig. 65 with Fig. 66) for a mandrel temperature at 1348°K than 1298°K.

2. There were no significant differences in impurity contents between Specimen Set C_1 and Specimen Set C_2.

3. There was no significant difference in the degrees of (110) orientation between Specimen Set C_1 and Specimen Set C_2 although the axial distribution of the preferred orientation was slightly more uniform for the higher mandrel temperature (compare Fig. 63 with Fig. 64).

On the basis of these observations there does not seem to be any strong preference between a mandrel temperature of 1298°K and a mandrel temperature of 1348°K.

Effect of Oxygen and Nitrogen Impurity in the Gaseous Reactants. (U) Specimen Sets D_1 and D_2 were prepared for the study of the effect of the

TABLE 16

(U) DEPOSITION CONDITIONS AND EVALUATION RESULTS FOR SETS C_1 AND C_2 SPECIMENS

(This table is Unclassified)

Set No.	C_1			C_2		
Run No.	R-27	R-28	R-29	R-30	R-31	R-32
Deposition Time (Min.)	120	120	120	120	120	120
Deposition Conditions	Reference Conditions Except Mandrel Temperature = 1075°C			Reference Conditions Except Mandrel Temperature = 1025°C		
Unique Parameter Evaluated	Distribution of Preferred Orientation Fig. 63	Impurity Contents	Micro-structures Fig. 65	Distribution of Preferred Orientation Fig. 64	Impurity Contents	Micro-structures Fig. 66
Impurity Contents (ppm)						
N		<1			<1	
O		0.5			2	
C		6			7	
F		<3			<3	
Cl		8 ± 1			14 ± 2	
Metallic		Si 1.5			Si 2	
		Fe <4			Fe 5	
		Mg <.02			Mg 1	
		Mn <0.1			Mn 0.1	
		Cu 0.6			Cu <0.3	
		Al <0.5			Al <0.3	
		Ni 0.5			Ni <0.3	
(110) Orientation						
1/8 inch from end	Yes	Yes	Yes	Yes	Yes	Yes
1 inch from end	Yes	Yes	Yes	Yes	Yes	Yes
2 inches from end	Yes	Yes	Yes	Yes	Yes	Yes

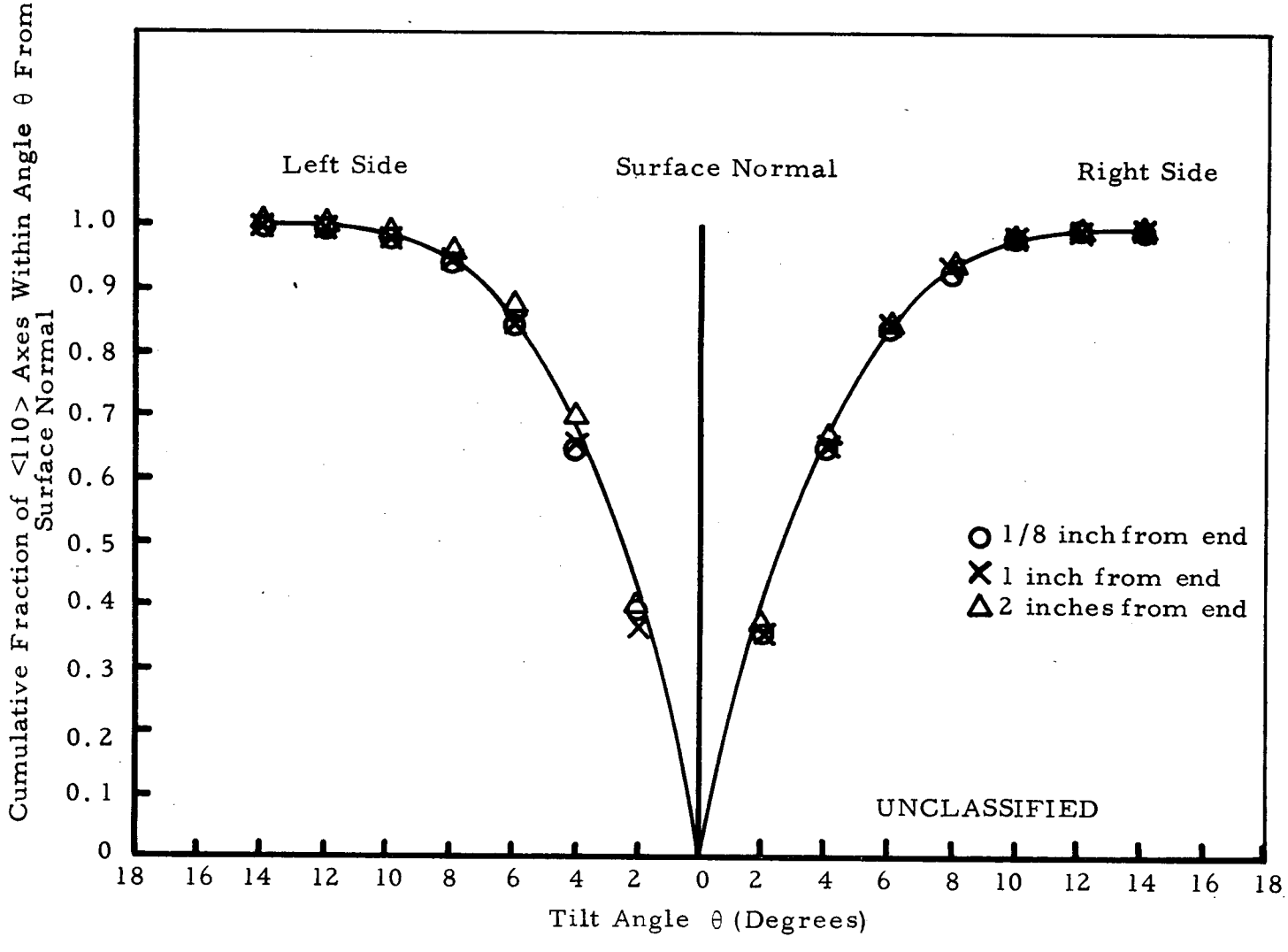

Fig. 63. (U) Distribution of <110> axes in R-27 of specimen set C_1

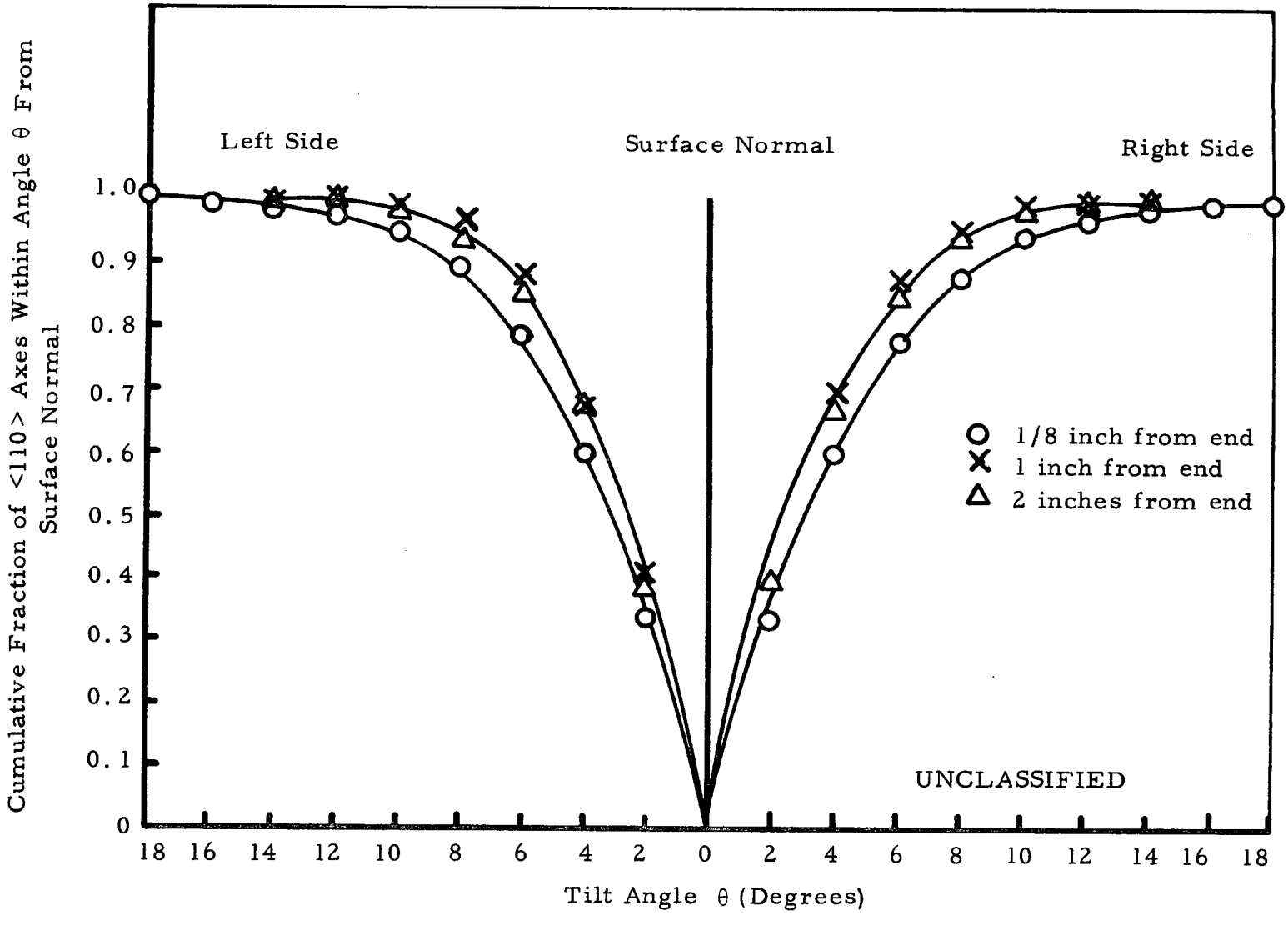

Fig. 64. (U) Distribution of <110> axes in R-30 of specimen set C_2

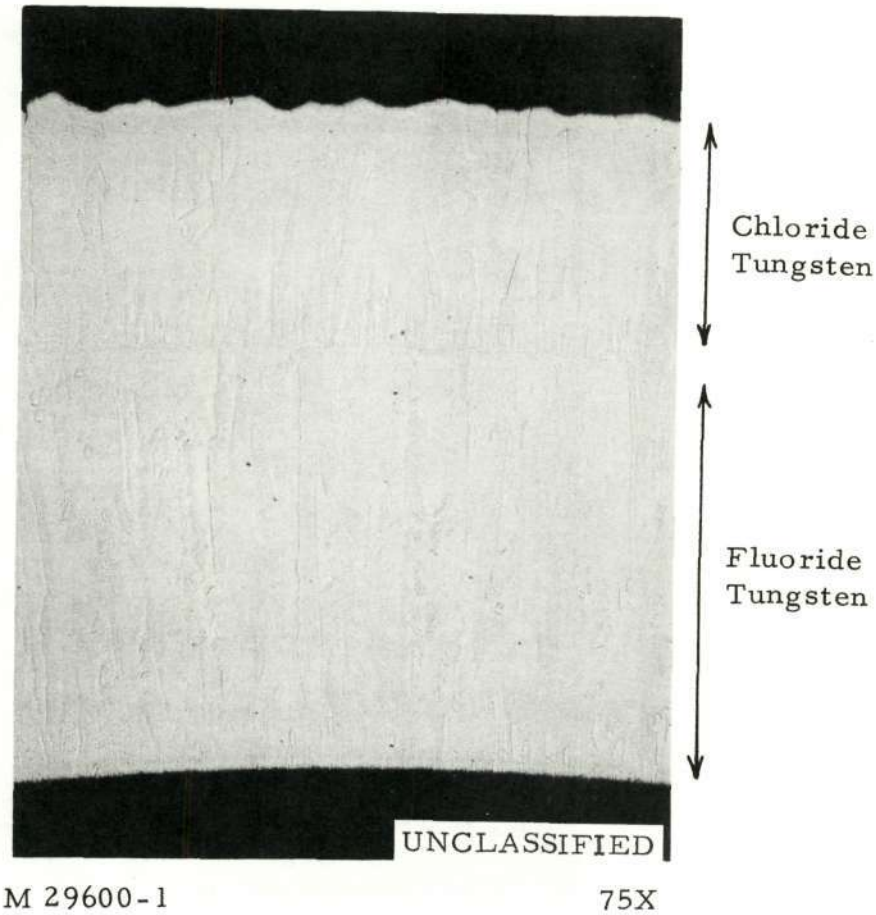

Fig. 65. (U) Cross section view of as-deposited specimen R-29 of Set C_1

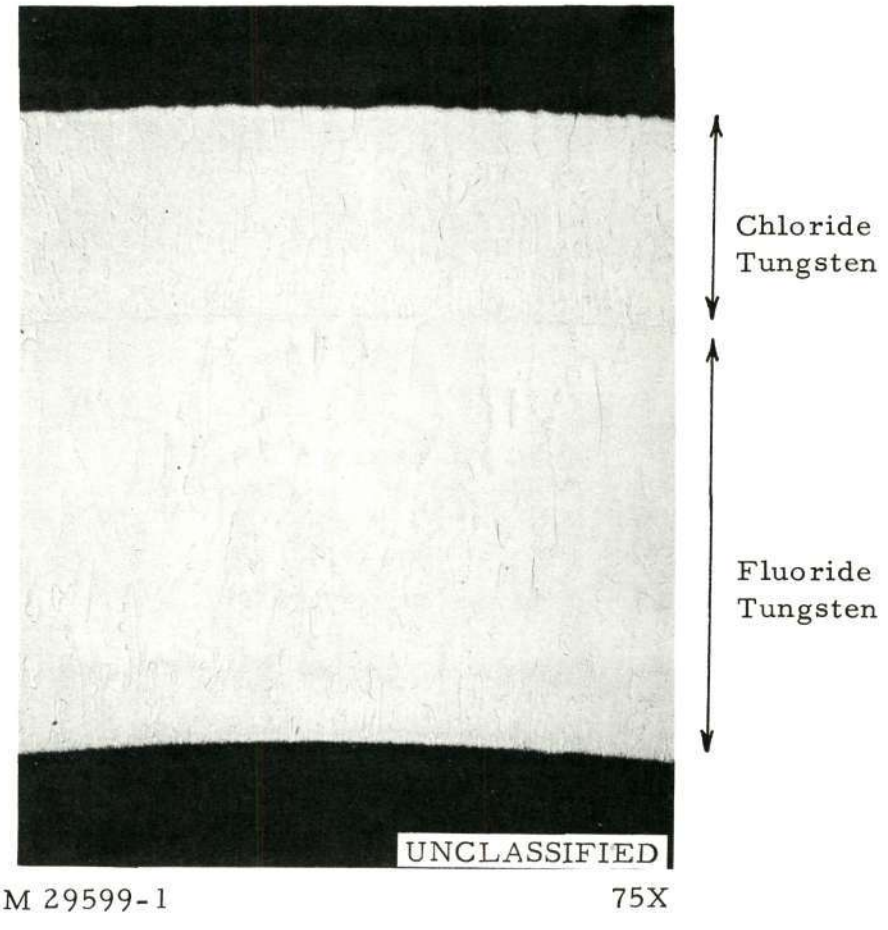

Fig. 66. (U) Cross section view of as-deposited specimen R-32 of Set C_2

presence of oxygen impurity in the gaseous reactants. Set D_1 (R-33, R-34, R-35) was deposited in the absence of oxygen addition to the plating gases i.e. reference conditions, while during the deposition of Set D_2 (R-36, R-37, R-38), a controlled amount of dry air was added, corresponding to 3 c.c./min. of oxygen addition. Table 17 lists the dimensions of the as-deposited Sets D_1 and D_2 specimens, with Set D_1 specimens in general having higher deposition rates. R-33 and R-36 were used to compare the impurity contents. R-34 and R-37 were used to compare the degree of (110) preferred orientation after grinding to 0.625 inch O.D. and electropolishing. R-35 and R-38 were used to compare the microstructures. All specimens were studied by X-rays for their preferred crystal orientation. The deposition conditions and evaluation results are shown in Table 18 and Figs. 67 through 70. It can be seen that the addition of dry air at a rate corresponding to 3 c.c./min. of oxygen to the chamber, and no significant effect in the degree of (110) preferred orientation, microstructures and impurity contents of the deposit, although the deposit prepared in the presence of the dry air addition had a higher nitrogen content distributed non-uniformly in the deposit.

Effect of Change of W/Cl Ratio in the Gaseous Reactants. (U) Set E_1 (R-39, R-40, R-41) was prepared from the hydrogen reduction of WCl_5. The WCl_5 was formed in the chlorinator by having the top 4 inches of the furnace maintained at 1173°K instead of 873°K. Table 19 lists the dimensions of the as-deposited specimens of Set E_1. R-39 was evaluated for its degree of (110) orientation after grinding to 0.625 inch O.D. and electropolishing. R-40

TABLE 17

(U) DIMENSION MEASUREMENTS OF AS-DEPOSITED SETS D_1, AND D_2 SPECIMENS

(This table is Unclassified)

Set	Run No.	Length (Inch)	Diameter (Inch)				
			1/8 Inch From End	1/2 Inch From End	1 Inch From End	1-1/2 Inch From End	2 Inches From End
D_1	R-33	5-1/2	.650	.653	.652	.645	.640
	R-34	5-1/2	.651	.648	.642	.638	.636
	R-35	5-1/2	.662	.656	.649	.645	.645
D_2	R-36	5-1/2	.648	.653	.649	.650	.639
	R-37	5-1/2	.640	.647	.636	.633	.630
	R-38	5-1/2	.640	.639	.634	.630	.626

TABLE 18

(U) DEPOSITION CONDITIONS AND EVALUATION RESULTS FOR SET D_1 AND SET D_2 SPECIMENS

(This table is Unclassified)

Set No.	D_1			D_2		
Run No.	R-33	R-34	R-35	R-36	R-37	R-38
Deposition Time (Min.)	120	120	120	120	120	120
Deposition Conditions	Reference Conditions			Reference Conditions Except Dry Air Was Added to the Chamber at a Rate Corresponding to 3 c. c. /min. of Oxygen Addition		
Unique Parameter Evaluated	Impurity Contents	Distribution of Preferred Orientation Fig. 67	Micro-structures Fig. 69	Impurity Contents	Distribution of Preferred Orientation Fig. 68	Micro-structures Fig. 70
Impurity Contents (ppm)						
N	<1			see footnote*		
O	18			10.5		
C	7			7		
F	4			5		
Cl	6 ± 1			12 ± 2		
Metallic	Si 1.4			Si 1.7		
	Fe <4			Fe <4		
	Mg 0.2			Mg 0.4		
	Mn <0.2			Mn <0.1		
	Cu 0.7			Cu 0.4		
	Al 0.5			Al 0.5		
	Ni 0.4			Ni <0.3		
(110) Orientation						
1/8 inch from end	Yes	Yes	Yes	Yes	Yes	Yes
1 inch from end	Yes	Yes	Yes	Yes	Yes	Yes
2 inches from end	Yes	Yes	Yes	Yes	Yes	Yes

*Nitrogen was <1 ppm in one analysis and 20 ppm in a second analysis, indicating non-uniformity of nitrogen content in the sample.

UNCLASSIFIED

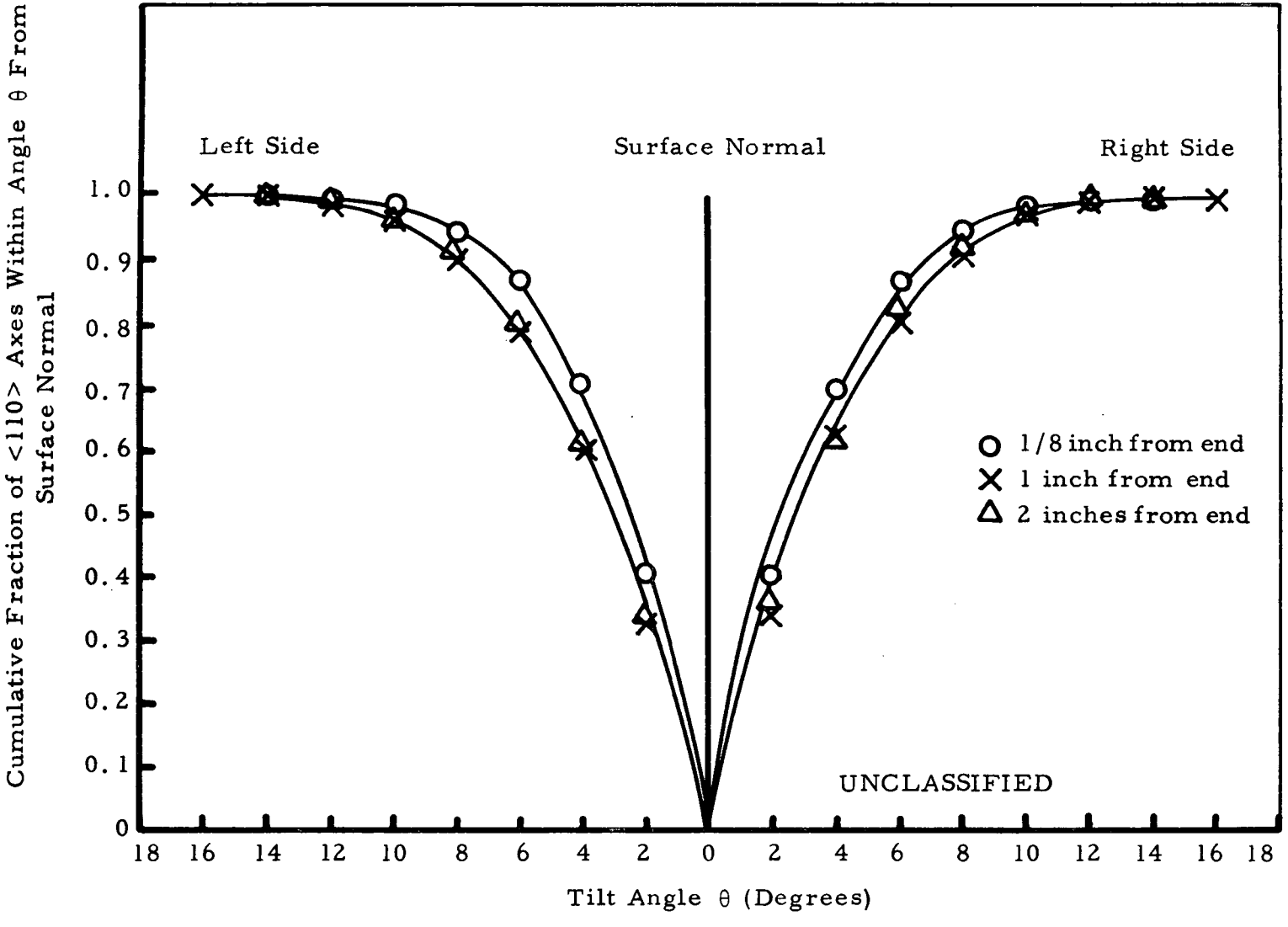

Fig. 67. (U) Distribution of <110> axes in R-34 of specimen set D_1

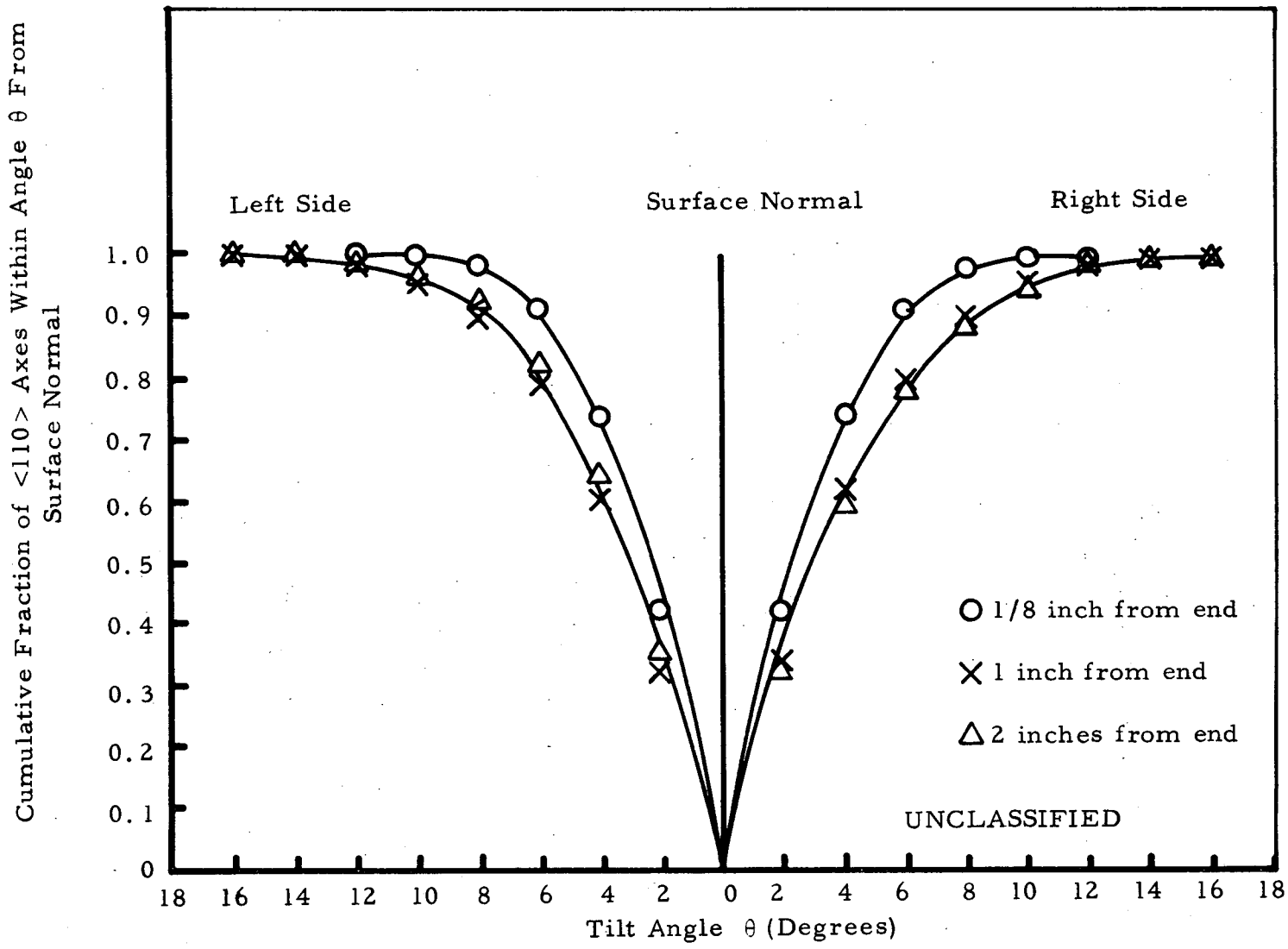

Fig. 68. (U) Distribution of <110> axes in R-37 of specimen set D_2

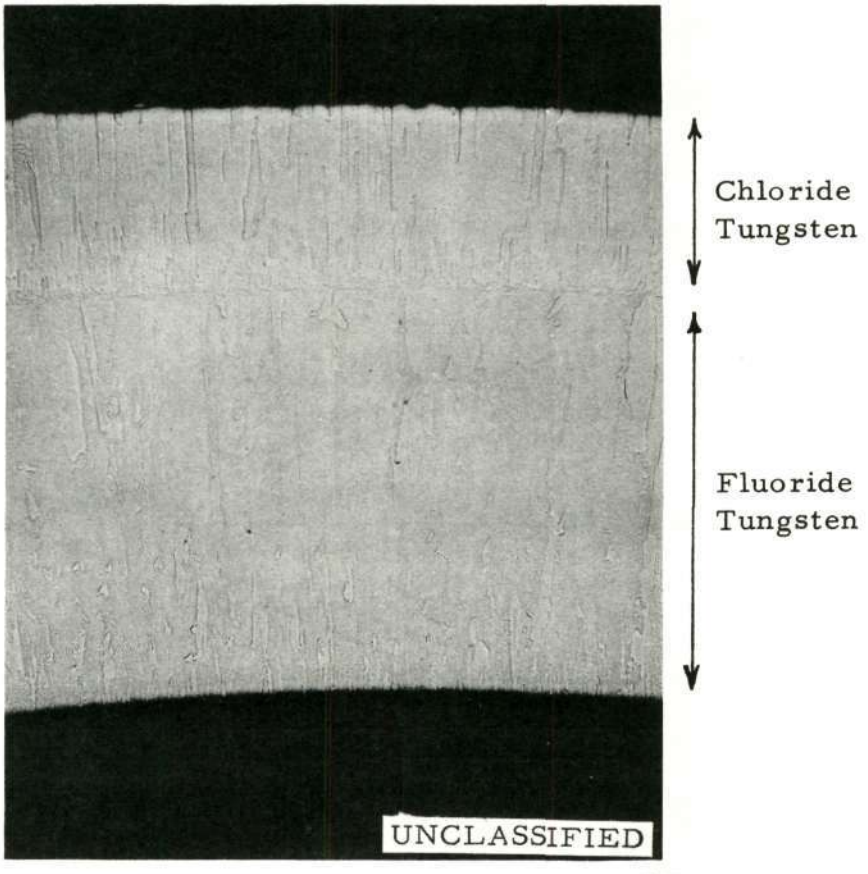

M 29601-1 75X

Fig. 69. (U) Cross section view of as-deposited specimen R-35 of Set D_1

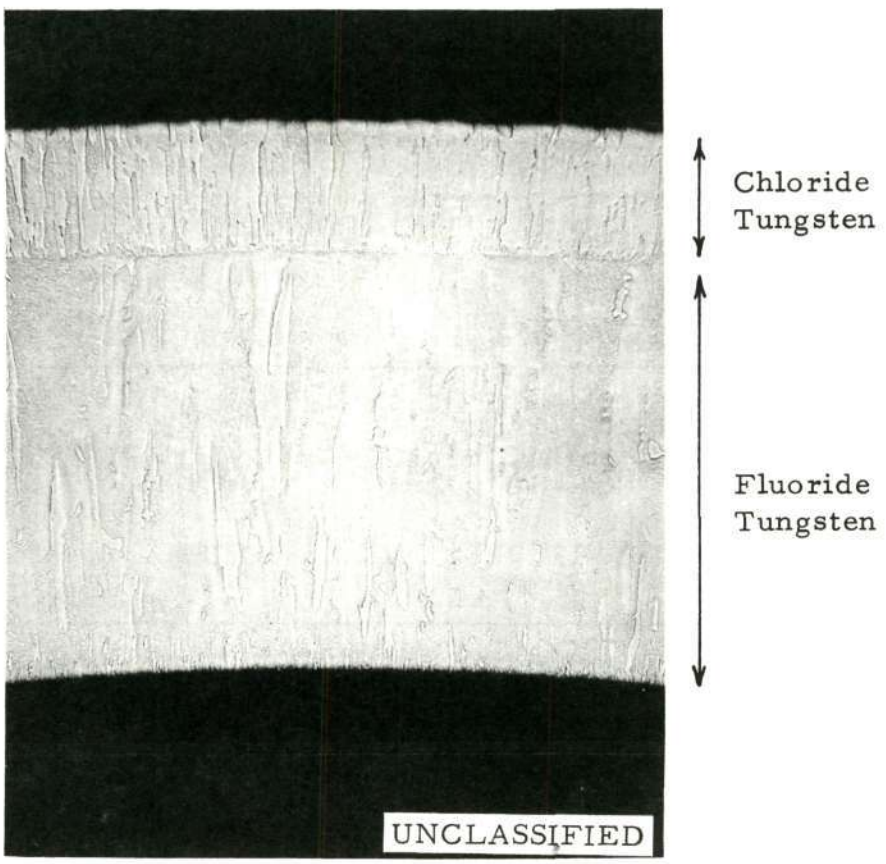

M 29603-1 75X

Fig. 70. (U) Cross section view of as-deposited specimen R-38 of Set D_2

TABLE 19

(U) DIMENSION MEASUREMENTS OF AS-DEPOSITED SET E_1 SPECIMENS

(This table is Unclassified)

Set	Run No.	Length	Diameter (Inch)				
			1/8 Inch From End	1/2 Inch From End	1 Inch From End	1-1/2 Inch From End	2 Inches From End
E_1	R-39	5-3/8	0.662	0.664	0.660	0.652	0.644
	R-40	5-1/2	0.661	0.662	0.658	0.652	0.646
	R-41	5-1/2	0.667	0.667	0.658	0.654	0.645

was analyzed for impurity contents. R-41 was used for microstructure study. All three specimens were examined by X-rays for the nature of preferred crystal orientation in the chloride tungsten deposit. The deposition conditions and evaluation results are shown in Table 20 and Figs. 71 and 72. It seems that the change of W/Cl ratio from 6 to 5 did not affect significantly the impurity contents, microstructures and degree of (110) orientation in the chloride tungsten deposit. (Compare results of R-39, R-40, and R-41 with that for R-9, R-12, R-13, and R-14.)

Effect of WF_6 Additions. (U) Since tungsten deposited by the hydrogen reduction of WF_6 exhibits different grain structures and preferred crystal orientation from that of tungsten deposited by the hydrogen reduction of tungsten chloride, it would be interesting to find out how the addition of WF_6 to the gaseous reactants affects the grain structures and preferred crystal orientation of the deposit. Sets F_1 (R-42, R-43, R-44), F_2 (R-45, R-46, R-47, R-48), and F_3 (R-49, R-50, R-51) were prepared for this purpose by incorporating various amounts of WF_6 into the H_2 + He stream. Table 21 lists the dimensions of these specimens in the as-deposited conditions. Table 22 summarizes the deposition conditions and the evaluation results. As shown in Table 22, some of the samples were prepared by using a H_2/W ratio of 3.0 with respect to the tungsten contained in the WCl_6, while others were prepared by using a H_2/W ratio of 3.0 with respect to the tungsten contained in both WCl_6 and WF_6. For the same deposition time, the rates of deposition were lower for the former samples, especially when the concentration of WF_6 addition was high (e.g. for

TABLE 20

(U) DEPOSITION CONDITIONS AND EVALUATION RESULTS FOR SET E_1 SPECIMENS

(This table is Unclassified)

Set No.	E_1		
Run No.	R-39	R-40	R-41
Deposition Time (Min.)	120	120	120
Deposition Conditions			
Cl_2 flow rate (c. c. /min.)	360	360	360
H_2 flow rate (c. c. /min.)	300	300	300
Chamber He flow rate (c. c. /min.)	450	450	450
Bleed He flow (c. c. /min.)	No	No	No
Chamber pressure (torr)	6	6	6
Mandrel temperature (°C)	1050	1050	1050
H_2/W mole ratio	2.5	2.5	2.5
Unique Parameter Evaluated	Distribution of Preferred Orientation Fig. 71	Impurity Contents	Micro-structures Fig. 72
Impurity Contents (ppm)			
N		1	
O		8	
C		8	
F		5	
Cl		8 ± 1	
Metallic		Si 2.2, Fe <4 Mg 0.3, Ni 0.6 Cu <0.3, Al 0.4 Mn <0.1	
(110) Orientation			
1/8 Inch from end	Yes	Yes	Yes
1 Inch from end	Yes	Yes	Yes
2 Inches from end	Yes	Yes	Yes

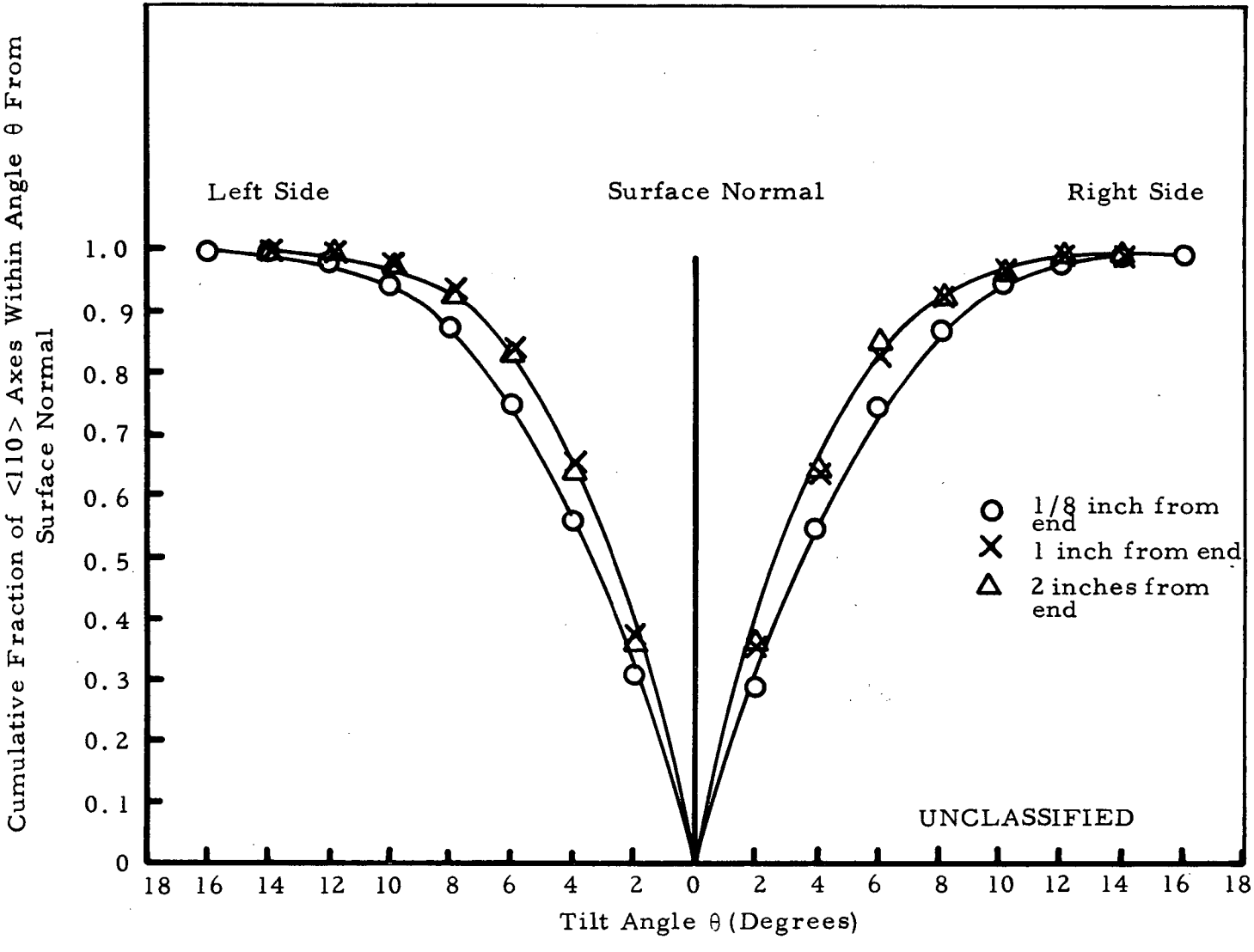

Fig. 71. (U) Distribution of <110> axes in R-39 of specimen Set E_1

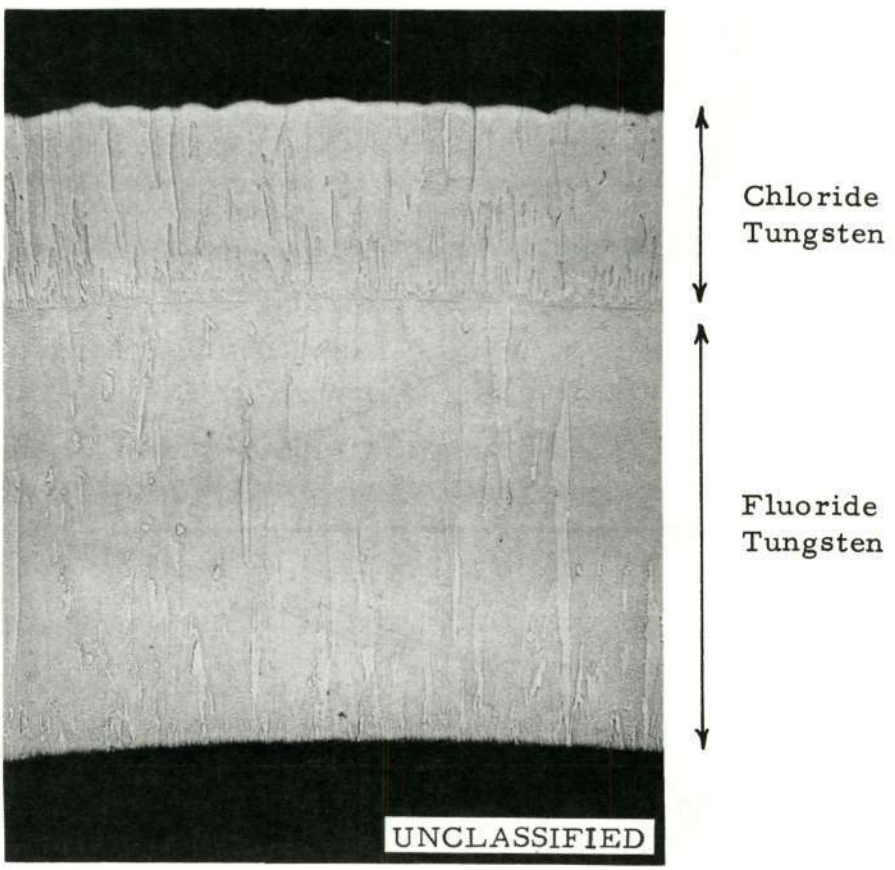

M 29603-1 75X

Fig. 72. (U) Cross section view of as-deposited specimen R-41 of Set E_1

TABLE 21

(U) DIMENSION MEASUREMENTS OF AS-RECEIVED SETS F_1, F_2, AND F_3 SPECIMENS

(This table is Unclassified)

Set	Run No.	Length (Inch)	Diameter (Inch)				
			1/8 Inch From End	1/2 Inch From End	1 Inch From End	1-1/2 Inch From End	2 Inches From End
F_1	R-42	5-1/2	.667	.668	.664	.654	.651
	R-43	5-1/2	.672	.673	.664	.656	.652
	R-44	5-1/2	.666	.667	.656	.649	.643
F_2	R-45	5-1/2	.649	.651	.649	.646	.640
	R-46	5-1/2	.648	.654	.652	.647	.640
	R-47	5-1/2	.640	.642	.638	.631	.626
	R-48	5-1/2	.695	.681	.672	.668	.665
F_3	R-49	5-1/2	.671	.668	.659	.652	.649
	R-50	5-1/2	.675	.673	.662	.653	.647
	R-51	5-1/2	.671	.667	.662	.658	.650

TABLE 22

(U) DEPOSITION CONDITIONS AND EVALUATION RESULTS FOR SETS F_1, F_2, AND F_3 SPECIMENS

(This table is Unclassified)

Set No.	F_1			F_2				F_3		
Run No.	R-42	R-43	R-44	R-45	R-46	R-47	R-48	R-49	R-50	R-51
Deposition Time (Min.)	120	120	120	120	120	150	150	120	120	120
Deposition Conditions										
Cl_2 flow rate (c. c. /min.)	360	360	360	360	360	360	360	360	360	360
H_2 flow rate (c. c. /min.)	360	360	360	360	360	360	420	396	396	396
Chamber He flow rate (c. c. /min.)*	400	400	400	400	400	400	400	400	400	400
Bleed He flow (c. c. /min.)	0	0	0	0	0	0	0	0	0	0
WF_6 flow rate (c. c. /min.)	7.5	7.5	7.5	24	24	24	20	12	12	12
Chamber pressure (torr.)	6	6	6	6	6	6	6	6	6	6
Mandrel temperature (°K)	1323	1323	1323	1323	1323	1323	1323	1323	1323	1323
H_2/W mole ratio	3.0	3.0	3.0	3.0	3.0	3.0	3.0**	3.0**	3.0**	3.0**
Unique Parameter Evaluated	Distribution of (110) Preferred Orientation (Fig. 78)	Impurity Contents	Microstructures (Fig. 73)	Impurity Contents	Microstructures and Distribution of (110) Preferred Orientation (Figs. 74 and 79)	Microstructures (Fig. 75)	Preferred Orientation	Impurity Contents	Microstructures and Distribution of (110) Preferred Orientation (Figs. 76 and 80)	Microstructures (Fig. 77)
Impurity Contents (ppm)										
N		<1		<1				<1		
O		10		8				12		
C		5		7				5		
F		<3		4				<3		
Cl		7		5				8		
Metallic		Si 3.0 Fe 5.0 Mg 0.3 Mn <0.1 Cu 0.5 Al 1.0 Ni 0.5		Si 1.5 Fe <4.0 Mg 0.4 Mn <0.1 Cu 0.5 Al 1.0 Ni <0.3				Si 1.5 Fe <4.0 Mg 0.5 Mn <0.1 Cu 1.0 Al 0.5 Ni <0.3		
Preferred Orientation										
1/8 inch from end	{110}	Random	{110} + {200}	{200}	{110}	{200}	{200}	{110}	{110} + {200}	Random
1 inch from end	{110}	{110} + {200}	{110} + {200}	{200}	{110}	{200}	Random	{110}	{110}	{200}
2 inches from end	{110} + {200}	{110} + {200}	{110} + {200}	{200}	{110}	{200}	Random	{200}	{110}	{200}

*One half of the total helium flow was injected to the chamber with the WF_6 stream to prevent plating of the WF_6 injector tip.

**With respect to W from both WCl_6 and WF_6. The other ratios are with respect to WCl_6 only.

UNCLASSIFIED

Specimens R-45, R-46, and R-47), as shown in Table 21. It appears that hydrogen reacted with WF_6 preferentially at the deposition temperature, and that the remaining hydrogen concentration in the gaseous phase was not high enough to maintain the expected rate of reaction with WCl_6. By raising the rate of hydrogen flow to that for a H_2/W ratio of 3.0 with respect to the tungsten contained in both WCl_6 and WF_6, the rate of deposition was increased. R-43, R-45, and R-49 were used to compare the impurity contents of these sets. No significant difference was observed. R-44, R-46, R-47, R-50, and R-51 were examined for their microstructures, (Figs. 73 through 77). They were found to be similar to the microstructures observed in the previous specimens except that the grain structures of R-51 were much finer and discontinuous. The reason for the "broken" grain structures could be due to local fluctuation of H_2/W ratio. All specimens were studied by X-rays for their preferred crystal orientation. It can be seen from Table 22 that the nature of the preferred orientation developed in the deposit was irreproducible among the three specimens in each set. It appears that as the concentration of WF_6 addition was increased, the tendency for the appearance of <100> preferred orientation in the deposit became enhanced. R-42, R-46, and R-50 were used to compare the degree of (110) preferred orientation after grinding to 0.625 inch O.D. and electropolishing (Figs. 78 through 80). It can be seen that these specimens, especially R-46, are not highly (110) oriented. Thus no special benefit can be derived by adding WF_6 to the gaseous reactants during chloride tungsten deposition.

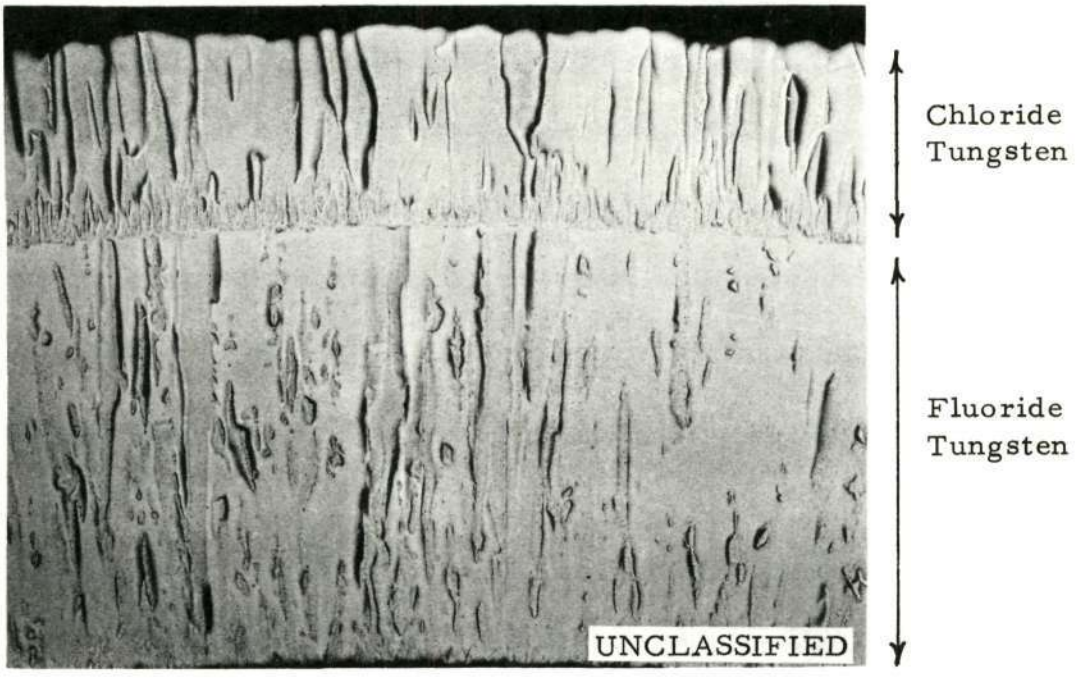

M 29914-1 75X

Fig. 73. (U) Cross section view of as-deposited specimen R-44 of Set F_1

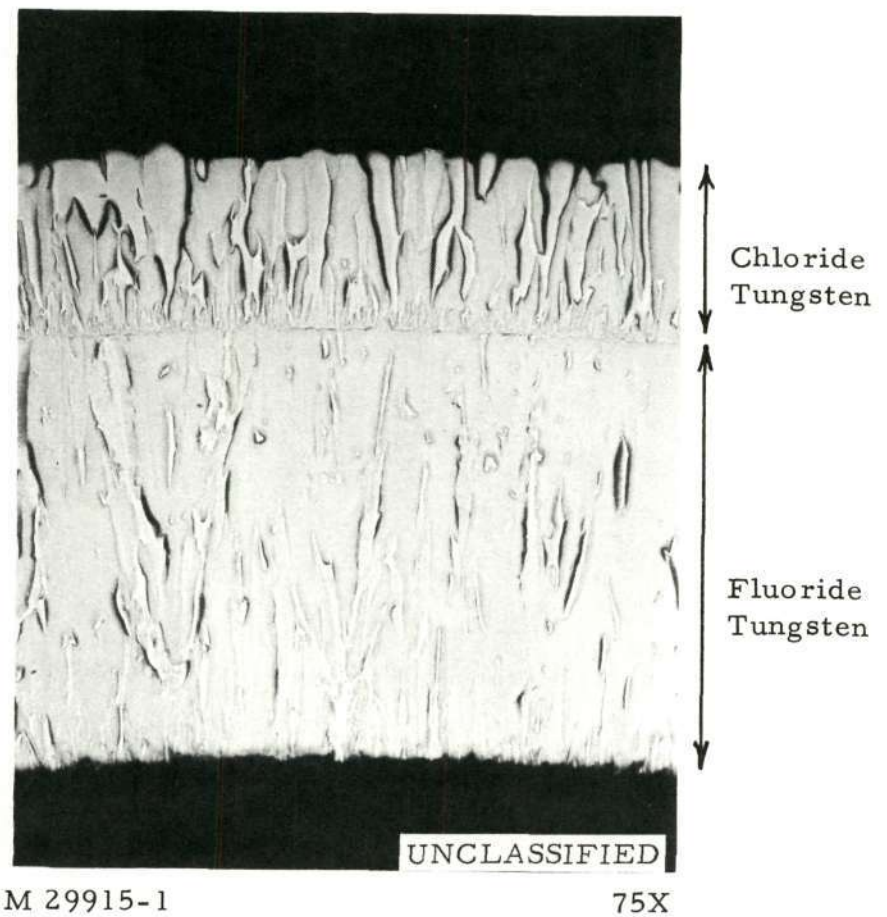

Fig. 74. (U) Cross section view of as-deposited specimen R-36 of Set F_1

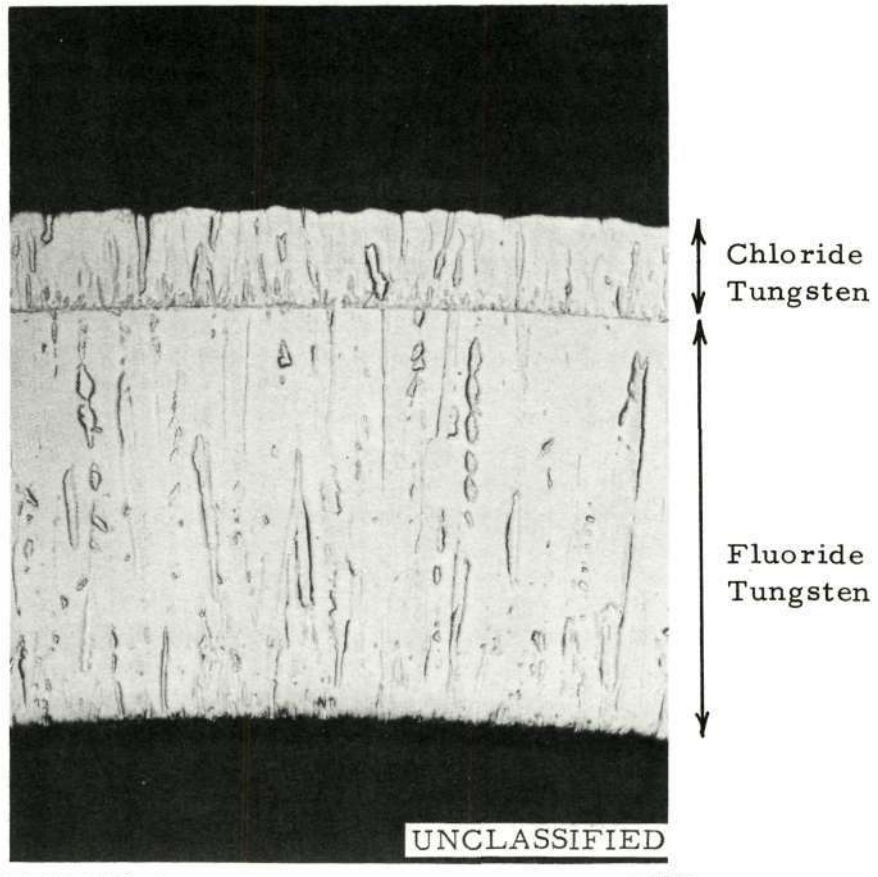

Fig. 75. (U) Cross section view of as-deposited specimen R-47 of Set F_2

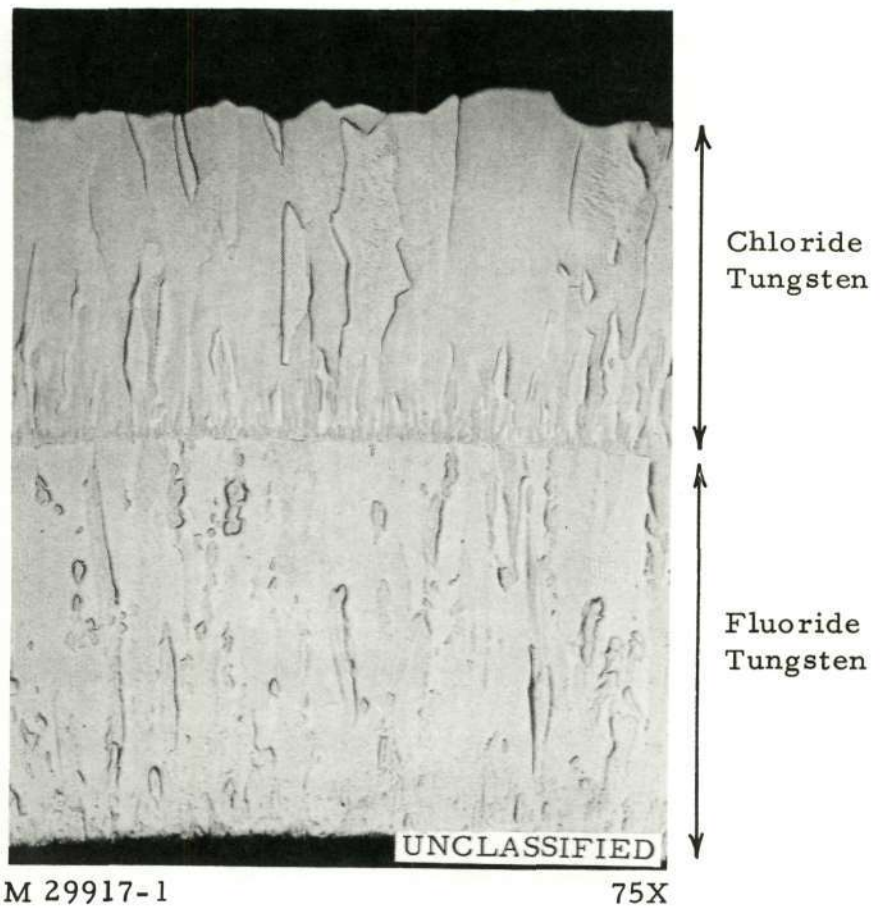

Fig. 76. (U) Cross section view of as-deposited specimen R-50 of Set F_3

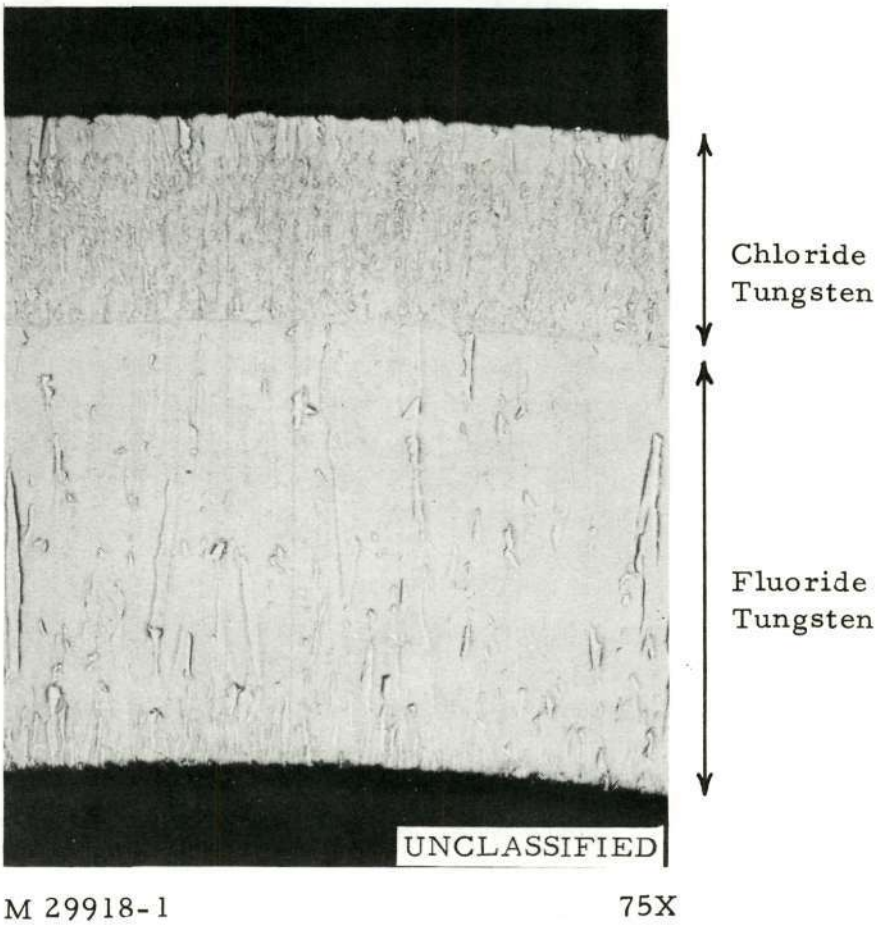

Fig. 77. (U) Cross section view of as-deposited specimen R-51 of Set F_3

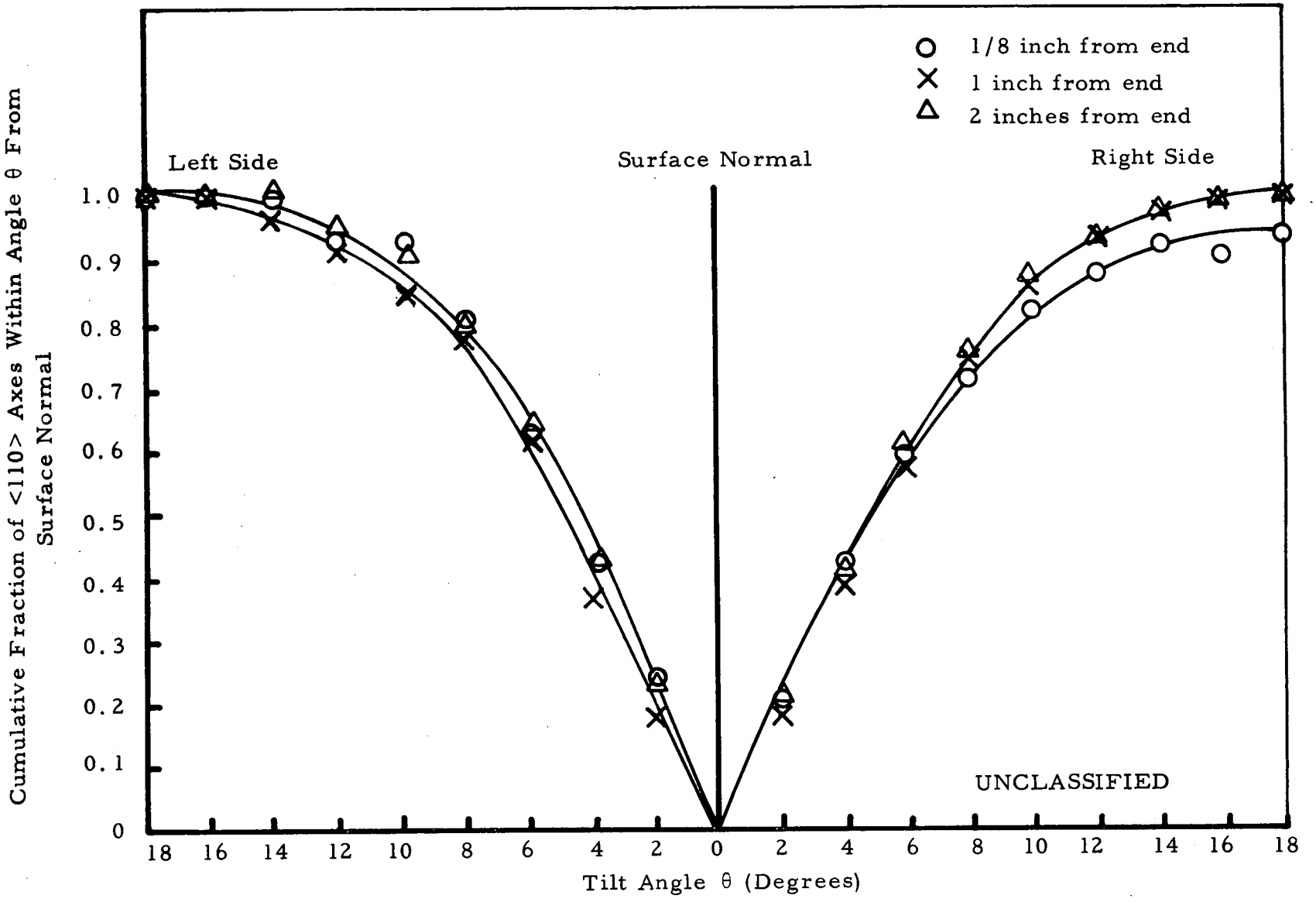

Fig. 78. (U) Distribution of <110> axes in R-42 of specimen Set F_1

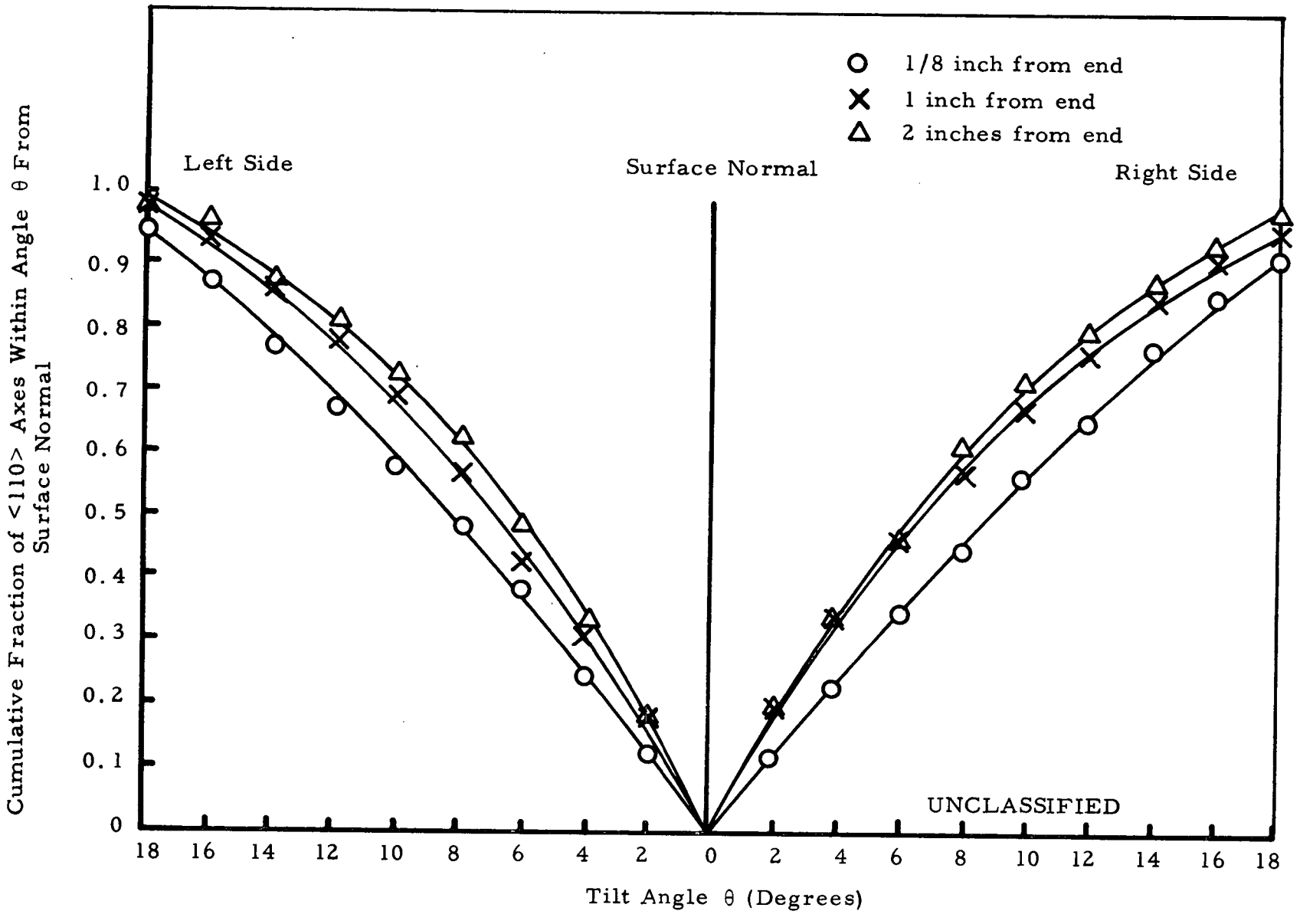

Fig. 79. (U) Distribution of <110> axes in R-46 of specimen Set F_2

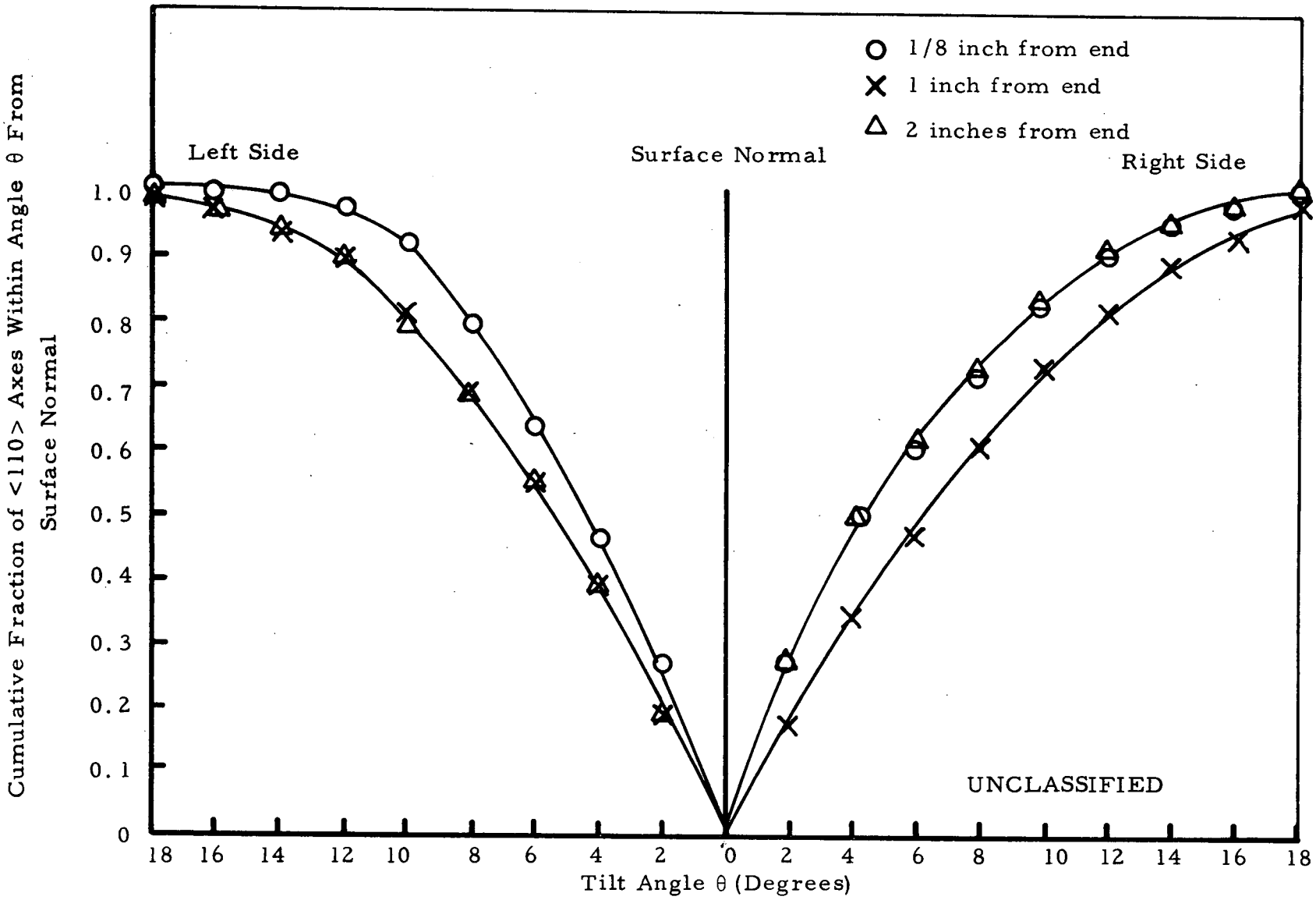

Fig. 80. (U) Distribution of <110> axes in R-50 of specimen Set F_3

Effect of Helium Diluent. (U) Set G (R-52, R-53, R-54) was prepared for the study of increasing the helium flow rate on the nature and the degree of preferred orientation in chloride tungsten deposit. Table 23 shows the dimensions of the three specimens prepared. Table 24 lists the deposition conditions and the evaluation results. R-53 was analyzed for its impurity contents. R-54 was examined for its microstructures (Fig. 81). R-52 was studied for its degree of {110} preferred orientation after grinding to 0.625 inch O. D. and electropolishing (Fig. 82). The preferred crystal orientations of all three specimens were determined by X-rays. No significant difference was observed between the impurity contents of R-53 and that of the other specimen sets prepared under this section. It was found, however, that the {110} orientation developed in these specimens, if any, was very weak and that some {200} orientation was present in R-53 and R-54. R-54 showed a fine and "broken" grain structure, probably caused by local fluctuations of H_2/W ratio by high helium flow rate. Thus a high helium flow rate is detrimental to the development of a strong {110} preferred crystal orientation in the chloride tungsten deposit.

2.3.2.3. Evaluation of Vacuum Work Functions of (110) Oriented Specimens. (U) For each (110) oriented set prepared under Section 2.3.2.2, one specimen was selected for the determination of its vacuum work function as a function

TABLE 23

(U) DIMENSION MEASUREMENTS OF AS-DEPOSITED SET G SPECIMENS

(This table is Unclassified)

Run No.	Length (Inch)	Diameter (Inch)				
		1/8 Inch From End	1/2 Inch From End	1 Inch From End	1-1/2 Inch From End	2 Inches From End
R-52	5-1/2	.662	.663	.660	.657	.650
R-53	5-1/2	.668	.670	.662	.657	.647
R-54	5-1/2	.671	.666	.657	.650	.643

TABLE 24

(U) DEPOSITION CONDITIONS AND EVALUATION RESULTS FOR SET G SPECIMENS

(This table is Unclassified)

Set No.	G		
Run No.	R-52	R-53	R-54
Deposition Time (Min.)	120	120	120
Deposition Conditions	Reference conditions except chamber He flow rate was 1100 c.c./min. rather than 650 c.c./min. and the chamber pressure was 6-8 torr rather than 6 torr		
Unique Parameter Evaluated	Distribution of {110} Preferred Orientation (Fig. 82)	Impurity Contents	Microstructures (Fig. 81)
Impurity Contents (ppm) N O C F Cl Metallic		1 14 8 3 10 Si 2.4 Fe 5.0 Mg 0.3 Mn <0.1 Cu <0.3 Al 0.4 Ni 1.0	
Preferred Orientation 1/8 inch from end 1 inch from end 2 inches from end	 weak {110} weak {110} weak {110}	 weak {110} weak {110} + weak {200} weak {110} + weak {200}	 weak {110} + weak {200} weak {110} + weak {200} weak {110} + weak {200}

UNCLASSIFIED

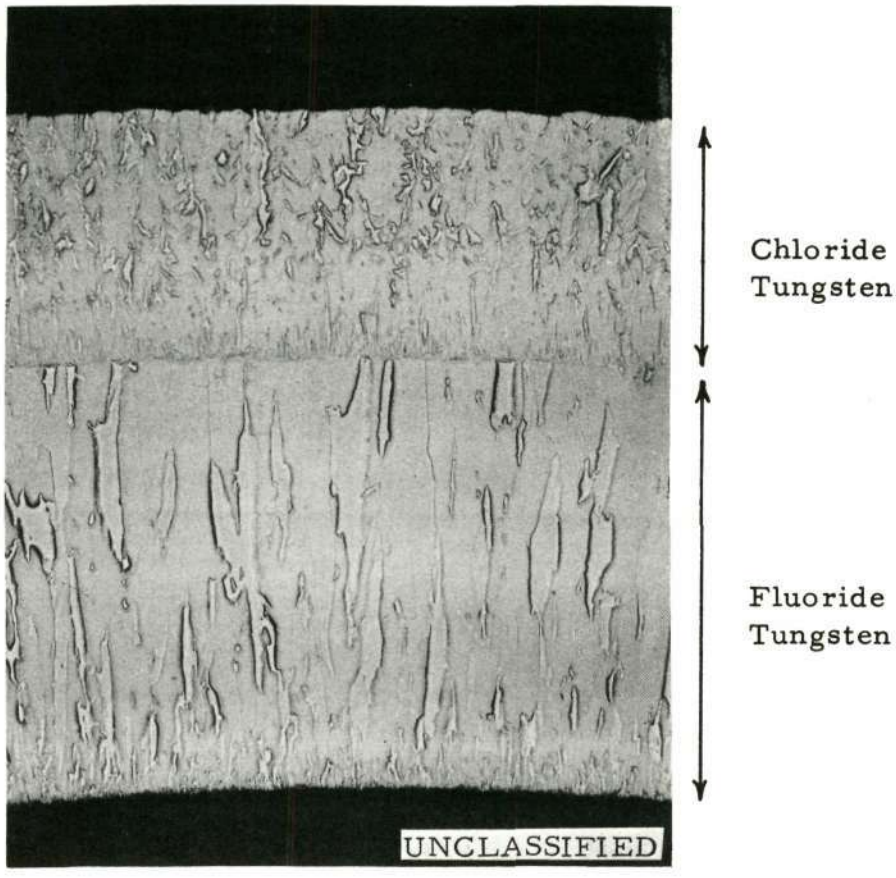

Fig. 81. (U) Cross section view of as-deposited specimen R-54 of Set G

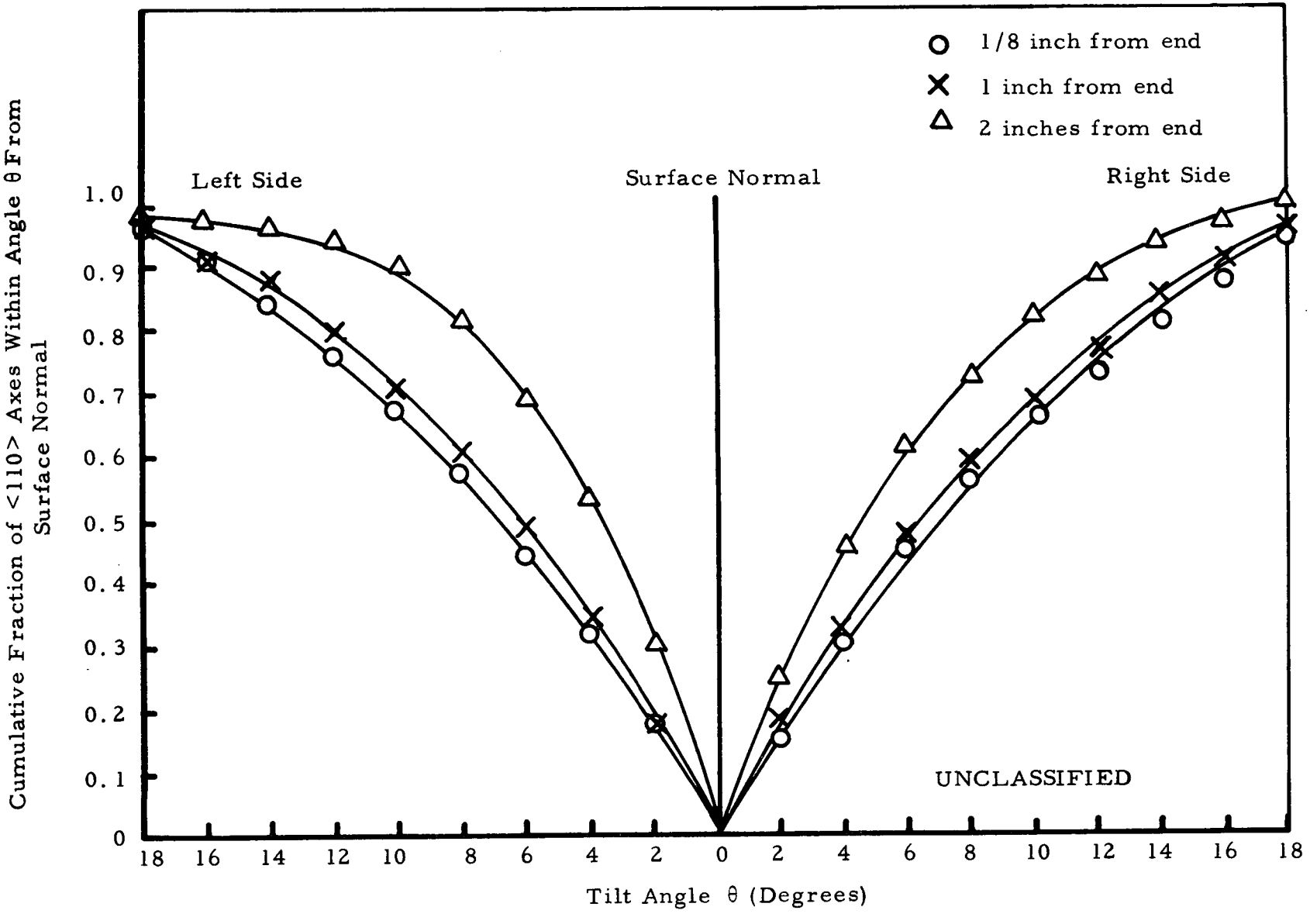

Fig. 82. (U) Distribution of <110> axes in R-52 of specimen Set G

of axial position and the correlation of work function data with X-ray pole figure results. The specimens selected were those whose spatial distributions of <110> axes as a function of axial position had been measured in the preceeding section. Prior to work function determination, each specimen was outgassed at 2073°K for 100 hours in 10^{-6} torr vacuum, and its distribution of <110> axes as a function of axial position was again determined, using the apparatus described in Section 2.3.1.3. The results are shown in Figs. 83 through 96. No significant change in the degree of (110) orientation by the 2073°K heat treatment was observed except in the cases of R-23, R-26, R-34, and R-37. (Compare Figs. 83 through 96 with corresponding (110) pole figure plots given in the preceeding section). R-23 and R-26 were prepared under the conditions where the H_2/W mole ratio was higher than the stoichiometric value of 3.0. R-37 was prepared in the presence of oxygen and nitrogen contaminations. Although R-34 was prepared under the reference conditions, the high oxygen content (18 ppm, see Table 18) of this specimen set seems to indicate that oxygen contamination may have occurred during the deposition. For these samples, the degree of (110) preferred orientation decreased after the heat treatment, indicating that H_2/W mole ratios higher than the stoichiometric value 3.0 and the presence of oxygen and nitrogen contaminations should be avoided if (110) preferred orientation stable to heat treatment is to be maintained in the deposit.

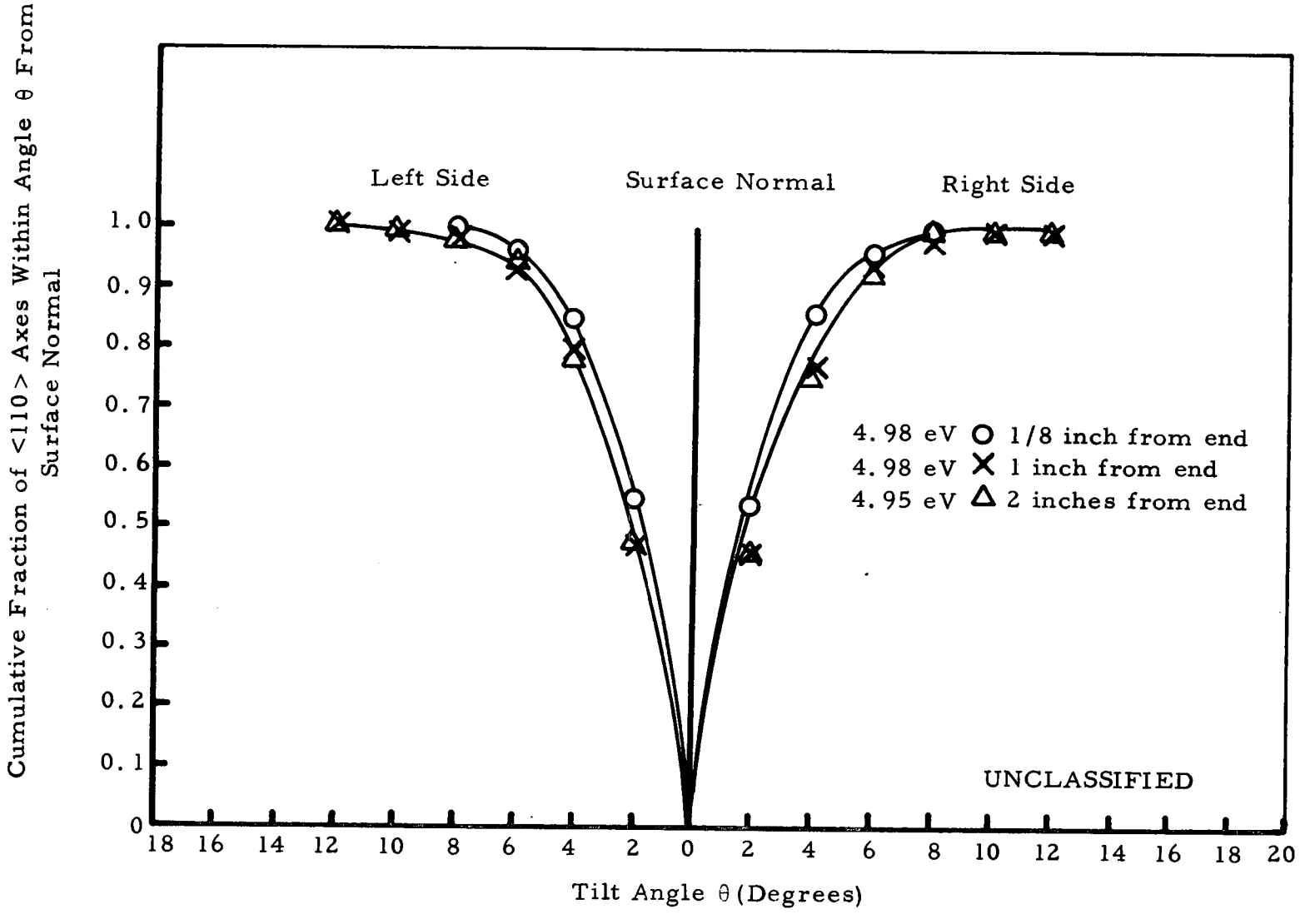

Fig. 83. (U) Distribution of <110> axes in cylindrical duplex tungsten specimen R-13 after 100 hours at 2073°K

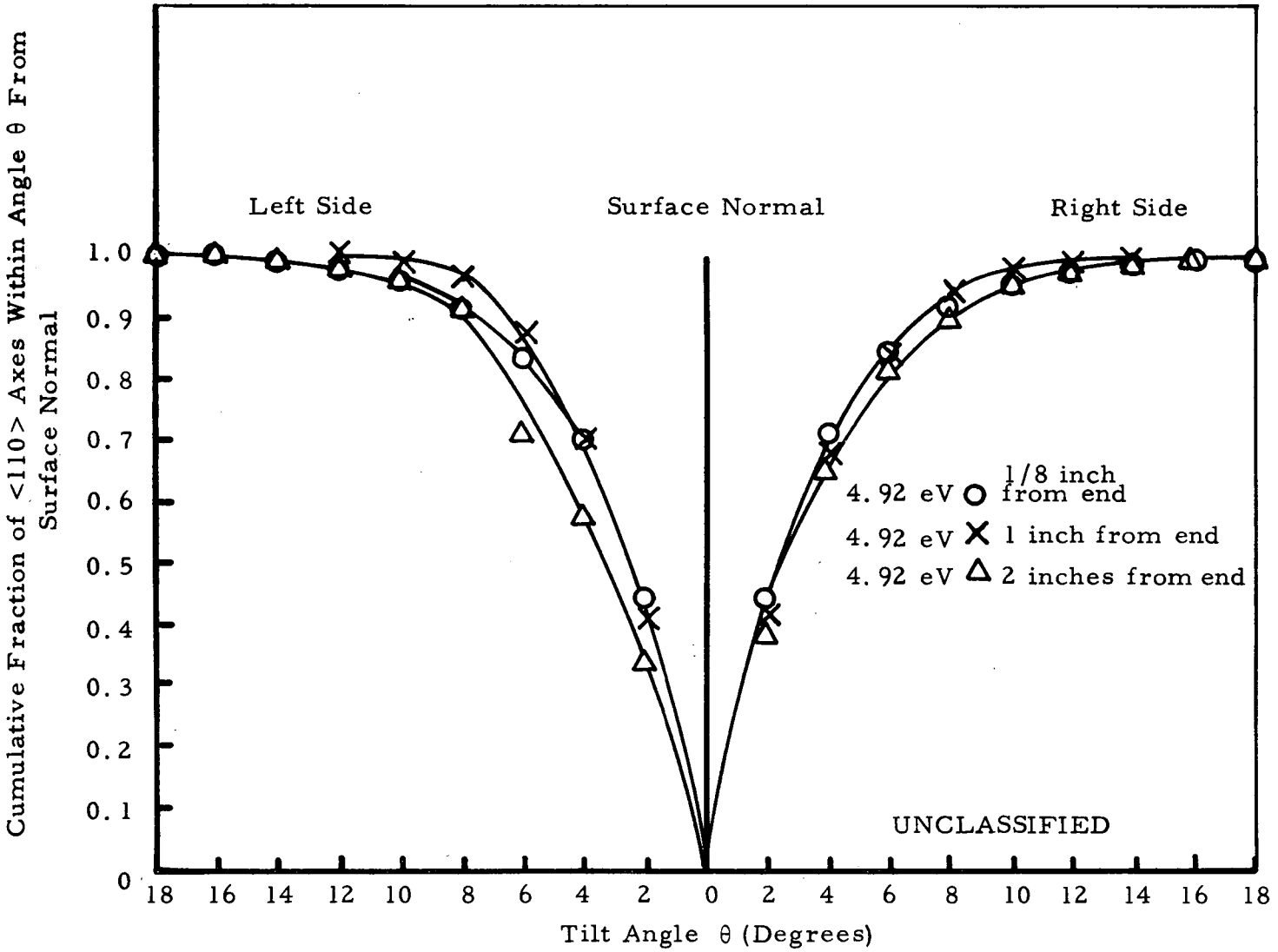

Fig. 84. (U) Distribution of <110> axes in cylindrical duplex tungsten specimen R-16 after 100 hours at 2073°K

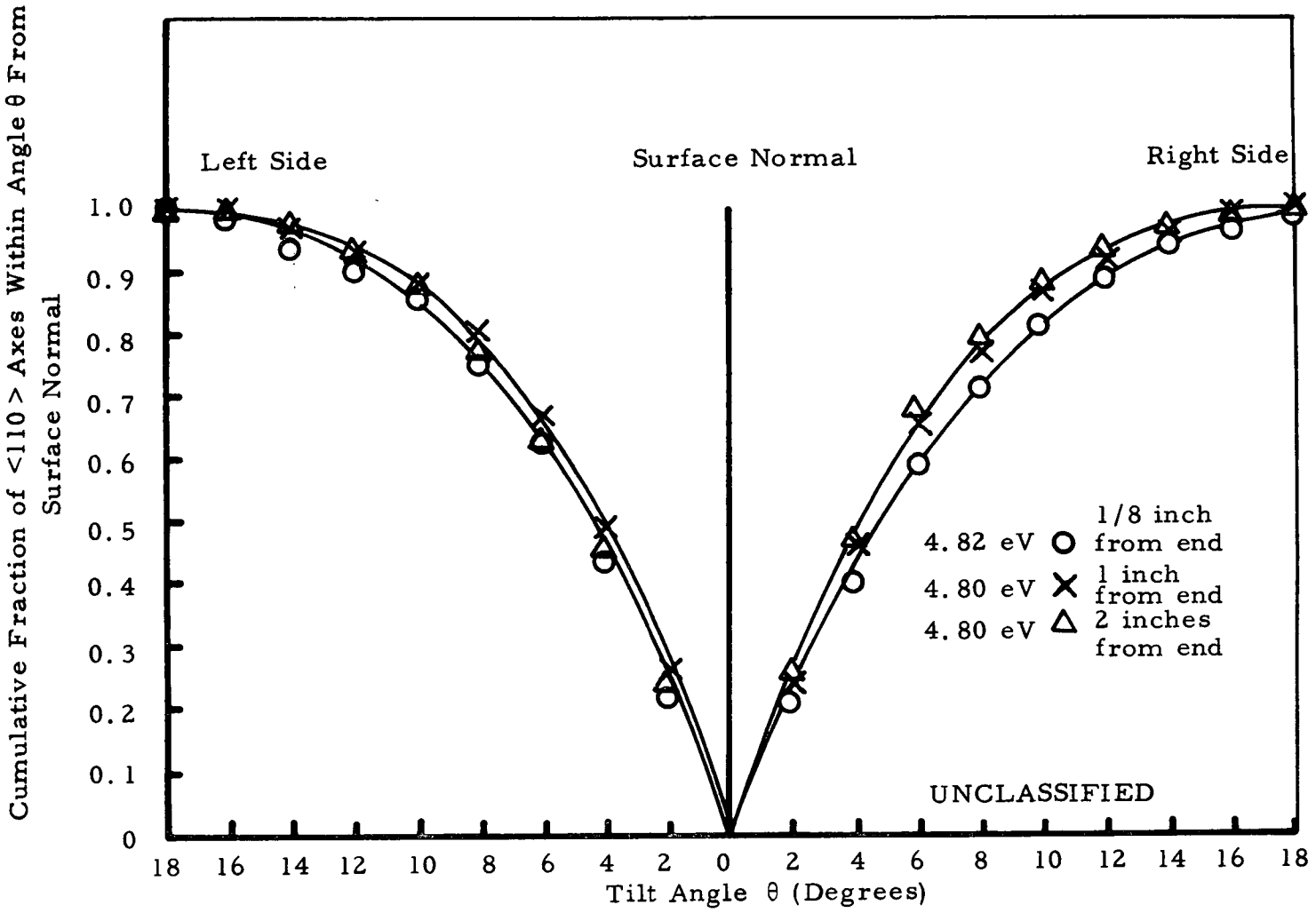

Fig. 85. (U) Distribution of <110> axes in cylindrical duplex tungsten specimen R-20 after 100 hours at 2073°K

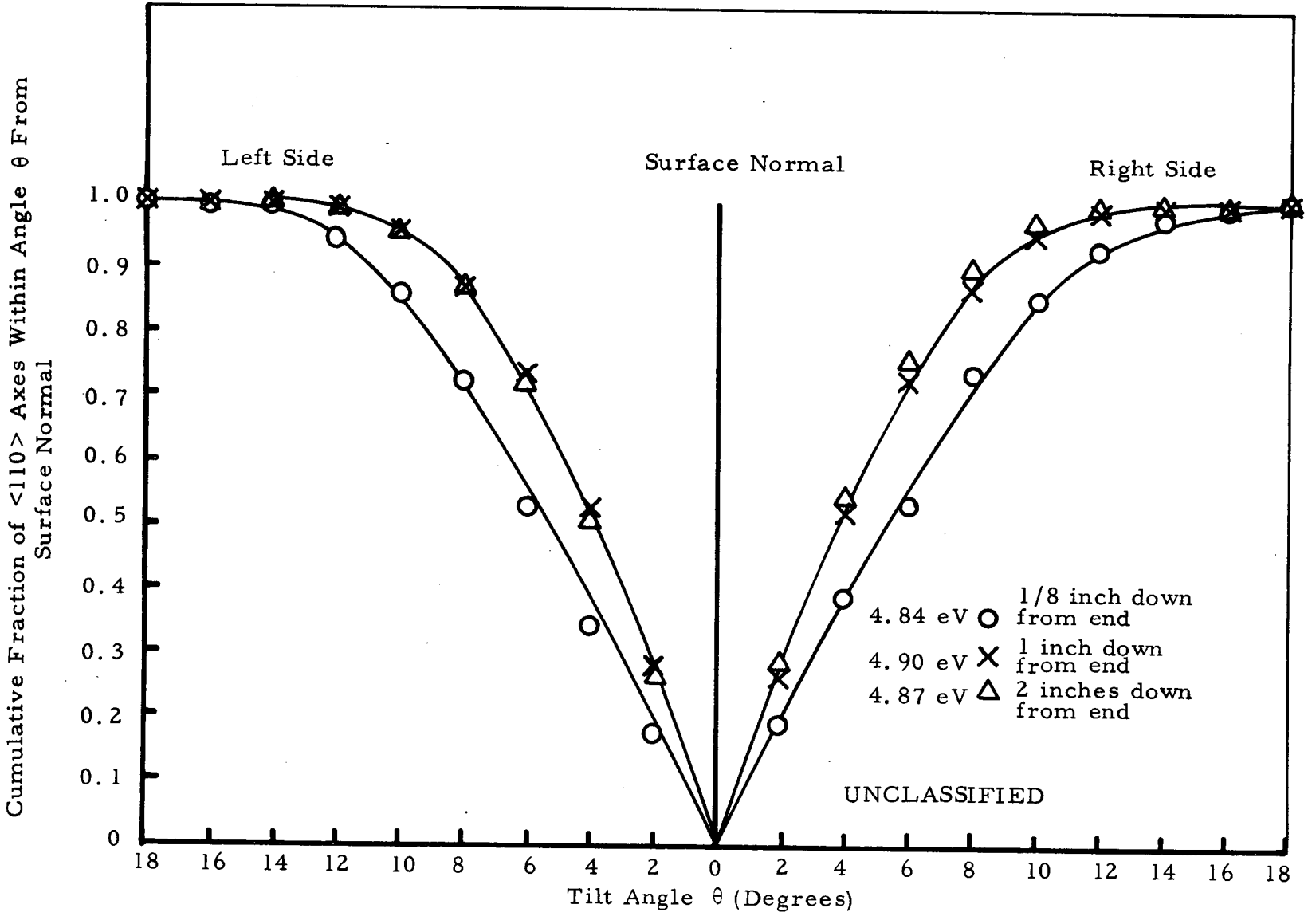

Fig. 86. (U) Distribution of <110> axes in cylindrical duplex tungsten specimen R-23 after 100 hours at 2073°K

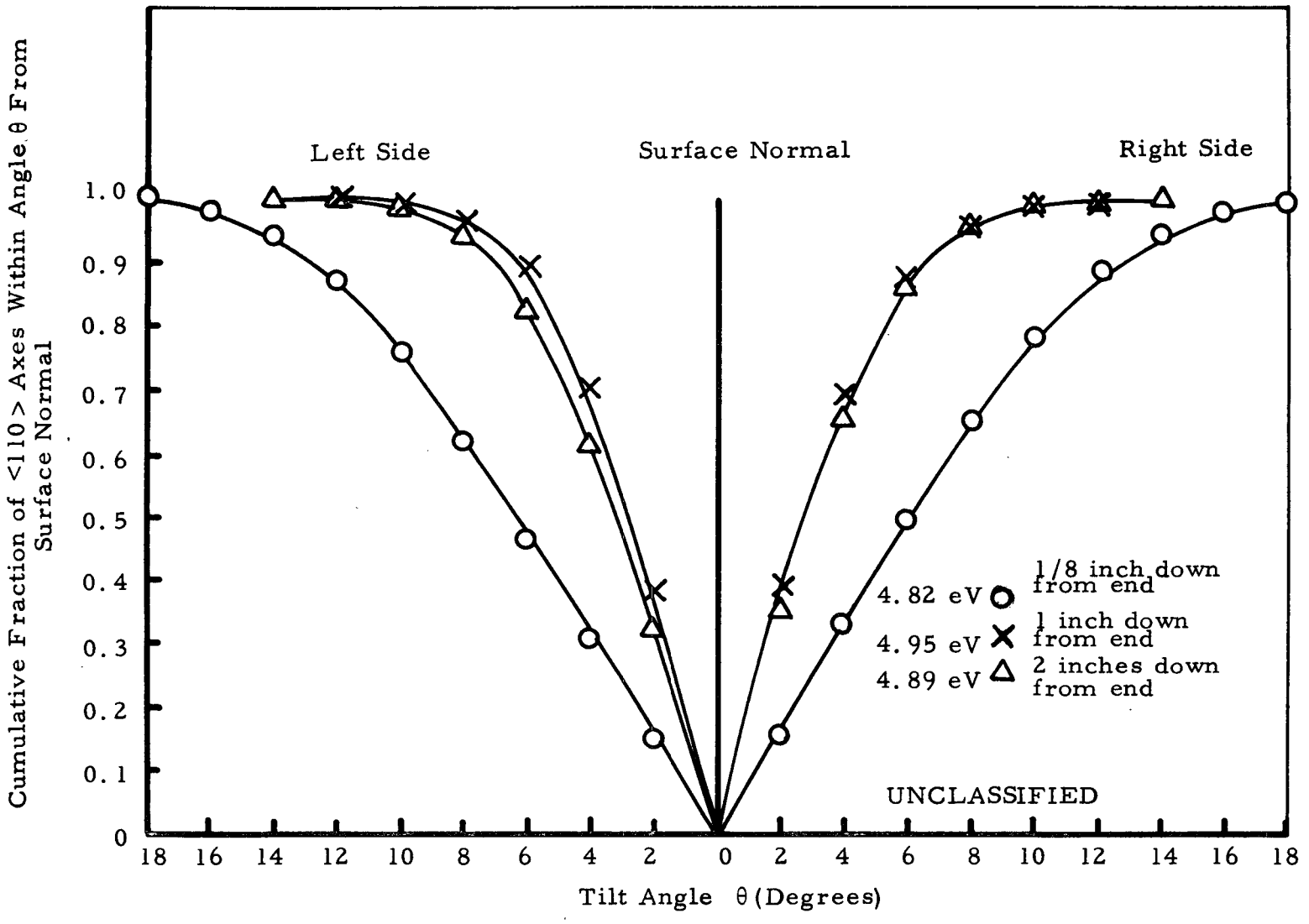

Fig. 87. (U) Distribution of <110> axes in cylindrical duplex tungsten specimen R-26 after 100 hours at 2073°K

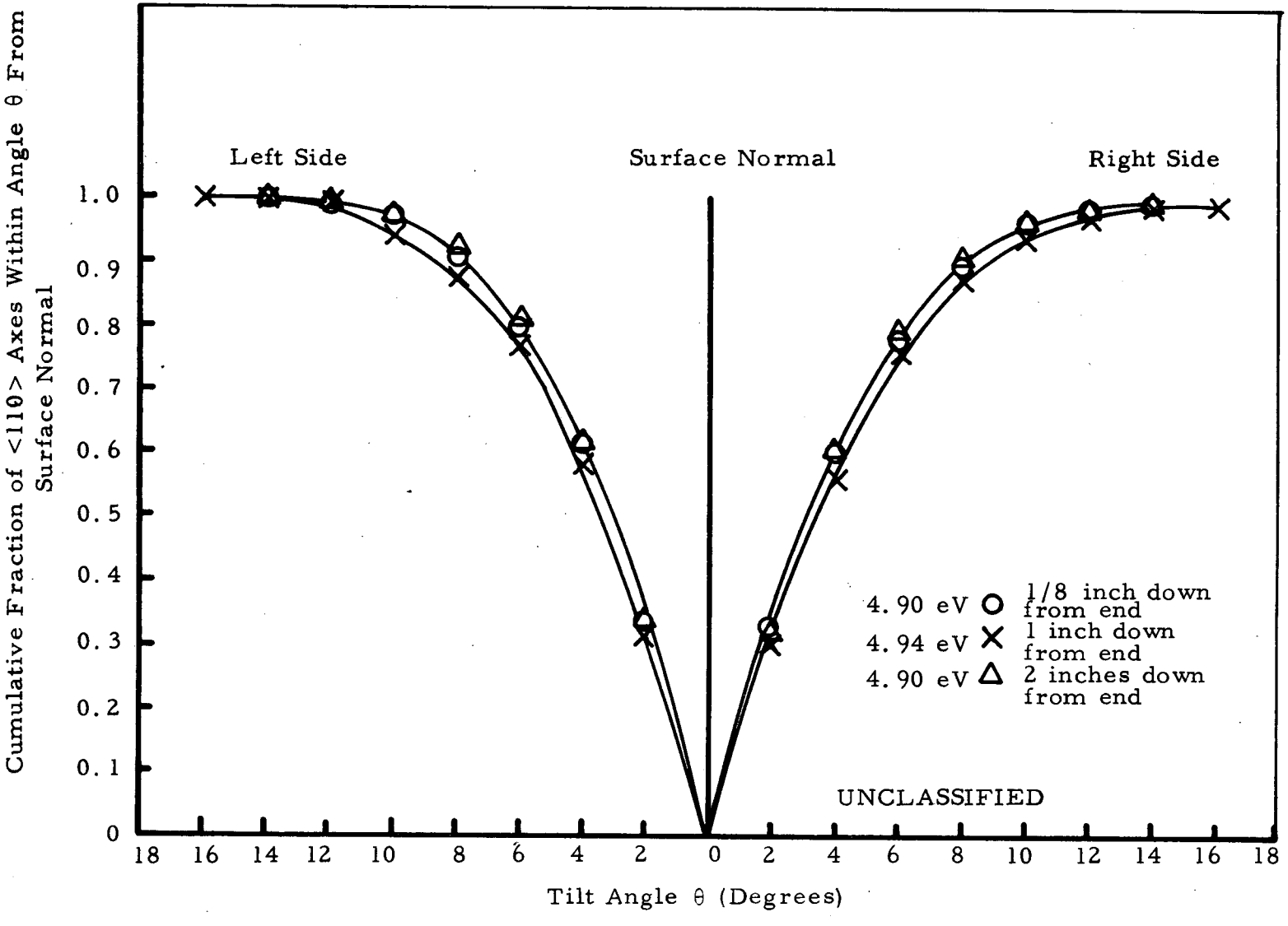

Fig. 88. (U) Distribution of <110> axes in cylindrical duplex tungsten specimen R-30 after 100 hours at 2073°K

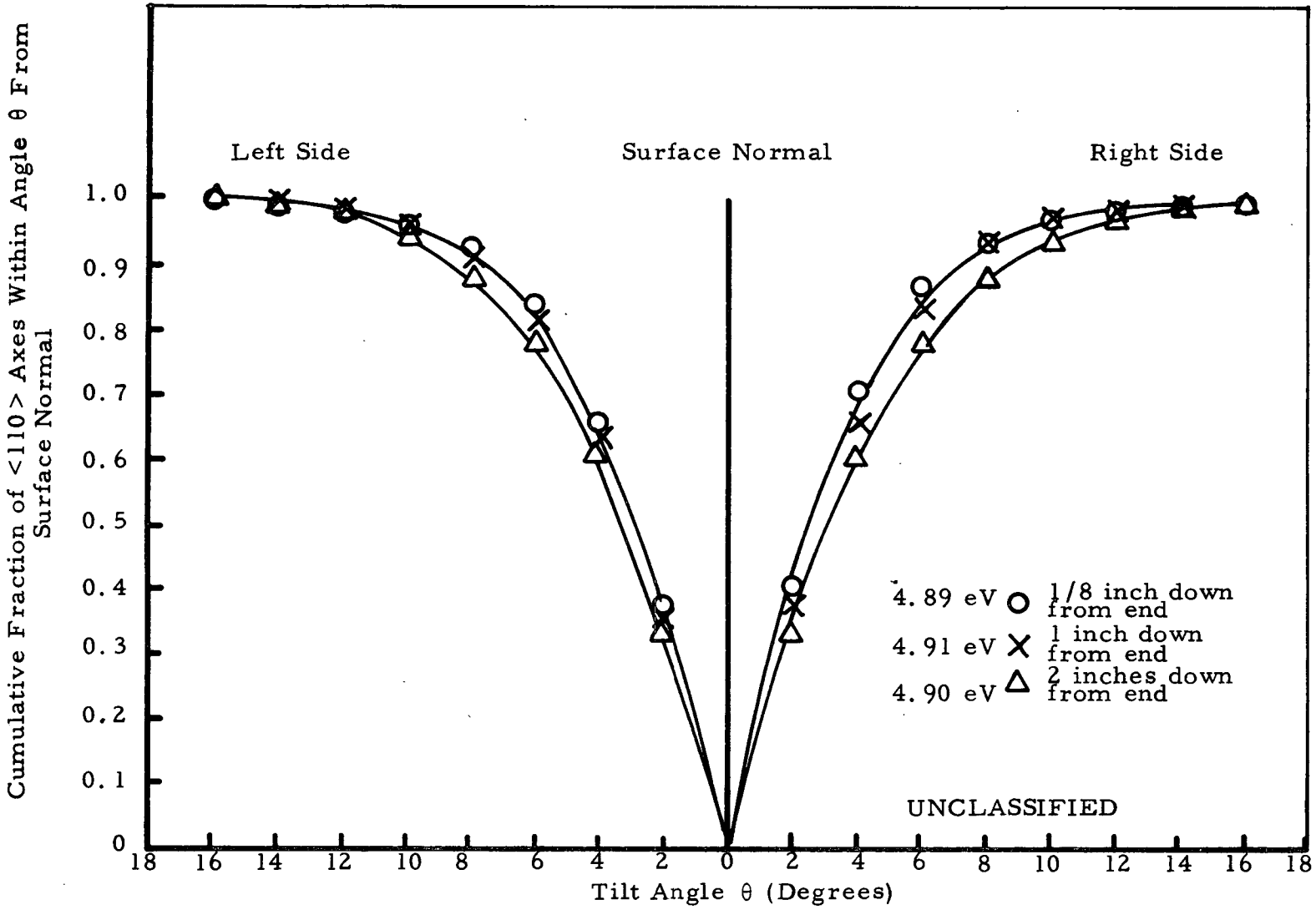

Fig. 89. (U) Distribution of <110> axes in cylindrical duplex tungsten specimen R-27 after 100 hours at 2073°K

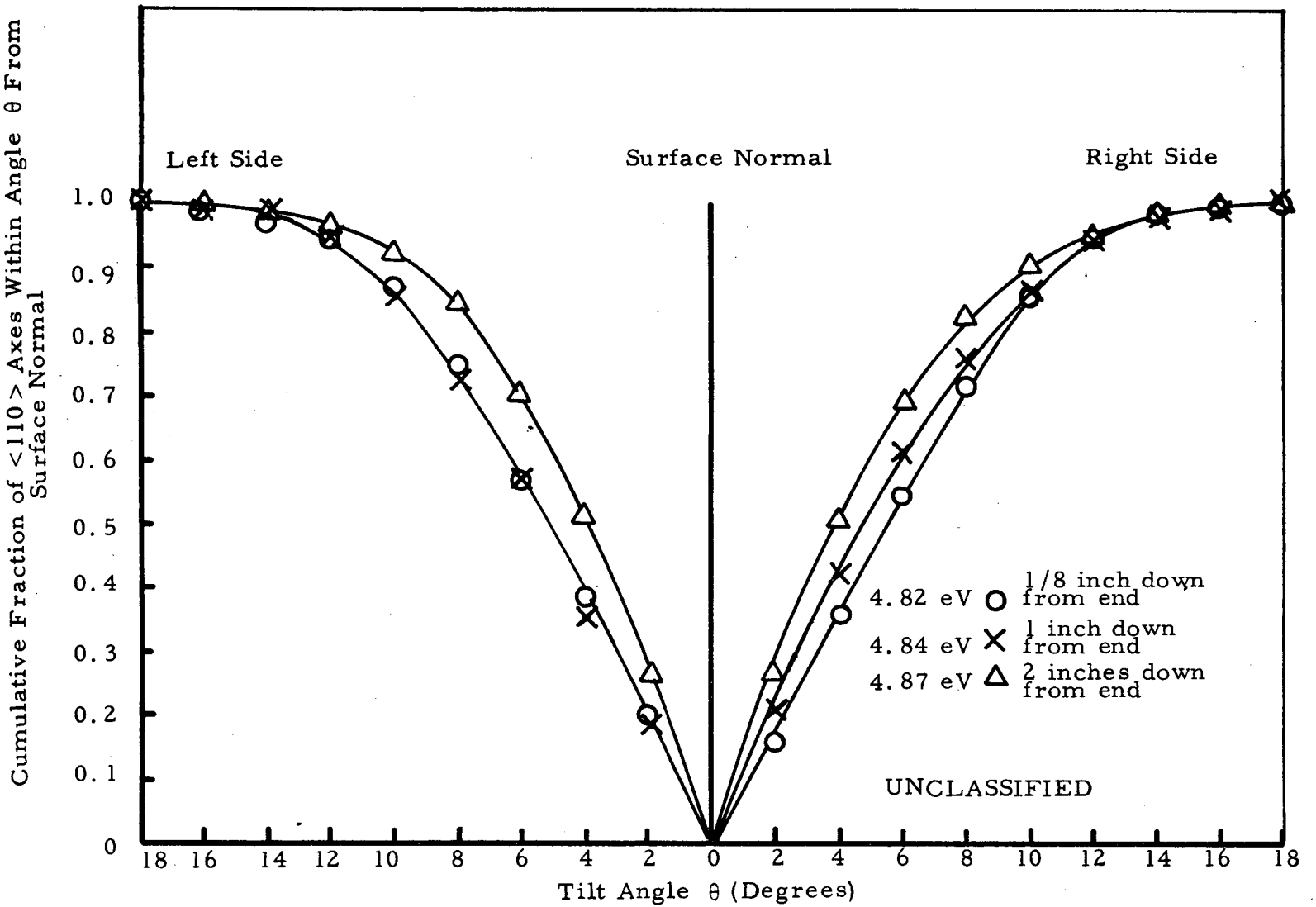

Fig. 90. (U) Distribution of <110> axes in cylindrical duplex tungsten specimen R-34 after 100 hours at 2073°K

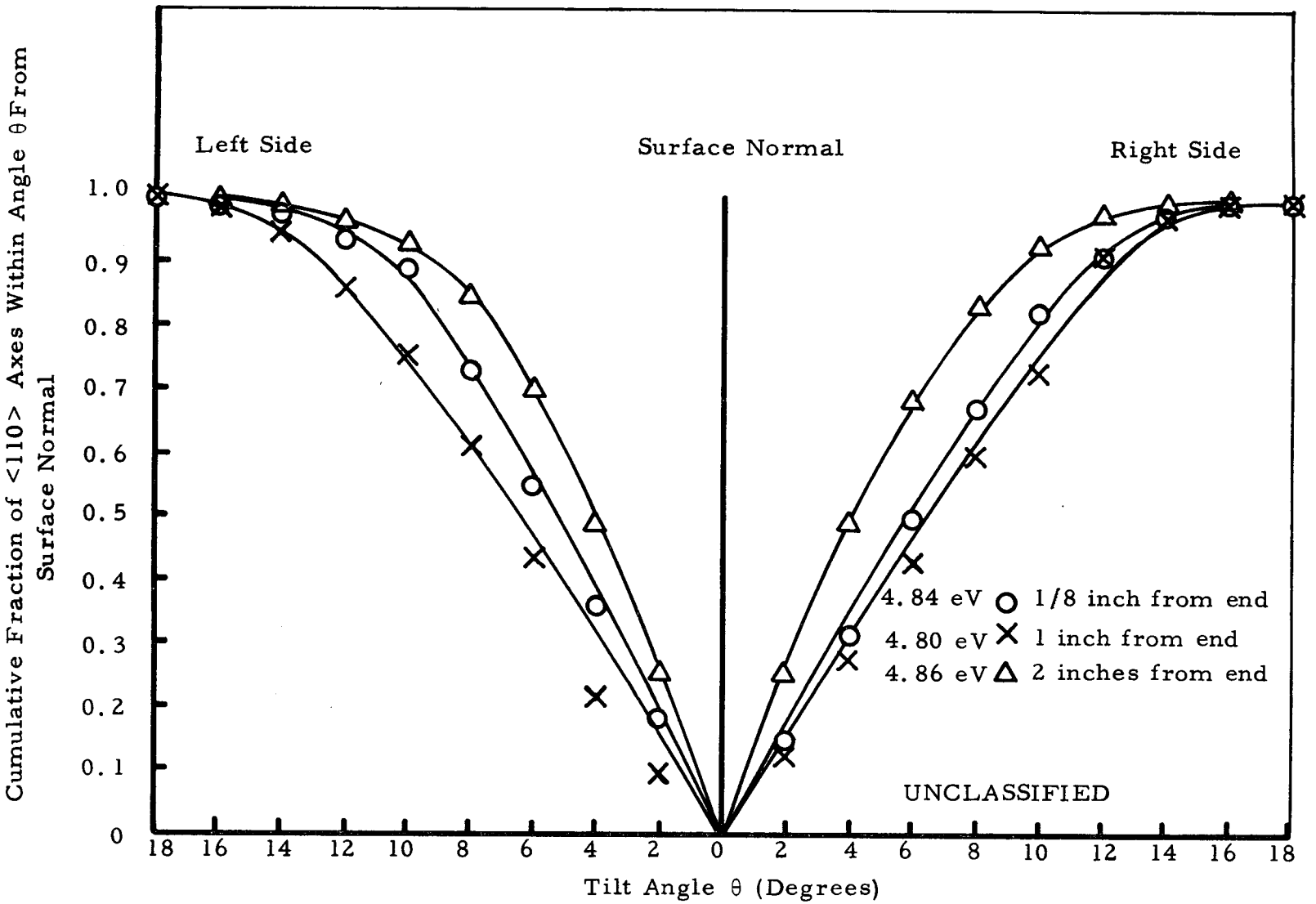

Fig. 91. (U) Distribution of <110> axes in cylindrical duplex tungsten specimen R-37 after 100 hours at 2073°K

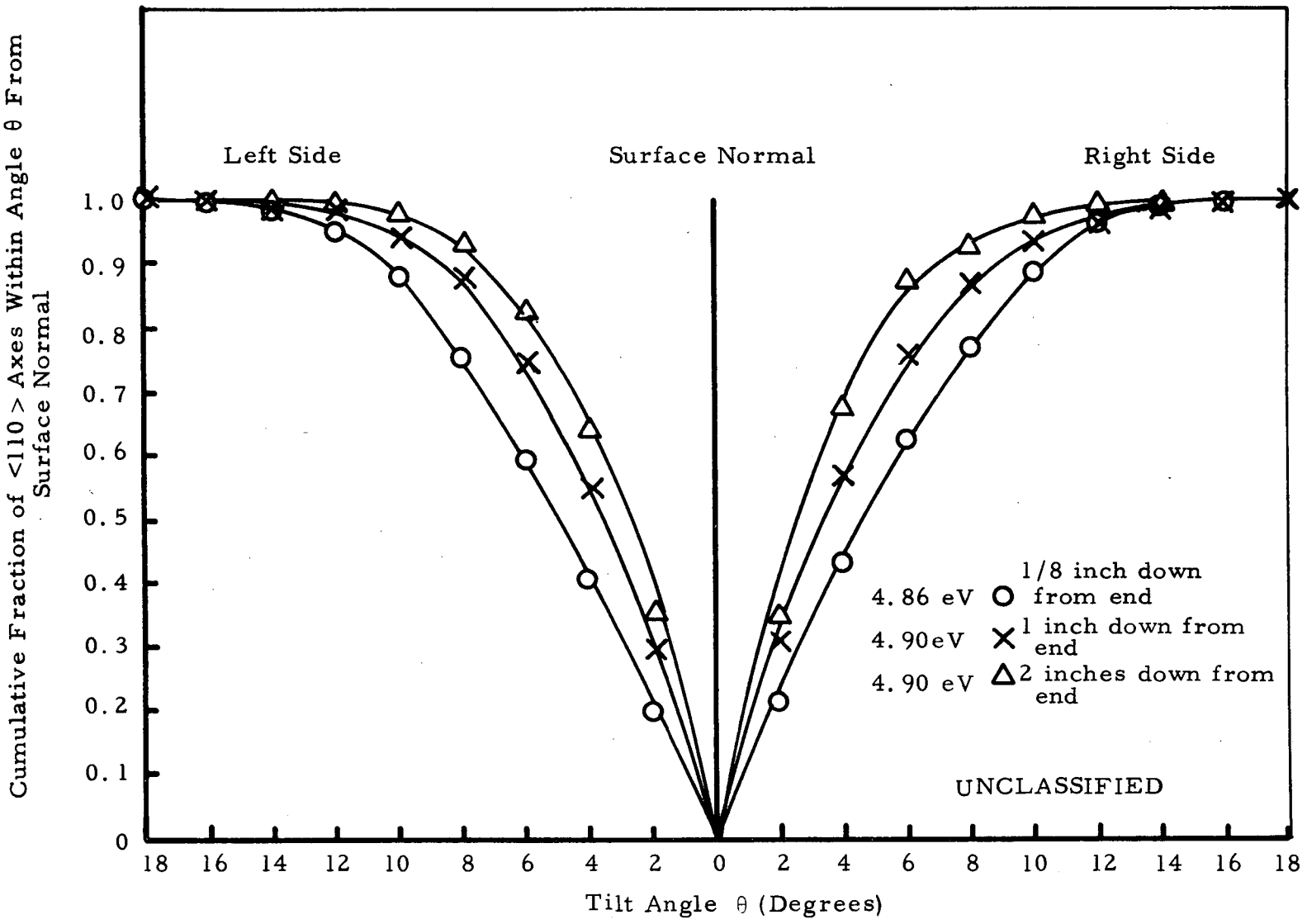

Fig. 92. (U) Distribution of<110> axes in cylindrical duplex tungsten specimen R-39 after 100 hours at 2073°K

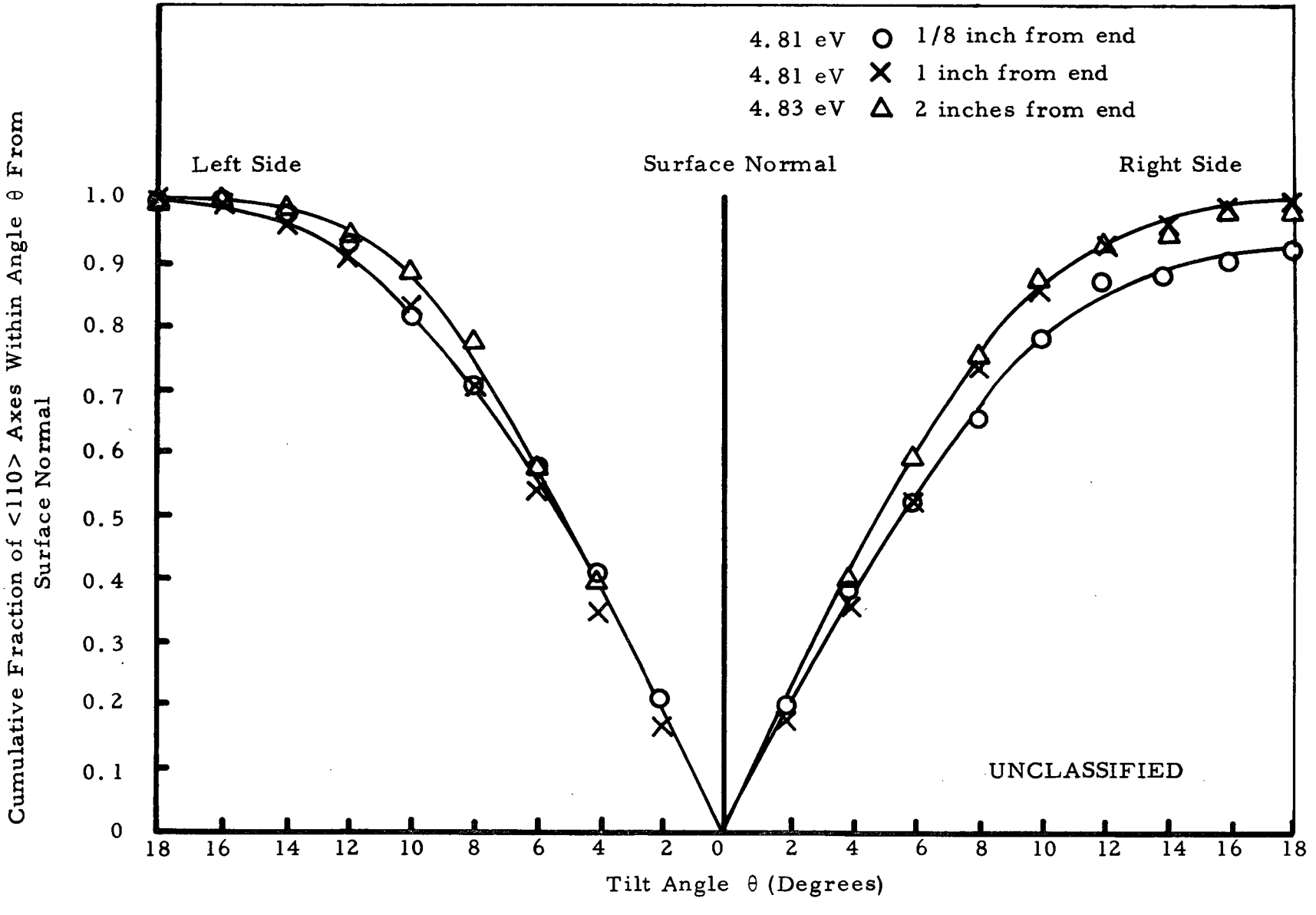

Fig. 93. (U) Distribution of <110> axes in cylindrical duplex tungsten specimen R-42 after 100 hours at 2073°K

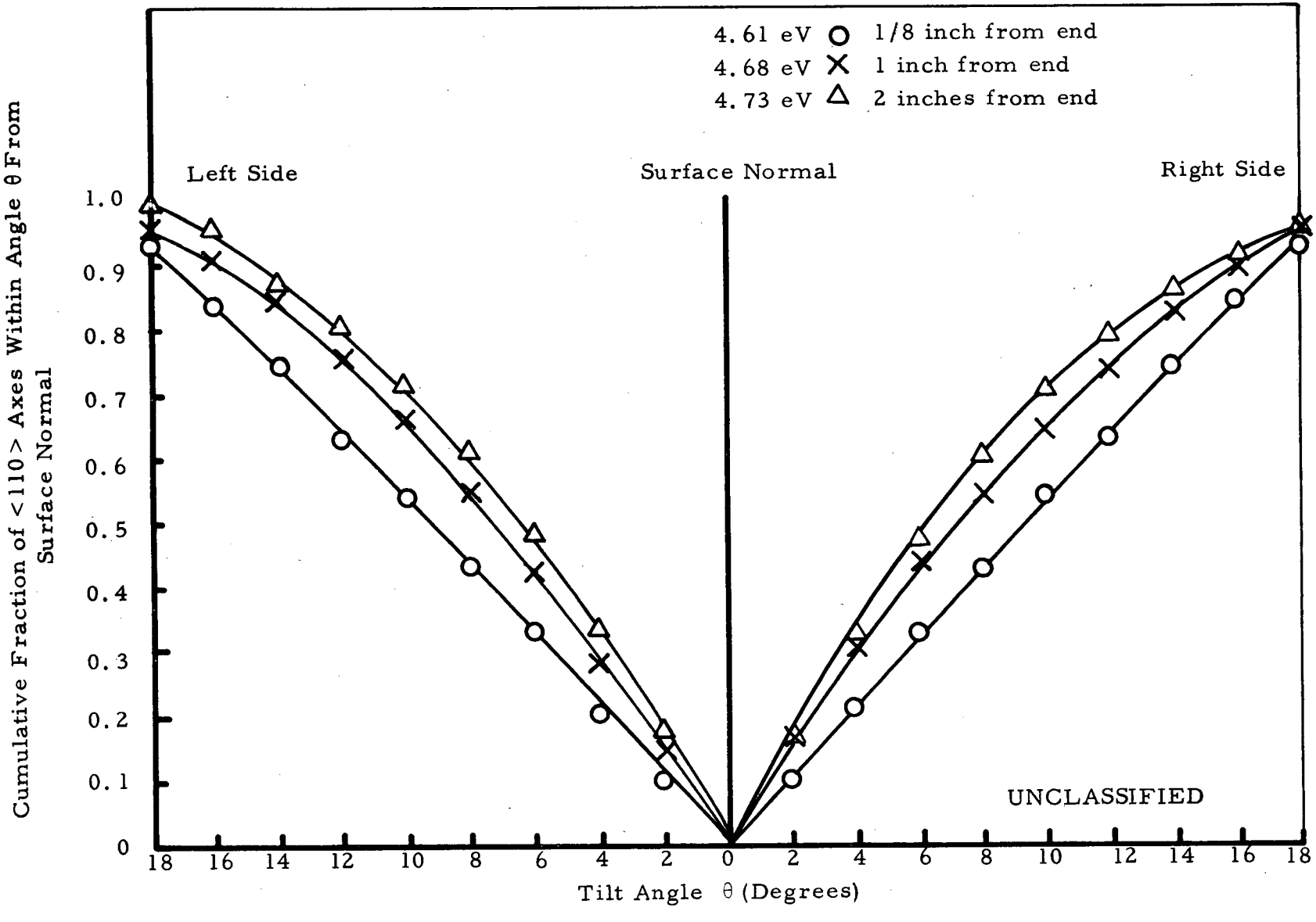

Fig. 94. (U) Distribution of <110> axes in cylindrical duplex tungsten specimen R-46 after 100 hours at 2073°K

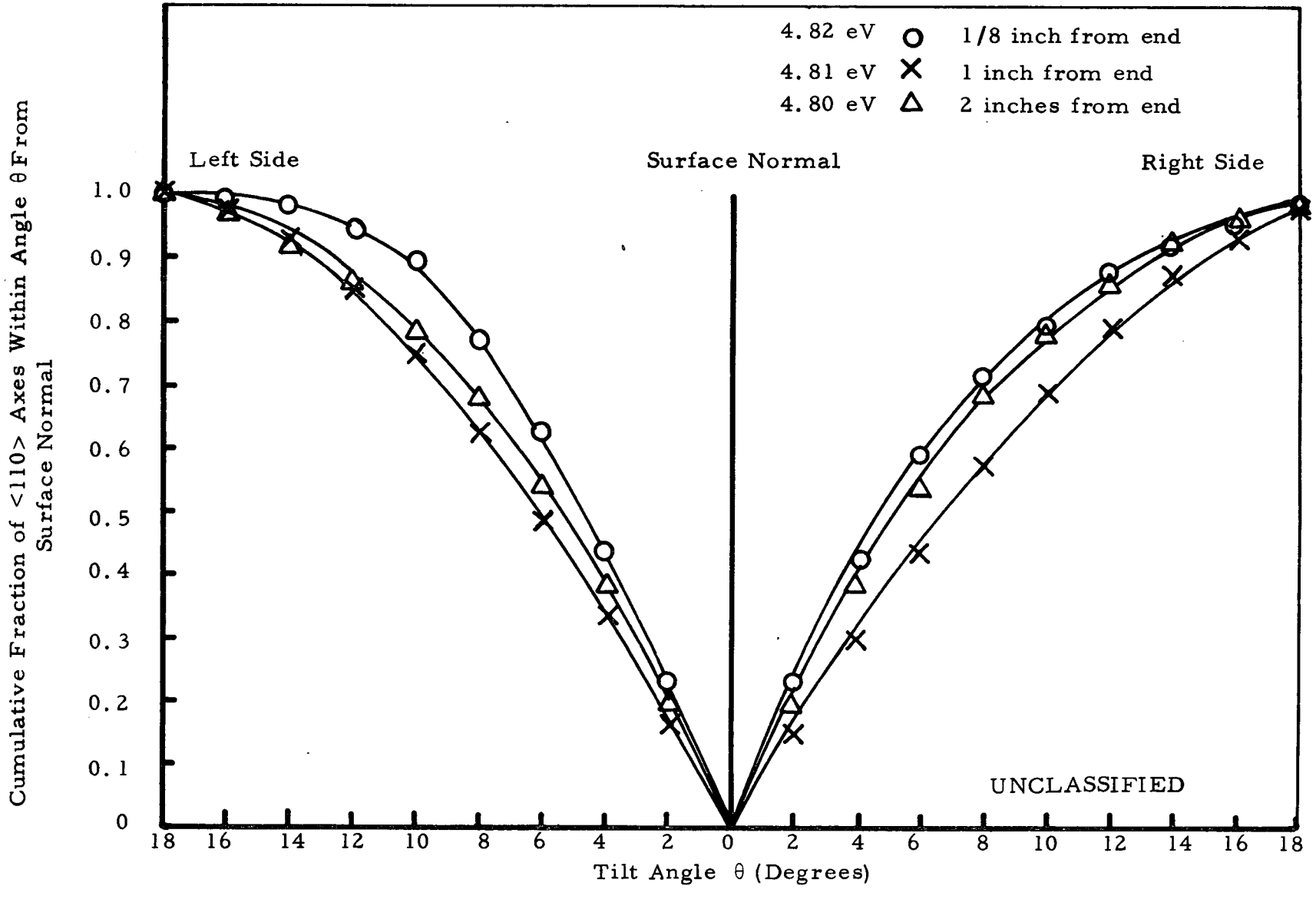

Fig. 95. (U) Distribution of <110> axes in cylindrical duplex tungsten specimen R-50 after 100 hours at 2073°K

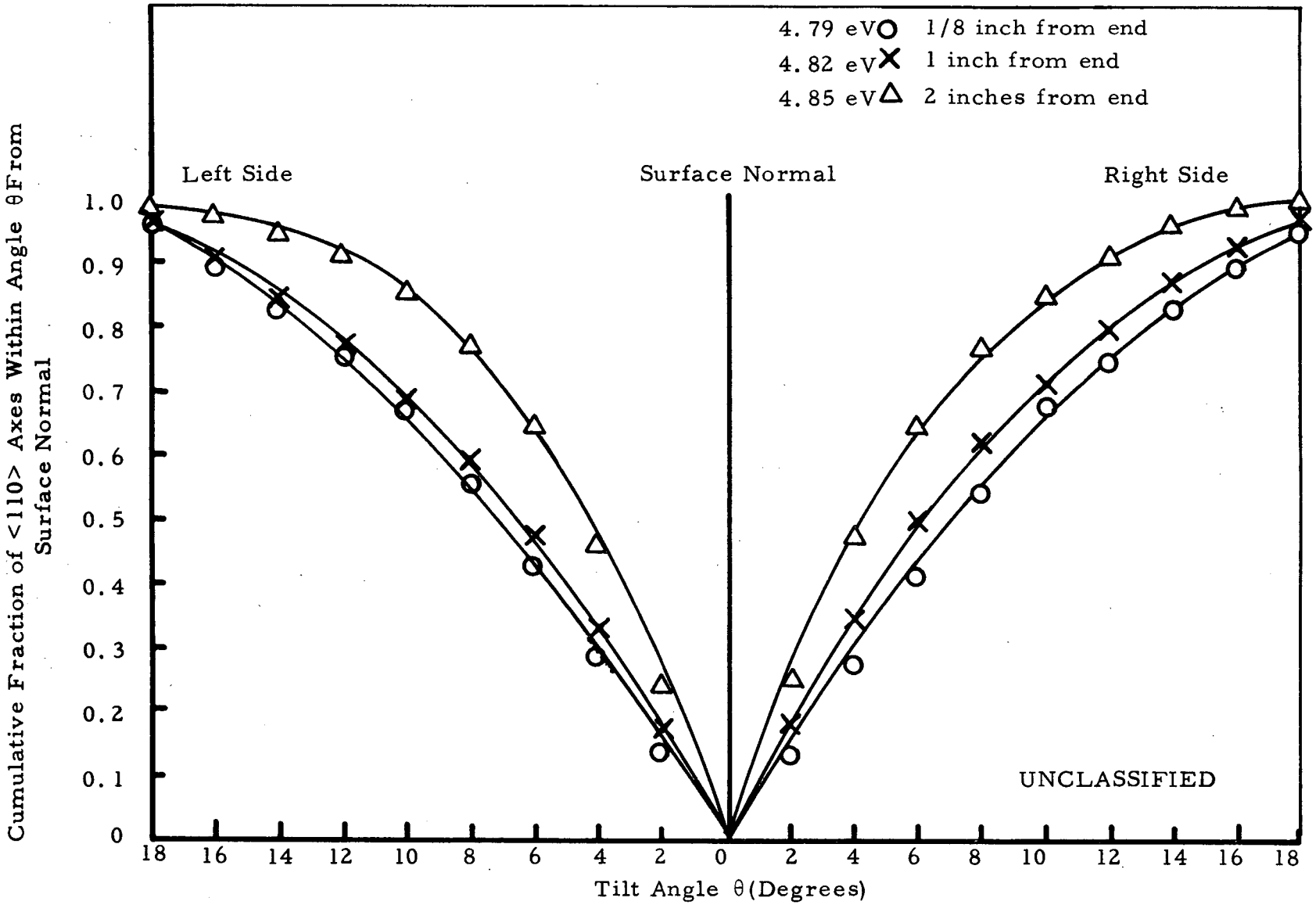

Fig. 96. (U) Distribution of <110> axes in cylindrical duplex tungsten specimen R-52 after 100 hours at 2073°K

(U) Vacuum work function measurements were carried out on each selected specimen at 2073°K in the apparatus described in Section 2.3.1.4 at the same axial locations where the degree of (110) preferred orientation was determined by X-rays. The measurements were continued for a period of 250 hours to insure that the work function had attained a stable value. The results are included in Figs. 83 through 96 and summarized in Table 25. It can be seen that deposits prepared under conditions which deviated not significantly from the reference conditions (e.g. R-13, R-16, R-27, R-30) had vacuum work functions between 4.9 and 5.0 eV over the entire 2 inch emitting length. The use of WCl_5 instead of WCl_6 as the starting material did not affect the vacuum work function significantly (e.g. compare R-39 with R-13, R-16, R-27, and R-30). More serious deviations from the reference conditions, such as the use of H_2/W ratios higher than the stoichiometric value 3.0, the addition of oxygen and nitrogen impurities, the addition of WF_6 and the use of high flow rate of helium diluent, led to vacuum work functions lower than 4.9 eV.

(U) In Table 25, the tilt angle θ for each specimen position, within which 90% of the <110> axes scanned by the X-ray beam are located, is shown in parentheses along with the corresponding vacuum work function value, ϕ. In Fig. 97, θ is plotted versus ϕ to show how the vacuum work function of the deposit varies with the degree of (110) orientation. It can be seen that there seems to be a linear relationship between θ and ϕ in the range of ϕ = 4.8 to 5.0 eV. Such a correlation of ϕ with θ serves as

TABLE 25

(U) VACUUM WORK FUNCTIONS OF SELECTED CYLINDRICAL DUPLEX TUNGSTEN SPECIMENS

(This table is Unclassified)

Specimen Set	Specimen Number	Vacuum Work Function (eV)		
		1/8 Inch From End	1 Inch From End	2 Inches From End
A_1	R-13	4.98 (4.5°)	4.98 (5°)	4.95 (5°)
A_2	R-16	4.92 (6.5°)	4.92 (7.5°)	4.92 (8°)
B_1	R-20	4.82 (11.5°)	4.80 (10.5°)	4.80 (10.5°)
B_2	R-23	4.84 (11°)	4.90 (8°)	4.87 (8°)
B_3	R-26	4.82 (12.5°)	4.95 (6°)	4.89 (6.5°)
C_1	R-27	4.89 (7.5°)	4.91 (7.5°)	4.90 (8.5°)
C_2	R-30	4.90 (8°)	4.94 (8.5°)	4.90 (8°)
D_1	R-34	4.82 (11°)	4.84 (11°)	4.87 (9.5°)
D_2	R-37	4.84 (11.5°)	4.80 (13°)	4.86 (9.5°)
E_1	R-39	4.86 (10.5°)	4.90 (8.5°)	4.90 (7.5°)
F_1	R-42	4.81 (13°)	4.81 (11.5°)	4.83 (11°)
F_2	R-46	4.61 (17.5°)	4.68 (16°)	4.73 (15.5°)
F_3	R-50	4.82 (12°)	4.81 (14°)	4.80 (13°)
G	R-52	4.79 (16°)	4.82 (15.5°)	4.85 (11.5°)

Note: The tilt angle within which 90% of the <110> axes scanned by the X-ray beam are located, is shown in parentheses along with the corresponding vacuum work function for each specimen position studied.

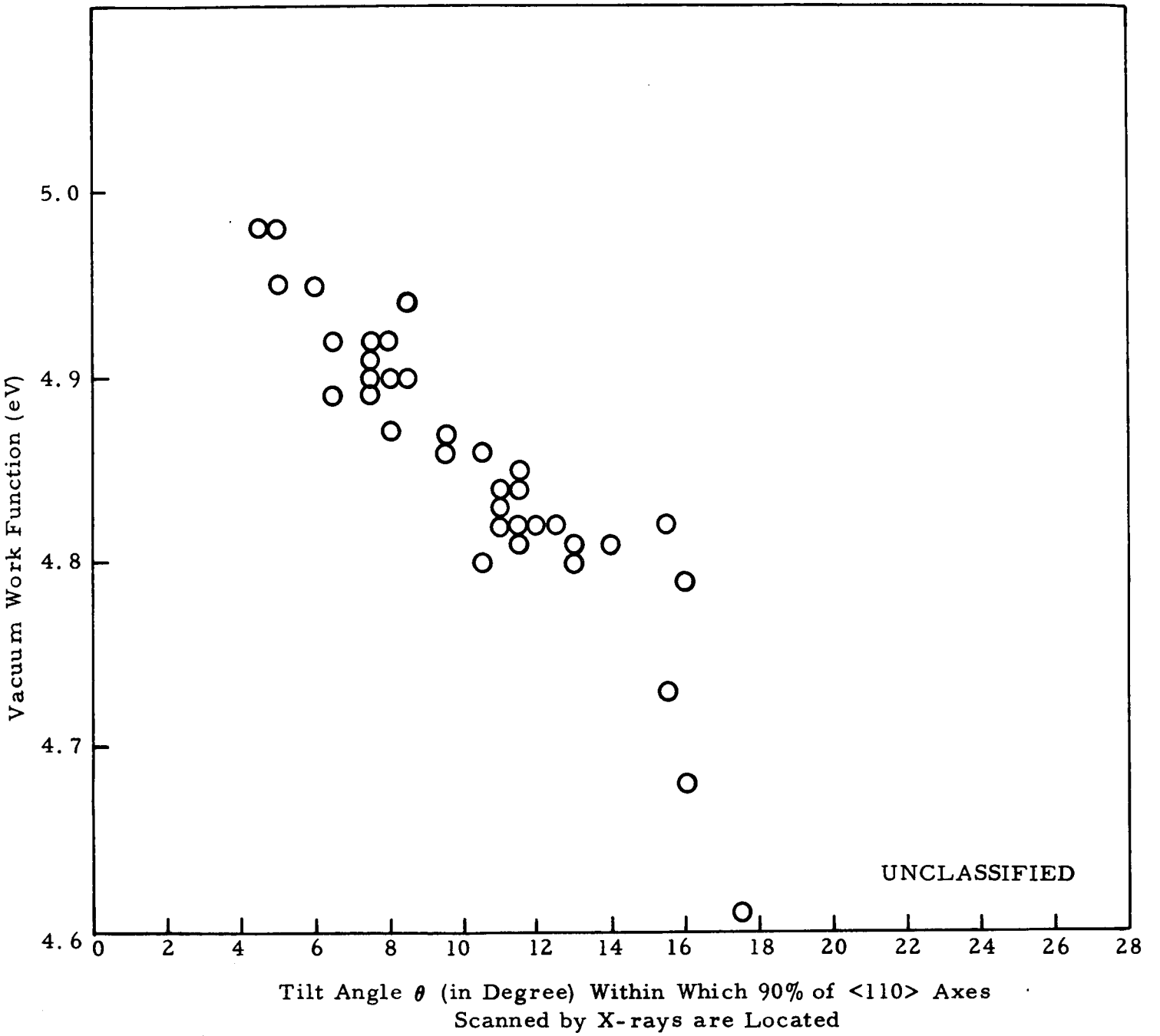

Fig. 97. (U) Vacuum work function as a function of tilt angle within which 90% of the <110> axes scanned by X-rays are located

a useful tool for screening emitters for thermionic fuel element application since it is easier and quicker to determine θ by X-rays than to determine ϕ.

2.3.2.4. Evaluation of Stability of Vacuum Work Function of (110) Oriented Specimens. (U) Specimens R-12 and R-14 of Set A_1, Specimens R-15 and R-17 for Set A_2, and Specimens R-36 and R-38 of Set D_2 were evaluated for the stability of their vacuum work functions at 2073°K. R-12 and R-14 were selected because they were prepared under the reference deposition conditions. R-15 and R-17 were selected because of the high and uniform vacuum work function values along the 2 inch emitting length of R-16 which belonged to the same specimen set as R-15 and R-17. R-36 and R-38 were selected in order to find out whether the presence of oxygen and nitrogen contaminants during deposition would affect the stability of the vacuum work function of the deposit. All these specimens were outgassed in 10^{-6} torr vacuum at 2073°K for 100 hours. Sufficient material was taken from each outgassed specimen for the analysis of its impurity contents and the determination of its microstructures. The vacuum work functions of these specimens were then measured every 50 hours at three different axial locations at 2073°K for a period of 500 hours. At the completion of the work function measurements, each specimen was leak checked and again analysed for its impurity contents and studied for its microstructures. The degree of (110) orientation was determined by X-rays at the axial locations where the vacuum work function was measured, and the surface morphology was studied by electron microscopy.

(U) Table 26 lists the pre-test and the post-test impurity contents of these specimens. By comparing the data shown in Table 26 and the impurity contents of the as-deposited specimens shown in the preceeding section, it can be seen that no significant changes occurred in the impurity contents of the Set A_1 and Set A_2 specimens by either the 100 hour outgassing operation at 2073°K or the 500 additional hours at 2073°K during the vacuum work function measurement, presumably because the as-deposited material was already of a high degree of purity. For the Set D_2 specimens prepared in the presence of oxygen and nitrogen contaminants, the nitrogen contents were reduced to very low levels (< 1 ppm) after a total of 600 hours at 2073°K but the oxygen contents were still slightly higher than that of other specimens after similar heat treatment. This is consistent with the fact that tungsten has a very low affinity and solubility for nitrogen.

(U) Figures 98(a) through (l) compare the pre-test and post-test microstructures of the test specimens. Good bond existed between the chloride tungsten and the fluoride tungsten substrate in each case both before and after the vacuum work function study. Compared with the as-deposited specimen of the same set, the fluoride tungsten substrate showed very little grain growth, while considerable grain growth occurred in the chloride tungsten layer. Most of the growth, however, seems to occur during the first 100 hour heat treatment at 2073°K. Leak check with a helium mass-spectrometer leak detector of 10^{-10} STP c.c./sec. failed to reveal any leak through each specimen.

TABLE 26

(U) COMPARISON OF PRE-TEST* AND POST-TEST** IMPURITY CONTENTS (IN PPM) OF SPECIMENS STUDIED FOR VACUUM WORK FUNCTION STABILITY

(This table is Unclassified)

	Specimen Designation											
	Set A_1				Set A_2				Set D_2			
	R-12		R-14		R-15		R-17		R-36		R-38	
Impurities	Pre-test	Post-test	Pre-test	Post-test	Pre-test	Post-test	Pre-test	Post-test	Pre-test	Post-test	Pre-test	Post-test
Non-Metallics												
C	10	8	8	7	7.5	6	8	7.5	6	5.5	7	6
O	4	3	3.7	2.8	6.0	4.8	6	4	9.8	9.0	10.0	9.0
N	<1	<1	<1	<1	<1	<1	<1	<1	9	<1	5	<1
F	<3	<3	<2	<2	<1	<1	3	<3	4	4	4	4
Cl	8	5	7	5	7.5	6.2	7	6	11	9	10	10
Metallics												
Si	<1.0	<1.0	1.2	<1.0	2.0	1.5	1.0	<1.0	2.0	1.5	2.0	1.0
Mg	0.5	<0.02	0.02	<0.02	1.0	1.0	1.0	0.6	0.5	0.2	1.0	0.4
Ni	1.0	<0.3	0.5	<0.3	7.0	5.4	8.5	6.8	0.4	<0.3	0.4	<0.3
Fe	<4.0	<4.0	4.5	<4.0	6.1	5.1	6.5	5.8	<4.0	<4.0	4.3	<4.0
Cu	<0.3	<0.3	<0.3	<0.3	3.0	3.0	4.2	3.1	0.6	0.4	0.5	0.4
Al	0.5	<0.3	<0.3	<0.3	<0.3	<0.3	<0.3	<0.3	0.5	<0.3	0.5	<0.3
Mn	<0.1	<0.1	<0.1	<0.1	<0.1	<0.1	<0.1	<0.1	<0.1	<0.1	<0.1	<0.1

*After 100 hours at 2073°K

**After additional 500 hours at 2073°K

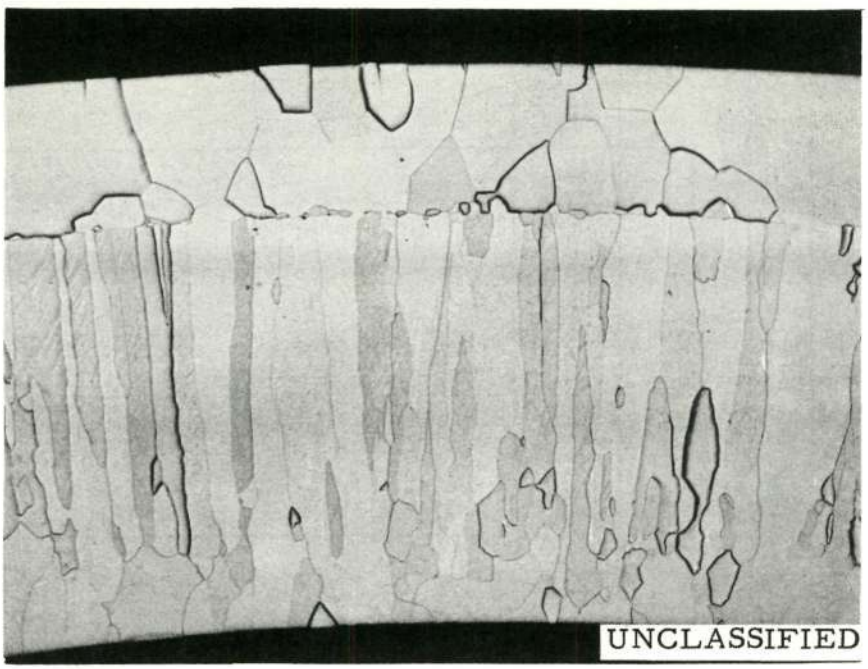

M 31970-4 75X

(a) R-12, pre-test

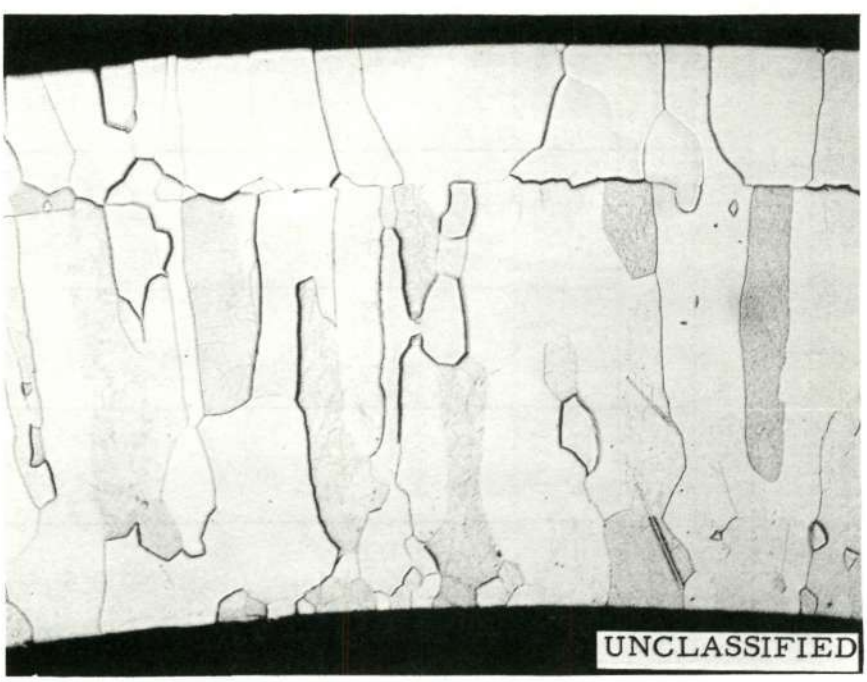

M 34217-2 75X

(b) R-12, post-test

Fig. 98. (U) Comparison of pre-test and post-test microstructures of specimens used for the study of vacuum work function study at 2073°K. Pre-test = 100 hours at 2073°K. Post-test = 600 hours at 2073°K (Sheet 1 of 6)

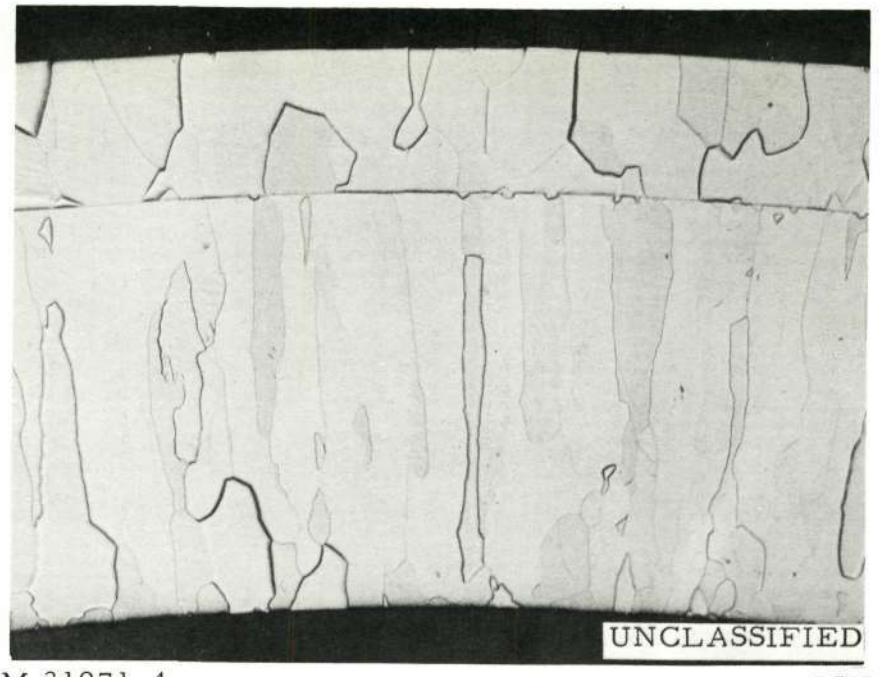

M 31971-4 75X

(c) R-14, pre-test

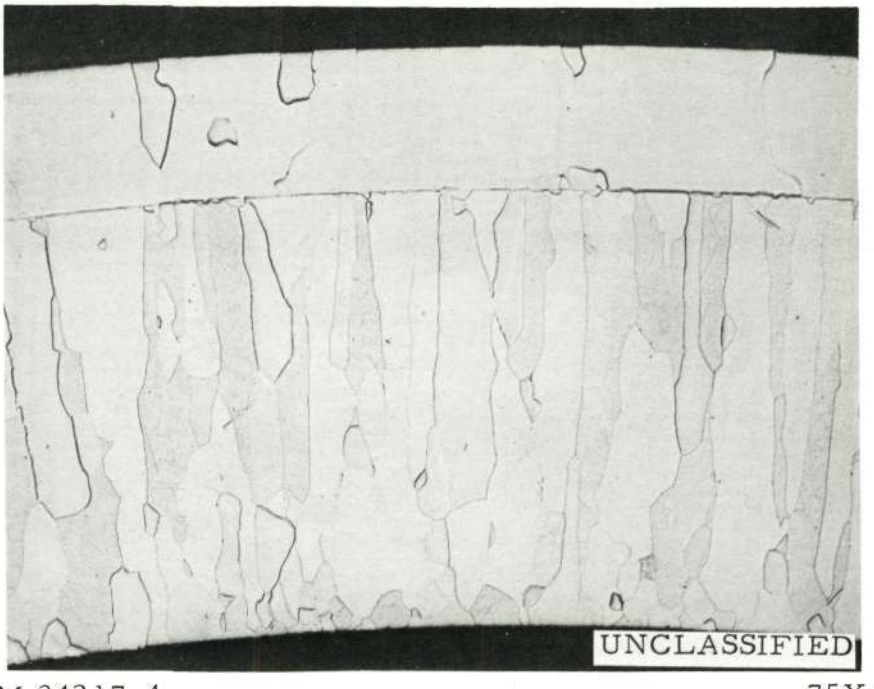

M 34217-4 75X

(d) R-14, post-test

Fig. 98. (U) Comparison of pre-test and post-test microstructures of specimens used for the study of vacuum work function study at 2073°K. Pre-test = 100 hours at 2073°K. Post-test = 600 hours at 2073°K (Sheet 2 of 6)

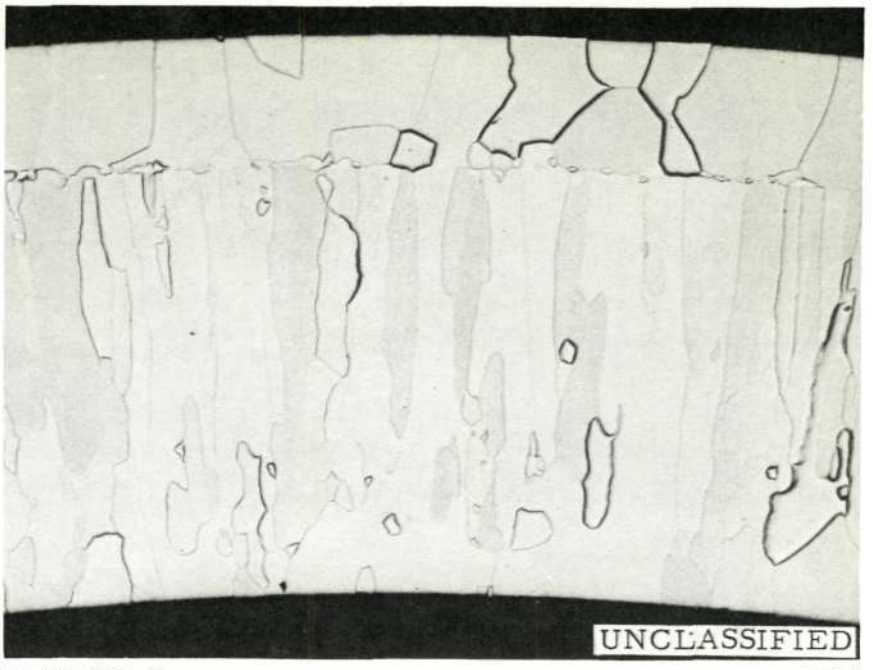

M 31970-2 75X

(e) R-15, pre-test

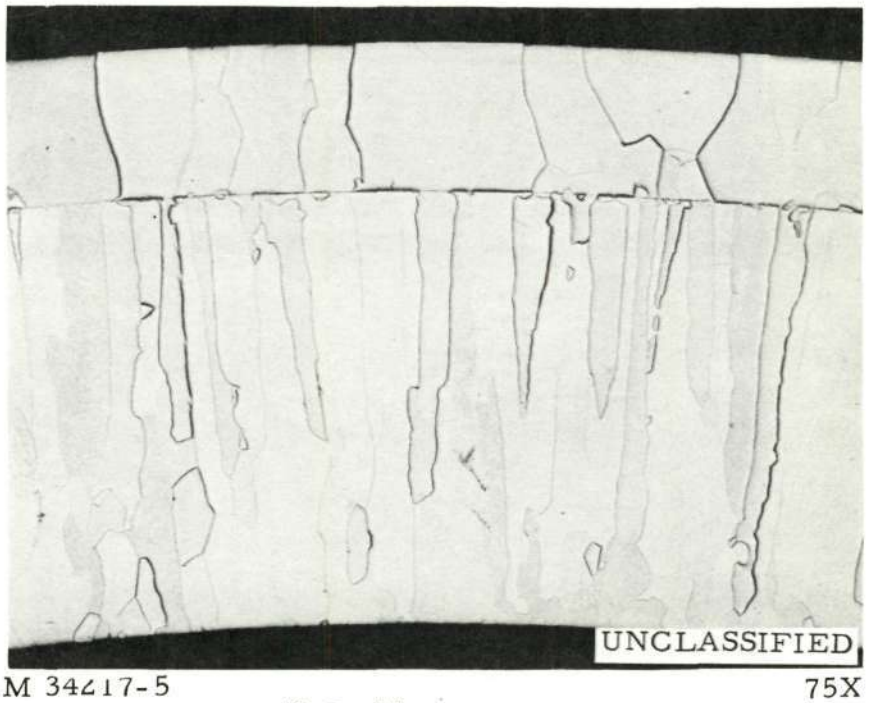

M 34217-5 75X

(f) R-15, post-test

Fig. 98. (U) Comparison of pre-test and post-test microstructures of specimens used for the study of vacuum work function study at 2073°K. Pre-test = 100 hours at 2073°K. Post-test = 600 hours at 2073°K (Sheet 3 of 6)

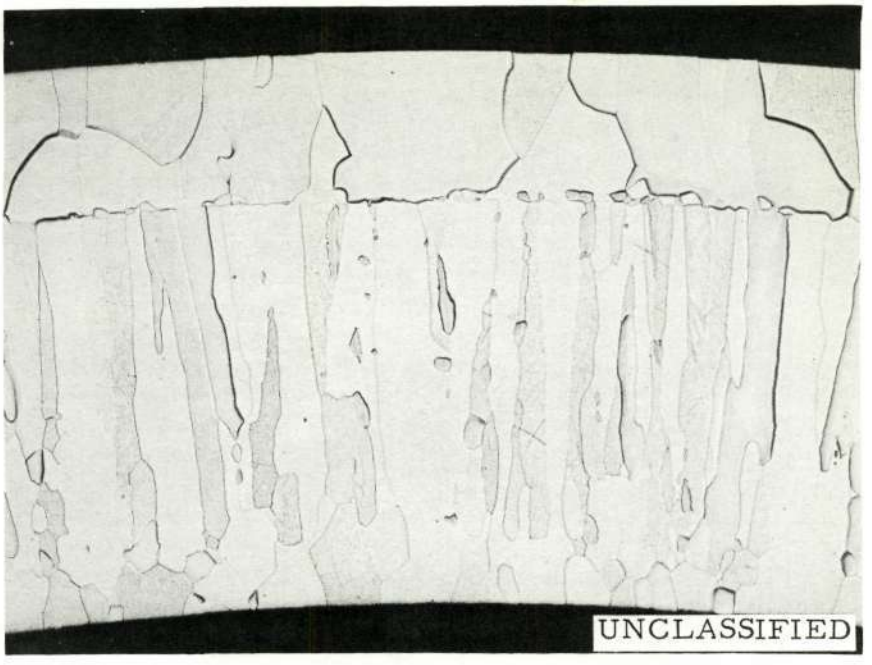

M 31970-6 75X

(g) R-17, pre-test

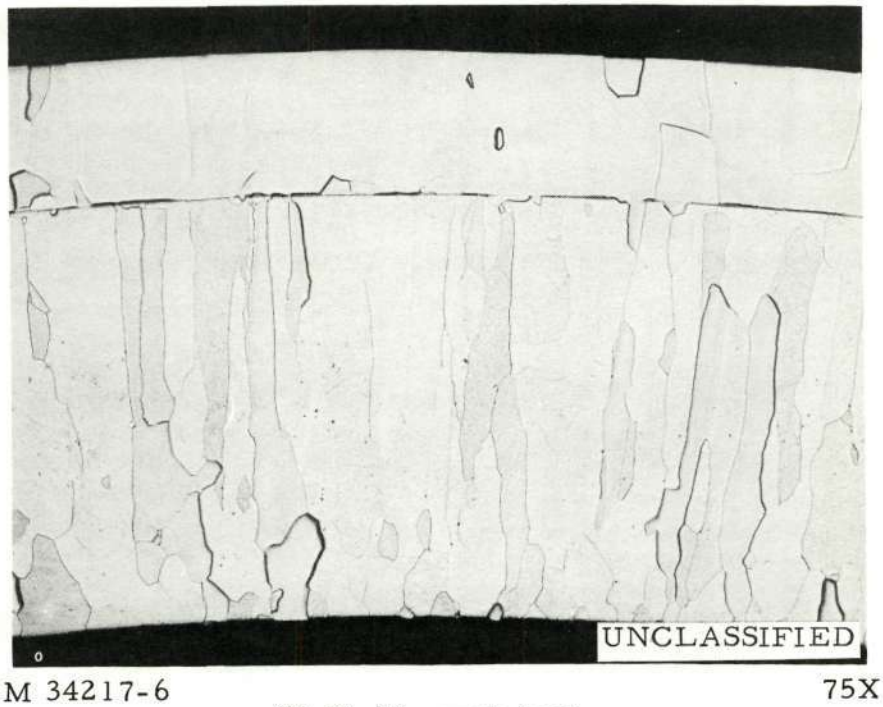

M 34217-6 75X

(h) R-17, post-test

Fig. 98. (U) Comparison of pre-test and post-test microstructures of specimens used for the study of vacuum work function study at 2073°K. Pre-test = 100 hours at 2073°K. Post-test = 600 hours at 2073°K (Sheet 4 of 6)

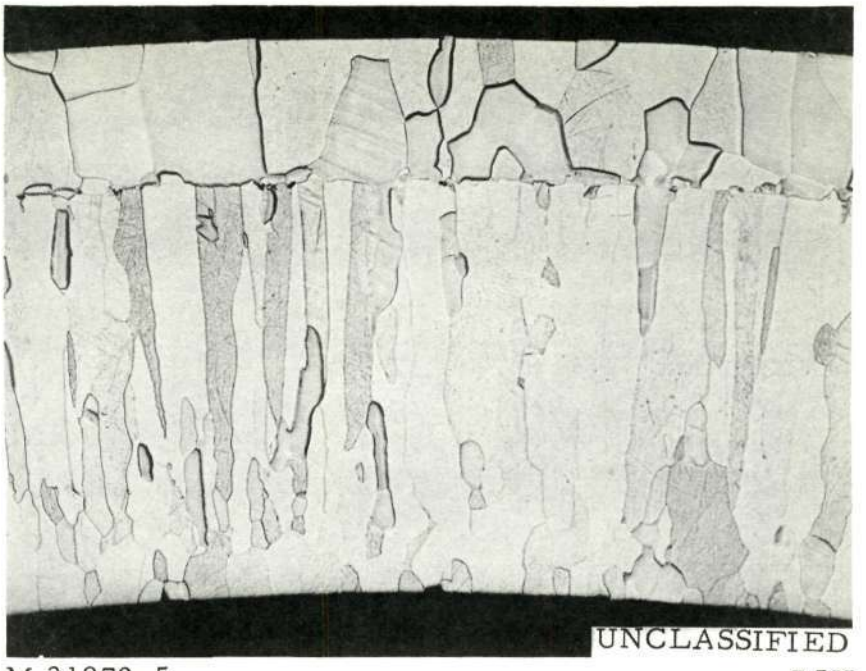

M 31970-5 75X

(i) R-36, pre-test

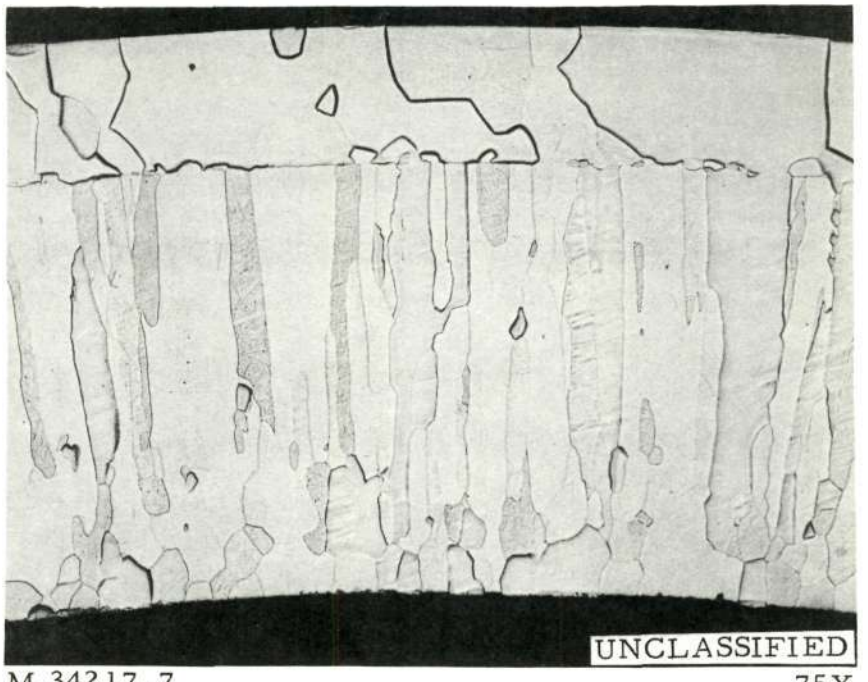

M 34217-7 75X

(j) R-36, post-test

Fig. 98. (U) Comparison of pre-test and post-test microstructures of specimens used for the study of vacuum work function study at 2073°K. Pre-test = 100 hours at 2073°K. Post-test = 600 hours at 2073°K (Sheet 5 of 6)

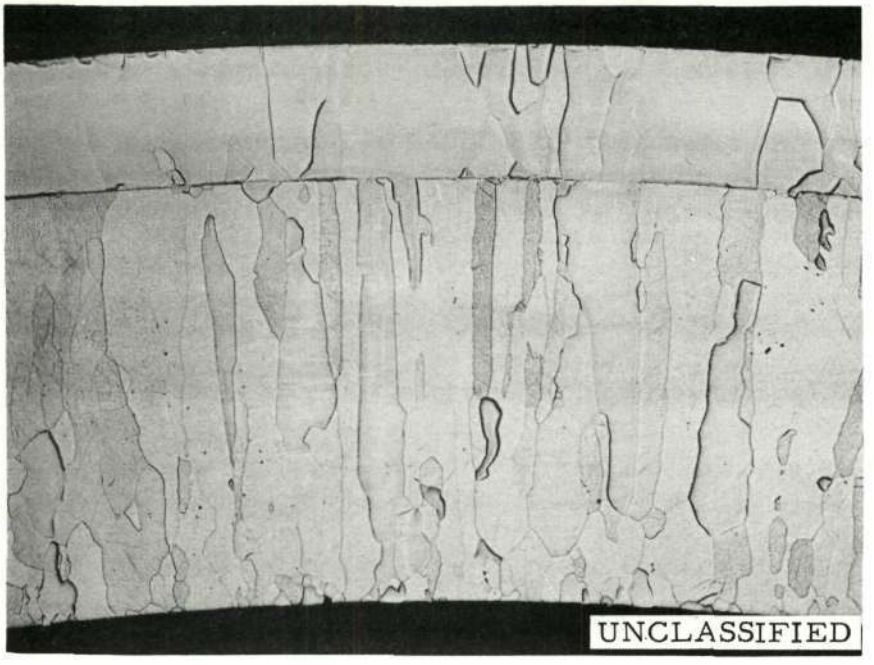

M 31971-6 75X

(k) R-38, pre-test

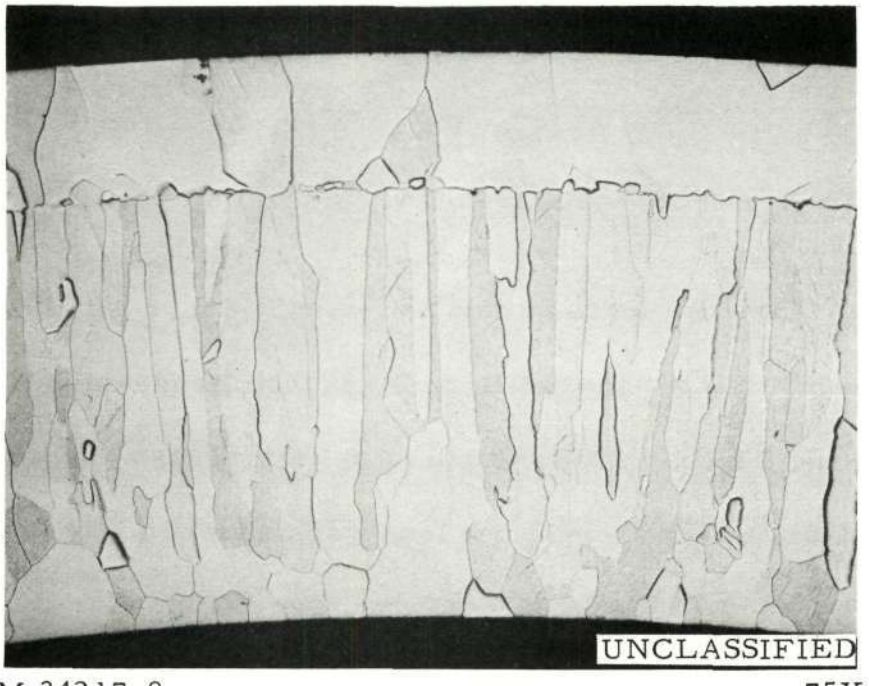

M 34217-8 75X

(l) R-38, post-test

Fig. 98. (U) Comparison of pre-test and post-test microstructures of specimens used for the study of vacuum work function study at 2073°K. Pre-test = 100 hours at 2073°K. Post-test = 600 hours at 2073°K (Sheet 6 of 6)

(U) Table 27 summarizes the vacuum work functions of the test specimens at 2073°K. Stable vacuum work functions were obtained from these specimens after 50 to 100 hours at temperature and no significant changes were observed afterward.

(U) Figures 99 through 104 contain the <110> axes distributions in the test specimens as a function of axial positions after vacuum emission measurements at 2073°K for 500 hours. The tilt angles θ within which 90% of the <110> axes scanned by the X-ray beam are located in these specimens are determined from these figures and included in Table 27 in parenthesis beside the corresponding work function value. In Fig. 105 these data are superposed onto the results shown in Fig. 97. It can be seen that for a given θ value, the spread of the work function value is about 0.1 eV, neglecting the points for $\theta > 14°$. Thus the graphical relationship should allow the prediction of ϕ value from θ value to within ± 0.05 eV.

(U) The work function data shown in Table 25 and Table 27 on specimens of Set A_1, Set A_2 and Set D_2 indicate that the maximum spread in ϕ value over the 2 inch emitting length is in general less than ± 0.06 eV, except for R-14 of Set A_1 and R-35 of Set D_2, which showed axial variation of ϕ values of 0.13 and 0.11 eV respectively. The ϕ values for the specimens of Set A_1 and Set A_2 fall in the range of 4.9 to 5.0 eV, while the ϕ values for the specimens of Set D_2 prepared on the presence of oxygen and nitrogen containments fall in the range of 4.8 to 4.95 eV. Thus the techniques developed

TABLE 27

(U) VACUUM WORK FUNCTIONS OF STABILITY TEST SPECIMENS

(This table is Unclassified)

Specimen Set	Specimen No.	Vacuum Work Function (eV)		
		1/8 Inch From End	1 Inch From End	2 Inches From End
A_1	R-12	4.90 (10°)	4.91 (9.5°)	4.96 (7.5°)
	R-14	4.90 (8°)	4.95 (8°)	5.03 (5.5°)
A_2	R-15	4.91 (7°)	4.91 (7°)	4.93 (6.5°)
	R-17	4.88 (9°)	4.90 (8.5°)	4.92 (7°)
D_2	R-36	4.89 (9°)	4.92 (7.5°)	4.93 (7°)
	R-38	4.84 (11.5°)	4.85 (11°)	4.95 (8.5°)

Note: Angle (in degree) shown in parenthesis beside work function value represents tilt angle θ within which 90% of the <110> axes scanned by X-ray beam are located.

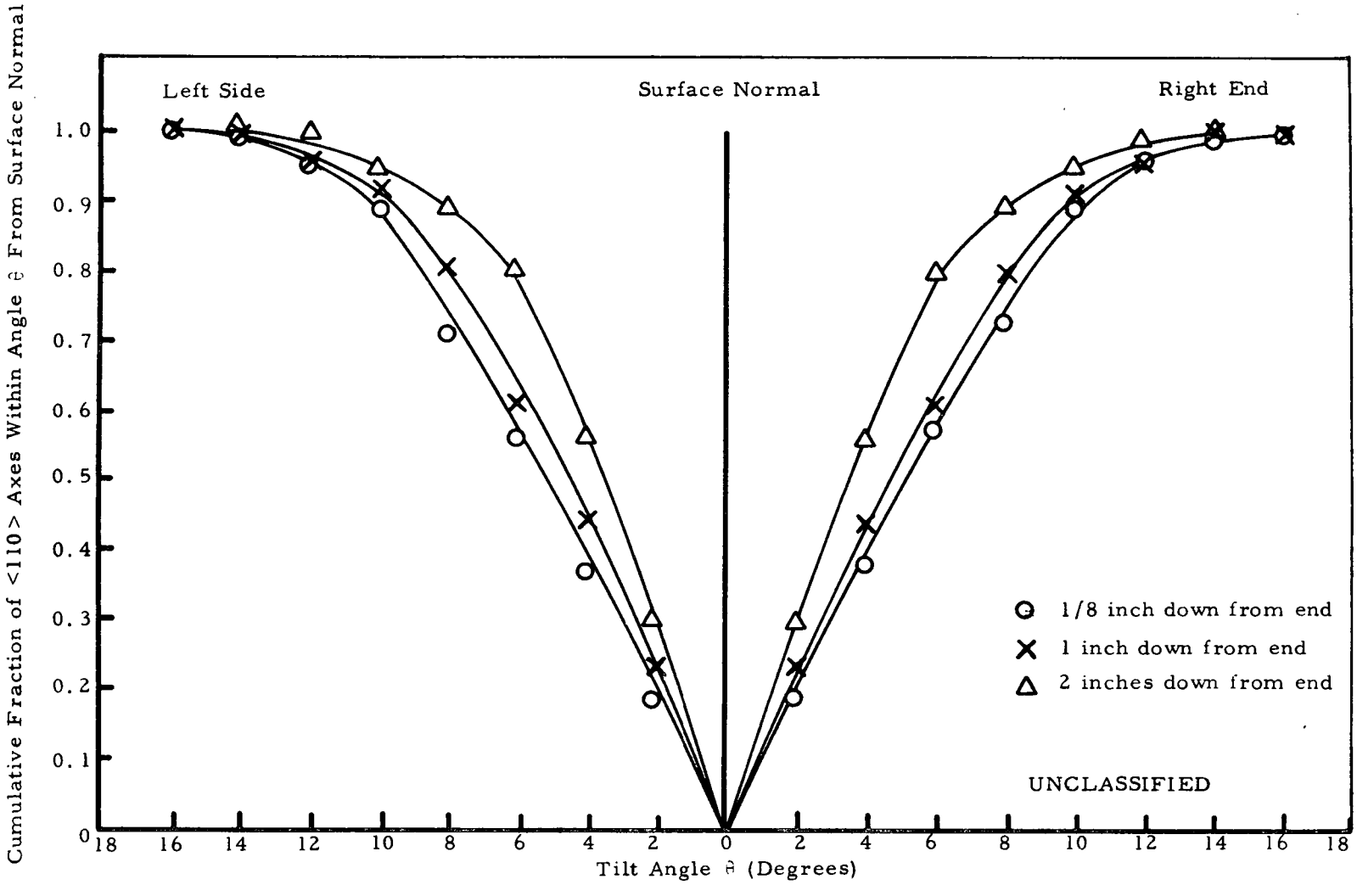

Fig. 99. (U) Distribution of the <110> axes in cylindrical duplex tungsten specimen R-12 after vacuum emission measurements at 2073°K for 500 hours

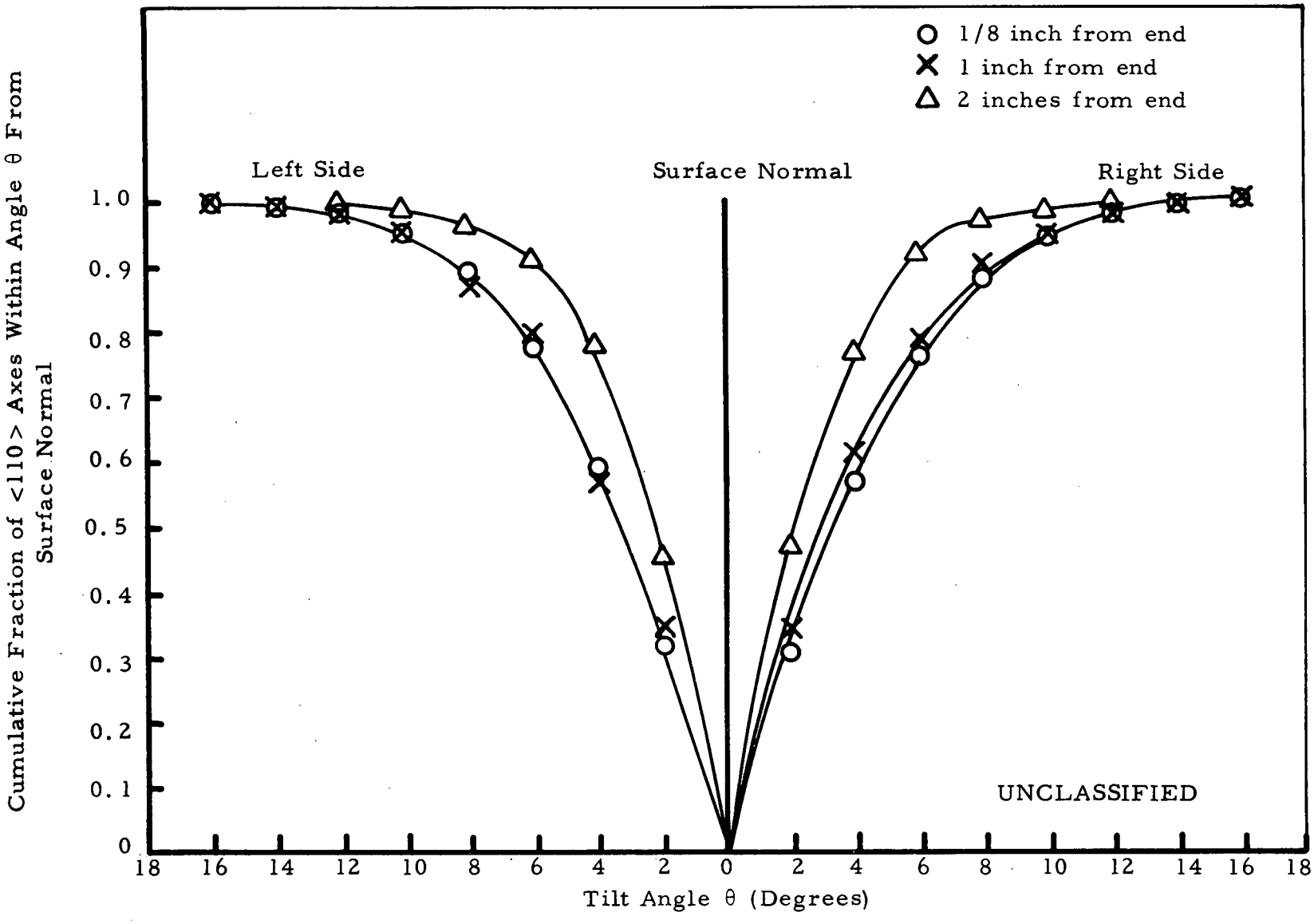

Fig. 100. (U) Distribution of the <110> axes in cylindrical duplex tungsten specimen R-14 after vacuum emission measurements at 2073°K for 500 hours

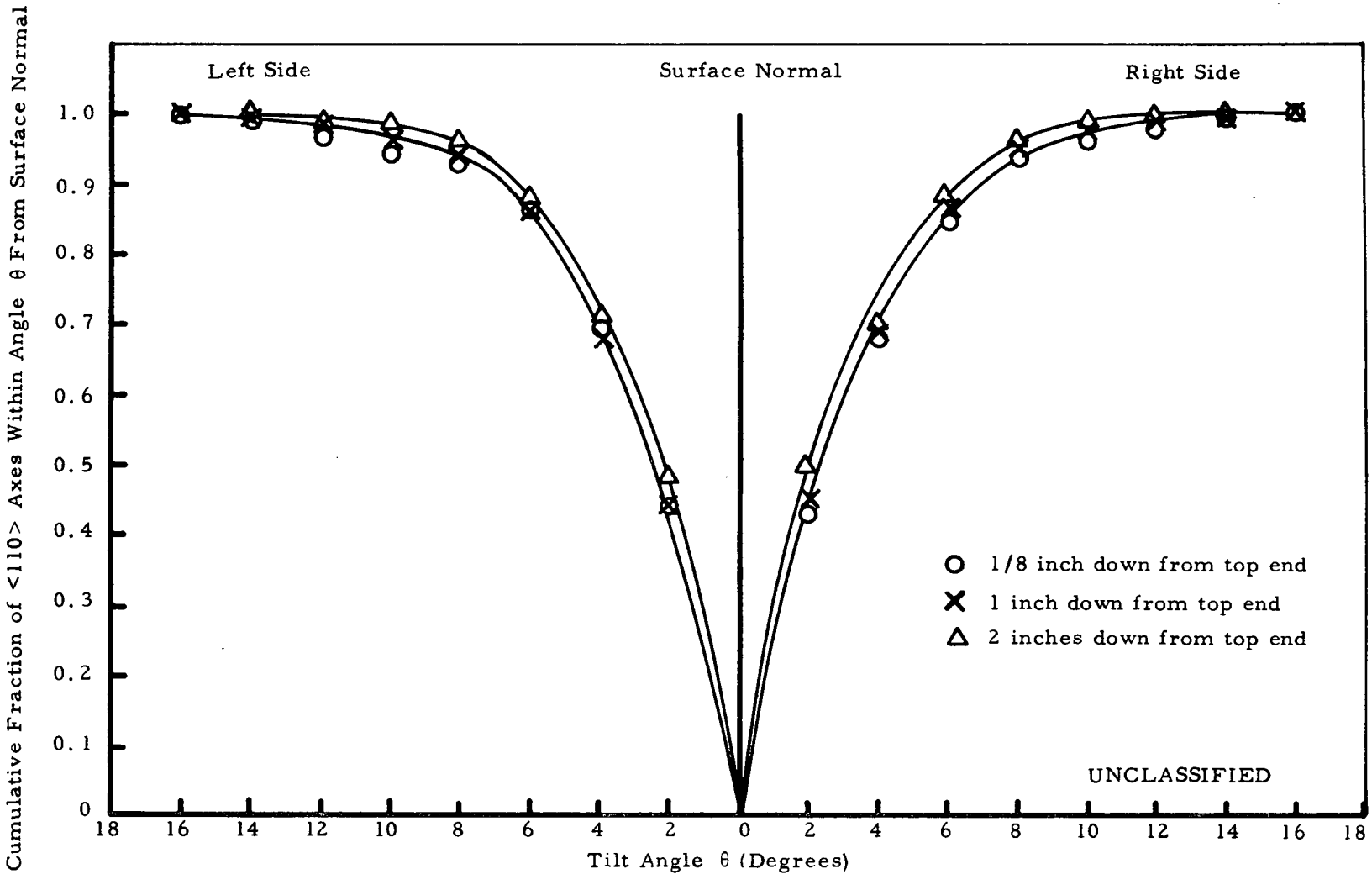

Fig. 101. (U) Distribution of the <110> axes in cylindrical duplex tungsten specimen R-15 after vacuum emission measurements at 2073°K for 500 hours

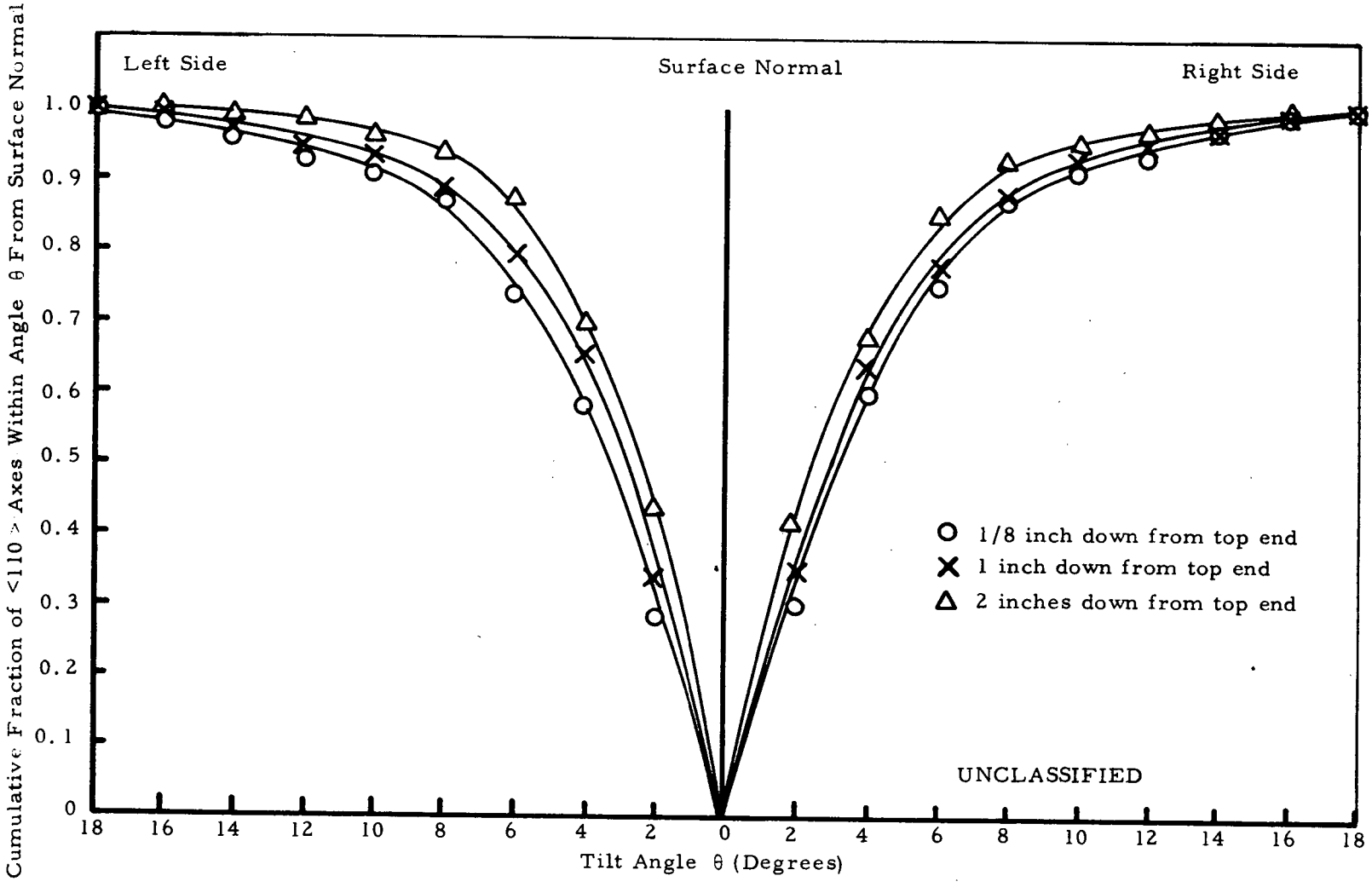

Fig. 102. (U) Distribution of the <110> axes in cylindrical duplex tungsten specimen R-17 after vacuum emission measurements at 2073°K for 500 hours

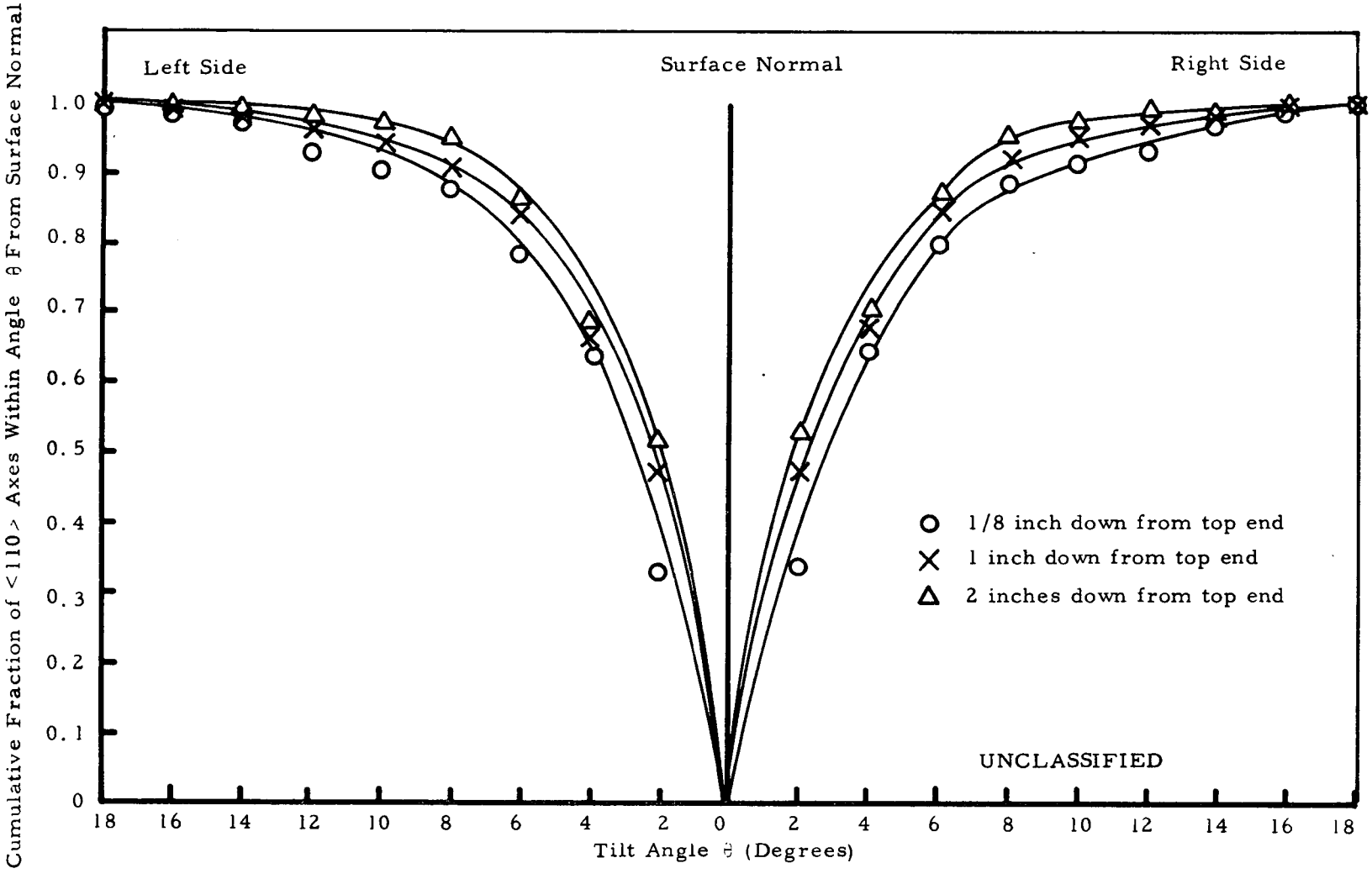

Fig. 103. (U) Distribution of the <110> axes in cylindrical duplex tungsten specimen R-36 after vacuum emission measurements at 2073°K for 500 hours

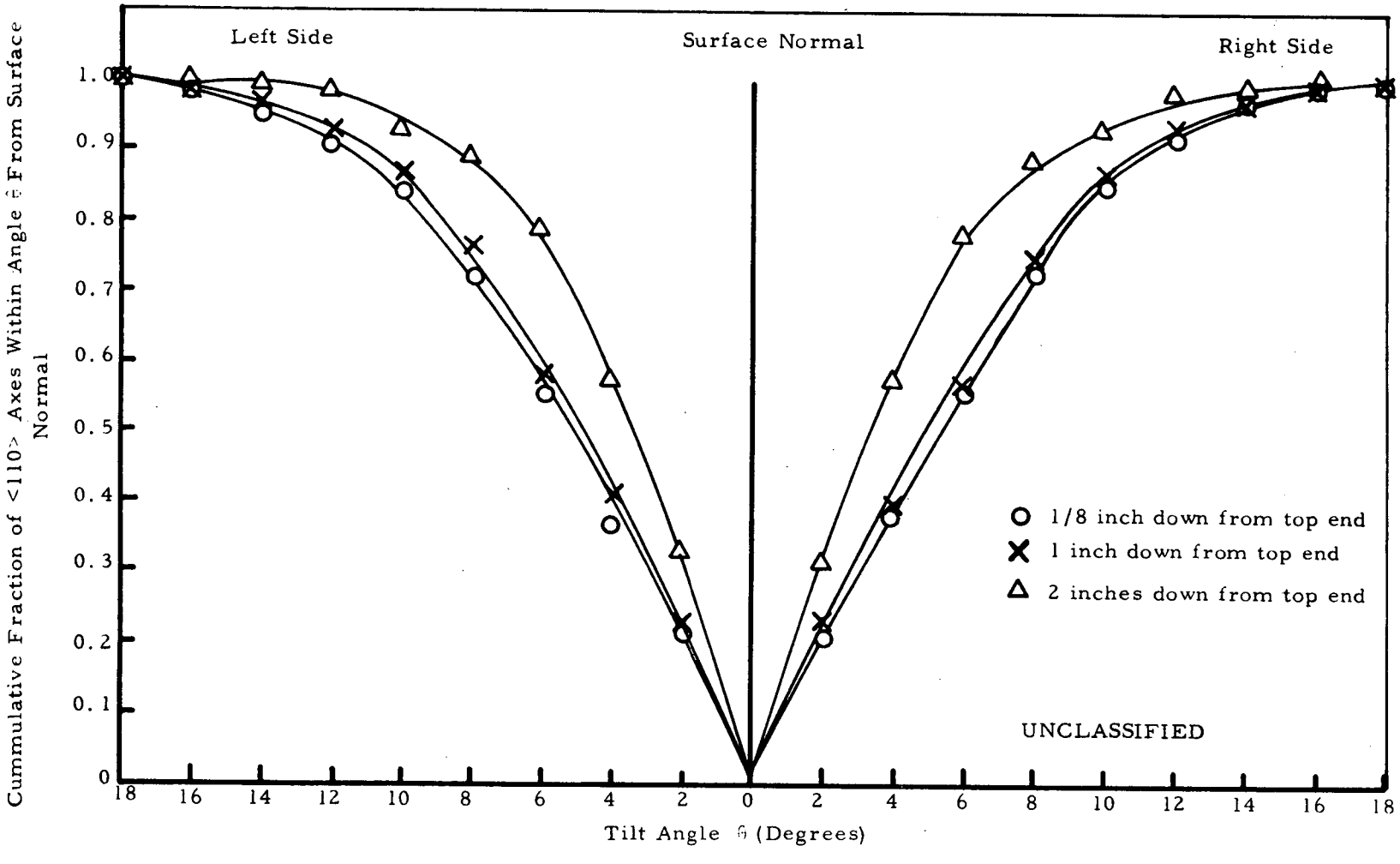

Fig. 104. (U) Distribution of the <110> axes in cylindrical duplex tungsten specimen R-38 after vacuum emission measurements at 2073°K for 500 hours

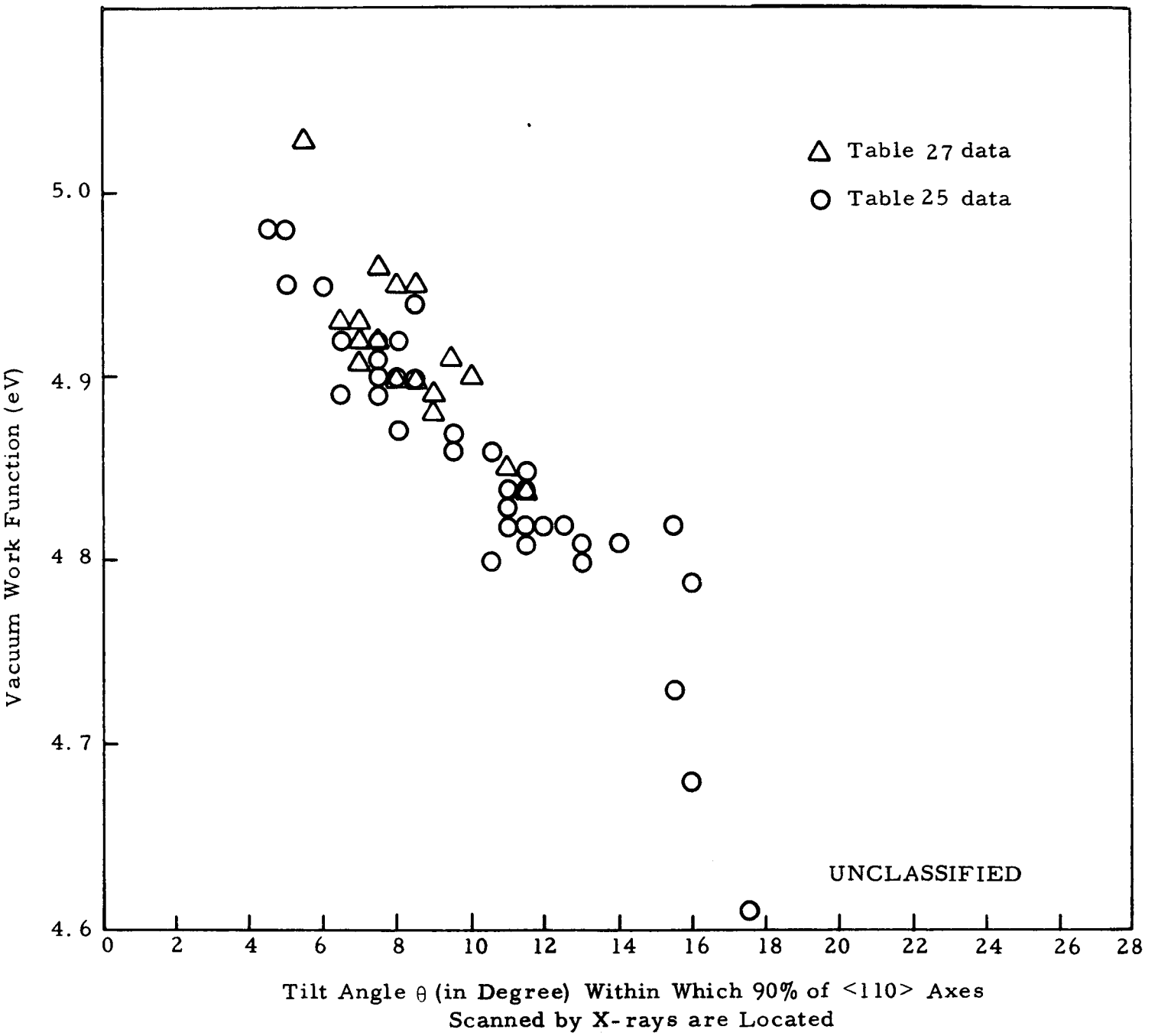

Fig. 105. (U) Superposition of Table 27 data onto Table 25 data

in this work are capable of preparing emitters of ϕ values between 4.9 to 5.0 eV in the absence of oxygen and nitrogen contaminants.

(U) The electron micrographs obtained from the replicas of the surfaces of the six test specimens are similar to that obtained from planar chloride tungsten surface. A typical example is shown in Fig. 106 which was obtained from R-12 of Set A_1.

(U) To assess the long-term stability of the vacuum work functions of the (110) oriented specimens prepared in this work, measurement of the vacuum work function of R-13 was continued after the 250 hour test (see Section 2.3.2.3) for another 4500 hours. Figure 107 shows the test results. It can be seen that the vacuum work function remained stable throughout the 4500 hour test period. Post-test leak check with a helium mass-spectrometer leak detector of 10^{-10} STP c.c./sec sensitivity showed that the specimen was leak tight. Table 28 compares the impurity contents in the specimen before and after the long term test. The change in impurity contents, if any, is small. Figure 108(a) and (b) show respectively the pre-test and the post-test microstructures of R-13. Some grain growth occurred in both the chloride tungsten deposit and the fluoride tungsten substrate. The bond between the two layers, however, remained excellent. Figure 109 contains the plots showing the <110> axes distribution at the three axial locations where the vacuum work functions were measured. The results compared favorably with that for R-13 prior to the 4500 hour test. Electron

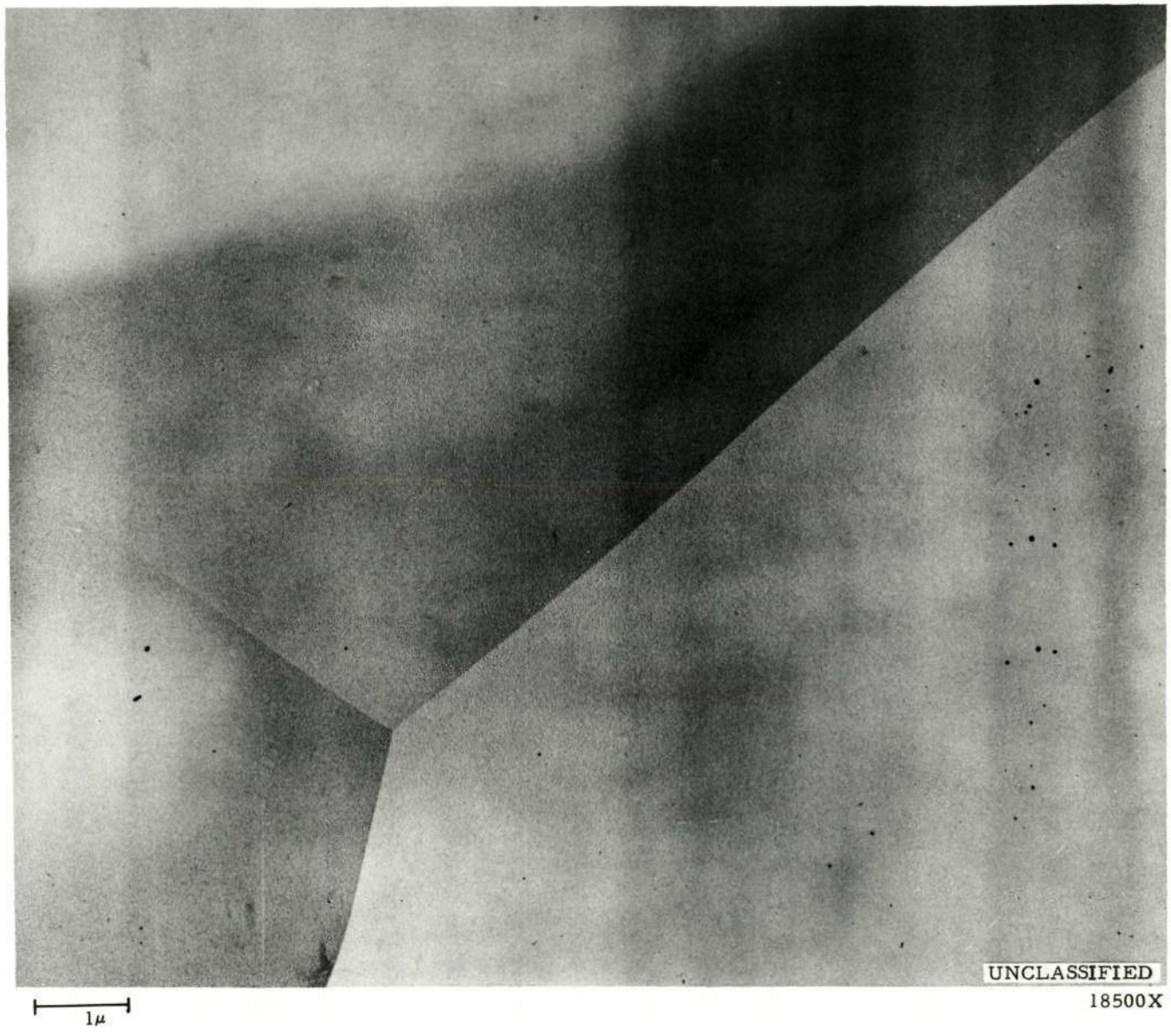

Fig. 106. (U) Electron micrograph of the replica of the surface of R-12 after the 500 hour vacuum work function stability test

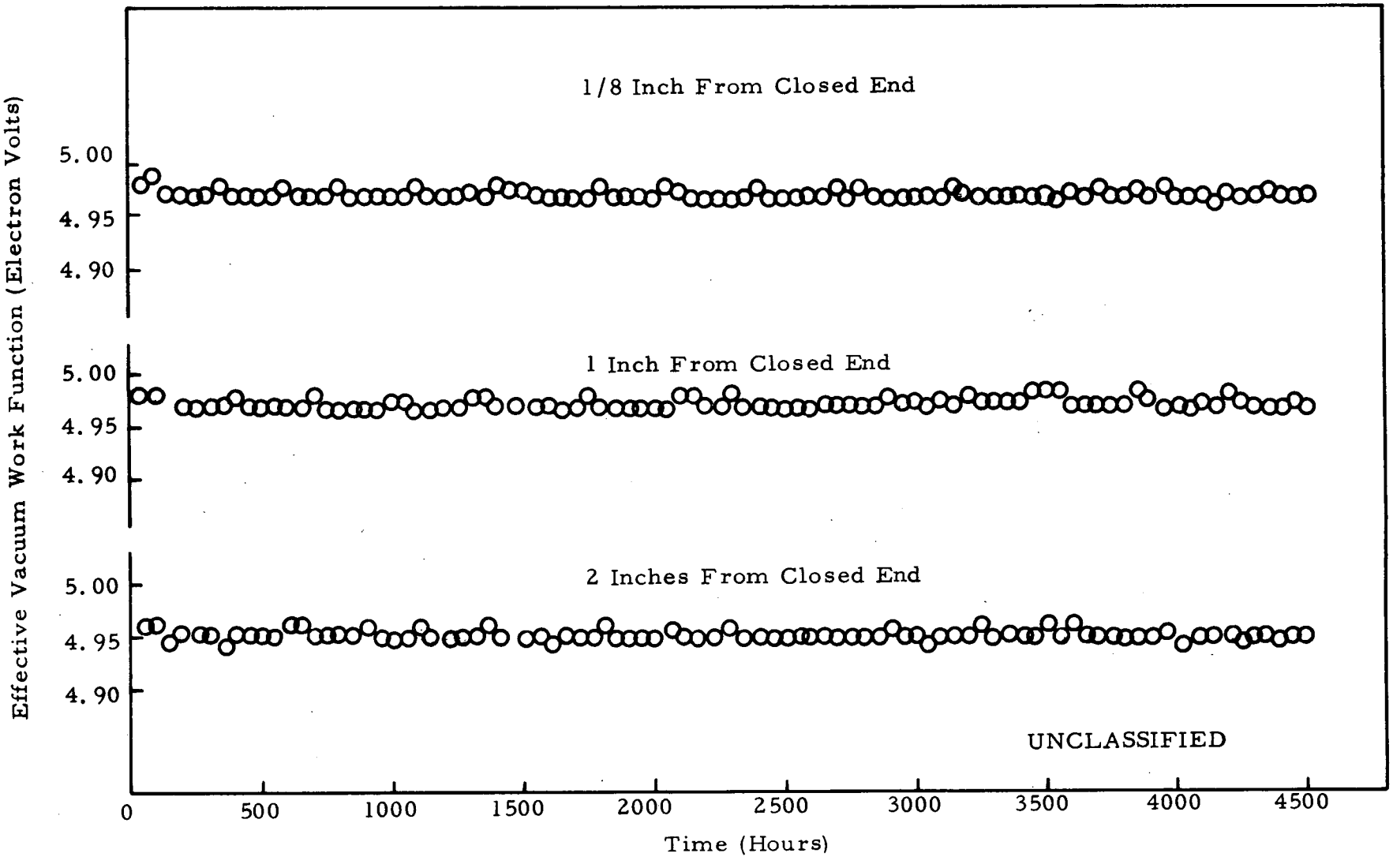

Fig. 107. (U) Effective vacuum work function of cylindrical duplex tungsten sample R-13 as a function of time at 2073°K

TABLE 28

(U) CHEMICAL ANALYSIS OF SAMPLE R-13
(Results are in ppm)
(This table is Unclassified)

Impurities	After 100 Hour Outgas at 2073°K	After 4500 Hour Life Test at 2073°K
N	<1	<1
O	4.0	2.5
C	9.5	6.0
F	1.5	<1.0
Cl	10	5
Metallics	Si <1.0; Fe <4.0 Mg <0.02; Mn <0.1 Ni 0.5; Cu 0.4 Al 0.4	Si <1.0; Fe <4.0 Mg <0.02; Mn <0.1 Ni<0.3; Cu < 0.3 Al< 0.3

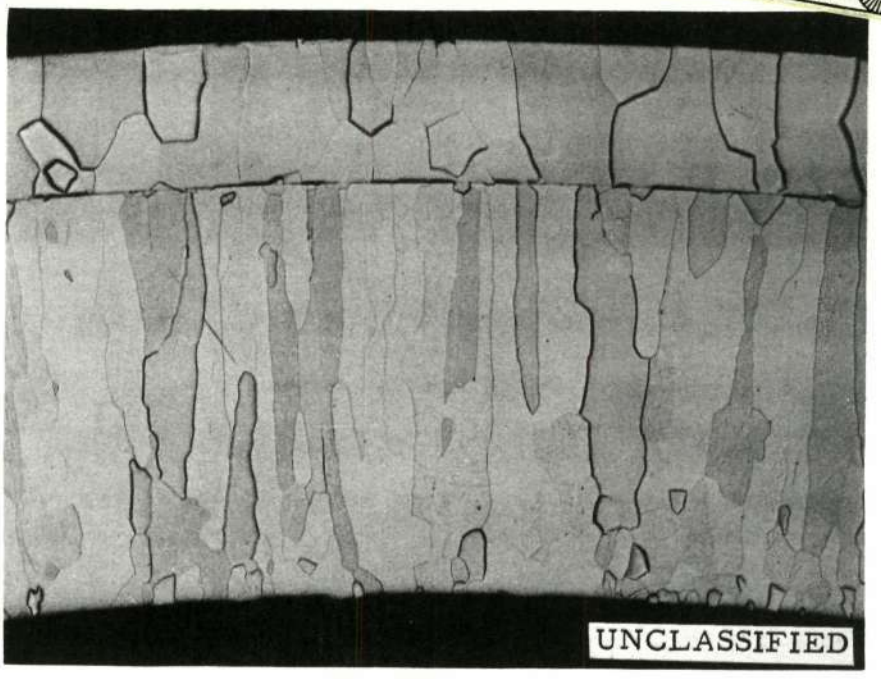

M 31971-3 75X

(a) R-13, pre-test

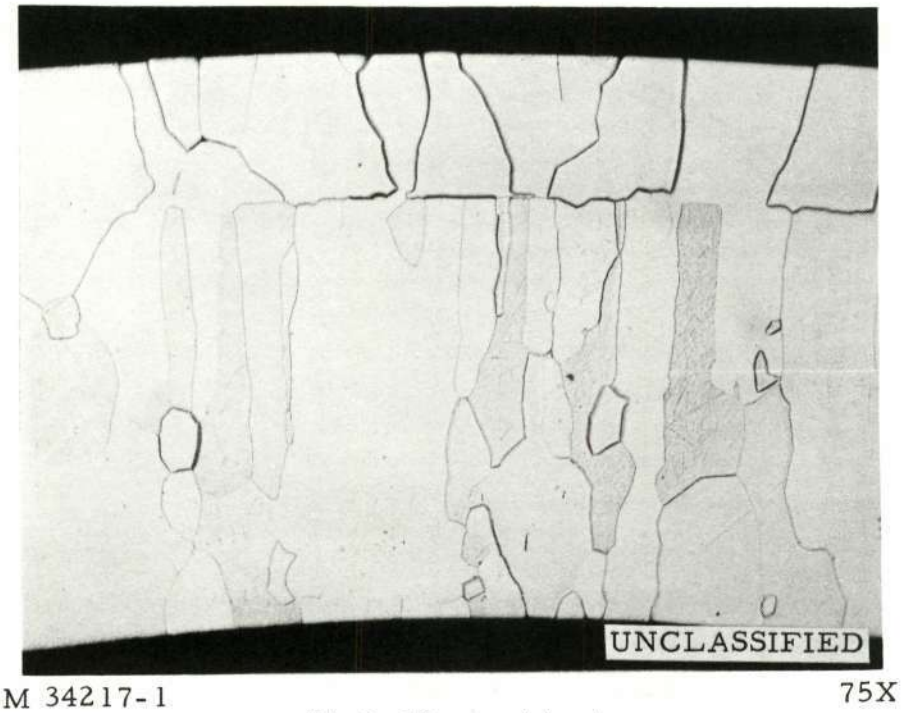

M 34217-1 75X

(b) R-13, post-test

Fig. 108. (U) Comparison of pre-test and post-test microstructures of R-13. Pre-test = 350 hours at 2073°K. Post-test = 4850 hours at 2073°K

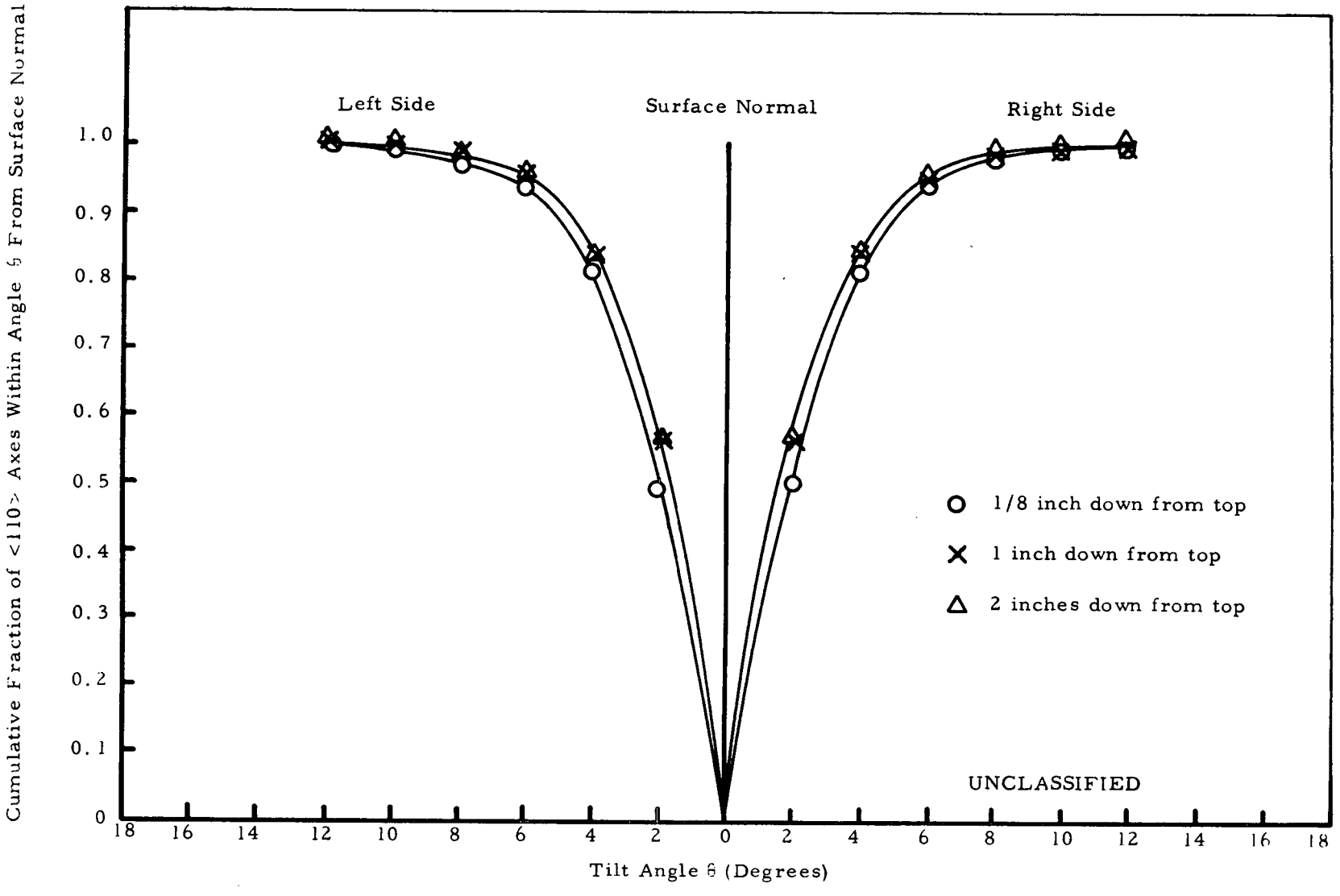

Fig. 109. (U) Distribution of the <110> axes in cylindrical duplex tungsten specimen R-13 after the 4500 hour life test at 2073°K

micrograph obtained from the replica of the surface of R-13 is similar to that shown for R-12 in Fig. 106.

(U) These results demonstrate that cylindrical duplex tungsten emitters prepared by the techniques established in this work can maintain stable and high vacuum work functions (4.9 - 5.0 eV) at temperatures of thermionic interest.

REFERENCES

(1) "Studies of Thermionic Materials For Space Power Applications"(U), Summary Report for the Period November 23, 1965 through January 31, 1967, p. 237, Contract NAS 3-8504, GA-7682, NASA-CR-72315. (C/RD)

(2) "Studies of Thermionic Materials For Space Power Applications"(U), Summary Report for the Period August 1, 1969 through December 7, 1970, p. 5, Contract NAS 3-8504, Gulf-GA-11035, NASA-CR-72947. (C/RD)

(3) "Studies of Thermionic Materials For Space Power Applications"(U), Summary Report for the Period September 1, 1964 through November 23, 1965, p. 165, Contract NAS 3-6471, GA-6860, NASA-CR-54980. (C/RD)

(4) "Studies of Thermionic Materials For Space Power Applications"(U), Summary Report for the Period February 1, 1967 through July 31, 1969, p. 5, Contract NAS 3-8504, GA-8956, NASA-CR-72627. (C/RD)

(5) "Studies of Thermionic Materials For Space Power Applications"(U), Summary Report for the Period August 1, 1969 through December 7, 1970, p. 17 and p. 44, Contract NAS 3-8504, Gulf-GA-11035, NASA-CR-72947. (C/RD)

(6) "Studies of Thermionic Materials For Space Power Applications"(U), Summary Report for the Period November 23, 1965 through September 30, 1968, p. 13, Contract NAS 3-6471, GA-8974, NASA-CR-72517. (C/RD)

(7) "Studies of Thermionic Materials For Space Power Applications"(U), Summary Report for the Period February 1, 1967 through July 31, 1969, p. 115, Contract NAS 3-8504, GA-8956, NASA-CR-72627. (C/RD)

(8) Kaznoff, A. I. and M. J. Sanderson, "Diffusion and Interactions in the Urania-Tungsten and Urania-Molybdenum Systems" (U), International Conference on Thermionic Electrical Power Generation, London, September 20-24, 1965. (C/RD)

REFERENCES (Continued)

(9) "Studies of Thermionic Materials For Space Power Applications" (U), Summary Report for the Period February 1, 1967 through July 31, 1969, p. 185, Contract NAS 3-8504, GA-8956, NASA-CR-72627. (C/RD)

(10) "Studies of Thermionic Materials For Space Power Applications" (U), Summary Report for the Period November 23, 1965 through September 30, 1968, p. 15, Contract NAS 3-6471, GA-8974, NASA-CR-72517. (C/RD)

(11) Yang, L., M. H. Horner and F. L. Cochran, "Post-Operational Examination of Two Carbide-Fueled In-Pile Converters" (U), Contract AT(04-3)-167, Project Agreement No. 14, GA-11004. (C/RD)

(12) "Studies of Thermionic Materials For Space Power Applications" (U), Summary Report for the Period November 23, 1965 through January 31, 1967, p. 140, Contract NAS 3-8504, GA-7682, NASA-CR-72315. (C/RD)

(13) Howard, R. C., L. Van Someren and L. Yang, Conference Record of 1967 Thermionic Conversion Specialist Conference, p. 10.

(14) "Studies of Thermionic Materials For Space Power Applications" (U), Summary Report for the Period November 23, 1965 through January 31, 1967, p. 291, Contract NAS 3-8504, GA-7682, NASA-CR-72315. (C/RD)

(15) Wang, Chi-Chung and James J. Ward, "Performance of Chloride and Fluoride Vapor-Deposited Tungsten Emitters in Thermionic Converters" (U), Conference Record of 1968 Thermionic Conversion Specialist Conference, p. 134.

(This page intentionally left blank)

DISTRIBUTION LIST

1. National Aeronautics and Space Administration
400 Maryland, S. W.
Washington, D. C. 20546
Attention: James J. Lynch, Code NS-1 (1)
Carl Johnson, Code NS-1 (1)

2. National Aeronautics and Space Administration
Lewis Research Center
21000 Brookpark Road
Cleveland, Ohio 44135
Attention: Report Control, MS 5-5 (1)
Technology Utilization Office, MS 3-19 (1)
Library, MS 60-3 (1)
Neal Saunders, MS 105-1 (1)
John W. R. Creagh, MS 49-2 (1)
H. H. Hinckley, MS 500-309 (1)
Roland Breitwieser, MS 302-1 (1)
James Ward, MS 302-1 (1)
Ralph Forman, MS 302-1 (1)
Vince Hlavin, MS 3-10 (1)
L. V. Humble, MS 49-2 (1)
P. L. Donoughe, MS 49-2 (1)

3. National Aeronautics and Space Administration
Manned Spacecraft Center
Attention: Technical Information Program Division
Houston, Texas 77058
For: B. J. Bragg (1)
W. Eugene Rice (1)

4. National Aeronautics and Space Administration
Marshall Space Flight Center
Huntsville, Alabama 35812
Attention: Library
For: Robert Aden (1)

5. National Aeronautics and Space Administration
Scientific and Technical Information Facility
P. O. Box 33
College Park, Maryland 20740
Attention: NASA Representative (10)

6. National Aeronautics and Space Administration
Ames Research Center
Moffett Field, California 94035
Attention: Library (1)

7. National Aeronautics and Space Administration
Goddard Space Flight Center
Greenbelt, Maryland 20771
Attention: Library (1)
Joseph Epstein (1)

8. National Aeronautics and Space Administration
Langley Research Center
Langley Field, Virginia 23365
Attention: Library (1)

9. Aerojet General Nucleonics
San Ramon, California 94583
Attention: Library (1)

10. Aerospace Corporation
P. O. Box 95085
Los Angeles, California 90045
Attention: Library (1)

11. Air Force Cambridge Research Laboratories
L. G. Hanscom Field
Bedford, Massachusetts 01731
Attention: CRZAP (1)

12. Air Force Weapons Laboratory
Kirtland Air Force Base
New Mexico 87117
Attention: Library (1)

13. Babcock and Wilcox Company
1201 Kemper Street
Lynchburg, Virginia 24501
Attention: Library (1)

14. Battelle Memorial Institute
505 King Avenue
Columbus, Ohio 43201
Attention: Don Kizer (1)
Don Keller (1)

15. The Boeing Company
P. O. Box 3707
Seattle, Washington 98101
Attention: Library (1)

16. Electro-Optical Systems, Inc.
300 North Halstead Street
Pasadena, California 91107
Attention: A. Jensen (1)

17. Fairchild-Hiller
Republic Aviation Division
Farmingdale, L. I., New York 11735
Attention: Alfred Schock (1)

18. General Electric Company
Electronic Components Division
One River Road
Schenectady, New York 12306
Attention: Dr. D. A. Wilbur,
Manager-Tube Research (1)

19. General Electric Company
Nuclear Systems Programs
P. O. Box 132
Evendale, Ohio 45215
Attention: J. E. Wood (1)

20. General Electric Company
Research Laboratory
Schenectady, New York 12300
Attention: Volney C. Wilson (1)

21. General Electric Company
Missile and Space Division
P. O. Box 8555
Philadelphia, Pennsylvania 19101
Attention: ANSE (1)

22. General Electric Company
Knolls Atomic Power Laboratory
Schenectady, New York 12300
Attention: R. Ehrlich (1)

23. General Motors Corporation
Research Laboratories
12 Mile and Mound Roads
Warren, Michigan 48092
Attention: F. E. Jamerson (1)

24. Institute for Defense Analysis
400 Army Navy Drive
Arlington, Virginia 48092
Attention: R. C. Hamilton (1)

25. McDonnell Douglas Corporation
Missile and Space Engineering
Nuclear Research (A2-260)
3000 Ocean Park Boulevard
Santa Monica, California 90405
Attention: Library (1)

26. Jet Propulsion Laboratory
California Institute of Technology
4800 Oak Grove Drive
Pasadena, California 91103
Attention: Peter Rouklove (1)
J. Mondt (1)
V. Truscello (1)

27. Lockheed Missile and Space Division
Lockheed Aircraft Corporation
Sunnyvale, California 94086
Attention: H. H. Greenfield (1)

28. Los Alamos Scientific Laboratory
P. O. Box 1663
Los Alamos, New Mexico 87544
Attention: W. A. Ranken (1)

29. Marquardt Corporation
Astro Division
16555 Saticoy Street
Van Nuys, California 91406
Attention: A. N. Thomas (1)

30. Naval Ship Systems Command
Department of the Navy
Washington, D. C. 20360
Attention: E. P. Lewis, Code 08 (1)

31. North American Rockwell Corporation
Atomics International Division
P. O. Box 309
Canoga Park, California 91305
Attention: Robert C. Allen (1)
Charles E. Smith (1)

32. North American Rockwell Corporation
S&ID Division
12214 Lakewood Boulevard
Downey, California 90241
Attention: C. L. Gould (1)

33. Oak Ridge National Laboratory
Oak Ridge, Tennessee 37831
Attention: Library
For: A. C. Schaffhauser (1)

34. Office of Naval Research
Power Branch
Department of the Navy
Washington D. C. 20325
Attention: Cmdr. Ollie J. Loper (1)

35. Radiation Effects Information Center
Battelle Memorial Institute
505 King Avenue
Columbus, Ohio 43201
Attention: R. E. Bowman (1)

36. Radio Corporation of America
New Holland Avenue
P. O. Box 1140
Lancaster, Pennsylvania 17601
Attention: Fred Block (1)

37. Radio Corporation of America
David Sarnoff Research Center
Princeton, New Jersey 08640
Attention: Paul Rappaport (1)

38. The Rand Corporation
1700 Main Street
Santa Monica, California 90401
Attention: Ben Pinkel (1)

39. Space Systems Division (SSTRE)
AF Unit Post Office
Los Angeles, California 90045
Attention: Major W. Iller (1)

40. Thermo Electron Corporation
85 First Avenue
Waltham, Massachusetts 02154
Attention: George Hatsopoulous (1)
Robert Howard (1)

41. TRW Inc.
TRW Systems Group
One Space Park
Redondo Beach, California 90278
Attention: Library (1)

42. United Aircraft Corporation
Pratt & Whitney Aircraft Division
East Hartford, Connecticut 06108
Attention: Library (1)

43. U. S. Army Erdl
Fort Monmouth, New Jersey 07703
Attention: Emil Kittl (1)

44. U. S. Atomic Energy Commission
Space Nuclear Systems Division, F309
Reactor Power Systems Branch
Washington, D. C. 20545
Attention: D. S. Beard (1)

45. U.S. Atomic Energy Commission
Technical Reports Library
Washington, D. C. 20545
Attention: J. M. O'Leary (3)

46. U. S. Atomic Energy Commission
Division of Technical Information Extension
P. O. Box 62
Oak Ridge, Tennessee 37831 (3)

47. Varian Associates
611 Hansen Way
Palo Alto, California 94304
Attention: Ira Weismann (1)

48. Westinghouse Electric Corporation
Astronuclear Laboratory
Attention: Document Custodian
P. O. Box 10864
Pittsburgh, Pennsylvania 15236
For: Carrol Sinclair (1)